NASA TECHNICAL HANDBOOK

NASA-HDBK-6024

National Aeronautics and Space Administration
Washington, DC 20546-0001

Approved: 06-27-2014

SPACECRAFT POLYMERS ATOMIC OXYGEN DURABILITY HANDBOOK

MEASUREMENT SYSTEM IDENTIFICATION: METRIC (SI)

DOCUMENT HISTORY LOG

Status	Document Revision	Approval Date	Description
Baseline		06-27-2014	Initial Release

FOREWORD

This Handbook is published by the National Aeronautics and Space Administration (NASA) as a guidance document to provide engineering information; lessons learned; possible options to address technical issues; classification of similar items, materials, or processes; interpretative direction and techniques; and any other type of guidance information that may help the Government or its contractors in the design, construction, selection, management, support, or operation of systems, products, processes, or services. This Handbook specifically provides information on low Earth orbit (LEO) atomic oxygen and atomic oxygen interaction with materials, particularly erosion of organic materials.

This Handbook is approved for use by NASA Headquarters and NASA Centers, including Component Facilities and Technical and Service Support Centers.

This Handbook establishes a source reference for the determination of atomic oxygen erosion durability of polymers being considered for spaceflight and provides spacecraft designers with materials durability data for long-duration exposure to the LEO atomic oxygen environment.

Requests for information, corrections, or additions to this Handbook should be submitted via "Feedback" in the NASA Standards and Technical Assistance Resource Tool at http://standards.nasa.gov.

Original Signed By: **06/27/2014**

Ralph R. Roe, Jr. Approval Date

NASA Chief Engineer

TABLE OF CONTENTS

TABLE OF CONTENTS (Continued)

TABLE OF CONTENTS (Continued)

APPENDICES

LIST OF FIGURES

LIST OF FIGURES (Continued)

LIST OF FIGURES (Continued)

LIST OF TABLES

SPACECRAFT POLYMERS
ATOMIC OXYGEN DURABILITY HANDBOOK

1. SCOPE

1.1 Purpose

The purpose of this Handbook is to provide spacecraft designers with materials durability data for long-duration exposure to the low Earth orbit (LEO) atomic oxygen environment. The Handbook provides spacecraft designers a single source for the determination of atomic oxygen erosion durability of polymers being considered for spaceflight.

This Handbook provides background information on LEO atomic oxygen and documents the atomic oxygen erosion yield (E_y, volume loss per incident oxygen atom (cm^3/atom)) of 38 different polymer materials and pyrolytic graphite, which were exposed to LEO atomic oxygen for ~4 years on the exterior of the International Space Station (ISS). Also included in this Handbook are ground-laboratory to in-space correlation data for 38 polymer materials and pyrolytic graphite in a radio frequency (RF) plasma asher, optical property changes for 38 polymer materials and pyrolytic graphite after 4 years of space exposure, an atomic oxygen erosion yield predictive tool that allows the prediction of erosion yields of new or non-flown polymers, tools for using atomic oxygen erosion yield data for spacecraft durability applications, and lessons learned on the environmental durability of spacecraft materials from spaceflight experiments.

1.2 Applicability

To the extent specified or referenced in governing documents, this Handbook is applicable to space systems that have atomic oxygen durability requirements.

Spacecraft performance and durability rely upon the space environmental durability of many polymer-containing components, such as thermal control blankets, solar array blankets, and composite structural materials. Such components are almost always subject to atomic oxygen degradation if the spacecraft spends any duration of its mission in LEO.

This Handbook is approved for use by the National Aeronautics and Space Administration (NASA) Headquarters and NASA Centers, including Component Facilities and Technical and Service Support Centers. This Handbook may also apply to the Jet Propulsion Laboratory or to other contractors, grant recipients, or parties to agreements only to the extent specified or referenced in their contracts, grants, or agreements.

This Handbook, or portions thereof, may be referenced in contract, program, and other Agency documents for guidance. When this Handbook contains procedural or process requirements, they may be cited in contract, program, and other Agency documents for guidance.

2. APPLICABLE DOCUMENTS

None.

3. ACRONYMS AND DEFINITIONS

3.1 Acronyms and Abbreviations

^3P	triplet P
~	approximately
≈	approximately equal
≥	equal to or greater than
>	greater than
<	less than
≤	less than or equal to
±	plus or minus
μm	micrometer(s)
α_s	solar absorptance
∂	partial derivative
δ	uncertainty
ε	thermal emittance
π	pi
σ	standard deviation
Σ	sum of
Å	angstrom(s)
°	degree(s)
°C	degree(s) Celsius
#	number
%	percent
®	registered trademark
™	trademark
ABS	acrylonitrile butadiene styrene
ADC	allyl diglycol carbonate
AF	amorphous fluoropolymer
AFM	atomic force microscopy
Ag-FEP	silvered fluorinated ethylene propylene
AIAA	American Institute of Aeronautics and Astronautics
AIP	American Institute of Physics
AL	Alabama
Al	aluminum atom
Al_2O_3	aluminum oxide
Al-FEP	aluminized fluorinated ethylene propylene
AO	atomic oxygen
Ar	argon atom
ASTM	ASTM, International (formerly American Society for Testing and Materials)

Au	gold atom
AVS	American Vacuum Society
AZ	Arizona
BPDA	biphenyltetracarboxylic dianhydride
C	carbon atom
C	coulomb
CA	California
CA	cellulose acetate
CH_2	methylene
CH_3	methyl
CCl_4	carbon tetrachloride
$CHBr_3$	bromoform
cm	centimeter(s)
CO	carbon monoxide
CO	Colorado
COTS	Commercial Orbital Transportation System
CP	conference proceedings
CR	contract report
CsCl	cesium chloride
CTFE	chlorotrifluoroethylene
CVCM	collected volatile condensable material
CVD	chemical vapor deposition
DoD	Department of Defense
DR	diffuse reflectance
DT	diffuse transmittance
ECTFE	ethylene-chlorotrifluoroethylene
ELC	EXPRESS Logistics Carrier
EOIM I	Effects of Oxygen Interactions with Materials I; also Evaluation of Oxygen Interactions with Materials I
EOIM III	Evaluation of Oxygen Interactions with Materials III
EP	epoxide; epoxy
ESA	European Space Agency
ESH	equivalent sun hours
ETFE	ethylene-tetrafluoroethylene
EURECA	European Retrievable Carrier
eV	electron volt(s)
EVA	extravehicular activity
EXPRESS	EXpedite the PRocessing of Experiments in Space Station
FEP	fluorinated ethylene propylene
FL	Florida
g	gram(s)
Ge	germanium atom
GRC	Glenn Research Center
H_2O	water
H	hydrogen atom
HCO	aldehyde

He	helium atom
HPGT	high-pressure gas tank
hr	hour(s)
HST	Hubble Space Telescope
IAC	International Astronautical Congress
ICPMSE	International Space Conference on Protection of Materials and Structures from the Space Environment
IEEE	Institute of Electrical and Electronics Engineers
ISMSE	International Symposium on Materials in the Space Environment
ISS	International Space Station
ITO	indium tin oxide
JAXA	Japanese Aerospace Exploration Agency
JPL	Jet Propulsion Laboratory
JSC	Johnson Space Center
K	degree(s) Kelvin
kg	kilogram(s)
km	kilometer(s)
kmol	kilomol(s)
krad	kilorad(s)
kV	kilovolt(s)
LaRC	Langley Research Center
LeRC	Lewis Research Center
LDEF	Long Duration Exposure Facility
LEO	low Earth orbit
LLC	limited liability company
m	meter(s)
m	milli
MA	Massachusetts
MD	Maryland
mg	milligram(s)
MHz	megahertz
MIL	military
mil	one thousandth of an inch (0.0254 mm)
MISSE	Materials International Space Station Experiment
mL	milliliter(s)
mm	millimeter(s)
MMOD	micrometeoroids and orbital debris
MRS	Materials Research Society
MSDS	Material Safety Data Sheet
MSFC	Marshall Space Flight Center
MSIS-86	Mass Spectrometer-Incoherent Scattered-86 (model)
MW	Merriam-Webster (dictionary)
N_2	diatomic nitrogen
N/A	not applicable
NASA	National Aeronautics and Space Administration

NATO	North Atlantic Treaty Organization
nm	nanometer(s)
NOAA	National Oceanic and Atmospheric Administration
NRL	Naval Research Center
NSMMS	National Space & Missile Materials Symposium
NV	Nevada
NY	New York
O	oxygen atom
O_2	diatomic oxygen
O_3	ozone
ODA	oxydianiline
OH	Ohio
ORMatE-III R/W	Optical Reflector Materials Experiment III Ram/Wake
PA	Pennsylvania
Pa	pascal(s)
PA 6	polyamide 6
PA 66	polyamide 66
PAN	polyacrylonitrile
PBI	polybenzimidazole
PBO	poly(p-phenylene-2 6-benzobisoxazole)
PBT	polybutylene terephthalate
PC	polycarbonate
PE	polyethylene
PEACE	Polymer Erosion And Contamination Experiment
PEC	Passive Experiment Container
PEEK	polyetheretherketone
PEI	polyetherimide
PEO	polyethylene oxide
PET	polyethylene terephthalate
PFA	perfluoroalkoxy copolymer resin
PG	pyrolytic graphite
PI	polyimide
PMDA	pyromellitic acid dianhydride
PMMA	polymethyl methacrylate
PMR	polymerization of monomer reactants
POM	polyoxymethylene
PP	polypropylene
PPD-T	poly-(p-phenylene terephthalamide)
PPPA	polyphenylene isophthalate
PS	polystyrene
PSU	polysulfone
PTFE	polytetrafluoroethylene
PU	polyurethane
PVDF	polyvinylidene fluoride
PVF	polyvinylfluoride
PVF-W	polyvinylfluoride (white Tedlar®)

RF	radio frequency
RI	Rhode Island
SAMPE	Society for the Advancement of Material and Process Engineering
sec	second(s)
SEE	Space Environmental Effects
SEED	Space Environment Exposure Device
SEM	scanning electron microscopy
SI	Système International
Si	silicon atom
SiO_2	silica
SM2	Servicing Mission 2
SM/MPAC	Service Module/Micro-Particles Capturer
SP	special publication
SPRAT	Space Photovoltaic Research and Technical Conference
SR	specular reflectance
ST	specular transmittance
STD	standard
STS	Space Transportation System
TLD	thermo-luminescent dosimeter
TM	technical memorandum
TMS	The Minerals, Metals & Materials Society
TML	total mass loss
TOPS	Technical Operations Support
TR	total reflectance
TT	total transmittance
TX	Texas
U.S.	United States
UK	United Kingdom
USAF	United States Air Force
UV	ultraviolet
VA	Virginia
VUV	vacuum ultraviolet
W	watt(s)
WPAFB AFRL	Wright-Patterson Air Force Base, Air Force Research Laboratory
XPS	x-ray photoelectron spectroscopy
yr	year(s)

3.2 Definitions

Atomic Oxygen Erosion: For the purposes of this Handbook, the thickness loss of a polymer (or other material that has volatile oxidation products), as a result of reaction with atomic oxygen. Generally, atomic oxygen erosion is measured in terms of mass loss per area but can also be measured as thickness loss through recession.

Erosion Yield: The volume loss per incident atomic oxygen atom, expressed in cm^3/atom. Knowing the density of a polymer, its mass loss, and the number of oxygen atoms that have arrived, the atomic oxygen erosion yield can then be calculated based on mass loss. The term erosion yield does not have meaning for polymers or materials that have nonvolatile oxidation products. For such materials, such as silicones, there may be degradation by oxidation without significant change in mass.

3.3 Symbols

A	mass fraction ash in the material
A_K	surface area of Kapton® H witness sample exposed to atomic oxygen (cm^2)
A_s	surface area of the test sample exposed to atomic oxygen (cm^2)
$C_{C/t}$	coefficient for the ratio of number of carbon atoms to total atoms in the repeat unit
$C_{Cl/C}$	coefficient for the ratio of number of chlorine atoms to carbon atoms in the repeat unit
$C_{Cl/t}$	coefficient for the ratio of number of chlorine atoms to total atoms in the repeat unit
$C_{dO/t}$	coefficient for the ratio of number of double bonded oxygen atoms to total atoms in the repeat unit
$C_{F/C}$	coefficient for the ratio of number of fluorine atoms to carbon atoms in the repeat unit
$C_{F/t}$	coefficient for the ratio of number of fluorine atoms to total atoms in the repeat unit
$C_{H/C}$	coefficient for the ratio of number of hydrogen atoms to carbon atoms in the repeat unit
$C_{H/t}$	coefficient for the ratio of number of hydrogen atoms to total atoms in the repeat unit
$C_{N/C}$	coefficient for the ratio of number of nitrogen atoms to carbon atoms in the repeat unit
$C_{N/t}$	coefficient for the ratio of number of nitrogen atoms to total atoms in the repeat unit
C_O	proportionality constant that resulted from the best-fit linear equation relating the measured atomic erosion yield to predicted erosion yield
$C_{O/C}$	coefficient for the ratio of number of oxygen atoms to carbon atoms in the repeat unit
$C_{S/C}$	coefficient for the ratio of number of sulfur atoms to carbon atoms in the repeat unit
$C_{sO/t}$	coefficient for the ratio of number of single bonded oxygen atoms to total atoms in the repeat unit
$C_{S/t}$	coefficient for the ratio of number of sulfur atoms to total atoms in the repeat unit
C_ρ	coefficient for the density of the material

$C_{\Sigma/r}$	coefficient for ratio of the sum of the volume of the atoms making up the polymer repeat unit based on their covalent radii to actual volume of the repeat unit determined based on its chemical structure, molecular weight and density
D	diameter of exposed area of sample
D_K	diameter of exposed area of Kapton® H
D_{K1}	diameter of exposed area of Kapton® H sample 1
D_{K2}	diameter of exposed area of Kapton® H sample 2
D_S	exposed diameter of flight sample
e	electron charge (1.6×10^{-19} C)
E	atomic oxygen erosion yield, cm^3/atom
E_1	situation 1 erosion yield
E_2	situation 2 erosion yield
E_3	situation 3 erosion yield
E_A	actual erosion yield (cm^3/atom)
E_K	erosion yield of Kapton® H witness sample in LEO (3.0×10^{-24} cm^3/atom)
E_{PE}	ram energy at perigee for equatorial orbits (eV)
E_R	atomic oxygen erosion resistance (atoms/cm^3) or erosion resistance of the mixed material
E_{Rf}	atomic oxygen erosion resistance of fibers (atoms/cm^3)
E_{Rp}	atomic oxygen erosion resistance of polymer matrix (atoms/cm^3)
E_S	sample erosion yield
E_y	atomic oxygen erosion yield of a material (cm^3/atom)
E_{ya}	erosion yield of epoxy with ash content (cm^3/atom)
E_{yf}	atomic oxygen erosion yield of the fibers in the composite (cm^3/atom)
E_{yo}	erosion yield of epoxy without any ash content in end Hall test (cm^3/atom)
E_{yp}	atomic oxygen erosion yield of the polymer in the composite (cm^3/atom)
F	fluence of atomic oxygen (atoms/cm^2)
$F_{AVG\,K}$	average of the F values of the two Kapton® H witness samples
F_E	atomic oxygen Kapton® H effective fluence in ground laboratory facility (atoms/cm^2)
F_f	fractional volume fill of fibers in the composite or fractional volume of fibers in the composite
F_K	fluence of Kapton® witness sample
F_p	fractional volume of polymer in the composite
G	gravitational constant (6.67×10^{-11} $N\cdot m^2/kg^2$)
K	erosion yield attenuation constant
M_A	average sample mass per layer (g)
M_C	pre-flight mass of control sample Part A (g)
M_E	mass of Earth (6.67×10^{24} kg)

M'_E	post-flight mass of flight sample Part B (g)
M_F	pre-flight mass of flight sample Part A (g)
M'_F	post-flight mass of flight sample Part A (g)
M'_S	post-flight mass of flight sample Parts A and B weighed together (entire sample) (g)
m_o	mass of an oxygen atom (2.66×10^{-26} kg)
n	number of sample layers
N	total number of layers
N_C	number of carbon atoms in the repeat unit
N_{Cl}	number of chlorine atoms in the repeat unit
N_{dO}	number of double bonded oxygen atoms in the repeat unit
N_F	number of fluorine atoms in the repeat unit
N_H	number of hydrogen atoms in repeat unit
N_N	number of nitrogen atoms in the repeat unit
N_O	number of oxygen atoms in the repeat unit
N_S	number of sulfur atoms in the repeat unit
N_{sO}	number of single bonded oxygen atoms in the repeat unit
N_t	total number of atoms in the repeat unit
R	variable replacing $\frac{\Delta M_{K1}}{D_{K1}^2}+\frac{\Delta M_{K2}}{D_{K2}^2}$ (from Eq. B-14)
R^2	correlation coefficient
R_A	altitude at apogee (m)
R_E	radius of Earth (m)
R_P	altitude at perigee (m)
V_p	orbital velocity at perigee (m/sec)
V_r	actual volume of a repeat unit determined based on its chemical structure, molecular weight, and density (cm^3)
V_Σ	sum of the volume of the atoms making up the polymer repeat unit based on their covalent radii (cm^3)
X	exponential weighted sum of all the numbers and types of bonds in the polymer repeat unit
	expected thickness loss
x_i	*i*th variable in erosion yield equation
y	erosion step height (cm)
ΔM	mass loss (g)
ΔM_K	mass loss of Kapton® H witness sample (g)
ΔM_{K1}	situation 1 Kapton® witness sample mass loss (g)
ΔM_{K2}	situation 2 Kapton® witness sample mass loss (g)
ΔM_s	mass loss of the test sample (g)
ΔM_1	situation 1 mass loss (g)
ΔM_2	situation 2 mass loss (g)
ΔM_3	situation 3 mass loss (g)
ρ	density (g/cm^3)
ρ^{Cp}	variations in density of materials with an exponential constant

ρ_f	density of foam polymer (g/cm^3)
ρ_K	density of Kapton® H witness sample (1.4273 g/cm^3)
ρ_S	density of flight sample (g/cm^3)

4. INTRODUCTION

Polymers such as polyimide Kapton® and Teflon® fluorinated ethylene propylene (FEP) are commonly used spacecraft materials because of their flexibility and low density, as well as desirable electrical, thermal, and optical properties. Materials used on the exterior of spacecraft are subjected to many environmental threats that can cause degradation. In LEO, these threats include photon radiation, ultraviolet (UV) radiation, vacuum ultraviolet (VUV) radiation, x-rays, solar wind particle radiation (electrons, protons), temperature effects and thermal cycling, impacts from micrometeoroids and orbital debris (MMOD), spacecraft self-contamination, and atomic oxygen. While all of these environmental exposures can cause serious degradation to spacecraft components, atomic oxygen is a particularly serious structural, thermal, and optical threat, especially to exterior polymeric spacecraft components. An example of the complete loss of a Kapton® H (a DuPont™ polyimide derived from pyromellitic acid dianhydride (PMDA) and 4,4'-oxydianiline (ODA)) thermal blanket insulation layer, as well as degradation of other polymeric materials caused by atomic oxygen erosion in LEO, is provided in by O'Neal et al. (1996) in figure 1, Atomic Oxygen Erosion of a Kapton® Insulation Blanket. Figure 1 includes pre-flight, on-orbit, and post-flight images of experiment Tray F09, located on the leading edge of the Long Duration Exposure Facility (LDEF). This experiment tray was exposed to direct-ram atomic oxygen on LDEF for 5.8 years.

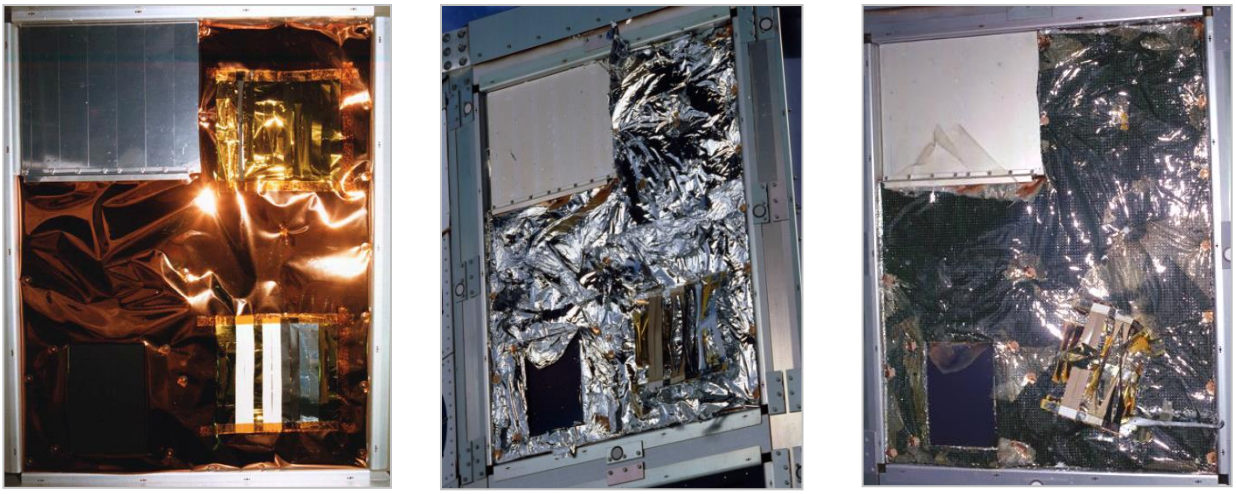

(a) Pre-Flight (b) On Orbit just before Retrieval (c) Post-Flight

Figure 1—Atomic Oxygen Erosion of a Kapton® Insulation Blanket

As part of the Polymer Erosion and Contamination Experiment (PEACE) Polymers experiment, 39 samples (38 different polymer materials and pyrolytic graphite), along with two Kapton® H atomic oxygen fluence witness samples, were exposed to LEO atomic oxygen as part of the Materials International Space Station Experiment 2 (MISSE 2) for ~4 years on the exterior of the ISS. The objective of the MISSE 2 PEACE Polymers experiment was to accurately determine

the atomic oxygen erosion yields of a wide variety of polymeric materials exposed for an extended period of time to the LEO space environment. The polymers range from those commonly used for spacecraft applications, such as Teflon® FEP, to more recently developed polymers, such as high-temperature polyimide polymerization of monomer reactants (PMR). Additional polymers were included to explore erosion yield dependence upon chemical composition. Error analyses were conducted to determine the error in the erosion yield values for each of the MISSE 2 PEACE Polymers flight samples. This Handbook provides details on the specific polymers flown, flight sample fabrication, pre-flight and post-flight characterization techniques, and atomic oxygen fluence calculations, along with a summary of the atomic oxygen erosion yield results and the corresponding erosion yield error analyses.

Also included are ground-laboratory to in-space correlation data for the PEACE polymers in an RF plasma asher, an atomic oxygen erosion yield predictive tool that was developed based on the MISSE 2 PEACE flight data, tools for using atomic oxygen erosion yield data for spacecraft durability applications, and lessons learned on the environment durability of spacecraft materials from spaceflight experiments.

5. THE LEO ATOMIC OXYGEN ENVIRONMENT

Atomic oxygen and its reactions with materials have been studied for many decades (Hansen et al., 1965). In NASA-TM-X-74335, U.S. Standard Atmosphere 1976, NASA, the National Oceanic and Atmospheric Administration (NOAA), and the United States Air Force (USAF) documented that atomic oxygen and its related reactions with materials exist in space. However, the damaging effects of atomic oxygen on spacecraft materials were not recognized until the Space Shuttle began flying missions in LEO. Although definitions vary greatly, according to one source, LEO is considered to be satellite orbits between about 140 and 970 km above the surface of Earth (low earth orbit, n.d. in *Merriam-Webster*). Early in-space observation that the residual atmosphere was interacting with spacecraft surfaces came in part as a result of comparison of day and night pictures of the Space Shuttle, as shown in figure 2, Space Shuttle with the Bay Oriented in the Direction of Travel (Ram Direction), where the glow from de-excitation atoms and molecules leaving Shuttle surfaces oriented in the ram (forward-facing) direction are visible in the night image (Banks et al., 2004, AIAA; Mende, 1984).

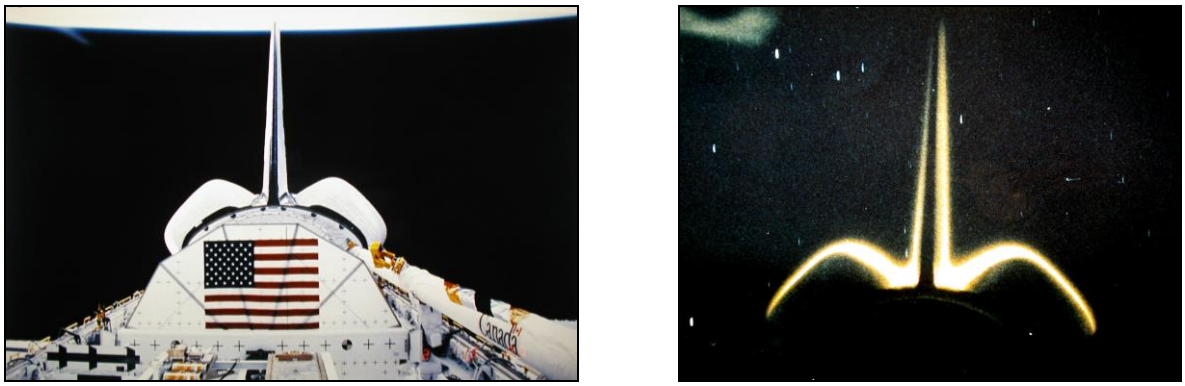

(a) In Sunlight

(b) Time-Lapsed Image Taken at Night with "Shuttle Glow" Visible

Figure 2—Space Shuttle with the Bay Oriented in the Direction of Travel (Ram Direction)

A second indication of LEO atomic oxygen interactions with spacecraft materials was observations of increases in the diffuse reflectance of polymers related to surface texturing. Specifically, after the first Shuttle mission (Space Transportation System (STS)-1) returned to Earth, engineers examining materials surfaces in the payload bay found that exterior Kapton® television camera thermal blankets had been altered during flight from a glossy amber color to a flat, milky yellow color (Leger, 1982; Leger, 1983). This was originally thought to be the result of contamination, but high-resolution electron microscopy examination revealed a recessed, carpet-like texture with a directional pattern associated with the vehicle velocity direction. It was concluded that degradation was caused by oxidation of organic materials through high-velocity collision with atmospheric atomic oxygen, resulting in volatile reaction products (carbon dioxide (CO_2), carbon monoxide (CO), water (H_2O), etc.,) that resulted in erosion and mass loss (Leger, 1982; Leger, 1983).

Further tests documented the rate of atomic oxygen erosion of commonly used spacecraft polymers. The first dedicated atomic oxygen experiment was proposed for flight on STS-5 to provide quantitative data on atomic oxygen reaction rates of materials. The reaction rate, given in volume loss per incident oxygen atom (cm^3/atom), is known as the atomic oxygen erosion yield. This experiment was called the Effects of Oxygen Interactions with Materials I (Visentine et al., 1985; Silverman, 1995, Part 1) or the Evaluation of Oxygen Interactions with Materials I, both abbreviated as EOIM I. Many additional materials spaceflight experiments have since been flown to assess atomic oxygen durability. The knowledge gained from these experiments of atomic oxygen erosion of commonly used spacecraft materials has led to modifications in spacecraft design in efforts to increase spacecraft durability in the LEO atomic oxygen environment.

5.1 Atomic Oxygen Formation and Density

Atomic oxygen is formed in the LEO environment through photodissociation of diatomic oxygen (O_2). Short wavelength (<243 nm) solar radiation has sufficient energy to break the 5.12-eV O_2 diatomic bond (Dickerson et al., 1979) in an environment where the mean free path is sufficiently long (~10^8 m) that the probability of re-association or the formation of ozone (O_3) is small. Between the altitudes of 180 and 650 km, atomic oxygen is the most abundant species, as shown in figure 3, Density of Atmospheric Species as a Function of Altitude, from NASA-TM-X-74-335 (NOAA 1976). This figure and the data plotted in figure 4, Atomic Oxygen Number Density versus Altitude for Solar Minimum, Nominal (Standard Atmosphere), and Solar Maximum Conditions, figure 5, Atomic Oxygen Fluence per Year during a Solar Cycle, figure 6, Average Molecular Weight as a Function of Altitude, and figure 7, Kinetic Temperature of LEO Atomic Oxygen as a Function of Altitude, show general trends. More accurate and recent values can be obtained from Picone et al., (2002) and from the NASA Marshall Space Flight Center's (MSFC's) solar activity website[1]. Although excited states of atomic oxygen can be formed, their lifetimes are sufficiently short that the triple P (^3P) ground state dominates the LEO atomic oxygen formation and is dependent upon the O_2 density and solar UV flux. Solar heating of Earth's atmosphere from VUV radiation causes an increase in the number density of atoms at a

[1] http://sail.msfc.nasa.gov. Retrieved December 18, 2013.

given altitude as Earth rotates from sunrise toward solar noon. Because the thermosphere rotates with Earth, the solar-heated bulge in the atmosphere is pushed forward such that the peak of the atomic oxygen density occurs in the late afternoon rather than at solar noon. As a consequence, anti-solar-facing surfaces, such as the back side of solar arrays, receive 25 percent more atomic oxygen fluence than the solar-facing surfaces as the spacecraft orbits Earth (Banks et al., 1991).

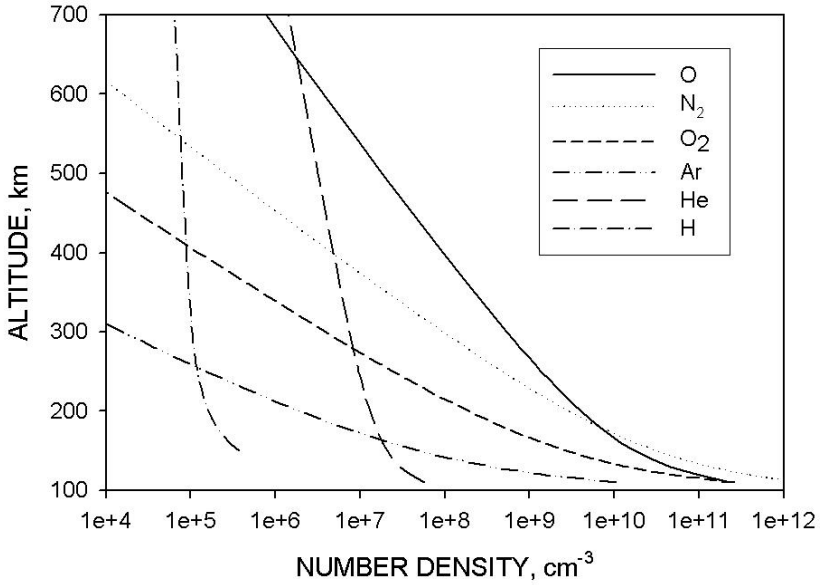

Figure 3—Density of Atmospheric Species as a Function of Altitude

5.2 Atomic Oxygen Solar Activity Flux Dependence

Solar-caused variations in the UV radiation incident upon the LEO atmosphere can greatly change the atomic oxygen production rate and, therefore, the arriving flux on spacecraft surfaces. Periods of high and low solar activity can change the arriving flux by several orders of magnitude depending on altitude (Banks et al., 2004, AIAA[2]). (See figure 4.) Because of this uncertainty in solar activity, the atomic oxygen flux cannot be predicted accurately over short durations of time. The average atomic oxygen number density varies as a result of the solar activity consistent with the 11-year sun spot cycle (Hedin, 1987). (See figure 5.) The Mass Spectrometer-Incoherent Scattered-86 (MSIS-86) atmospheric model takes into account the variation in number density with the 11-year solar cycle, and hence, the atomic oxygen flux and fluence vary with the solar cycle (Hedin, 1987). Atomic oxygen can also be produced in other planetary environments, such as the Mars orbital environment, where oxygen is present.

[2] Data for figure 4 were obtained from NASA-TM-X-74335 (NOAA 1976).

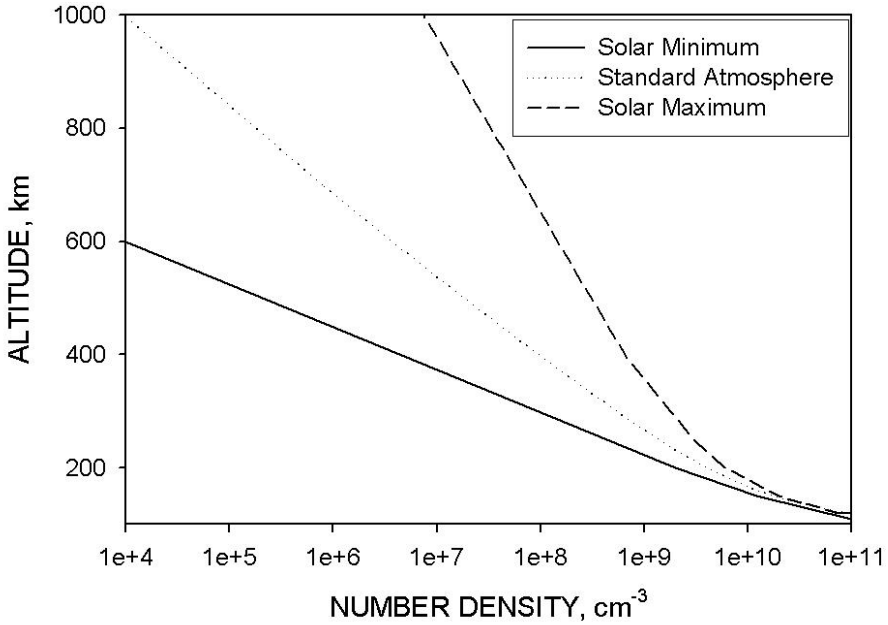

Figure 4—Atomic Oxygen Number Density versus Altitude for Solar Minimum, Nominal (Standard Atmosphere), and Solar Maximum Conditions

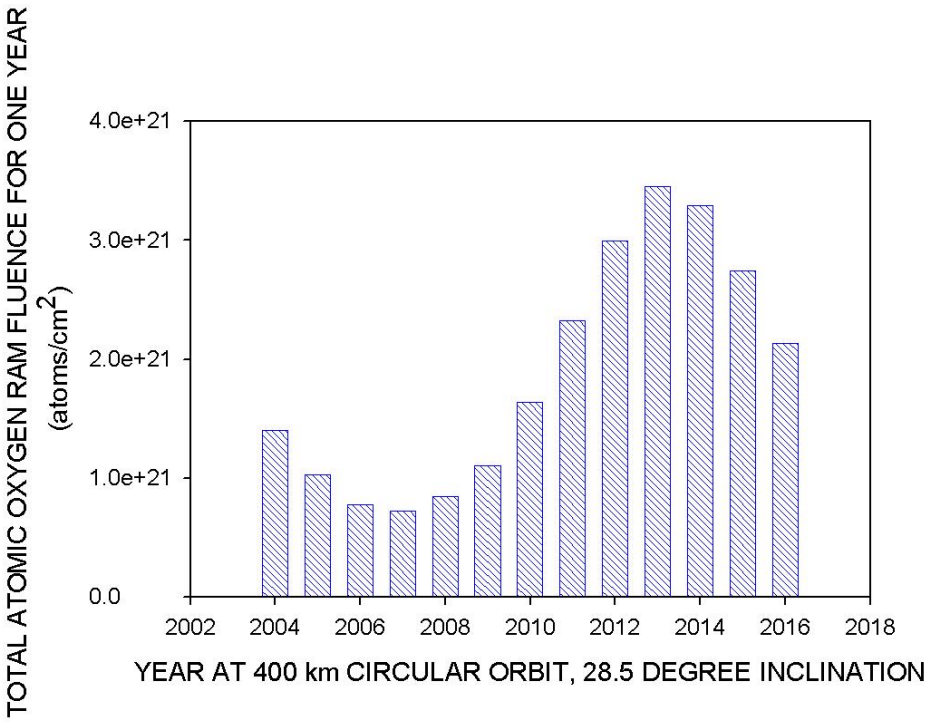

Figure 5—Atomic Oxygen Fluence per Year during a Solar Cycle

5.3 Altitude Effects

As altitude increases, average molecular weight decreases, and temperature gradually increases, as shown in figures 6 and 7, respectively (NASA-TM-X-74335).

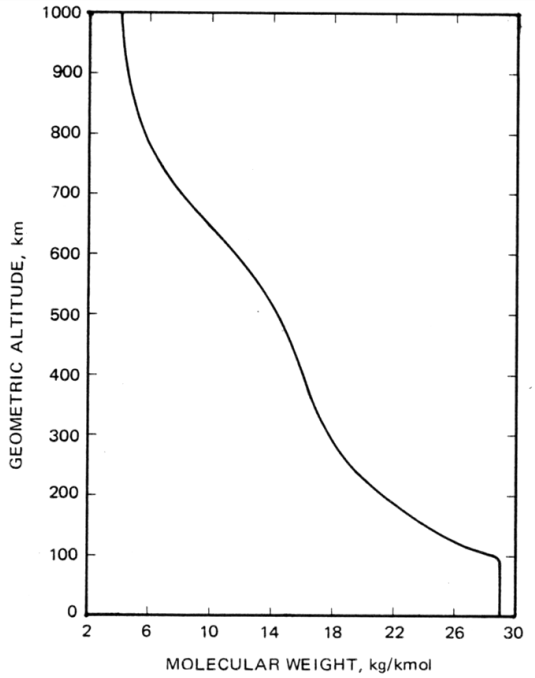

Figure 6—Average Molecular Weight as a Function of Altitude

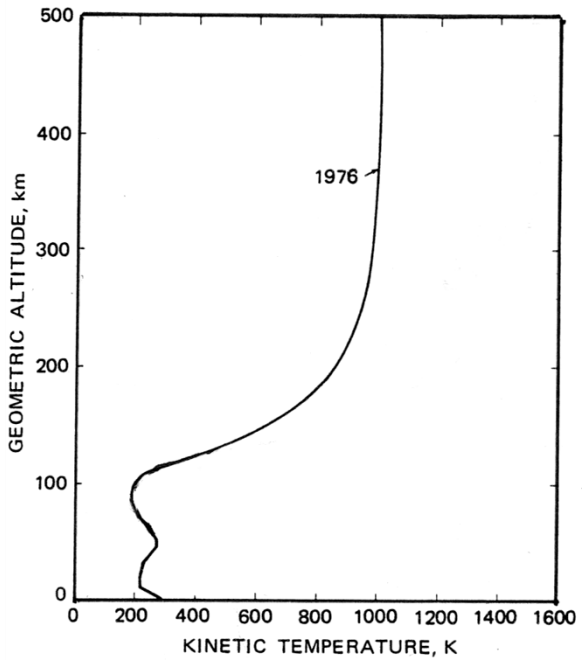

Figure 7—Kinetic Temperature of LEO Atomic Oxygen as a Function of Altitude

5.4 Atomic Oxygen Angular Distribution for Circular Orbits

As a spacecraft orbits Earth at a velocity on the order of 7.7 km/sec, it collides with atomic oxygen (hence the term "ram" atomic oxygen). If the spacecraft is in an orbit that has 0° inclination, then the average angle of attack of the atomic oxygen is perpendicular to surfaces whose surface normal vector points in the direction of travel. However, most spacecraft have orbits that are inclined with respect to Earth's equatorial plane. This causes the average angle of attack of the arriving atomic oxygen to vary sinusoidally around the orbit as a result of the vectoral contributions from the orbital spacecraft velocity vector and the atmosphere's co-rotation velocity vector (de Groh and Banks, 1994). Because the co-rotation velocity vector is in approximately the same direction as the orbital velocity vector, the actual oxygen atom impact energy is slightly lower than what would be predicted based on the orbital velocity alone. In addition, atomic oxygen atoms have thermal velocities associated with their Maxwell-Boltzman velocity distribution at the high temperatures of LEO, typically around 1000 K (NASA-TM-X-74335). The high-velocity tail of the Maxwell-Boltzman distribution actually allows a very small fraction of the atomic oxygen atoms to catch up with the trailing surfaces of a LEO spacecraft to produce a small flux that is orders of magnitude lower than the ram flux. Thus, the thermal velocities of the atomic oxygen associated with their Maxwell-Boltzman velocity distribution contribute as an additional vectoral component to the overall impact velocity of the atomic oxygen, which results in an angular distribution of arrival directions.

If the three vectoral components are summed and averaged over a typical 400-km orbit at 28.5° inclination, the angular distribution of arriving atoms is as shown in figure 8, Atomic Oxygen Arrival Flux Relative to the Ram Direction for a 400-km Orbit at 28.5° Inclination and

1000-K Thermosphere, where the arrival distribution in the horizontal plane is shown as a function of incidence angle for surfaces normal to the ram direction (Banks et al., 2004, AIAA). The flux is plotted relative to the normal incident flux.

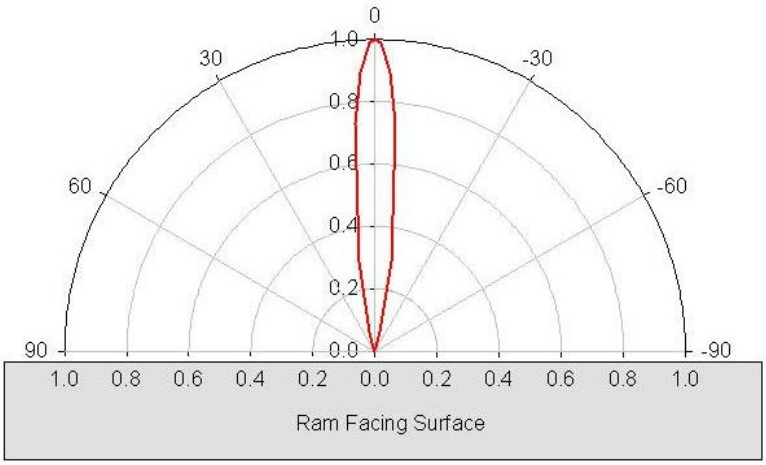

Figure 8—Atomic Oxygen Arrival Flux Relative to the Ram Direction for a 400-km Orbit at 28.5° Inclination and 1000-K Thermosphere

Atomic oxygen can arrive at angles beyond 90° from the orbital direction. For example, figure 9, Polar Plot of Relative Atomic Oxygen Flux as a Function of the Angle between the Ram Direction and the Normal of the Arrival Surface for a LEO Spacecraft in a 400-km Orbit at 28.5° Inclination and 1000-K Thermosphere, shows that a surface whose normal is 98° with respect to the ram direction receives approximately 4 percent of the flux that occurs for a surface whose normal is parallel to the ram direction (Banks et al., 2004, AIAA). Note that, for angles significantly off-normal incidence, figure 9 provides a more accurate representation of the flux than does figure 8.

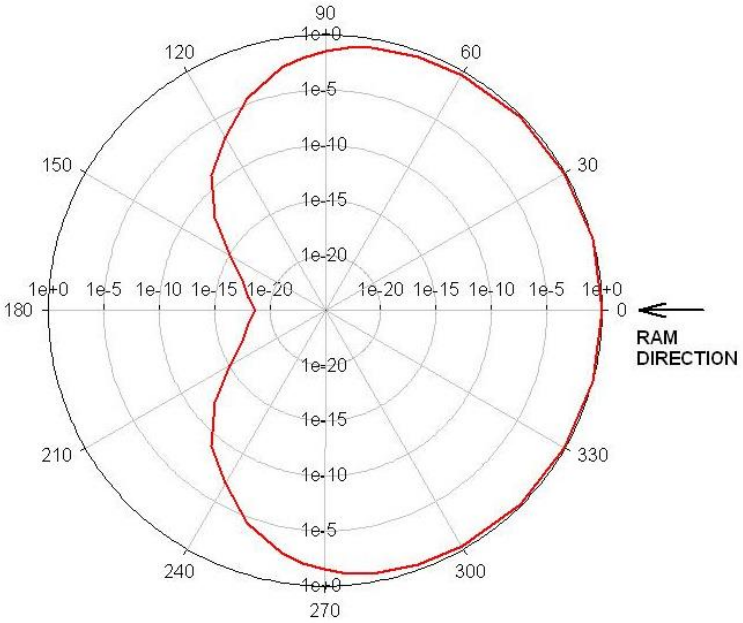

Figure 9—Polar Plot of Relative Atomic Oxygen Flux as a Function of the Angle between the Ram Direction and the Normal of the Arrival Surface for a LEO Spacecraft in a 400-km Orbit at 28.5° Inclination and 1000-K Thermosphere

The flux of atomic oxygen at ISS altitudes is approximately 5.23×10^{13} atoms/cm^2·sec for normal incident ram surfaces (at 400-km altitude averaged over the 11-year solar cycle) (Banks et al., 1990). At ISS altitudes, the atomic oxygen fluence for a 15-year mission (averaged over the variations with solar cycle) is approximately 4.5×10^{22} atoms/cm^2. This was computed for a 15-year mission starting with the first ISS element launch (Zarya) on November 20, 1998, assuming an altitude of 348 km, using Environmental WorkBench software. This fluence level is high enough to cause significant degradation to a number of susceptible spacecraft materials, posing a significant potential threat to the durability of long-duration spacecraft systems.

Although figure 9 shows the relative flux as a function of arrival direction around a spacecraft, it is often more useful to look at a more detailed plot in the region near tangential arrival, such as for the LDEF spacecraft orbit, as shown in figure 10, Atomic Oxygen Flux Relative to the Ram Direction as a Function of Angle from the Ram Direction for the LDEF Spacecraft, (with data for figure 10 provided in table 1, Numerical Values of Atomic Oxygen Flux Relative to the Ram Direction as a Function of Angle from the Ram Direction for the LDEF Spacecraft) (Bourassa and Gillis, 1991). As can be seen in table 1, at 90° from the ram direction, the atomic oxygen flux is 4.15 percent that for the ram direction. This relative flux also depends slightly on the orbital inclination and on whether the surface is facing in an Earth-radial or Earth-tangential direction because of vectoral contributions caused by the co-rotation of the thermosphere.

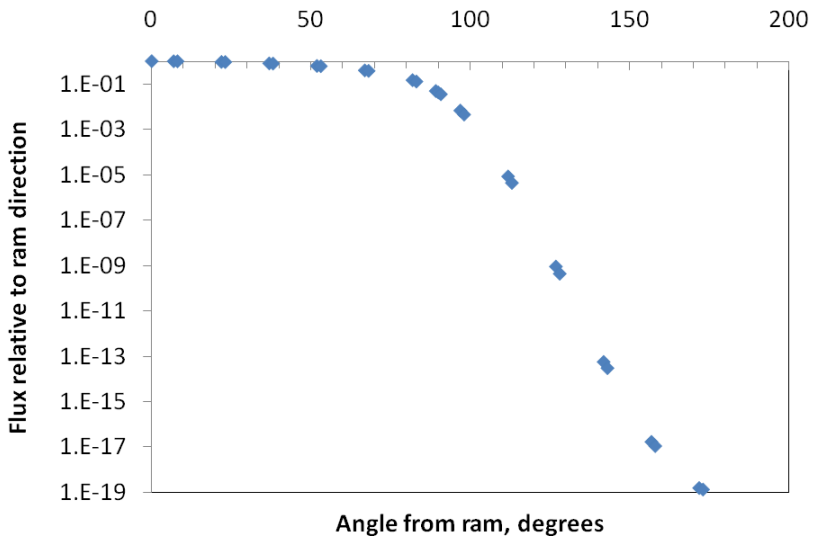

Figure 10—Atomic Oxygen Flux Relative to the Ram Direction as a Function of Angle from the Ram Direction for the LDEF Spacecraft

Table 1—Numerical Values of Atomic Oxygen Flux Relative to the Ram Direction as a Function of Angle from the Ram Direction for the LDEF Spacecraft

Angle From Ram (°)	Fluence Relative To Ram
0	1.00E+00
6.9	9.92E–01
8.1	9.90E–01
21.9	9.27E–01
23.1	9.19E–01
36.9	7.99E–01
38.1	7.87E–01
51.9	6.16E–01
53.1	6.00E–01
66.9	3.92E–01
68.1	3.72E–01
81.9	1.45E–01
83.1	1.27E–01
89.2	4.85E–02
90	4.15E–02
90.8	3.46E–02
96.9	6.62E–03
98.1	4.42E–03
111.9	8.27E–06
113.1	4.28E–06
126.9	8.77E–10
128.1	4.23E–10
141.9	5.46E–14
143.1	2.91E–14
156.9	1.63E–17
158.1	1.06E–17
171.9	1.50E–19
173.1	1.28E–19

5.5 Atomic Oxygen Impact Energy

5.5.1 Circular Orbits

The impact energy of arriving atomic oxygen atoms is also dependent on the following three contributions to the resulting velocity vectors: the orbital spacecraft velocity, Earth's atmospheric co-rotation velocity, and atomic oxygen thermal velocity. As can be seen in figure 11, Energy Distribution of Atomic Oxygen Atoms as a Function of Altitude for a Circular Orbit at 28.5° Inclination and 1000-K Thermosphere, the average impact energy is 4.5 (±1) eV for a 400-km orbit, and the impact energy decreases with altitude (Banks, 2004, AIAA).

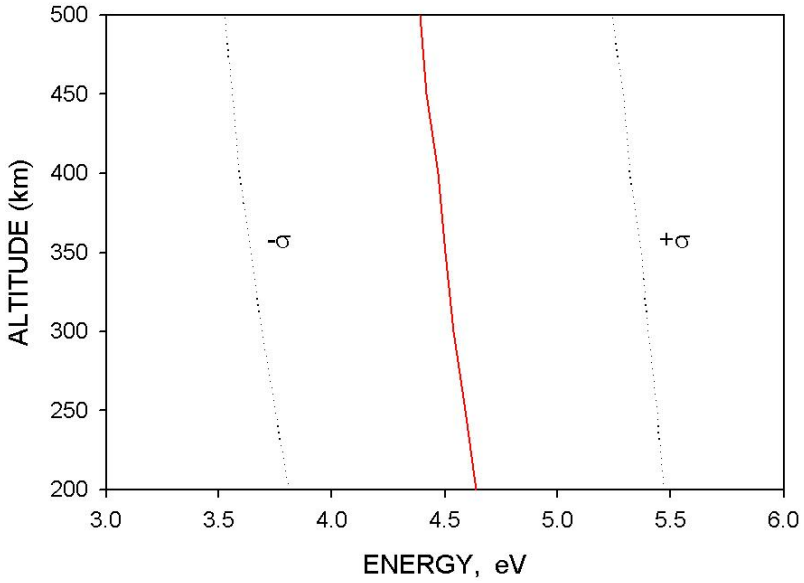

Figure 11—Energy Distribution of Atomic Oxygen Atoms as a Function of Altitude for a Circular Orbit at 28.5° Inclination and 1,000-K Thermosphere

5.5.2 Elliptical LEO Orbits

Many low Earth orbital spacecraft fly in highly elliptical orbits for Earth-observing missions. As a LEO spacecraft travels through the part of its orbit that is the closest distance to Earth, it has the highest velocity relative to the atomic oxygen in the residual atmosphere of Earth, i.e., it travels faster than it does when it is farther from Earth. Therefore, for the low-altitude duration of the spacecraft's orbit, the ram energy of impacting atomic oxygen is higher than it is during the rest of the orbit (and also than it would be in a typical circular LEO orbit). Although erosion yield dependence on ram energy has not been accurately measured for most polymers, there is general agreement that erosion yield increases as ram energy increases.

A spacecraft traveling in an elliptical orbit around Earth also experiences the largest atomic oxygen flux at the perigee of its orbit. Figure 12, Elliptical Orbit Definition of Perigee, Apogee, Earth Radius, and Orbital Velocity, shows the orbital parameters perigee (R_P), apogee (R_A), Earth radius (R_E), and orbital velocity at perigee (V_P). A spacecraft in elliptical orbit can ultimately accumulate a very high atomic oxygen fluence if the perigee is low and the mission is of a long

duration. If this is the case, then spacecraft in highly elliptical orbits with low perigees could experience significant erosion of organic materials on lengthy missions because of a combination of increased ram energy and increased fluence of impacting atomic oxygen.

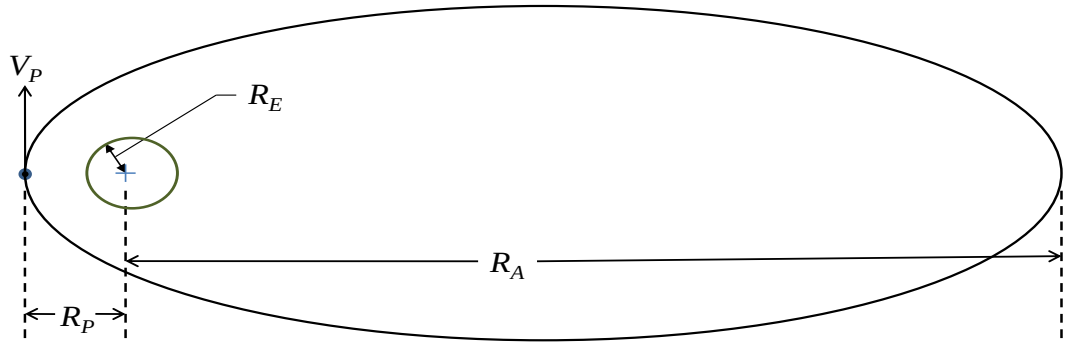

Figure 12—Elliptical Orbit Definition of Perigee, Apogee, Earth Radius, and Orbital Velocity

Subtracting Earth's atmospheric co-rotation velocity from the equatorial orbital velocity of a spacecraft at perigee yields the highest ram energy (the energy at perigee) (E_{PE}) for equatorial orbits:

$$E_{PE} = \frac{(m_o/2 \cdot e)[2 \cdot G \cdot M_E(R_A + R_E)]}{(R_P + R_E)(R_P + R_A + 2 \cdot R_E)} \quad \text{(Eq. 1)}$$

where:

E_{PE} = ram energy at perigee for equatorial orbits (eV)
m_o = mass of an oxygen atom (2.66×10^{-26} kg)
e = electron charge (1.6×10^{-19} C)
G = gravitational constant (6.67×10^{-11} N·m^2/kg^2)
M_E = mass of Earth (6.67×10^{24} kg)
R_A = altitude at apogee (m)
R_E = radius of the Earth (m)
R_P = altitude at perigee (m).

As can be seen in figure 13, Maximum Atomic Oxygen Ram Energy as a Function of Apogee Altitude for Equatorial Elliptical Orbits, as expected, the maximum ram energy increases as apogee altitude increases and decreases as perigee altitude increases.

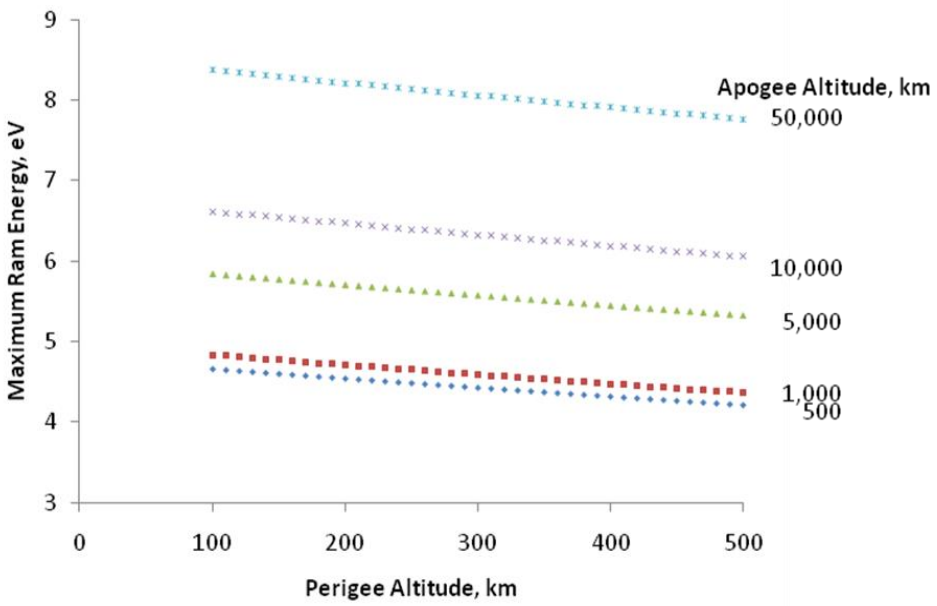

Figure 13—Maximum Atomic Oxygen Ram Energy as a Function of Apogee Altitude for Equatorial Elliptical Orbits

6. ATOMIC OXYGEN INTERACTION WITH MATERIALS

Although LEO atomic oxygen possesses sufficient energy to react with most organic materials and break most organic polymer bonds with sufficient flux to cause oxidative erosion of polymers, there was little known about or interest in atomic oxygen interaction with materials until the start of the Space Shuttle missions. This is primarily because most prior missions occupied high-altitude orbits, where atomic oxygen densities are inconsequential.

6.1 Atomic Oxygen Processes

A number of processes can take place when an oxygen atom strikes a spacecraft surface at an orbital velocity. These include chemical reaction with surface molecules, elastic scattering, scattering with partial or full thermal accommodation, and recombination or excitation of ram species (Gregory, 1986). Atomic oxygen can react with polymers, carbon, and many metals to form oxygen bonds with atoms on the exposed surface. For most polymers, hydrogen abstraction, oxygen addition, or oxygen insertion can occur (Dever, 1991; Dever, 2005), as shown in figure 14, Atomic Oxygen Reaction Pathways with Polymers. With continued atomic oxygen exposure, all oxygen interaction pathways eventually lead to volatile oxidation products. This results in gradual erosion of hydrocarbon or halocarbon material, with the exception of silicone materials. The amount of erosion of a hydrocarbon or halocarbon material that is acceptable depends on the material's function and functional performance requirements and on the associated margins and factors of safety relevant to the specific material and mission.

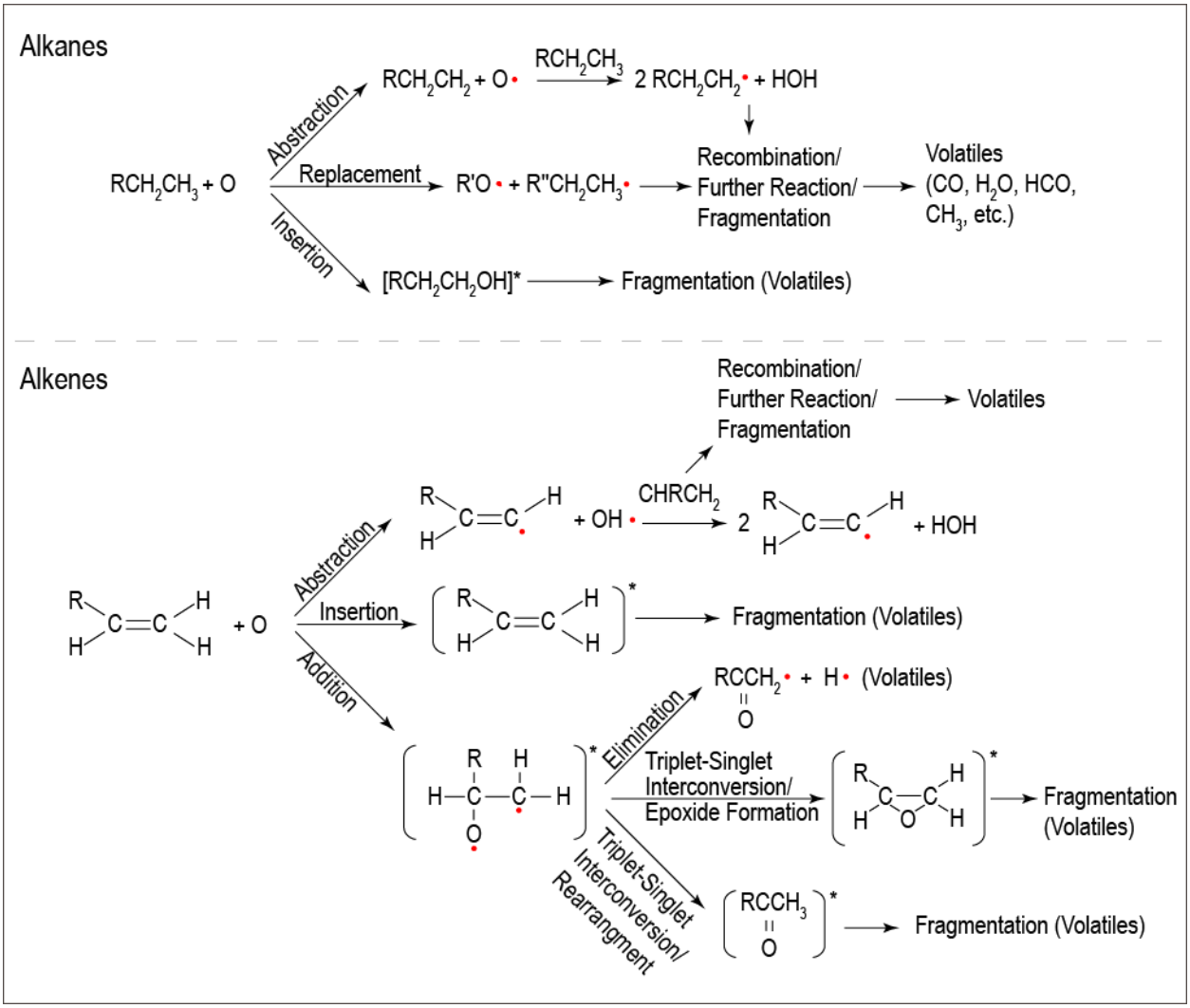

Figure 14—Atomic Oxygen Reaction Pathways with Polymers

Surfaces of polymers exposed to atomic oxygen also develop increases in oxygen content. One example is provided in figure 15, Surface Oxygen Content of CTFE as a Function of Atomic Oxygen in an RF Plasma Asher, where the surface oxygen content, measured using x-ray photoelectron spectroscopy (XPS), as a function of atomic oxygen exposure level is provided for chlorotrifluoroethylene (CTFE) exposed to atomic oxygen in an RF air plasma asher (Mata et al., 2003).

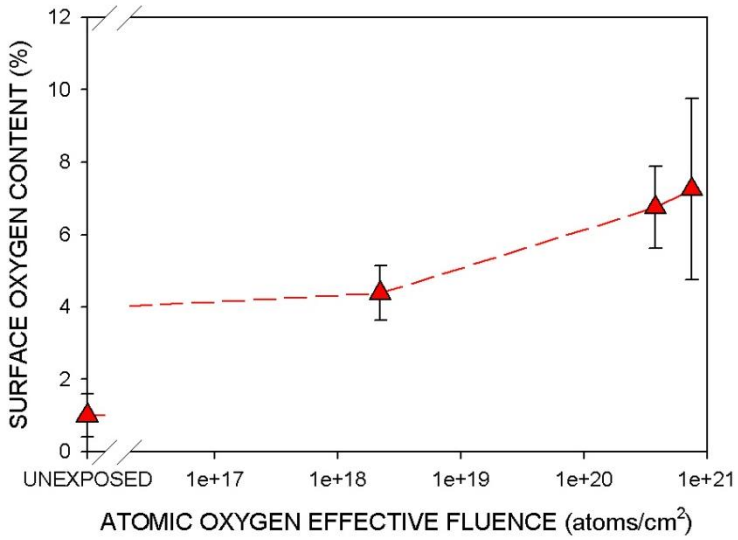

Figure 15—Surface Oxygen Content of CTFE as a Function of Atomic Oxygen in an RF Plasma Asher

Silicones, a family of commonly used spacecraft materials, are an exception to polymeric materials that erode away with atomic oxygen exposure. With atomic oxygen exposure, oxidation reactions cause the surface of silicones to oxidize and volatilize their hydrocarbon content and convert to a hardened silica-based surface layer, which is resistant to atomic oxygen erosion (de Groh et al., 2006, JSR). In this oxidation and volatilization process, silicones tend to form a surface that is under tension relative to the underlying polymer. Eventually, with sufficient fluence, the surfaces can form microscopic mud-tile-like cracks. A sample flown as part of the Evaluation of Oxygen Interactions with Materials III (EOIM III) provides an example of mud-tile cracking in response to exposure to a low fluence of atomic oxygen in LEO (de Groh and McCollum, 1995). (See figure 16, DC 93-500 Silicone Exposed to LEO Atomic Oxygen as Part of the EOIM III Shuttle Experiment.)[3] This sample was exposed to an atomic oxygen fluence of 2.3×10^{20} atoms/cm^2 during STS-46. Even with volatilization of hydrocarbons, silicones often do not lose mass (Hung and Cantrell, 1994), and some silicones actually gain mass during atomic oxygen exposure. Therefore, the atomic oxygen durability of silicones should not be based on erosion, as with other spacecraft polymers. Another consequence of atomic oxygen interaction with some silicones is the production of dark contamination on neighboring surfaces in LEO, particularly with UV exposure (Banks et al., 2000; de Groh and McCue, 1999).

[3] The product name for DC 93-500 is Dow Corning® 93-500 Space Grade Encapsulant.

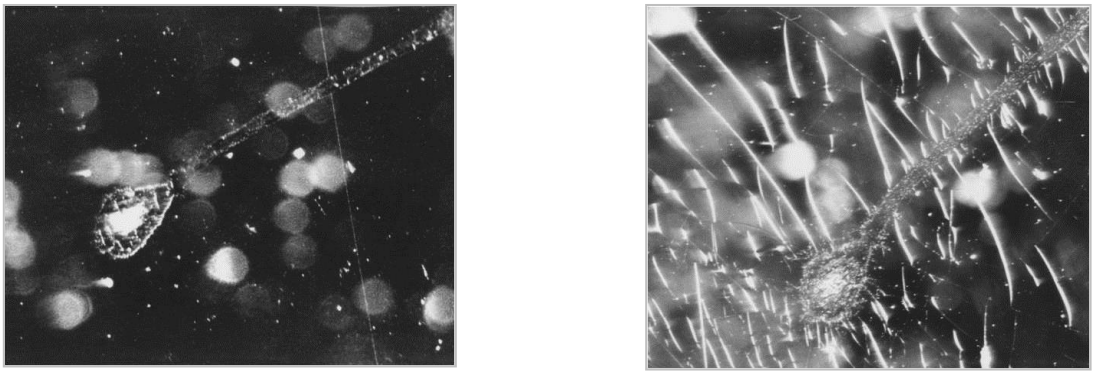

(a) Pre-Flight

(b) Post-Flight with Mud-Tile Cracking Observed

Figure 16—DC 93-500 Silicone Exposed to LEO Atomic Oxygen as Part of the EOIM III Shuttle Experiment

6.2 Atomic Oxygen Texture

Surfaces of materials that have volatile oxidation products, such as hydrocarbon polymers, and that are oriented in a fixed position with respect to the ram direction gradually develop left-standing cones that point in the direction of arriving atomic oxygen. Thus, the microscopic roughness of the surfaces increases with time. Because the erosion of one location is independent of any other location and because the atomic oxygen arrives at microscopically random locations on the surface, the development of surface roughness obeys Poisson statistics: as the atomic fluence increases, the surface roughness increases as the square root of the fluence (Banks et al., 2001). Figure 17, Scanning Electron Microscope Images of Directed LEO Atomic Oxygen Textured Materials, shows examples of atomic-oxygen-textured surfaces of three materials from the EOIM III and LDEF spaceflight experiments after fixed-orientation exposure to atomic oxygen in LEO (Banks et al., 2004, MRS). In addition to polymer thickness loss, such texturing causes an increase in diffuse reflectance and a decrease in specular transmittance of polymers (Banks et al., 1985, AIAA).

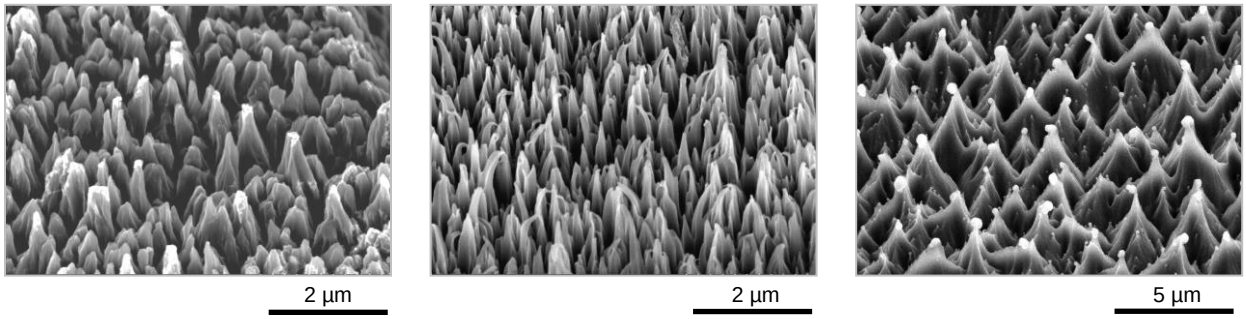

(a) Pyrolytic Graphite (EOIM III, Atomic Oxygen F = 2.3×10^{20} atoms/cm^2)

(b) Kapton® H (EOIM III, Atomic Oxygen F = 2.3×10^{20} atoms/cm^2)

(c) Teflon® FEP (LDEF, Atomic Oxygen F = 8.43×10^{21} atoms/cm^2)

Figure 17—Scanning Electron Microscope Images of Directed LEO Atomic Oxygen Textured Materials

The development of surface texture occurs whether the material is crystalline or amorphous and is a stochastic process that occurs in a manner similar to the spatial variation of ionizing radiation arriving at a surface. Computational modeling of the surfaces also predicts the development of such surface cones (Banks et al., 2001; Banks et al., 1997). Atomic oxygen textured surfaces have significant biomedical applications because they have greatly decreased water contact angles and cell attachment (Banks et al., 2001; Berger et al., 2007).

The peak-to-valley distance of the cones increases with atomic oxygen fluence as the square root of the fluence (Banks et al., 2001). Figure 18, Scanning Electron Microscope Images at Protected Mesas of Directed LEO Atomic Oxygen Textured Materials, shows the heights of the cones relative to the average erosion depths for pyrolytic graphite, polyimide Kapton® H, and Teflon® FEP at protected mesa locations (Banks et al., 2004, MRS).

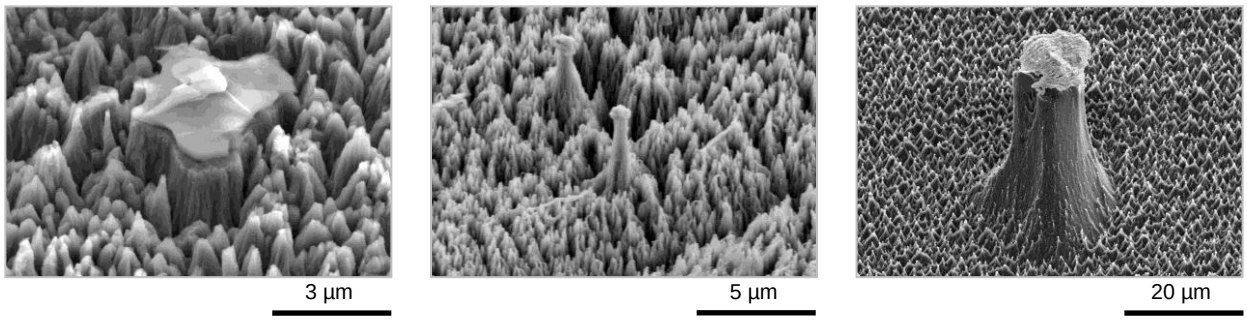

(a) Pyrolytic Graphite (EOIM III, Atomic Oxygen F = 2.3×10^{20} atoms/cm^2)

(b) Kapton® H (EOIM III, Atomic Oxygen F = 2.3×10^{20} atoms/cm^2)

(c) Teflon® FEP (LDEF, Atomic Oxygen F = 8.43×10^{21} atoms/cm^2)

Figure 18—Scanning Electron Microscope Images at Protected Mesas of Directed LEO Atomic Oxygen Textured Materials

Atomic oxygen exposure of hydrocarbon or halocarbon polymers that are pigmented or filled with metal oxide particles results in erosion of the polymeric content, which, in turn, results in gradual exposure of an increasing surface population of metal or metal oxide particles that are loosely attached to each other (Silverman, 1995, Part 2). The particles remain in contact with each other and gradually, as more are exposed, shield the underlying polymer content from further atomic oxygen erosion, unless they are loosened or moved by external contact or abrasion. Thus, the erosion yield of such polymers can gradually decrease with atomic oxygen fluence.

It is interesting to note that the 100 plane of carbon in the form of single crystal class IIa diamond does not erode with atomic oxygen exposure (Banks and Stueber, 1997; Shpilman et al., 2010). This is thought to be because of the formation of a protective surface formed by close-together oxygen atoms that have replaced hydrogen atoms at the terminations of tetrahedrally coordinated carbon on the external surface of diamond.

6.3 Atomic Oxygen Protective Coatings and Undercutting Erosion

The most common approach to protecting susceptible spacecraft materials from atomic oxygen erosion is to coat the material with a thin atomic oxygen protective film, such as a metal, metal oxide, or fluoropolymer-filled metal oxide protective coating (Banks et al., 1984; Banks et al., 2002; Dever et al.,1996; Goode et al., 1994; Rutledge and Mihelcic, 1990). Thin film coatings of silicon dioxide (SiO_2), aluminum oxide (Al_2O_3), indium tin oxide (ITO), germanium (Ge), silicon (Si), aluminum (Al), and gold (Au) with thicknesses ranging from a few hundred angstroms to more than 100 nm are typically applied by sputter deposition or vapor deposition (Dever et al., 2005). Although metal oxide coatings as thin as ~5.0 nm can provide atomic oxygen protection on extremely smooth surfaces, usually thicknesses of ~100 nm are used to provide coverage over irregularities such as debris, pits, and rills on polymer surfaces (Dever et al., 2005). It is critical that the substrate to be coated be extremely smooth and free from surface roughness, such as scratches, rills, pits, and abrupt ridges, to prevent pin windows from developing in protective coatings. The application of 130-nm SiO_2 protective coatings on Kapton® H polyimide can frequently reduce the rate of weight loss caused by atomic oxygen erosion of Kapton® to less than 1 percent of that of unprotected Kapton® (Rutledge and Olle, 1993). Coatings that are factors thicker than 100 nm can more easily crack or spall because of their intrinsic stress or their inability to conform with flexure compression or expansion at the polymer substrate interface (Dever et al., 2005). The addition of small amounts of fluoropolymer to metal oxide coatings allows greater strain-to-failure ratios in the coatings. Such coatings can be deposited by co-sputter deposition of SiO_2 and polytetrafluoroethylene (PTFE) Teflon® (Banks et al., 1985, AIAA; Banks et al., 1984). Because only limited flexibility of the solar array blankets is needed at array segment hinge locations, 130-nm-thick SiO_2 magnetron sputter deposition coatings are used on Kapton® H polyimide solar array blankets on the ISS (Rutledge and Olle, 1993).

Unfortunately, microscopic scratches, dust particles, or other imperfections in the substrate surface can result in defects in the protective coating. These coating defects can provide pathways for atomic oxygen attack, and undercutting erosion of the substrate can occur, even under directed ram atomic oxygen exposure in LEO. Figure 19, Scanning Electron Microscope

Images of Undercutting Erosion at Defect Sites in Aluminized Kapton® Exposed to LEO on the LDEF, shows scanning electron microscope images of LEO-exposed aluminized-Kapton® from the LDEF at sites of pinhole and crack defects in the Al protective coating (deGroh and Banks, 1994; Banks et al., 2004, AIAA). After removal of the Al coating, undercut cavities developed during flight at the coating defect sites, as shown in figure 19 (b).

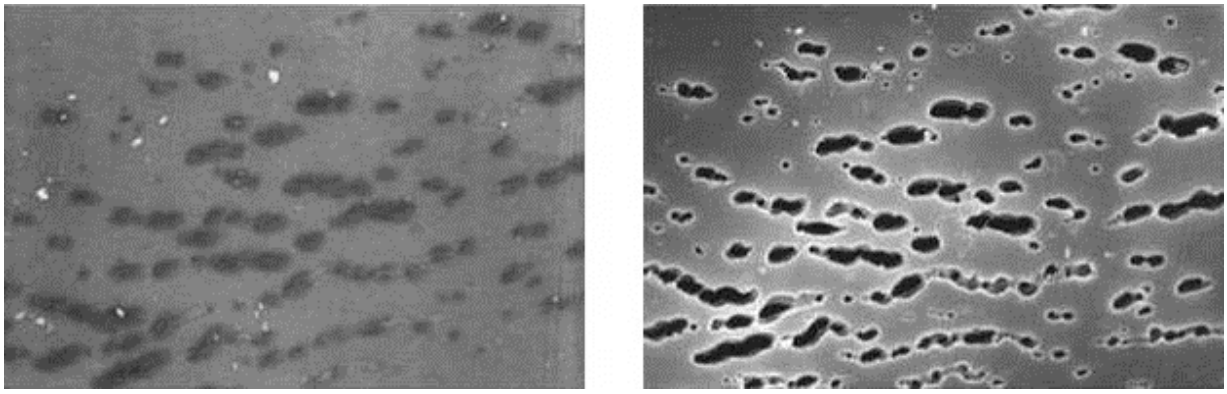

(a) Before Removal of the Al Coating (b) After Chemical Removal of the Al Coating

Figure 19—Scanning Electron Microscope Images of Undercutting Erosion at Defect Sites in Aluminized Kapton® Exposed to LEO on the LDEF

Undercutting erosion can be a serious threat to component survivability. An example is shown in figure 20, Atomic Oxygen Undercutting Degradation of the Solar Array Wing Blanket Box Cover on the ISS after 1 Year of LEO Space Exposure, where atomic oxygen undercutting erosion has severely degraded the P6 Truss port solar array wing two-surface aluminized-Kapton® blanket box cover on the ISS (Banks et al., 2004, JSR). Therefore, the atomic oxygen durability of polymers that are protected by thin-film coatings is largely dependent upon the number and size of pinhole and scratch defects in the protective coatings. The growth of undercut cavities has been studied for polymer films coated on one side or both sides through the use of Monte Carlo computational modeling (Banks et al., 1998; Banks et al., 1990; Banks et al., 1992; Banks and Stueber, 1997; Banks et al., 2003; Banks et al., 2004, JSR). Modeling the double-coated Kapton® solar array wing blanket box covers on the ISS indicated that the extent of undercutting damage would have been significantly less, because of less scattering in the undercut cavity, if the blanket had been coated only on the front (space-facing) side and not on both sides (Banks et al., 2004, JSR). The model predictions are shown in figure 21, Monte Carlo Computational Atomic Oxygen Undercutting Erosion Predictions for a 45°-from-Perpendicular Angle of Attack of Atomic Oxygen at a Crack or Scratch Defect of the Aluminized Kapton® Surfaces.

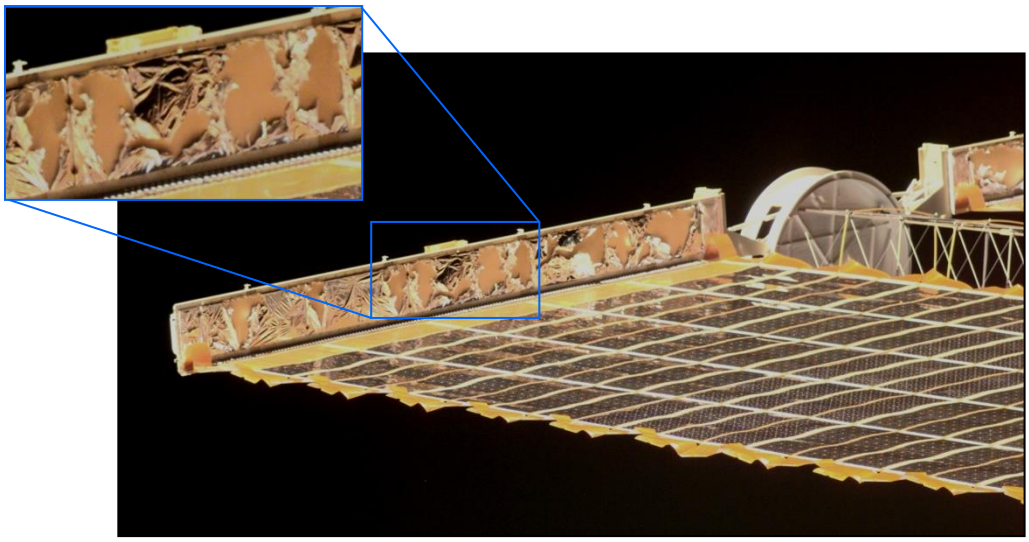

Figure 20—Atomic Oxygen Undercutting Degradation of the Solar Array Wing Blanket Box Cover on the ISS after 1 Year of LEO Space Exposure

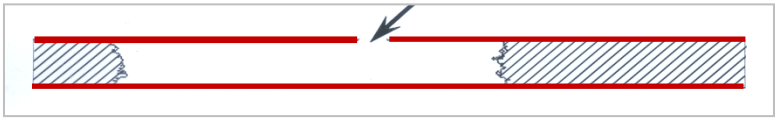

(a) Aluminized on Both Sides

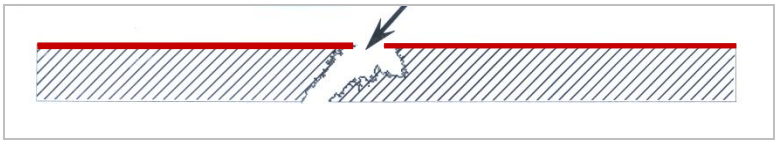

(b) Aluminized on Exposed Side Only

Figure 21—Monte Carlo Computational Atomic Oxygen Undercutting Erosion Predictions for a 45°-from-Perpendicular Angle of Attack of Atomic Oxygen at a Crack or Scratch Defect of the Aluminized Kapton® Surfaces

7. ATOMIC OXYGEN EROSION YIELD

The sensitivity of a hydrocarbon material to reaction with atomic oxygen is quantified by the atomic oxygen erosion yield of the material. The atomic oxygen erosion yield is the volume of a material that is removed (through oxidation) per incident oxygen atom and is measured in units of cm^3/atom. The atomic oxygen erosion yield is also often referred to as the recession rate and, in the past, has been called atomic oxygen reaction efficiency. The most well-characterized atomic oxygen erosion yield is that of polyimide Kapton® H, which has an erosion yield of 3.0×10^{-24} cm^3/atom for LEO 4.5-eV atomic oxygen (Banks et al., 1985, TSF; Visentine et al., 1985; Koontz et al., 1995; Silverman, 1995, P1). As atomic oxygen erosion of polymers in LEO is a serious threat to spacecraft performance and durability, it is essential to understand the atomic oxygen erosion yield of polymers for spacecraft applications so that the durability of materials being considered for spacecraft design can be predicted. Because spaceflight opportunities are rare, expensive, space-limited, and time-consuming, ground laboratory testing

is often relied upon for spacecraft material environmental durability prediction. However, differences exist between ground facilities and actual space exposures, which may result in material-dependent differences in rates of reactions. Therefore, actual spaceflight atomic oxygen erosion yield data (volume loss in cm^3 per incident oxygen atom) are needed to best assess the durability of a material for spacecraft mission applicability. In addition, data from actual materials spaceflight experiments can be used to determine correlations between exposures in ground test facilities and space exposure, allowing for more accurate predictions of in-space materials performance based on ground facility testing.

7.1 Techniques for Measuring Atomic Oxygen Erosion Yield

The two main techniques used to measure the erosion yield of a material after space or ground laboratory atomic oxygen exposure are mass loss and recession depth. Advantages and disadvantages to both techniques are discussed below.

7.1.1 Mass Loss Technique

A common technique for determining the erosion yield of materials exposed to atomic oxygen uses mass loss measurements. The mass loss measurements should be made by weighing vacuum-dehydrated samples before and after atomic oxygen exposure, as described in ASTM E 2089-00, Standard Practices for Ground Laboratory Atomic Oxygen Interaction Evaluation of Materials for Space Applications. Measurements for dehydration are to be performed using equipment calibrated to national requirements for accuracy. The erosion yield of the sample is calculated through the following equation:

$$E_y = \frac{\Delta M_S}{\left(A_S \cdot \rho_S \cdot F\right)} \qquad \text{(Eq. 2)}$$

where:

E_y = atomic oxygen erosion yield of test sample (cm^3/atom)
ΔM_s = mass loss of test sample (g)
A_s = surface area of test sample exposed to atomic oxygen (cm^2)
ρ_s = density of test sample (g/cm^3)
F = fluence of atomic oxygen (atoms/cm^2).

Because Kapton® H has a well-characterized erosion yield in LEO (3.0×10^{-24} cm^3/atom) (Banks et al., 1985, TSF; Visentine et al., 1985; Koontz et al., 1995; Silverman, 1995, P1), it is commonly used as a witness sample to compute the atomic oxygen fluence during flight experiments in LEO. In ground laboratory equipment, such as an RF plasma asher or an atomic oxygen beam facility, the energy, flux, and arrival of atomic oxygen can vary from that in LEO. For example, the Kapton® H effective fluence for a thermal energy plasma measured in a ground laboratory facility is not the actual number of atoms/cm^2 striking the surface, because thermal energy atoms (≈0.04 eV) require orders of magnitude more atoms to erode as much material as LEO atoms arriving at ≈4.5 eV. Therefore, in a ground facility, the effective fluence (F_E) of the

exposure is the atomic oxygen fluence in LEO that would produce the same amount of erosion in the ground-based facility (ASTM E 2089-00).

Both the atomic oxygen F and F_E are calculated using the following equation:

$$F \text{ or } F_E = \frac{\Delta M_K}{\left(A_K \cdot \rho_K \cdot E_K\right)} \quad \text{(Eq. 3)}$$

where:

F = atomic oxygen fluence in LEO (atoms/cm^2)
F_E = atomic oxygen effective fluence in ground laboratory facility (atoms/cm^2)
ΔM_K = mass loss of Kapton® H witness sample (g)
A_K = surface area of Kapton® H witness sample exposed to atomic oxygen (cm^2)
ρ_K = density of Kapton® H witness sample (1.4273 g/cm^3) (de Groh et al., 2008)
E_K = erosion yield of Kapton® H witness sample in LEO (3.0×10^{-24} cm^3/atom).

Therefore, the erosion yield can be determined through the following equation:

$$E_y = E_K \frac{\Delta M_S \cdot A_K \cdot \rho_K}{\Delta M_K \cdot A_S \cdot \rho_S} \quad \text{(Eq. 4)}$$

One of the critical issues with using mass loss data to obtain accurate erosion yield data is that dehydrated mass measurements are needed. Many polymer materials, such as Kapton®, are very hygroscopic and can absorb up to several percent of their weight in moisture and, therefore, can fluctuate in mass with humidity and temperature. Small changes in mass loss related to atomic oxygen erosion can be difficult to measure accurately if the state of hydration is variable; weighing the samples in a dehydrated state largely eliminates this source of error. Therefore, for accurate mass loss measurements, it is necessary that the samples be fully dehydrated, e.g., in a vacuum desiccator, before both pre-flight and post-flight measurements. Full dehydration for samples ≤127 µm (≤5 mil) thick requires a minimum of 48 hours for vacuum dehydration at pressures below 200 mtorr.

Figure 22, Fractional Mass Gain of 127-µm- (5-mil-) Thick Kapton® H related to Rehydration as a Function of Time after Removal from Vacuum Dehydration, provides an example of a rehydration curve for Kapton® H shortly after removal from a vacuum dehydration environment. The graph shows the fractional mass gained during rehydration of a 127-µm- (5-mil-) thick Kapton® H film after dehydration in a vacuum desiccator for >72 hours.

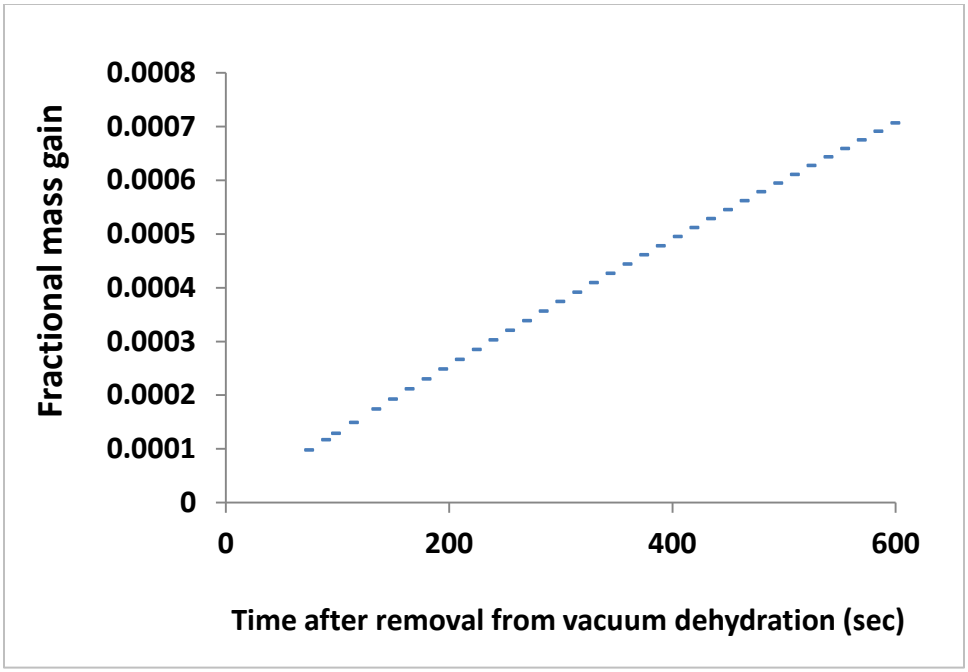

Figure 22—Fractional Mass Gain of 127-µm- (5-mil-) Thick Kapton® H related to Rehydration as a Function of Time after Removal from Vacuum Dehydration

There is a large variation in the erosion yield values for spaceflight data from early LEO missions. This is partly because some flight experiments, such as short-duration Shuttle flight experiments, were exposed to low atomic oxygen fluences on orbit, but variations in much of the early LEO space data also occurred because some erosion yield data were not determined based on dehydrated mass measurements, introducing large error for hygroscopic materials, especially for low fluence exposures or low erosion yield samples.

7.1.2. Recession Depth Techniques

Recession measurements have been used for erosion yield determination based on erosion depth step heights. The erosion or recession depth can be measured from a protected surface using profilometry with a stylus profilometer or with scanning electron microscopy (SEM), optical interferometry, or atomic force microscopy (AFM) (Minton, 1995). If the surface is protected by an intimate tin mask or mesh or a protective film, the erosion yield can be calculated through the following equations:

For LEO exposures:

$$E_y = y / F \qquad \text{(Eq. 5a)}$$

For ground laboratory testing:

$$E_y = y / F_E \qquad \text{(Eq. 5b)}$$

where:

y = erosion step height (cm)
F = atomic oxygen fluence in LEO (atoms/cm^2)
F_E = atomic oxygen effective fluence in ground laboratory facility (atoms/cm^2).

For very small erosion depths, techniques for step-height determination, such as stylus profilometry, SEM, and optical interferometry, are not sensitive enough or have other faults. For example, an SEM is not suited for obtaining accurate erosion depth measurements (z-direction), and making stylus measurements on soft polymers can be problematic. One technique that maintains accuracy for very small step-height measurements is AFM. AFM can have a lateral resolution of 10 to 20 Å and sub-angstrom vertical resolution (Howland and Benatar, 1996).

7.1.2.1 Mesh Techniques

Metal meshes, such as a stainless-steel or nickel-etched meshes, have been used to protect surfaces from atomic oxygen attack, resulting in step-height changes between the eroded areas and covered areas (Minton, 1995). A frequent problem with using a mesh is that it needs to be very thin and in close contact with the surface of the polymer for accurate step-height measurement. However, it is very difficult to place a thin mesh in close contact with a polymer. In de Groh et al. (2001, AFM), the quantification of the error associated with the thickness and closeness of a mesh with respect to the polymer, i.e., the distance of the exposed mesh surface to the protected polymer surface, is reviewed. It was found that the height of the mesh with respect to the protected surface plays a critical role in the error of erosion yield measurements.

7.1.2.2 Film Techniques

Coatings such as metals, SiO_2, and Al_2O_3 are listed as serving as potential effective masks as long as the coatings are ≥20 nm thick (Minton, 1995). The problem with the mask technique is that the thickness of the coating needs to be very accurately known for low fluence exposures, and the coating must end cleanly and sharply. A gradual thinning of the protective coating at its margin, which commonly occurs, will contribute to step-height errors (de Groh et al., 2001, AFM).

7.1.2.3 Salt-Spray/AFM Recession Technique

A recession depth technique was developed at NASA Glenn Research Center (GRC) that involves pre-flight protection of the sample surface using small, isolated particles in contact with the sample surface (de Groh, et al., 2001, AFM). These particles, such as salt crystals or mica powder, are applied either by salt spraying or mica dusting, resulting in isolated protective particles. The particles are removed post-flight, e.g., the salt is washed off with distilled water and the surface is then dried with nitrogen gas; erosion depth step-height or recession measurements are then obtained using AFM. Salt-spraying and mica-dusting techniques and AFM profiling are discussed in detail in de Groh et al., (2001, AFM). Figure 23, High-Magnification Image of a Graphite Epoxy Composite Sample Flown as Part of the EOIM III Experiment aboard STS-46 and Exposed to an Atomic Oxygen Fluence of 2.3×10^{20} atoms/cm^2,

is an example of how a small particle can protect the underlying polymer from atomic oxygen erosion (de Groh et al., 2001, AFM).

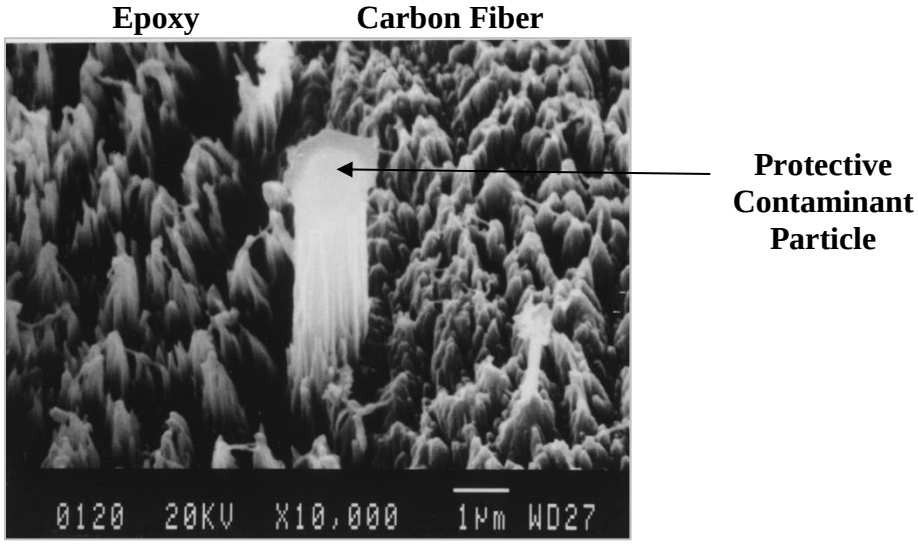

Figure 23—High-Magnification Image of a Graphite Epoxy Composite Sample Flown as Part of the EOIM III Experiment aboard STS-46 and Exposed to an Atomic Oxygen Fluence of 2.3×10^{20} atoms/cm^2

Protective salt particles can be applied to the sample substrate by spraying a saturated sodium chloride salt solution using an atomizer. A uniform distribution of small cubic crystals is ideal. Experiments conducted for the development of the PEACE Polymers experiment have shown that salt spraying can result in the formation of a variety of different salt particles (de Groh et al., 2001, AFM), such as small or large cubic crystals, oval or asymmetric spherical particles, crystals with salt "rings" around them, and ring deposits that form doughnut-shaped appearances after drying. Figure 24, Different Types of Sodium Chloride Salt Particles Formed on a Kapton® HN Substrate during Salt-Spraying, shows examples of these different salt particle formations (de Groh et al., 2001, AFM). Issues related to salt rings and possible condensation build-up effects on experiments in the Shuttle bay (while in the Cape Canaveral environment) are provided by de Groh et al. (2001, AFM).

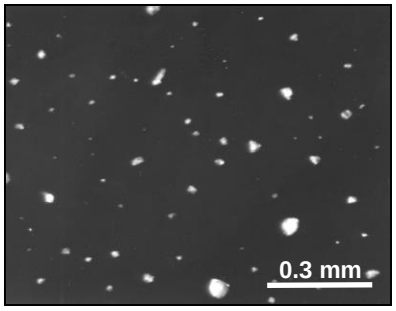

(a) Small, Irregularly Shaped Particles

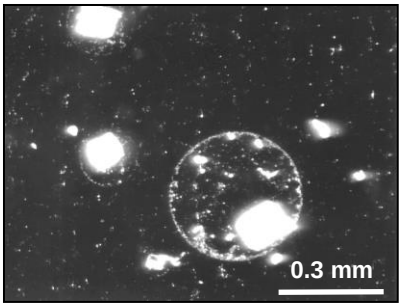

(b) Salt Rings around Large, Roughly Cubic Crystals

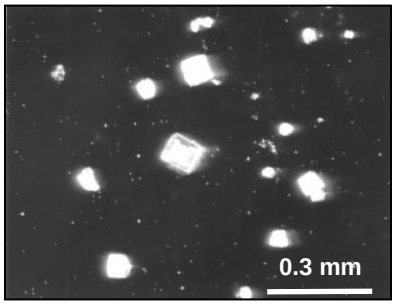

(c) Large Cubic and Irregularly Shaped Crystals

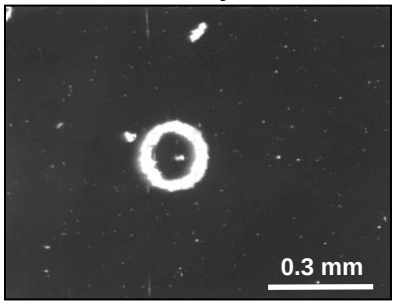

(d) Ring Deposits

Figure 24—Different Types of Sodium Chloride Salt Particles Formed on a Kapton® HN Substrate during Salt-Spraying

The recession measurement technique developed by GRC has the advantage that very small sample areas can be used to obtain erosion yield data, and multiple polymers can be put together as one flight sample. Error analyses were performed for this technique and for the traditional erosion yield determination technique based on mass loss; as expected, both were highly dependent on atomic oxygen fluence. Also, the recession technique was found to be very dependent on protective particle height and to be more accurate than the mass loss technique for protective particles <17 μm thick (de Groh et al., 2001, AFM). For example, for a fluence of 1×10^{19} atoms/cm^2, the probable error in atomic oxygen erosion yield found using the AFM recession technique (using a 10-μm-thick protective particle) is approximately 60 percent of the error in the erosion yield found using the mass loss technique (7.74 percent versus 13.1 percent, respectively) (de Groh et al., 2001, AFM). These error analysis results stress the importance of using small particles in contact with the test material, such as cubic salt crystals, or very thin mica dust particles.

8. MATERIALS INTERNATIONAL SPACE STATION EXPERIMENT

8.1 MISSE Overview

MISSE is a United States (U.S.) program that includes participants from NASA, various Department of Defense (DoD) organizations, industry, and universities. For more than a decade, MISSE has studied the long-duration environmental durability of spacecraft materials and devices in the LEO environment through a series of materials spaceflight experiments. The

overall objective of MISSE is to test the stability and durability of materials and devices in the space environment to gain valuable knowledge of the performance of materials in space, as well as to enable lifetime prediction of new materials and components that may be used in future spaceflight.

Experiments developed by principal investigators are loaded onto hinged, suitcase-like containers, called Passive Experiment Containers (PECs) (de Groh et al., 2009). (See figure 25, Pre-Flight Photograph of MISSE PEC 2). The PECs are exposed to the space environment on the exterior of the ISS (de Groh, 2010). During transport to the ISS on the Space Shuttle, the PECs are closed with the samples facing each other for protection; once the Space Shuttle reaches the ISS, the PECs are attached to its exterior during an extravehicular activity (EVA) and opened back-to-back, exposing the samples to space (de Groh et al., 2006, ESA; de Groh et al., 2006, NSMMS; Groh et al., 2009). (See figure 26, During a spacewalk on August 16, 2001, astronaut Patrick Forrester installs MISSE PEC 2 on the ISS Quest Airlock, and figure 27, MISSE 1 during an EVA in January 2003 after 17 Months of Space Exposure.) The PECs are retrieved after 1 or more years of space exposure and returned to Earth for post-flight evaluations of the experiments.

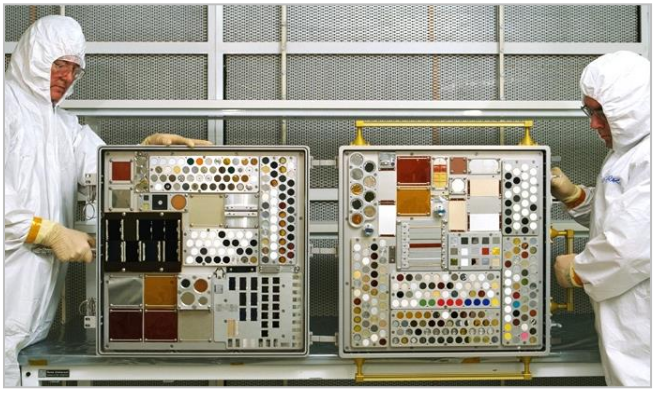

Figure 25—Pre-Flight Photograph of MISSE PEC 2

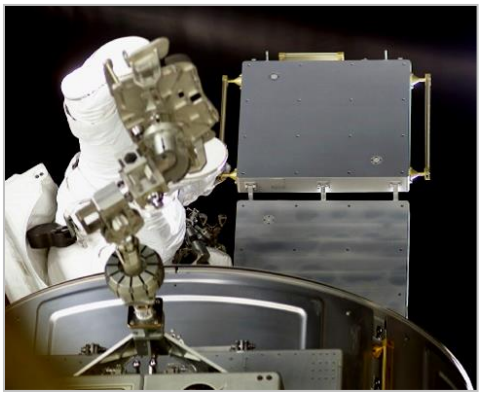

(a) Opening the Attached PEC

(b) Securing the PEC in the Opened Position, Exposing the Samples to Space

Figure 26—During a spacewalk on August 16, 2001, astronaut Patrick Forrester installs MISSE PEC 2 on the ISS Quest Airlock.

Figure 27—MISSE 1 during an EVA in January 2003 after 17 Months of Space Exposure

The MISSE PECs are flown in either a ram/wake orientation, i.e., leading edge/trailing edge facing, or a zenith/nadir orientation, i.e., space facing/Earth facing. Each of these orientations provides different space environmental exposures. For example, samples in a ram orientation receive the greatest amount of atomic oxygen exposure combined with solar radiation exposure, while those in a wake orientation receive solar radiation exposure with very little atomic oxygen exposure. Zenith-facing samples receive the highest amount of solar radiation and grazing atomic oxygen exposure, and nadir-facing samples receive little solar exposure (only ambient reflected solar exposure) with grazing atomic oxygen exposure. Ten MISSE PECs have flown, along with a small passive tray called the Optical Reflector Materials Experiment III Ram/Wake (ORMatE-III R/W). Table 2, Mission Exposure Summary of MISSEs 1-8, provides mission information for the 10 MISSE PECs, including their PEC locations, orientations, and durations on the ISS.

Table 2—Mission Exposure Summary of MISSEs 1-8

MISSE	Launch Mission	Placed Outside ISS	Location on ISS	Tray Orientation	Retrieval Mission	Retrieved from ISS	Exposure (yr)
1, 2	STS-105	8/16/01	MISSE 1: High-Pressure Gas Tank (HPGT) MISSE 2: Quest Airlock	Ram and Wake	STS-114	7/30/05	3.95
3, 4	STS-121	8/3/06[1]	MISSE 3: HPGT MISSE 4: Quest Airlock	Ram and Wake	STS-118	8/18/07	1.04
5	STS-114	8/3/05	Aft P6 Trunion Pin Handrail	Zenith and Nadir	STS-115	9/15/06	1.12
6A, 6B	STS-123	3/22/08	Columbus Laboratory	Ram and Wake	STS-128	9/1/09	1.45
7A, 7B	STS-129	11/23/09	EXPRESS[2] Logistics Carrier 2 (ELC 2) on the S3 Truss	7A: Zenith and Nadir 7B: Ram and Wake	STS-134	5/20/11	1.49
8 and ORMatE-III R/W	STS-134	8: 5/20/11; ORMatE-III R/W: 7/12/11[3]	ELC 2 on the S3 Truss	8: Zenith and Nadir; ORMatE-III R/W: Ram and Wake	SpaceX-3 Dragon	7/9/2013	8: 2.14; ORMatE-III R/W: 2.00

Notes:
1. Deployed during Expedition 13
2. EXpedite the PRocessing of Experiments to Space Station (EXPRESS)
3. Deployed during STS-135

MISSE has evolved over the years in its complexity and infrastructure. The original concept of attaching PECs to the exterior of the ISS to passively expose materials to space has grown to include increasingly complex in situ characterizations utilizing active experiments with telemetry down-linking of data (Jenkins et al., 2008). MISSEs 1-4 contained primarily passive experiments, while MISSE 5 included active experiments that were battery powered and included direct telemetry to ground. MISSE 6 was intended to be battery powered with data captured by data-loggers for post-flight data retrieval, but the battery approach was discarded, and power was provided directly by the ISS for 6A and 6B. Figure 28, The ISS with a Close-Up Photo of MISSEs 6A and 6B on the Columbus Laboratory (March 2008), shows MISSEs 6A and 6B on the ISS Columbus Laboratory shortly after deployment, (Yang and deGroh, 2010). MISSEs 7A and 7B contained the most active experiments of the MISSE series. MISSEs 7A, 7B, and 8 were powered from the ISS, and the data link was through the ISS communications system.

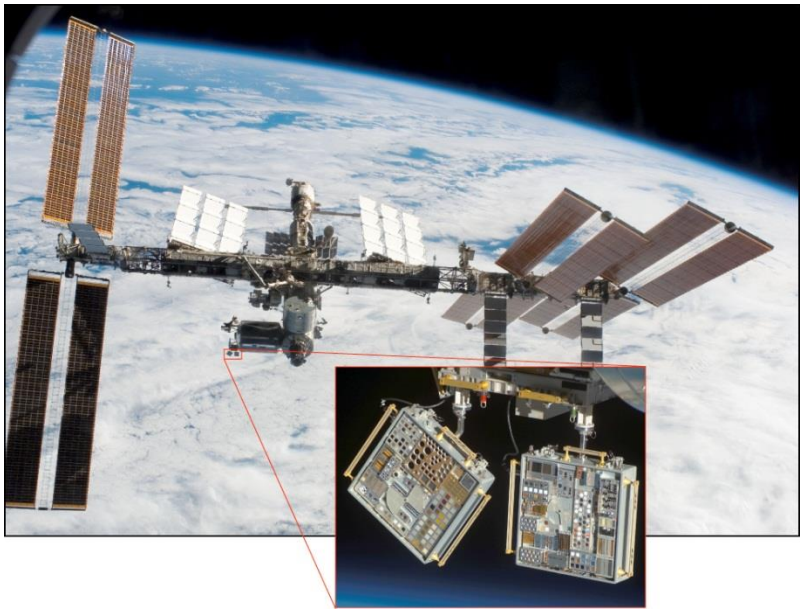

Figure 28—The ISS with a Close-up Photograph of MISSEs 6A and 6B on the Columbus Laboratory (March 2008)

Materials flown in MISSE have included polymers, ceramics, composites, coatings (protective, thermal, and optical), beta cloth, adhesives, foams, and dielectrics. Special applications materials have included radiation shields, inflatables, markers, labels, optics, and gossamer films. Components or devices flown have included switches, sensors (radiation, temperature, UV, atomic oxygen, and contamination), solar cells, semiconductors, mirrors, optical filters, optical diodes, optical modulators, and tethers. Also flown have been biological specimens including seeds, spores, and bacteria.

Data from the MISSE experiments have had a direct impact on numerous space programs such as the Hubble Space Telescope (HST), the Commercial Orbital Transportation System (COTS), and the ISS and have impacted satellite design (de Groh et al., 2009). MISSE has provided rapid access to space, producing mission-critical solar cell performance data for groups such as the Naval Research Center (NRL) (Walters et al., 2005). MISSE solar cell experiments have provided anomaly resolution data for on-orbit spacecraft, real-time data that have enabled DoD mission hardware to be designed and built in a timely manner, and on-orbit data for ground-test data validation. The Wright-Patterson Air Force Base, Air Force Research Laboratory (WPAFB AFRL) has also seen immeasurable benefits from MISSE, such as new higher power solar cell technology, electromagnetic-shielding nano-materials, and improved understanding of atomic oxygen erosion (Juhl, 2010; de Groh et al., 2011). Boeing has obtained space radiation dose measurements through experiments on MISSE (Wert, 2010; de Groh et al., 2011). The Aerospace Corporation has found that MISSE experiments reduce the risk of incorporating new technology into future satellite systems and provide an inexpensive way to evaluate vendor space readiness on a small scale (Palusinski, 2010; de Groh et al., 2011). The Aerospace Corporation uses MISSE data to educate vendors on surviving space environments, with an emphasis on material processes (quality, packaging, contamination, etc.) (Palusinski, 2010; de Groh et al., 2011). Like many MISSE investigators, The Aerospace Corporation uses the MISSE flight data

to compare on-orbit results with ground-based testing to improve the fidelity of material modeling for space survivability (Palusinski, 2010; de Groh et al., 2011).

In summary, MISSE is the longest running technology development and materials testing project on the ISS, resulting in many impacts on spacecraft materials and device design choices. The MISSE experiments are yielding long-duration space environmental performance and durability data that enable material validation, processing recertification, and space qualification; improved predictions of materials and component lifetimes in space; model verification and development; and correlation factors between space exposure and ground facilities that enable more accurate in-space performance predictions based on ground laboratory testing.

MISSE has also provided educational opportunities to interest students in science and engineering, such as the NASA GRC experiments conducted in collaboration with students from Hathaway Brown School in Shaker Heights, OH. Student involvement includes pre-flight research, flight sample fabrication and characterization, and post-flight characterization. The students have authored research papers, presented their work at an international conference, and entered their research in science fairs, winning significant scholarships and awards (de Groh et al., 2009).

8.2 MISSE 2

MISSEs 1 and 2 were the first exterior experiments on the ISS hull. MISSE 2 was attached to the exterior of the Quest Airlock on August 16, 2001, during the STS-105 Shuttle mission (de Groh et al., 2009). The MISSE 2 PEACE Polymers tray is visible in figure 29, MISSE PEC 2 (Ram-Facing Tray) on the ISS Quest Airlock (August 17, 2001, 1 Day after Deployment during the STS-105 Mission. Figure 30, The Quest Airlock and MISSE PEC 2 (STS-105 Mission), shows the location of MISSE PEC 2 (de Groh et al., 2008).

Although MISSEs 1 and 2 were originally planned as a 1-year mission, their retrieval was significantly delayed because of the Columbia Shuttle accident. MISSEs 1 and 2 were successfully retrieved after 3.95 years of space exposure during a spacewalk on July 30, 2005, as part of Discovery’s STS-114 Return to Flight mission.

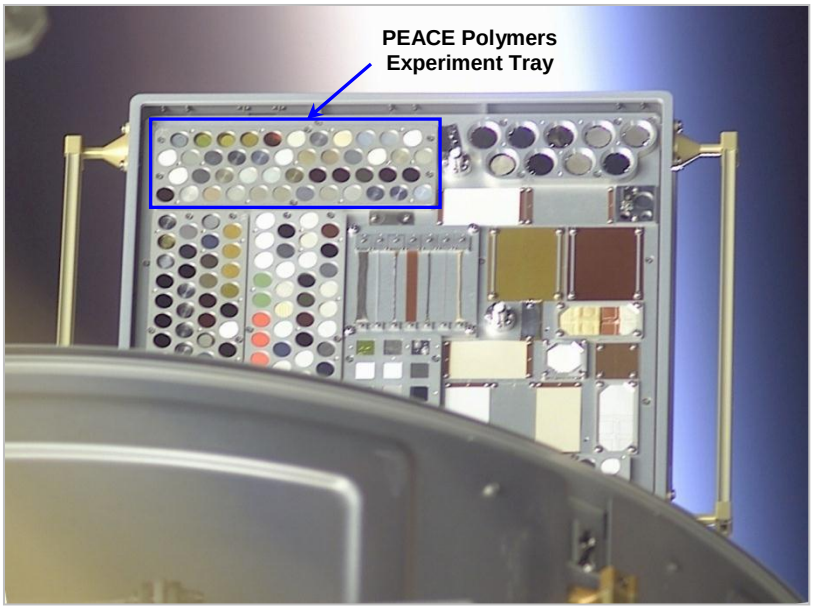

Figure 29—MISSE PEC 2 (Ram-Facing Tray) on the ISS Quest Airlock (August 17, 2001, 1 Day after Deployment during the STS-105 Mission)

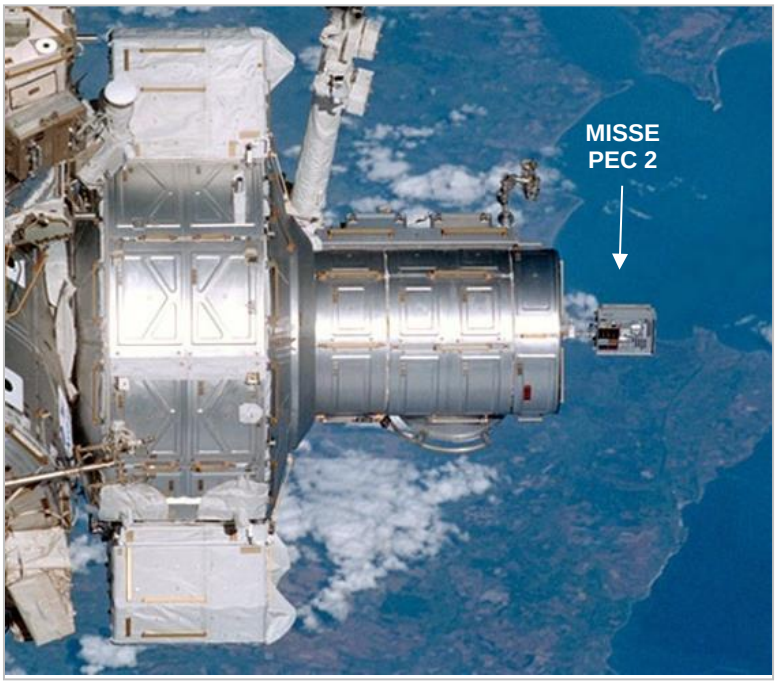

Figure 30—The Quest Airlock and MISSE PEC 2 (STS-105 Mission)

9. MISSE 2 POLYMER EROSION AND CONTAMINATION EXPERIMENT POLYMERS

As part of MISSE 2, 41 samples, collectively called the PEACE Polymers, were exposed to the LEO space environment on the exterior of the ISS for nearly 4 years. The purpose of the MISSE 2 PEACE Polymers experiment was to accurately determine the atomic oxygen erosion yield of a wide variety of polymeric materials exposed to the LEO space environment for an extended period of time (de Groh et al., 2001, AIAA). The polymers range from those commonly used for spacecraft applications, such as Teflon® FEP, to more recently developed polymers, such as high-temperature polyimide PMR. Additional polymers were included to explore erosion yield dependence upon chemical composition, with the goal of developing a predictive model for erosion yield.

It was decided that mass loss was the best measurement technique for this flight experiment because many of the PEACE Polymers are composed of multiple thin-film layers, as described in section 9.2.2 of this Handbook, and erosion can occur through multiple layers (de Groh et al., 2008). In addition, individual layers can be so fragile after erosion that recession depth measurements would be impossible to obtain. With mass loss measurements, an average mass of the fragile pieces and layers and underlying non-eroded supportive layers can be obtained. Extensive error analysis was conducted to determine the error in the erosion yield values for each of the MISSE 2 PEACE Polymers flight samples. The uncertainty values are provided in section 9.3.6 of this Handbook, and the specifics of the error analysis are provided in Appendix B of this Handbook. In addition to the LEO erosion yield of the flight samples, optical and thermal properties of the flight samples were also obtained post-flight and compared with control sample properties, as reviewed in section 9.3.7 of this Handbook. Appendices C and D of this Handbook provide the optical properties and summary pages for each individual flight sample. Details on the specific polymers flown, flight sample fabrication, pre-flight and post-flight characterization techniques, and atomic oxygen fluence determination are discussed in this section, along with a summary of the atomic oxygen erosion yield results.

9.1 PEACE Polymer Materials

The specific polymers chosen for the MISSE PEACE Polymers experiment represent a wide range of polymeric materials and bonding types. The polymers chosen included those commonly used for spacecraft applications, such as Teflon® FEP and white Tedlar®, as well as more recently developed polymers, such as high-temperature PMR. Pyrolytic graphite and polymers such as polyethylene oxide (PEO) and cellulose acetate (CA) were also included based solely on their chemical composition to provide LEO erosion yield data for modeling purposes. Two polyimide Kapton® H samples were included to serve as atomic oxygen fluence witness samples. The 40 polymers and pyrolytic graphite, their associated polymer abbreviations, and the MISSE serial numbers are listed in table 3, MISSE PEACE Polymers List.

Table 3—MISSE PEACE Polymers List

MISSE Serial #	Material	Abbreviation	Trade Names
2-E5-6	Acrylonitrile butadiene styrene	ABS	Cycolac®, Absylux®, Lustran®
2-E5-7	Cellulose acetate	CA	Tenite™ Acetate; Dexel, Cellidor®
2-E5-8	Poly-(p-phenylene terephthalamide)	PPD-T	Kevlar® 29 fabric
2-E5-9	Polyethylene	PE	
2-E5-10	Polyvinylfluoride	PVF	Tedlar® TTR10SG3 (clear)
2-E5-11	Crystalline polyvinylfluoride with white pigment	PVF-W	white Tedlar® TW#10B53
2-E5-12	Polyoxymethylene; acetal; polyformaldehyde	POM	Delrin® Acetal (natural)
2-E5-13	Polyacrylonitrile	PAN	Barex® 210
2-E5-14	Allyl diglycol carbonate	ADC	CR-39®, Homalite™ H-911
2-E5-15	Polystyrene	PS	Trycite® 1000
2-E5-16	Polymethyl methacrylate	PMMA	Plexiglas®; Acrylite® (Impact Modified)
2-E5-17	Polyethylene oxide	PEO	Alkox® E-30 (powder)
2-E5-18	Poly(p-phenylene-2,6-benzobisoxazole)	PBO	Zylon® (balanced biaxial film)
2-E5-19	Epoxide or epoxy	EP	Hysol® EA 956
2-E5-20	Polypropylene	PP	Contour® 28, GOEX
2-E5-21	Polybutylene terephthalate	PBT	VALOX® 357
2-E5-22	Polysulfone	PSU	Thermalux® P1700-NT11; Udel® P-1700
2-E5-23	Polyurethane	PU	Dureflex® PS8010
2-E5-24	Polyphenylene isophthalate	PPPA	Nomex® Crepe Paper T-410
2-E5-25	Pyrolytic graphite	PG	Pyrolytic graphite
2-E5-26	Polyetherimide	PEI	Ultem® 1000
2-E5-27	Polyamide 6	PA 6	Nylon 6, Akulon® K, Ultramid® B
2-E5-28	Polyamide 66	PA 66	Nylon 66, Maranyl™ A, Zytel®
2-E5-29	Polyimide	PI	LaRC CP1 (CP1-300)
2-E5-30	Polyimide (PMDA)	PI	Kapton® H
2-E5-31	Polyimide (PMDA)	PI	Kapton® HN
2-E5-32	Polyimide (BPDA)	PI	Upilex-S®
2-E5-33	Polyimide (PMDA)	PI	Kapton® H
2-E5-34	High-temperature polyimide resin	PI	PMR-15
2-E5-35	Polybenzimidazole	PBI	Celazole™ PBI 22
2-E5-36	Polycarbonate	PC	PEEREX® 61
2-E5-37	Polyetheretherketone	PEEK	Victrex® PEEK™ 450
2-E5-38	Polyethylene terephthalate	PET	Mylar® A-200
2-E5-39	Chlorotrifluoroethylene	CTFE	Kel-F®; Neoflon® M-300
2-E5-40	Ethylene-chlorotrifluoroethylene	ECTFE	Halar® 300
2-E5-41	Ethylene-tetrafluoroethylene	ETFE	Tefzel® ZM
2-E5-42	Fluorinated ethylene propylene	FEP	Teflon® FEP 200A
2-E5-43	Polytetrafluoroethylene	PTFE	Chemfilm® DF 100
2-E5-44	Perfluoroalkoxy copolymer resin	PFA	Teflon® PFA 200 CLP
2-E5-45	Amorphous fluoropolymer	AF	Teflon® AF 1601
2-E5-46	Polyvinylidene fluoride	PVDF	Kynar® 740

9.2 Sample Fabrication and Pre-Flight Characterization

9.2.1 Flight Sample Dimensions and Fabrication

The MISSE PEACE Polymers samples were ~2.54-cm-diameter discs. Most polymers were in thin-film form and typically ranged from 0.0025 to 0.051 cm thick. Samples were punched into circular discs using a double-bow punch cutter and an Arbor press.

Several samples, however, did not come in thin-film form. Allyl diglycol carbonate (ADC, 2-E5-14), typically used as lens material, was ordered from a manufacturer in 2.54-cm-diameter, 0.079-cm-thick samples. Pyrolytic graphite (PG, 2-E5-25) was also ordered in 2.54-cm-diameter pieces, 0.203 cm thick. Hysol® EA 956 epoxy (EP, 2-E5-19) was purchased as a two-part kit. Although epoxy is available as reasonably mixed systems, care should be exercised to ensure that the mixtures are accurate so that the epoxy results in verifiable characteristics, as specified. Flight samples were fabricated by mixing and curing the epoxy and then carefully sawing out 2.54-cm-diameter samples from brittle sheets of cured epoxy. The thickness of the epoxy flight sample was ≈0.231 cm. Polyethylene oxide (PEO, 2-E5-17) was purchased as a powder and fabricated into sheet material by pressing the powder with heated plates using a Carver Laboratory Press. To keep the PEO from sticking to the plates, two sheets of Kapton® were placed between the press plates and the PEO powder. The PEO powder was pressed at 10.5 metric tons for 5 to 10 sec with the press plates heated to 260 °C. Although the press pressure and temperate are somewhat arbitrary, what is important is the density of the individual sample, because PEO erosion yields for samples of different densities are simply inversely proportional to the ratio of the densities, so that a PEO sample of half the density would have twice the erosion yield. After pressing and cooling the PEO, the Kapton® sheets were carefully separated from the PEO sheet, which was between 0.74 and 0.94 cm thick, from which 2.54-cm-diameter samples were punched. High-temperature polyimide resin (PI, 2-E5-34), also known as PMR-15, was fabricated by the Polymers Branch at GRC in 2.54-cm-diameter, 0.030-cm-thick pieces. Poly-(p-phenylene terephthalamide) (PPD-T, 2-E5-8), also known as Kevlar® 29, was obtained in fabric form, from which flight samples were cut. Al discs were applied to the backs of the flight samples and wrapped around the non-spaced exposed edges to protect against fraying or loss of small filaments. Polyphenylene isophthalate (PPPA), also known as Nomex®, was supplied as 0.005-cm-thick sheets of paper, from which flight samples were punched.

9.2.2 Sample Stacking

MISSEs 1 and 2 were originally planned as a 1-year mission. The expected atomic oxygen fluence for a 1-year exposure on the ISS is 3.28×10^{21} atoms/cm^2 for directed atomic oxygen exposed surfaces, based on a mission launch date of June 2001, a 400-km circular orbit, and a 51.6° inclination. For many of the thin-film polymers, a single layer would be completely eroded away after a 1-year mission. In addition, flight experiments are not always retrieved on the original planned date and can be left in space much longer. Depending on the polymer thickness and estimated erosion yield, stacking of several layers was necessary for many polymers. The total number of layers to be stacked for flight was determined based on the amount of material that would theoretically survive a 3-year mission (three times the duration of the original planned mission).

Stacking the sample layers is complicated by the fact that increasing the mass of the sample causes a decrease in the sensitivity of the mass change; a sample with the lowest possible mass is ideal so that the mass loss is a significant percent of the total mass of the sample. With this in mind, two different sets of samples were stacked together for flight. The first set, called Part A, included the number of sample layers needed to survive an atomic oxygen exposure period of 1.5 years (chosen to be 0.5 years longer than the mission). The second set, called Part B, was added behind the weighed set and included the number of additional sample layers needed to survive a 3-year mission.

The number of layers needed for each sample to survive 1.5 years of exposure (Part A) was determined based on the estimated erosion yield of each polymer and the expected atomic oxygen fluence for a 1.5-year mission, computed to be 4.55×10^{21} atoms/cm^2. The total number of layers to be stacked together as one flight sample (Parts A and B) was calculated based on the expected atomic oxygen fluence for a 3-year mission, computed to be 9.1×10^{21} atoms/cm^2 (twice the 1.5-year fluence). The additional unweighed set (Part B) was placed behind the weighed set (Part A) in the flight hardware. Figure 31, Flight Sample Setup, shows an illustration of the flight sample.

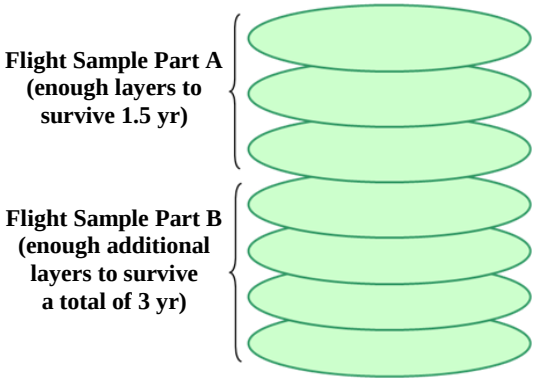

Figure 31—Flight Sample Setup

For example, the estimated erosion yield for CA is 6.8×10^{-24} cm^3/atom (Integrity Testing Laboratory Inc., 1998). Based on this erosion yield, the estimated thickness loss for 1.5 years in LEO is 0.031 cm. The thickness of one sample layer is only 0.005 cm; therefore, seven sample layers were stacked for mass measurements. A total of 0.062 cm was expected to be eroded away after 3 years, so 13 total layers were stacked for flight (the 7 weighed Part A layers plus 6 additional unweighed Part B layers).

For each complete flight sample, an identical backup sample was prepared from the same sheet of stock material (or from the same batch of fabricated material) and characterized. All individual sample layers were carefully scribe marked at the edges to indicate sample identification, orientation (front), flight or backup sample, and whether the sample had been vacuum heat treated. The backup sample, prepared in case something happened to the flight sample before installation in the flight hardware, was used as a ground-control sample. It is typically referred to as the control sample.

9.2.3 Outgassing and Vacuum Heat Treatment

Samples to be flown in the space environment need to meet outgas requirements as outlined in ASTM E 595, Standard Test Method for Total Mass Loss and Collected Volatile Condensable Materials from Outgassing in a Vacuum Environment. This test method evaluates, under carefully controlled conditions, the changes in mass (total mass loss (TML)) of a test specimen exposed to a temperature of 125 °C under vacuum and the mass of the products that leave the specimen and condense on a cooler collector plate set at a temperature of 25 °C (collected volatile condensable materials (CVCMs)) (ASTM E 595). MISSE management decided that materials being flown as part of MISSEs 1 and 2 should meet the historical screening levels of <1.00 percent TML and <0.10 percent CVCM. Of the 41 PEACE polymers, 10 did not meet the outgas requirements, based on previous testing or because they had not been tested. It was decided that these polymers could be flown if they were vacuum heat treated before flight to remove volatile products. Vacuum heat treatment was conducted at MSFC at a pressure of 7×10^{-5} Pa. Ideally, samples were to be vacuum baked for 24 hours at 125 °C (similar to ASTM E 595), but some polymers were heated at lower temperatures because of low maximum operating temperatures. Table 4, Vacuum Heat Treated MISSE PEACE Polymers, lists the vacuum heat treated samples, their maximum operating temperatures, and the vacuum heat treatment temperature and time.

Table 4—Vacuum-Heat-Treated MISSE PEACE Polymers

MISSE Serial #	Material	Abbreviation	Maximum Operating Temperature (°C)	Vacuum Heat Treatment
2-E5-6	Acrylonitrile butadiene styrene	ABS	105	24 hr at 90 °C
2-E5-7	Cellulose acetate	CA	230-245	68.75 hr at 128 °C
2-E5-8	Poly-(p-phenylene terephthalamide) fabric in Al foil	PPD-T	149-177	24 hr at 128 °C
2-E5-10	Polyvinylfluoride	PVF	107	36 hr at 100 °C
2-E5-13	Polyacrylonitrile	PAN	200-210	24.25 hr at 126 °C
2-E5-17	Polyethylene oxide	PEO	65	24 hr at 60 °C
2-E5-24	Polyphenylene isophthalate	PPPA	220	24 hr at 125 °C
2-E5-27	Polyamide 6	PA 6	98	24 hr at 90 °C
2-E5-28	Polyamide 66	PA 66	120	24 hr at 90C
2-E5-35	Polybenzimidazole	PBI	343	24 hr at 125C

The polymer polybenzimidazole (PBI (2-E5-35)) curled severely at its edges during vacuum heat treatment. For this reason, the four layers of the flight sample were stacked together (after mass measurements were obtained) and held flat for flight by being mounted in an Al holder similar to the one used for the Kevlar® fabric.

9.2.4 Pre-Flight Dehydrated Mass Measurements

Pre-flight mass measurements were obtained using the dehydrated Part A sample sets (after vacuum heat treatment, where applicable). The Part A sample sets were dehydrated in a vacuum desiccator maintained at a pressure of 8.0 to 13.3 Pa with a mechanical roughing pump. Typically, 5 flight sample sets and their corresponding control samples were placed together in a desiccator (a total of 10 sample sets). The sets of samples were placed in the desiccator and left under vacuum for a minimum of 4 days. The vacuum desiccator was put back under vacuum

immediately after a sample set was removed to keep the other samples in the desiccator under vacuum. Previous tests showed that the mass of a given dehydrated sample was not adversely affected if the desiccator was opened and quickly closed again and pumped back down to approximately 20 Pa before that sample was weighed. This process allows multiple samples to be dehydrated together. Three mass readings for each sample was obtained and averaged, and the time at which each sample was first exposed to air was recorded, along with the times at which it was weighed. The total time it took to obtain the three readings for one sample, starting from the time air was let into the desiccator, was typically 5 minutes. The samples were weighed using either a Mettler Balance 3M (0.000001-g sensitivity) or a Sartorius Balance R160P (0.00001-g sensitivity), depending on total sample mass. Records were kept of the following: the sequence of sample weighing, the number of layers in each Part A set, the time under vacuum before weighing, the temperature and humidity in the room, the time air was let into the desiccator, the time each sample set was taken out of the desiccator, and the time of each weighing. The same procedure and sequence were repeated with the same samples post-flight.

9.2.5 Density Data

A material's theoretical density, which is provided by the manufacturer, is not always accurate because of processing variations among the sheets of the materials. To obtain more accurate density values control for this variation, density measurements were obtained for 36 of the 41 polymers using calibrated density gradient columns. Density gradient columns were created in a 50-mL buret with varying proportions of either cesium chloride (CsCl), $\rho \approx 2$ g/cm^3, andH_2O, $\rho = 1$ g/cm^3, for less dense polymers, or carbon tetrachloride (CCl_4), $\rho = 1.594$ g/cm^3, and bromoform ($CHBr_3$), $\rho = 2.899$ g/cm^3, for denser polymers. Because of the variation in density of the polymers, numerous columns with variations in initial mixed solutions were made that allowed a wide range of densities to be determined. Glass standards of known densities (± 0.0001 g/cm^3) were placed in the column and allowed to settle, and then small pieces of various polymers were placed in the columns. A curve was fit to the positions and relative known densities of the glass standards. Plotting the positions of the test polymers on this curve yielded density values for each material (de Groh et al., 2006, ESA; de Groh et al., 2006, NSMMS; de Groh et al., 2008). The density values for approximately half of the polymers were determined based on averages obtained from more than one density column.

Five polymers either had density values out of the range of the density columns or were of a form not easily sectioned for density column measurements. The densities for these materials (acrylonitrile butadiene styrene (ABS), polyethylene (PE), polypropylene (PP), PPPA, and PG) were obtained from referenced literature or manufacturers' Material Safety Data Sheets (MSDSs). The densities of the PEACE Polymer samples, along with uncertainty values, are provided in table 5, Density Gradient Column Data for the PEACE Polymers.

Table 5—Density Gradient Column Data for the PEACE Polymers

MISSE 2 Serial #	Material	Abbreviation	Trial #				# of Trials	Average Density (g/cm^3)	Std. Dev. (g/cm^3)
			1	2	3	4			
6	Acrylonitrile butadiene styrene	ABS						1.05 (a)	
7	Cellulose acetate	CA	1.2893	1.2928			2	1.2911	0.0025

MISSE 2 Serial #	Material	Abbreviation	Trial #				# of Trials	Average Density (g/cm^3)	Std. Dev. (g/cm^3)
			1	2	3	4			
8	Poly-(p-phenylene terephthalamide)	PPD-T	1.4422				1	1.4422	
9	Polyethylene	PE						0.9180 (b)	
10	Polyvinylfluoride	PVF	1.3801	1.3783			2	1.3792	0.0013
11	Crystalline polyvinylfluoride with white pigment	PVF-W	1.5661	1.6657	1.6406		3	1.6241	0.0518
12	Polyoxymethylene; acetal; polyformaldehyde	POM	1.3819	1.4148			2	1.3984	0.0233
13	Polyacrylonitrile	PAN	1.1273	1.1596			2	1.1435	0.0228
14	Allyl diglycol carbonate	ADC	1.3173				1	1.3173	
15	Polystyrene	PS	1.0503				1	1.0503	
16	Polymethyl methacrylate	PMMA	1.1628				1	1.1628	
17	Polyethylene oxide	PEO	1.1450	1.1489			2	1.1470	0.0028
18	Poly(p-phenylene-2,6-benzobisoxazole)	PBO	1.3444	1.4507			2	1.3976	0.0752
19	Epoxide or epoxy	EP	1.115				1	1.1150	
20	Polypropylene	PP						0.9065 (c)	
21	Polybutylene terephthalate	PBT	1.3289	1.3346			2	1.3318	0.0040
22	Polysulfone	PSU	1.2254	1.1956	1.2387		3	1.2199	0.0221
23	Polyurethane	PU	1.2468	1.2222			2	1.2345	0.0174
24	Polyphenylene isophthalate	PPPA						0.7200 (d)	
25	Pyrolytic graphite	PG						2.2200 (e)	
26	Polyetherimide	PEI	1.2873				1	1.2873	
27	Polyamide 6	PA 6	1.1177	1.1289			2	1.1233	0.0079
28	Polyamide 66	PA 66	1.1318	1.3993	1.1446		3	1.2252	0.1509
29	Polyimide	PI (CP1)	1.4246	1.4328	1.4006		3	1.4193	0.0167
30, 33	Polyimide (PMDA)	PI (Kapton® H)	1.4333	1.4301	1.416	1.4296	4	1.4273	0.0077
31	Polyimide (PMDA)	PI (Kapton® HN)	1.4348	1.4355	1.4322	1.4359	4	1.4346	0.0017
32	Polyimide (BPDA)	PI (Upilex-S®)	1.4002	1.3550	1.3974	1.3937	4	1.3866	0.0212
34	High-temperature polyimide resin	PI (PMR-15)	1.3232				1	1.3232	
35	Polybenzimidazole	PBI	1.273	1.2744	1.2799		3	1.2758	0.0036
36	Polycarbonate	PC	1.1231				1	1.1231	
37	Polyetheretherketone	PEEK	1.1936	1.2582			2	1.2259	0.0457
38	Polyethylene terephthalate	PET	1.3926	1.3953	1.3895		3	1.3925	0.0029
39	Chlorotrifluoroethylene	CTFE	2.1327				1	2.1327	
40	Ethylene-chlorotrifluoroethylene	ECTFE	1.6802	1.6719			2	1.6761	0.0059
41	Ethylene-tetrafluoroethylene	ETFE	1.7417	1.7376			2	1.7397	0.0029
42	Fluorinated ethylene	FEP	2.1443				1	2.1443	

MISSE 2 Serial #	Material	Abbreviation	Trial #				# of Trials	Average Density (g/cm^3)	Std. Dev. (g/cm^3)
			1	2	3	4			
	propylene								
43	Polytetrafluoroethylene	PTFE	2.1503				1	2.1503	
44	Perfluoroalkoxy copolymer resin	PFA	2.1383				1	2.1383	
45	Amorphous fluoropolymer	AF	2.1463				1	2.1463	
46	Polyvinylidene fluoride	PVDF	1.7562	1.7684			2	1.7623	0.0086

Notes:
(a) IDES, http://www.ides.com/generics/ABS/ABS_typical_properties.htm (ρ = 1.01–1.09 g/cm^3). Retrieved October 2007.
(b) Consolidated Thermoplastics manufacture's density.
(c) Average of data from Brady, G.S., Clauser, H.R., Vaccari, J.A. (1997). *Materials Handbook 14th ed.* New York: McGraw-Hill. p. 699 (ρ = 0.913 g/cm^3) and MSDS (ρ = 0.895–0.905 g/cm^3).
(d) DuPont Nomex® Crepe Paper Type 410 Technical Data Sheet.
(e) Brady, G.S., Clauser, H.R., Vaccari, J.A. (1997). *Materials Handbook 14th ed.* New York: McGraw-Hill. p. 427.

9.2.6 Area Measurements

The exposed area of each sample was determined by measuring the diameter of the sample tray opening using digital calipers. The area of each tray opening for each sample location was calculated by averaging measurements from 10 different diameter orientations.

9.3 MISSE 2 PEACE Flight Exposure and Results

9.3.1 Flight Sample Mounting (Tray E5)

The MISSE PEACE Polymers resided in sample Tray E5, which holds a total of 46 2.54-cm-diameter flight samples. The PEACE Polymer samples started in the sixth sample position from the left in the top row. Each sample was assigned a serial number to indicate its position; for example, ABS, with serial number 2-E5-6, represents the sample in MISSE PEC 2, Tray E5, sample position 6. Five other samples (four DC 93-500 silicone samples and one atomic oxygen scattering chamber) were also on this tray in positions 2-E5-1 through 2-E5-5. Sample positions were assigned based on anticipated erosion yields or by grouping samples by polymer family, such as the polyimides. Samples with high erosion yields were located next to the silicone samples, as they were less likely to be affected by silicone cross-contamination. Figure 32, GRC's 41 MISSE PEACE Polymers Loaded into Sample Tray E5, shows a pre-flight photo of the PEACE Polymers samples, along with the five other samples, with each sample's identification overlaid. The five samples on the top row at the left were not part of the MISSE PEACE Polymers experiment and, therefore, do not have an overlaid identification.

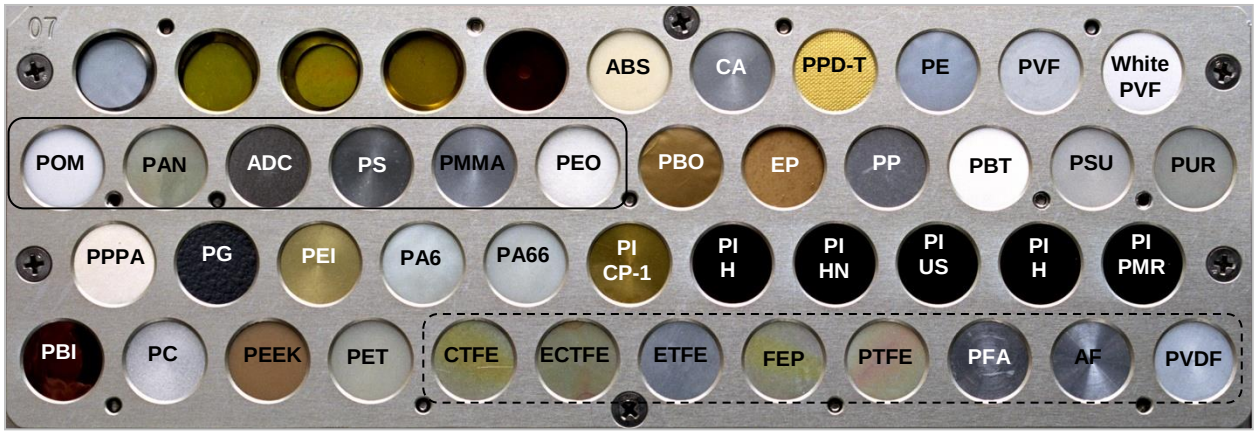

Legend:
Solid line: Samples within the solid line (2-E5-12 through 2-E5-17) were expected to have high erosion yields.
Dashed line: Samples within the dashed line (2-E5-39 through 2-E5-46) were from the fluoropolymer family.
PI: Indicates samples in the polyimide family.

Figure 32—GRC's 41 MISSE PEACE Polymers Loaded into Sample Tray E5

9.3.2 Environmental Exposure

The atomic oxygen fluence exposure for the MISSE 2 PEACE Polymers is described in section 9.3.4 of this Handbook. Estimated environmental conditions of solar exposure, tray temperatures, and ionizing radiation doses on MISSEs 1 and 2 are described in detail by Pippin (2006). For the ram-facing side of MISSE PEC 2 (exposed to atomic oxygen and solar radiation), the total equivalent sun hours (ESH) was estimated to be 5,000 to 6,700 ESH. This total includes Earth-reflected illumination (650 to 820 ESH). The spectrum of Earth reflection solar radiation has a reduced contribution from the VUV portion of the spectrum because of absorption by Earth's atmosphere (Pippin, 2006). Tray E5 was computed to have received approximately 6,300 ESH. The 3.95-year exposure in LEO resulted in approximately 22,800 thermal cycles; Pippin reports the baseplate thermal cycling temperature range for MISSE 2 to be nominally between 40 and -30 °C, with occasional short-term excursions to more extreme temperatures.

Data from Pippin (2006) also provide insight into the ionizing radiation environment on MISSE 2. Data from thermoluminescent dosimeters (TLDs) with thin shielding layers are most relevant to estimates of doses for the PEACE Polymer experiment thin polymer films. The TLD data indicated that the wake surface of MISSE 2 received approximately 26 krad (Si) through 0.005 cm of Al (Pippin, 2006).

The MISSE 2 environment was found to be unusually clean with very low spacecraft-induced molecular contamination, compared to the LDEF spacecraft and in-bay Space Shuttle experiments. Black-light inspection of the trays showed minimal to no contamination visible on the MISSE surfaces (Pippin, 2006), and results of XPS contamination analyses of two MISSE 2 sapphire witness samples in sample Tray E6 (located next to Tray E5) indicated an extremely thin silica contaminant layer (1.3 and 1.4 nm on each slide, respectively) (Dever et al., 2006). A small amount of fluorine was also detected (Dever et al., 2006). These low levels of contamination are caused by low outgassing of other MISSE 2 Tray 1 materials and are also related to the position of MISSE 2 on the ISS. Therefore, the flight erosion yield data were

measurably affected by contamination, which further increases the importance of these long-duration flight data.

9.3.3 PEACE Polymers Post-Flight Characterization

Figure 33, PEACE Polymers Experiment Tray in the NASA LaRC Clean Room during Post-Flight Retrieval Examination, is a post-retrieval photograph of the experiment tray as observed directly after PEC 2 was opened for the first time at NASA Langley Research Center (LaRC). As expected, many of the polymer samples were significantly degraded. Figure 34, Post-Flight Photograph of the MISSE 2 PEACE Polymers Experiment Tray**,** shows the experiment (Tray E5) after de-integration from MISSE PEC 2.

Figure 33—PEACE Polymers Experiment Tray in the NASA LaRC Clean Room during Post-Flight Retrieval Examination

Figure 34—Post-Flight Photograph of the MISSE 2 PEACE Polymers Experiment Tray

Planning for a 3-year exposure (rather than for the anticipated 1-year exposure) was found to be crucial to this experiment's success: even though the experiment received nearly 4 years of atomic oxygen exposure, material was left for all samples except one (PBI, 2-E5-35).

Once Tray E5 was brought back to NASA GRC, post-flight photo-documentation of the samples was conducted. Photographs were taken of the individual samples before removal of the try, after removal from the tray (left in a flight stack next to the control stack), and with the individual sample layers separated. Details on the number of layers for each sample that were eroded completely, the number that were textured by erosion, and the number remaining non-eroded were recorded. For samples for which additional stacked layers (Part B) had been placed behind the weighed layers (Part A), Parts A and B were separated for weighing. For some samples, however, the individual layers could not be separated from each other without damaging the sample texture or losing gossamer pieces of residual material; in these cases, all layers were kept together for post-flight sample weighing. The post-flight weighing procedures replicated the pre-flight weighing procedures in terms of the vacuum dehydration process (dehydration time, sample order, and weighing technique) as closely as possible, with the only exception occurring when Parts A and B could not be separated because of the extent of the erosion, which could cause intermingling and/or loss of sample mass during weighing.

As previously mentioned, each flight sample included two sets of sample layers: Part A was enough material to last for 1.5 years in space, theoretically, and the additional layers of Part B extended the time to approximately 3 years. Each flight sample also had a corresponding identical backup sample (including both Parts A and B) that was kept on the ground as a control sample. Though flight sample Parts A and B were not separated during flight, they were separated for pre- and post-flight weighing. This is because, with mission time constraints, only Part A of each sample was weighed pre-flight; therefore, a theoretical value for the pre-flight mass of Part B was calculated. The pre-flight mass of flight sample Part A (M_F) and the pre-flight mass of control sample Part A (M_C) were used to calculate the average mass per layer (M_A), which was multiplied by the number (n) of layers in flight sample Part B to get Part B's theoretical pre-flight mass ($n \cdot M_A$).

There were three different situations (Situations 1 through 3) for post-flight sample weighing; therefore, three different equations to determine mass loss were required. Details of the mass loss equations are provided in Appendix B of this Handbook, along with the error analysis equations.

9.3.3.1 Mass Loss Situation 1

In Situation 1 (figure 35, Illustration of Situation 1 Sample Erosion), either only one sample layer was flown or the atomic oxygen eroded through only some of the layers in flight sample Part A and all layers of flight sample Part B were still pristine (non-eroded). Because flight sample Part A and flight sample Part B were weighed separately pre-flight, in this situation, only Part A needed to be weighed post-flight and compared with its pre-flight mass. This was the ideal situation, because it minimized error by omitting the variable of the mass of Part B.

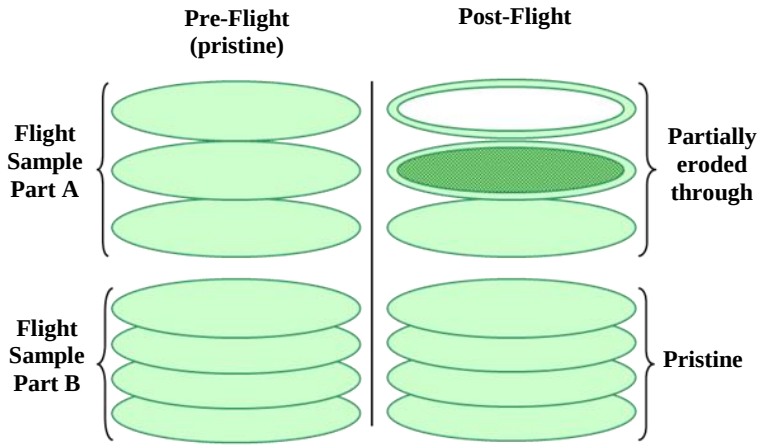

Figure 35—Illustration of Situation 1 Sample Erosion

Upilex-S® (biphenyltetracarboxylic dianhydride (BPDA) and diamine) (PI, 2-E5-32) is an example of a Situation 1 sample. Figure 36, Post-Flight Photograph of PI (Upilex-S®) (11 Layers, each 0.0025 cm thick), shows the stacked flight sample next to the stacked control sample. Eleven layers was stacked together and flown; Part A was comprised of 6 layers, and Part B was comprised of 5 layers. The individual layers of the flight sample are shown in figure 37, Post-Flight Photograph of PI (Upilex-S®) with Layers Separated (11 Layers, each 0.025 cm thick), alongside the layers of the control sample. During flight, only the top four layers of Part A experienced erosion: the top two layers were completely eroded, leaving the ring under the lip of Tray E5. The third layer was eroded with holes at the atomic oxygen textured cone valleys, and the fourth layer was eroded in places corresponding to the cone valley holes in the third layer. Because only Part A of this flight sample experienced erosion, Part A was separated from Part B post-flight, and only Part A was weighed and compared to the pre-flight mass of Part A to calculate its flight experiment mass loss.

(a) Flight Sample Stack (2-E5-32) (b) Control Sample Stack

Figure 36—Post-Flight Photograph of PI (Upilex-S®) (11 Layers, each 0.0025 cm thick)

(a) Flight Sample (2-E5-32) (b) Control Sample

Figure 37—Post-Flight Photograph of PI (Upilex-S®) with Layers Separated (11 Layers, each 0.025 cm thick)

Pyrolytic graphite (PG, 2-E5-25), shown in figure 38, Post-Flight Photograph of Pyrolytic Graphite (1 Layer, 2,032 μm thick), is another example of a Situation 1 sample. A single thick layer (0.203 cm) was flown; Part A was one layer, and there was no Part B. The post-flight sample is shown next to the control sample in figure 38. The resulting atomic oxygen erosion texture produced a velvety-looking matte black surface in the area of exposure.

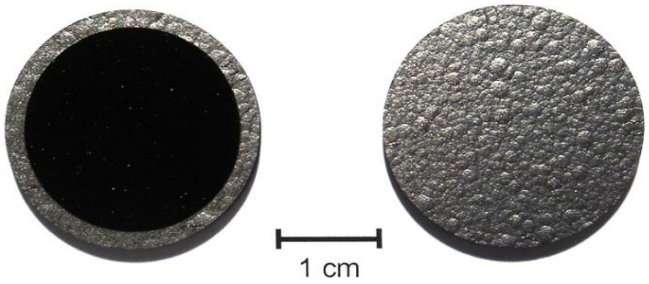

(a) Flight Sample (2-E5-25) (b) Control Sample

Figure 38—Post-Flight Photograph of Pyrolytic Graphite (1 Layer, 2,032 μm thick)

9.3.3.2 Mass Loss Situation 2

In Situation 2 (figure 39, Illustration of Situation 2 Sample Erosion), atomic oxygen erosion occurred through all of the layers of flight sample Part A and through some of flight sample Part B. In this situation, flight sample Parts A and B were able to be separated to be weighed post-flight. Because flight sample Part B was not weighed pre-flight, its theoretical pre-flight mass was used.

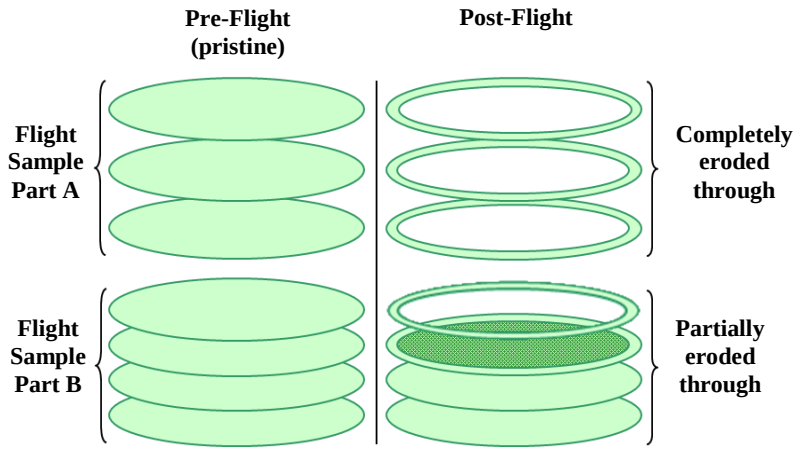

Figure 39—Illustration of Situation 2 Sample Erosion

Atomic oxygen fluence witness sample Kapton® H (2-E5-30) is an example of a Situation 2 sample. As shown in figure 40, Post-Flight Photograph of Kapton® H with Layers Separated (3 Layers, each 0.0127 cm thick), three 0.0127-cm-thick layers were flown. Part A consisted of two layers, and Part B consisted of one layer. During flight, atomic oxygen eroded the top layer completely and eroded partially through the second layer, leaving a gossamer-thin cone-like textured film. Holes in the valleys of the cones of the second layer allowed the third layer to be exposed to and textured by atomic oxygen. In this case, therefore, pre-flight and post-flight mass measurements were needed for both Parts A and B.

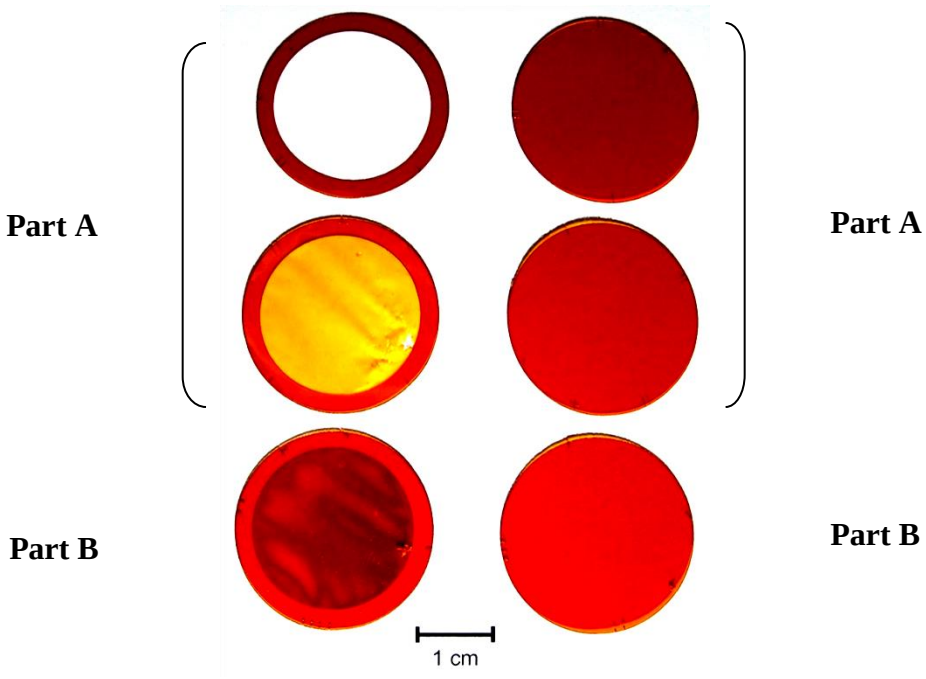

(a) Flight Sample (2-E5-30) (b) Control Sample

Figure 40—Post-Flight Photograph of Kapton® H with Layers Separated (3 Layers, each 0.0127 cm thick)

9.3.3.3 Mass Loss Situation 3

In Situation 3 (figure 41, Illustration of Situation 3 Sample Erosion), the sample layers were stuck together and fragmented and were too fragile to separate without losing particles of the material and therefore compromising the erosion yield data. Because of this, flight sample Parts A and B were weighed together post-flight.

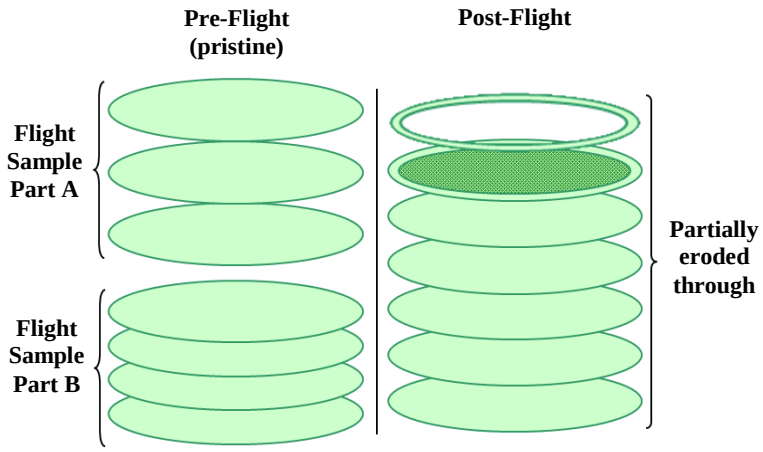

Figure 41—Illustration of Situation 3 Sample Erosion

Atomic oxygen fluence witness sample Kapton® H (PI, 2-E5-33) is an example of a Situation 3 sample (figure 42, Post-Flight Photograph of Kapton® H (3 Layers, each 0.0127 cm thick)). Three 0.0127-cm-thick layers were flown; Part A consisted of two layers, and Part B consisted of one layer. During flight, atomic oxygen eroded the top layer completely and eroded the second layer to a cone-like texture. Holes in the valleys of the cones in the second layer allowed the third layer to be exposed to and textured by atomic oxygen. For this sample, it was not possible to separate the second layer from the third layer without causing damage; therefore, the post-flight mass measurements were taken with Part A and B together.

(a) Flight Sample (2-E5-33) (b) Control Sample

Figure 42—Post-Flight Photograph of Kapton® H (3 Layers, each 0.0127 cm thick)

9.3.4 Tray 1 E5 Atomic Oxygen Fluence

The atomic oxygen fluence for PEC 2 Tray 1 E5 was computed based on the mass loss of two Kapton® H witness samples (2-E5-30 and 2-E5-33). Each Kapton® H witness sample consisted of three 0.0127-cm-thick layers for a total thickness of 0.0381 cm. As stated previously, Kapton® H is commonly used for fluence calibration because it has a well-characterized erosion yield in LEO (3.0×10^{-24} cm^3/atom).

The atomic oxygen fluence was determined using vacuum-dehydrated mass loss measurements. Two techniques for mass loss determination were evaluated: averaging the first three mass readings and back-extrapolation of the mass data to time zero using linear curve fits to get theoretically dehydrated mass values. The results of these measurements are provided in table 6, Atomic Oxygen Fluence for Kapton® H Calibration Samples.

Table 6—Atomic Oxygen Fluence for Kapton® H Calibration Samples

Mass Loss Technique	Kapton® H 2-E5-30 Mass Loss (g)	Kapton® H 2-E5-30 AO Fluence (atoms/cm^2)	Kapton® H 2-E5-33 Mass Loss (g)	Kapton® H 2-E5-33 AO Fluence (atoms/cm^2)	Average AO Fluence (atoms/cm^2)
Average of first 3 readings	0.124785	8.425 E+21	0.129219	8.436 E+21	8.43 E+21
Back-extrapolation to time zero	0.124579	8.411 E+21	0.128811	8.409 E+21	8.41 E+21

The atomic oxygen fluence values for the two fluence witness samples using the same techniques (either the average of first three readings or back-extrapolation) were very similar. The average atomic oxygen fluences for the two different techniques were also very similar. Therefore, it was decided to use the average mass value instead of the linear back-extrapolation value for

determining the atomic oxygen fluence for the experiment and also for obtaining the pre- and post-flight mass values necessary to determine the erosion yields for the individual PEACE Polymer samples. The average atomic oxygen fluence for the PEACE Polymers experiment exposure (Tray E5) on MISSE 2 was determined to be 8.43×10^{21} atoms/cm^2 (de Groh et al., 2006, ESA; de Groh et al., 2006, NSMMS; de Groh et al., 2008).

9.3.5 MISSE 2 PEACE LEO Erosion Yield Data

Table 7, MISSE 2 PEACE Polymers Erosion Yield Data, provides the erosion yield data for the MISSE 2 PEACE Polymers experiment, along with mass loss, density, and exposure area data. After the 4-year mission, 6 of the 41 samples had experienced full-thickness erosion of part of the sample area (such as one edge) or of the entire sample area. These samples are listed in table 8, MISSE 2 Samples Partially or Fully Eroded through All Layers, along with a summary of extent of erosion. Therefore, the erosion yield for each of these samples is actually greater than the value provided, as indicated in table 7. These six materials were flown again for erosion yield determination as part of the MISSE 6A Stressed Polymers Experiment, which experienced 1.45 years of space exposure.

Table 7—MISSE 2 PEACE Polymers Erosion Yield Data

MISSE Serial #	Material	Abbreviation	MISSE 2 Mass Loss (g)	Density (g/cm^3)	Area (cm^2)	MISSE 2 Erosion Yield (cm^3/atom)
2-E5-6	Acrylonitrile butadiene styrene	ABS	0.033861	1.05 (a)	3.4944	1.09E–24
2-E5-7	Cellulose acetate	CA	0.191482	1.2911	3.4831	5.05E–24
2-E5-8	Poly-(p-phenylene terephthalamide)	PPD-T	0.026790	1.4422	3.5099	6.28E–25
2-E5-9	Polyethylene	PE	0.102760	0.9180 (b)	3.5489	>3.74E–24*
2-E5-10	Polyvinylfluoride	PVF	0.132537	1.3792	3.5737	3.19E–24
2-E5-11	Crystalline polyvinylfluoride with white pigment	PVF –W	0.004714	1.6241	3.4176	1.01E–25
2-E5-12	Polyoxymethylene; acetal; polyformaldehyde	POM	0.378378	1.3984	3.5119	9.14E–24
2-E5-13	Polyacrylonitrile	PAN	0.047281	1.1435	3.4768	1.41E–24
2-E5-14	Allyl diglycol carbonate	ADC	0.267295	1.3173	3.5392	>6.80E–24*
2-E5-15	Polystyrene	PS	0.115947	1.0503	3.5043	3.74E–24
2-E5-16	Polymethyl methacrylate	PMMA	0.194588	1.1628	3.5456	>5.60E–24*
2-E5-17	Polyethylene oxide	PEO	0.066395	1.1470	3.5591	1.93E–24
2-E5-18	Poly(p-phenylene-2,6-benzobisoxazole)	PBO	0.056778	1.3976	3.5526	1.36E–24
2-E5-19	Epoxide or epoxy	EP	0.140720	1.1150	3.5576	4.21E–24
2-E5-20	Polypropylene	PP	0.072357	0.90657 (c)	3.5336	2.68E–24
2-E5-21	Polybutylene terephthalate	PBT	0.036429	1.3318	3.5619	9.11E–25
2-E5-22	Polysulfone	PSU	0.105948	1.2199	3.5010	2.94E–24
2-E5-23	Polyurethane	PU	0.057227	1.2345	3.5182	1.56E–24
2-E5-24	Polyphenylene isophthalate	PPPA	0.030549	0.7200 (d)	3.5626	1.41E–24
2-E5-25	Pyrolytic graphite	PG	0.02773	2.2200 (e)	3.5703	4.15E–25
2-E5-26	Polyetherimide	PEI	0.126853	1.2873	3.5352	>3.31E–24*
2-E5-27	Polyamide 6	PA 6	0.118376	1.1233	3.5646	3.51E–24
2-E5-28	Polyamide 66	PA 66	0.065562	1.2252	3.5249	1.80E–24
2-E5-29	Polyimide	PI (CP1)	0.080648	1.4193	3.5316	1.91E–24
2-E5-30	Polyimide (PMDA)	PI (Kapton® H)	0.124785	1.4273	3.4590	3.00E–24
2-E5-31	Polyimide (PMDA)	PI (Kapton® HN)	0.121315	1.4346	3.5676	2.81E–24
2-E5-32	Polyimide (BPDA)	PI (Upilex-S®)	0.038127	1.3866	3.5382	9.22E–25

MISSE Serial #	Material	Abbreviation	MISSE 2 Mass Loss (g)	Density (g/cm^3)	Area (cm^2)	MISSE 2 Erosion Yield (cm^3/atom)
2-E5-33	Polyimide (PMDA)	PI (Kapton® H)	0.129219	1.4273	3.5773	3.00E–24
2-E5-34	High-temperature polyimide resin	PI (PMR-15)	0.118887	1.3232	3.5256	>3.02E–24*
2-E5-35	Polybenzimidazole	PBI	0.082708	1.2758	3.4762	>2.21E–24*
2-E5-36	Polycarbonate	PC	0.142287	1.1231	3.5010	4.29E–24
2-E5-37	Polyetheretherketone	PEEK	0.107764	1.2259	3.4821	2.99E–24
2-E5-38	Polyethylene terephthalate	PET	0.125187	1.3925	3.5432	3.01E–24
2-E5-39	Chlorotrifluoroethylene	CTFE	0.052949	2.1327	3.5452	8.31E–25
2-E5-40	Ethylene-chlorotrifluoroethylene	ECTFE	0.088869	1.6761	3.5103	1.79E–24
2-E5-41	Ethylene-tetrafluoroethylene	ETFE	0.049108	1.7397	3.4854	9.61E–25
2-E5-42	Fluorinated ethylene propylene	FEP	0.012479	2.1443	3.4468	2.00E–25
2-E5-43	Polytetrafluoroethylene	PTFE	0.008938	2.1503	3.4841	1.42E–25
2-E5-44	Perfluoroalkoxy copolymer resin	PFA	0.010785	2.1383	3.4570	1.73E–25
2-E5-45	Amorphous fluoropolymer	AF	0.012352	2.1463	3.4544	1.98E–25
2-E5-46	Polyvinylidene fluoride	PVDF	0.066860	1.7623	3.4993	1.29E–24

Notes:

* E_y is greater than this value because the sample was eroded partially, or fully, through all layers.

(a) IDES, http://www.ides.com/generics/ABS/ABS_typical_properties.htm (ρ = 1.01–1.09 g/cm^3). Retrieved October 2007.

(b) Consolidated Thermoplastics manufacture's density.

(c) Average of data from Brady, G.S., Clauser, H.R., Vaccari, J.A. (1997). *Materials Handbook 14th ed.* New York: McGraw-Hill. p. 699 (ρ = 0.913 g/cm^3) and MSDS (ρ = 0.895–0.905 g/cm^3).

(d) DuPont Nomex® Crepe Paper Type 410 Technical Data Sheet.

(e) Brady, G.S., Clauser, H.R., Vaccari, J.A. (1997). *Materials Handbook 14th ed.* New York: McGraw-Hill. p. 427.

Table 8—MISSE 2 Samples Partially or Fully Eroded through All Layers

MISSE Serial #	Material	Abbreviation	Thickness (cm)	Number of Sample Layers	Erosion Summary
2-E5-9	Polyethylene	PE	0.005	6	Eroded with residual material left
2-E5-14	Allyl diglycol carbonate	ADC	0.079	1	Eroded at one edge, sample curled up
2-E5-16	Polymethyl methacrylate	PMMA	0.005	10	Eroded through the center, edge material left
2-E5-26	Polyetherimide	PEI	0.025	2	Textured back surface (atomic oxygen valleys eroded through)
2-E5-34	High-temperature polyimide resin	PI (PMR-15)	0.30	1	Eroded through at one edge
2-E5-35	Polybenzimidazole	PBI	0.005	4	All four layers completely eroded away

9.3.6 MISSE 2 PEACE Erosion Yield Uncertainty

In any experiment, it is critical to determine the accuracy of the data obtained. To address this, the error in each polymer's experimental erosion yield value was calculated using equations for fractional uncertainty derived from the equation used to find erosion yield (McCarthy et al., 2010). The standard deviation or error of each measurement that was used to calculate the erosion yield was incorporated into the resulting fractional uncertainty of the erosion yield for each of three different error situations, which correspond to the three post-flight weighing procedures. The resulting error calculations showed the erosion yield values to be very accurate, with an average error of ±3.30 percent (McCarthy et al., 2010). Table 9, MISSE 2 PEACE Polymers Erosion Yield Uncertainty Data, provides the fractional uncertainty in erosion yield for each of the MISSE 2 PEACE Polymers samples (McCarthy et al., 2010). Details of the MISSE 2

PEACE Polymers experiment atomic oxygen erosion yield error analysis are provided in Appendix B of this Handbook.

Table 9—MISSE 2 PEACE Polymers Erosion Yield Uncertainty Data

MISSE Serial #	Material	Abbreviation	Uncertainty in E_y (σ) (cm^3/atom)	Fractional Uncertainty in Erosion Yield	Erosion Yield ±σ (cm^3/atom)
2-E5-6	Acrylonitrile butadiene styrene	ABS	2.96E–26	0.027017	1.09 (±0.03) E–24
2-E5-7	Cellulose acetate	CA	1.34E–25	0.026573	5.05 (±0.13) E–24
2-E5-8	Poly-(p-phenylene terephthalamide)	PPD-T	1.64E–26	0.026193	6.28 (±0.16) E–25
2-E5-9	Polyethylene	PE	9.59E–26	0.025620	>3.74 E–24*
2-E5-10	Polyvinylfluoride	PVF	8.17E–26	0.025612	3.19 (±0.08) E–24
2-E5-11	Crystalline polyvinylfluoride with white pigment	PVF -W	4.17E–27	0.041361	1.01 (±0.04) E–25
2-E5-12	Polyoxymethylene; acetal; polyformaldehyde	POM	2.79E–25	0.030556	9.14 (±0.28) E–24
2-E5-13	Polyacrylonitrile	PAN	4.63E–26	0.032801	1.41 (±0.05) E–24
2-E5-14	Allyl diglycol carbonate	ADC	1.76E–25	0.025824	>6.80 E–24*
2-E5-15	Polystyrene	PS	1.00E–25	0.026884	3.74 (±0.10) E–24
2-E5-16	Polymethyl methacrylate	PMMA	1.45E–25	0.025932	>5.60 E–24*
2-E5-17	Polyethylene oxide	PEO	5.01E–26	0.025948	1.93 (±0.05) E–24
2-E5-18	Poly(p-phenylene-2,6-benzobisoxazole)	PBO	8.08E–26	0.059587	1.36 (±0.08) E–24
2-E5-19	Epoxide or epoxy	EP	1.14E–25	0.027020	4.21 (±0.11) E–24
2-E5-20	Polypropylene	PP	7.00E–26	0.026127	2.68 (±0.07) E–24
2-E5-21	Polybutylene terephthalate	PBT	2.35E–26	0.025798	9.11 (±0.24) E–25
2-E5-22	Polysulfone	PSU	9.31E–26	0.031645	2.94 (±0.09) E–24
2-E5-23	Polyurethane	PU	4.59E–26	0.029353	1.56 (± 0.05) E–24
2-E5-24	Polyphenylene isophthalate	PPPA	4.10E–26	0.028987	1.41 (±0.04) E–24
2-E5-25	Pyrolytic graphite	PG	4.46E–26	0.107496	4.15 (±0.45) E–25
2-E5-26	Polyetherimide	PEI	8.63E–26	0.026088	>3.31 E–24*
2-E5-27	Polyamide 6	PA 6	9.33E–26	0.026617	3.51 (±0.09) E–24
2-E5-28	Polyamide 66	PA 66	2.27E–25	0.125851	1.80 (±0.23) E–24
2-E5-29	Polyimide	PI (CP1)	5.38E–26	0.028199	1.91 (±0.05) E–24
2-E5-30	Polyimide (PMDA)	PI (Kapton® H)	7.41E–26	0.024700	3.00 (±0.07) E–24
2-E5-31	Polyimide (PMDA)	PI (Kapton® HN)	7.24E–26	0.025748	2.81 (±0.07) E–24
2-E5-32	Polyimide (BPDA)	PI (Upilex-S®)	2.77E–26	0.030056	9.22 (±0.28) E–25
2-E5-33	Polyimide (PMDA)	PI (Kapton® H)	7.41E–26	0.024700	3.00 (±0.07) E–24
2-E5-34	High-temperature polyimide resin	PI (PMR-15)	7.77E–26	0.025696	>3.02 E–24*
2-E5-35	Polybenzimidazole	PBI	5.81E–26	0.026275	>2.21 E–24*
2-E5-36	Polycarbonate	PC	1.14E–25	0.026545	4.29 (±0.11) E–24
2-E5-37	Polyetheretherketone	PEEK	1.36E–25	0.045436	2.99 (±0.14) E–24
2-E5-38	Polyethylene terephthalate	PET	7.87E–26	0.026157	3.01 (±0.08) E–24
2-E5-39	Chlorotrifluoroethylene	CTFE	2.15E–26	0.025927	8.31 (±0.22) E–25
2-E5-40	Ethylene-chlorotrifluoroethylene	ECTFE	4.63E–26	0.025821	1.79 (±0.05) E–24
2-E5-41	Ethylene-tetrafluoroethylene	ETFE	2.46E–26	0.025598	9.61 (±0.25) E–25
2-E5-42	Fluorinated ethylene propylene	FEP	5.39E–27	0.026890	2.00 (±0.05) E–25
2-E5-43	Polytetrafluoroethylene	PTFE	3.69E–27	0.026089	1.42 (±0.04) E–25
2-E5-44	Perfluoroalkoxy copolymer resin	PFA	4.72E–27	0.027248	1.73 (±0.05) E–25
2-E5-45	Amorphous fluoropolymer	AF	5.13E–27	0.025975	1.98 (±0.05) E–25
2-E5-46	Polyvinylidene fluoride	PVDF	3.41E–26	0.026549	1.29 (±0.03) E–24

* E_y is greater than this value because the sample was eroded partially, or fully, through all layers.

9.3.7 MISSE 2 PEACE Optical and Thermal Data

Changes in optical and thermal properties as a result of LEO exposure have been analyzed for all of the MISSE 2 PEACE Polymers materials for which these properties could be measured; because of the long duration of exposure, several of the samples were too degraded. Total reflectance (TR) and diffuse reflectance (DR) and total transmittance (TT) and diffuse transmittance (DT) were measured as a function of wavelength and compared with the corresponding characteristics of non-exposed control samples. Specular reflectance (SR) and specular transmittance (ST) were then computed. Thermal emittance (ε) data were also generated for 35 samples. The wavelength-dependent data also allow for computation of the change in solar absorptance (α_s) and in ε, both of which are critical for predicting thermal control characteristics of a spacecraft.

Many of the MISSE PEACE Polymers samples were comprised of several layers so as to survive a 3-year LEO exposure. Because the mission was 3.95 years in duration, many of the polymers were eroded through several layers, several of the polymers were eroded through all layers in at least a portion of the exposed area, and one sample was completely eroded. It was determined, therefore, that the best way to measure the optical and thermal properties of the flight samples was to determine which layers should be measured and then compare the same number of layers from the control flight samples. If a sample was partially eroded, the layer or layers that experienced partial erosion (rather than full erosion, as with the layers above the partially eroded layers) and the intact layer immediately underneath were analyzed, and the control sample included the same number of layers, as shown in figure 43, Schematic Diagram of MISSE 2 Flight Sample Layer Erosion and the Corresponding Layers used for Optical and Thermal Property Measurements. If the top layers could be damaged by pulling the layers apart, the samples were left as a whole, and an equal number of control sample layers were used for analysis.

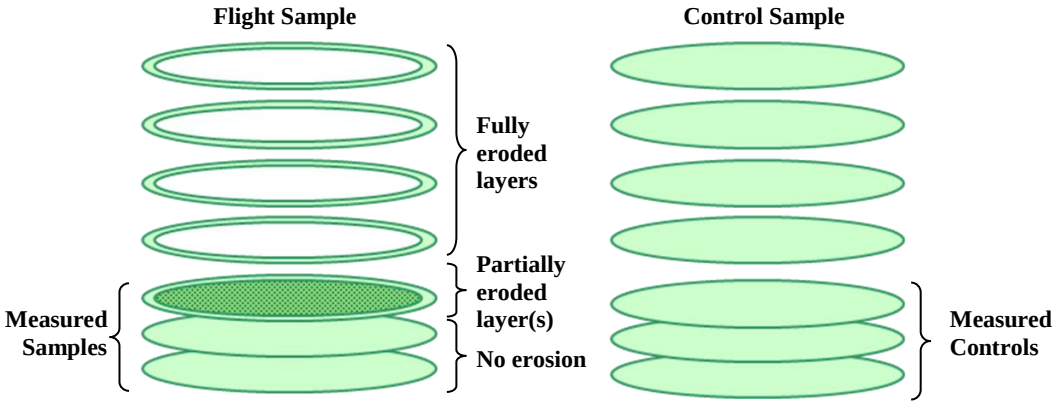

Figure 43—Schematic Diagram of MISSE 2 Flight Sample Layer Erosion and the Corresponding Layers used for Optical and Thermal Property Measurements

The materials too damaged for their optical and thermal properties to be measured were PE (2-E5-9), polymethyl methacrylate (PMMA, 2-E5-16), polyamide 66 (PA 66, 2-E5-28), polyimide (CP1, 2-E5-29), PBI (2-E5-35), and polyethylene terephthalate (PET, 2-E5-38). Three of these samples are shown in figure 44, Excessively Eroded MISSE 2 Polymers. Also, because samples were mounted upside down over an aperture opening on a SOC 400T infrared reflectometer, three additional samples (polystyrene (PS, 2-E5-15), poly(p-phenylene-2,6-benzobisoxazole) (PBO, 2-E5-18), and PPPA (2-E5-24)), could not have their thermal properties measured for fear of losing fragile pieces in the instrument.

(a) Partially Eroded PE (2-E5-9) (b) Partially Eroded PMMA (2-E-16) (c) Completely Eroded PBI (2-E5-35)

Figure 44—Excessively Eroded MISSE 2 Polymers

Post-flight and control optical measurements, including TR, DR, TT, and DT, as well as calculated values of the SR, ST, and α_s are provided in Appendix C of this Handbook, along with the number of layers measured for each sample and optical and thermal measurement procedures. For most samples, SR and DR properties changed significantly as a result of directed LEO atomic oxygen exposure. Generally, there was a decrease in SR with an increase in DR. These optical property changes are relevant to glare issues, Fresnel lens photovoltaic concentrator power loss issues, and issues with spatial variations in the thermal load on a spacecraft.

9.3.8 MISSE 2 PEACE Polymers Experiment Summary

The MISSE 2 PEACE Polymers flight data are important and unique for several reasons. They include the widest variety of well-characterized polymers collectively exposed to the LEO atomic oxygen space environment for a long duration. The erosion yield values of the MISSE 2 PEACE Polymers were based on mass loss, using dehydrated pre-flight and post-flight mass measurements. Erosion yield values for numerous prior flight experiments based on mass loss were not obtained using dehydrated mass values, which introduces large error for either low-fluence missions (such as Shuttle flight experiments) or low erosion yield samples exposed to high-fluence missions. The MISSE 2 PEACE Polymers experiment was an extremely clean experiment, receiving only ~1.3 nm of silica contamination (NASA/TM—2006-214482, MISSE PEACE Polymers Atomic Oxygen Erosion Results). Therefore, the erosion yield data were not measurably affected by on-orbit contamination. Other long-duration flight experiments, such as the LDEF, have experienced significant concentrations of silicone/silica contamination; such contamination adversely affects erosion yield data.

The polymers included in this experiment range from those commonly used for spacecraft applications, such as Teflon® FEP, Mylar®, and Kapton®, to more recently developed polymers, such as high-temperature polyimide PMR. Additional polymers typically not desired for spacecraft applications were also included to explore erosion yield dependence upon chemical composition for the purpose of the development of a predictive model. Extensive error analyses have been conducted of the MISSE 2 PEACE Polymers samples, documenting the uncertainty in the erosion yield values.

10. CORRELATION OF GROUND-LABORATORY DATA TO IN-SPACE DATA

Spaceflight experiments are unique, expensive, and time-consuming, which is why atomic oxygen ground laboratory testing, such as in an RF plasma asher, is often used for spacecraft material durability prediction. However, the correlation between in-space degradation and ground-testing degradation needs to be determined, because ground facilities and the space environment differ in many ways. These differences include variations in species, energies, thermal exposures, and radiation exposures, all of which may result in different reactions and erosion rates. For example, the direction of atomic oxygen arrival can differ between ground facilities and the space environment. Materials exposed to the LEO environment often receive either directed or sweeping ram atomic oxygen, whereas in a plasma asher, the atomic oxygen arrival is isotropic. Additionally, the atomic oxygen energy of a plasma asher is much lower (≈0.04 eV) than the atomic oxygen energy in LEO (≈4.5 eV). Furthermore, samples in a plasma asher receive an intense amount of UV radiation, whereas samples in LEO receive many different types of radiation, including broad spectrum UV radiation, electron and proton radiation, and solar flare x-rays. The plasma in ashers, operating on air as a feed gas, includes diatomic nitrogen, diatomic oxygen and oxygen ions, along with monatomic nitrogen and monatomic oxygen in both excited and ground-energy states. However, ground-state atomic oxygen is the predominant species of the LEO environment (NASA-TM-X-74335). All of these exposure differences may affect the rate of degradation of materials. As a consequence, the atomic oxygen erosion yield of a polymer measured in an RF plasma asher can be significantly

different than that measured in LEO. Studies have been conducted to try to understand the effects of various factors in ground test facilities on the erosion yields of certain polymers. For example, Miller et al. (2008) conducted a series of experiments to isolate UV radiation and charged species during atomic oxygen exposure of PE, Teflon® FEP, and Kapton® HN, relative to Kapton® H in a plasma asher (Miller et al., 2008). The same materials were also exposed to a hyperthermal atomic oxygen beam (Miller et al., 2008). The results were found to vary with the polymer and indicated that UV radiation, charged particle exposure, and beam energy affected the erosion yields of FEP and PE but not of Kapton® HN, relative to Kapton® H.

In an effort to improve the accuracy of ground-based durability testing, ground-laboratory to in-space atomic oxygen correlation experiments have been conducted. In these tests, the atomic oxygen erosion yields of the PEACE Polymers were determined relative to Kapton® H, using an RF plasma asher (operated on air). The asher erosion yields were compared to the MISSE 2 PEACE Polymers LEO erosion yields to determine the correlation between erosion rates in the two environments (Stambler et al., 2009).

10.1 Materials

The polymers used in this experiment were made from the same batch (and from the same sheet of film where possible) as the polymers used in the MISSE 2 PEACE Polymers flight experiment; therefore, they were a second set of control samples. Although stacked layers of polymer films were flown in the MISSE 2 flight experiment, only single-layer film samples were exposed in the plasma asher.

10.2 Mass Measurements

As in the MISSE 2 experiment, the erosion yield was determined based on mass loss. The samples were vacuum-dehydrated for at least 48 hours before their masses were measured both before and after atomic oxygen plasma exposure, as recommended by ASTM E 2089-00 (Stambler et al., 2009). The samples' dehydrated masses were obtained using a Mettler Balance with a sensitivity of ±0.000001 g.

10.3 Ground Laboratory RF Plasma Asher Exposure

Samples were exposed to an atomic oxygen environment in a Structure Probe, Inc., Plasma Prep II asher. This asher generates a plasma by exciting ambient air with 100 W of continuous RF power at 13.56 MHz (Gulino, 1986). The operating pressure was 6.67 to 13.33 Pa. The plasma is composed of oxygen and nitrogen ions and atoms (Rutledge et al., 1994); the nitrogen species have been found to have a negligible effect in the erosion processes (Rutledge et al., 1986). The Kapton® H effective atomic oxygen fluence was calculated based on mass loss data of dehydrated 127-μm (5-mil) Kapton® H polyimide samples, which were ashed with the test samples. Kapton® H is used as a standard material to measure effective fluence because the erosion yield in LEO is well characterized. The atomic oxygen erosion yield for Kapton® H was assumed to be 3.00×10^{-24} cm^3/atom based on these data (ASTM E 2089-00).

Six samples were ashed together using a specially designed holder with six sample openings (figure 45, Sample Holder with Six Polymer Samples). The holder protected the edges and the

backs of the samples from the plasma, which kept the samples from curling during exposure and provided a well-defined exposure area. The holder was always placed in the same position in the asher in an effort to provide the same flux for each sample position. The sample positions are indicated in figure 45. A Kapton® H fluence witness sample was placed in position 1 for every test so that the atomic oxygen effective fluence could be determined.

Figure 45—Sample Holder with Six Polymer Samples

The atomic oxygen flux (atoms/cm^2·sec) within a plasma asher can vary with position; therefore, calibration flux tests were conducted to determine the effective flux in each of the six sample positions relative to position 1. For these tests, Kapton® H witness samples were in all six positions. The effective flux was then determined for each position (based on dehydrated mass loss). During the plasma asher exposures, to calculate the fluence to which each sample was exposed during a test, the effective fluence was determined for the Kapton® H witness in position 1, and then that fluence was multiplied by the factor for each position to get the fluence for each sample position.

Samples were exposed to Kapton® H effective fluences ranging from 7.7×10^{19} to 2.2×10^{21} atoms/cm^2·sec. Details on the test procedures, including atomic oxygen flux tests, exposure area measurements and results, and individual sample text exposures, are provided by Stambler et al. (2009).

10.4 MISSE 2 Erosion Yields versus Asher Erosion Yields

Table 10, Ratio of Asher to MISSE 2 Erosion Yields, provides a list of the erosion yields of each of the PEACE Polymers in space, as determined during the MISSE 2 flight experiment, and in the asher based on the Kapton® H effective erosion yield. The table also provides the asher to in-space erosion yield ratios. All of the polymers had higher asher erosion yields than in-space erosion yields. This is related to the many differences that exist between in-space and asher exposure, as mentioned earlier.

Table 10—Ratio of Asher to MISSE 2 Erosion Yields

MISSE Serial #	Material	Abbreviation	MISSE 2 E_y (cm^3/atom)	Asher E_y (cm^3/atom)	Asher to In-Space E_y Ratio
2-E5-6	Acrylonitrile butadiene styrene	ABS	1.09E–24	6.8E–24	6.2
2-E5-7	Cellulose acetate	CA	5.05E–24	1.1E–23	2.1
2-E5-8	Poly-(p-phenylene terephthalamide)	PPD-T	6.28E–25	1.5E–23	24.0
2-E5-9	Polyethylene	PE	>3.74E–24*	6.8E–24	<1.8
2-E5-10	Polyvinylfluoride	PVF	3.19E–24	5.2E–24	1.6
2-E5-11	Crystalline polyvinylfluoride with white pigment	PVF-W	1.01E–25	3.7E–24	37.1
2-E5-12	Polyoxymethylene; acetal; polyformaldehyde	POM	9.14E–24	2.6E–23	2.8
2-E5-13	Polyacrylonitrile	PAN	1.41E–24	5.0E–24	3.6
2-E5-14	Allyl diglycol carbonate	ADC	>6.80E–24	1.5E–23	<2.2
2-E5-15	Polystyrene	PS	3.74E–24*	4.4E–24	1.2
2-E5-16	Polymethyl methacrylate	PMMA	>5.60E–24*	1.1E–23	<1.9
2-E5-17	Polyethylene oxide	PEO	1.93E–24	1.8E–23	9.3
2-E5-18	Poly(p-phenylene-2,6-benzobisoxazole)	PBO	1.36E–24	3.7E–24	2.8
2-E5-19	Epoxide or epoxy	EP	4.21E–24	1.0E–23	2.4
2-E5-20	Polypropylene	PP	2.68E–24	1.2E–23	4.6
2-E5-21	Polybutylene terephthalate	PBT	9.11E–25	5.7E–24	6.2
2-E5-22	Polysulfone	PSU	2.94E–24	4.0E–24	1.3
2-E5-23	Polyurethane	PU	1.56E–24	1.5E–23	9.3
2-E5-24	Polyphenylene isophthalate	PPPA	1.41E–24	8.3E–24	5.9
2-E5-25	Pyrolytic graphite	PG	4.15E–25	5.1E–25	1.2
2-E5-26	Polyetherimide	PEI	>3.31E–24*	3.9E–24	1.2
2-E5-27	Polyamide 6	PA 6	3.51E–24	9.8E–24	2.8
2-E5-28	Polyamide 66	PA 66	1.80E–24	8.4E–24	4.7
2-E5-29	Polyimide	PI (CP1)	1.91E–24	3.7E–24	1.9
2-E5-30	Polyimide (PMDA)	PI (Kapton® H)	3.00E–24	3.0E–24	1.0
2-E5-31	Polyimide (PMDA)	PI(Kapton® HN)	2.81E–24	3.0E–24	1.1
2-E5-32	Polyimide (BPDA)	PI (Upilex-S®)	9.22E–25	3.4E–24	3.6
2-E5-33	Polyimide (PMDA)	PI (Kapton® H)	3.00E–24	3.0E–24	1.0
2-E5-34	High-temperature polyimide resin	PI (PMR-15)	>3.02E–24*	3.1E–24	<1.0
2-E5-35	Polybenzimidazole	PBI	>2.21E–24*	2.6E–24	<1.2
2-E5-36	Polycarbonate	PC	4.29E–24	7.1E–24	1.7
2-E5-37	Polyetheretherketone	PEEK	2.99E–24	5.2E–24	1.7
2-E5-38	Polyethylene terephthalate	PET	3.01E–24	4.1E–24	1.4
2-E5-39	Chlorotrifluoroethylene	CTFE	8.31E–25	2.8E–24	3.3
2-E5-40	Ethylene-chlorotrifluoroethylene	ECTFE	1.79E–24	3.8E–24	2.1
2-E5-41	Ethylene-tetrafluoroethylene	ETFE	9.61E–25	2.1E–24	2.2
2-E5-42	Fluorinated ethylene propylene	FEP	2.00E–25	1.4E–24	7.2
2-E5-43	Polytetrafluoroethylene	PTFE	1.42E–25	1.1E–24	7.9
2-E5-44	Perfluoroalkoxy copolymer resin	PFA	1.73E–25	1.4E–24	8.0
2-E5-45	Amorphous fluoropolymer	AF	1.98E–25	1.2E–24	6.1
2-E5-46	Polyvinylidene fluoride	PVDF	1.29E–24	1.7E–24	1.4

* E_y is greater than this value because the sample was eroded partially, or fully, through all layers.

Most of the ratios of asher-to-in-space erosion yield were between 1 and 3. According to this table, it appears that PI (PMR-15) had an asher-to-in-space ratio of <1.0, but the asher erosion yield (3.1×10^{-24} cm^3/atom) was slightly higher than the in-space erosion yield ($>3.02\times10^{-24}$ cm^3/atom). Some of the fluoropolymers, such as amorphous fluoropolymer (AF), PTFE, perfluoroalkoxy copolymer resin (PFA), and FEP, had significantly higher asher-to-in-space ratios.

Kevlar® and white Tedlar® stand out as having ratios of 24.0 and 37.1, respectively, the highest of all the samples. The high asher to in-space ratio for the Kevlar® sample is likely because of its morphology: Kevlar® is a woven fabric, and atomic oxygen can attack a greater surface area per atomic oxygen fluence in the asher than in LEO. The high asher to in-space ratio for the white Tedlar® sample is likely a result of its white titanium dioxide pigment, which is atomic oxygen durable. When the polymeric content of white Tedlar® erodes during atomic oxygen exposure, it leaves a fine nonvolatile powder on the sample surface. This can shield the underlying polymer from atomic oxygen attack. For the MISSE flight experiment, the atomic oxygen arrival was primarily from the ram direction (normal to the polymer surface), and so the residual powder appears to have formed a protective layer (if not disturbed). In the asher, however, where atomic oxygen arrival is isotropic and at thermal energy (≈0.04 eV), the high atomic oxygen flux can get underneath the protective particles and cause significantly greater erosion than in space. In addition, the effective fluences for the asher tests were well below the in-space fluence of 8.43×10^{21} atoms/cm^2, which means that there was probably a higher density of atomic-oxygen-durable pigment particles during the later phases of the in-space exposure. Therefore, the erosion of white Tedlar® is substantially greater in the plasma asher than it is in space.

The atomic oxygen erosion yield for certain polymers whose composition includes atomic-oxygen-protective particles may be dependent on atomic oxygen fluence. It is possible that the atomic oxygen erosion yield of these polymers may decrease over time because more atomic-oxygen-durable particles are exposed on the sample surface with increasing fluence, providing increasingly greater protection of the underlying material. Therefore, it would be beneficial to obtain atomic oxygen erosion yields of polymers in LEO from several missions of different durations so that samples are exposed to several different LEO atomic oxygen fluences. In this way, erosion yield dependence on fluence could be assessed for different polymers.

11. ATOMIC OXYGEN EROSION YIELD PREDICTIVE TOOL

11.1 Erosion Yield Modeling Concepts

As a result of several decades of investigation into atomic oxygen erosion, it has become apparent that not all materials that form volatile oxidation products have the same erosion yield. For example, hydrocarbon polymers that have a high fractional oxygen content, such as polyoxymethylene (POM), tend to have higher erosion yields than those that have low fractional oxygen content. Polymers that have high fractional fluorine content, such as Teflon® FEP and PTFE, tend to have lower atomic oxygen erosion yields than those composed of hydrogen rather than fluorine, such as PE. Although it is not clear the degree to which the type and number of chemical bonds influence the probability of an atomic oxygen atom reacting, it is reasonable to

assume that there is some dependence of type and number of chemical bonds on atomic oxygen erosion yield.

A dense oxidizable material (one with many atoms per cubic centimeter), such as carbon, should have a lower atomic oxygen erosion yield than a less dense material, such as polystyrene foam, because it takes more oxygen atoms per square centimeter to oxidize a more dense material. Polymers that contain high fractions of non-oxidizable content, such as ash or metal oxide pigment particles, as does white Tedlar® polyvinylfluoride, should have lower erosion yields than polymers that have low ash contents, because the non-oxidizable particles can shield the polymer from reacting with the oxygen atoms. Similarly, as an ash-containing polymer erodes with time, an increasing proportion of the polymer surface becomes covered with ash, which causes the erosion yield to drop with fluence. Thus, atomic oxygen fluence should be considered a variable rather than a constant, because almost all polymers contain a small amount of non-oxidizable ash.

An atomic oxygen predictive tool was modeled using the MISSE 2 PEACE Polymers LEO atomic oxygen erosion yield data (de Groh et al., 2008; de Groh et al., 2006, NSMMS; de Groh et al., 2006, ESA), polymer chemical structure information concerning the number and types of chemical bonds, polymer density information, fractional ash content data, and atomic oxygen fluence data (de Groh et al., 2008; de Groh et al., 2006, NSMMS; de Groh et al., 2006, ESA; Banks et al., 2008). Although other environmental factors in addition to atomic oxygen, such as VUV radiation, ionizing radiation, and sample temperature, may have effects on the erosion yield of materials, they were not included in this model because they were not variable in the MISSE 2 experiment. The atomic oxygen predictive tool equation coefficients were sequentially and iteratively adjusted to achieve the highest correlation coefficient between actual LEO results and those of the predictive tool. Therefore, the physical properties and chemical structures discussed above were used to develop a formula that provided the closest match between predicted and actual erosion yields. The LEO atomic oxygen erosion yield data from MISSE 2 can be found in section 9.3.5 in this Handbook.

11.2 Modeling Variable Considerations

It is clear from the atomic oxygen erosion yield data from the MISSE 2 PEACE Polymers experiment, as well as from previous LEO flight experiments, that polymers with a significant abundance of pendant fluorine and/or chlorine atoms, such as FEP and CTFE, had low atomic oxygen erosion yields relative to Kapton® H polyimide in LEO. Conversely, polymers with significant oxygen content in their backbone, such as POM, had much higher atomic oxygen erosion yields. It is far less clear to what degree erosion yield depends on mixes of in-chain or pendant oxygen, nitrogen, and benzyl rings or whether the bonding is single, double, or triple. Therefore, many approaches were explored to correlate erosion yield with chemical structure, the number of atoms of each type in a polymer repeat unit, and the number of bonds of each type (single, double, or triple) in the polymer repeat unit.

Polymer density was also considered as a variable that potentially affects erosion yield because densely packed atoms should have lower erosion yields than loosely packed atoms. Data on

polymer density were obtained from either the suppliers or density gradient column testing (de Groh et al., 2008; de Groh et al., 2006, NSMMS; de Groh et al., 2006, ESA).

Most polymers contain some fraction of inorganic material that does not become volatile upon reaction with atomic oxygen. The residue that results after atomic oxygen exposure is called ash. The presence of fragile remaining ash may account for some of the debris shown on some samples in the MISSE 2 PEACE Polymers experiment post-flight photo in figure 34. As atomic oxygen erodes a polymer that contains inorganic material in LEO, the resulting nonvolatile ash begins to accumulate on the eroded surface of the polymer, shielding the underlying polymer from oxidation. As a result, a polymer's ash content can reduce its erosion yield. For example, as previously stated, the titanium dioxide pigment particles in white polyvinylfluoride (PVF-W, white Tedlar®) shield its surface, resulting in a very low erosion yield of 0.101×10^{-24} cm^3/atom, compared to the much higher erosion yield of 3.19×10^{-24} cm^3/atom of clear Tedlar®. The protection of oxidized polymers is more dependent upon the volume fraction of ash than on the mass fraction of ash because the surface coverage of ash plays a dominant role. However, it is much easier to use the mass fraction of ash because it is very difficult to measure ash volume unless you know the ash density.

The ash content data used to develop the predictive tool described in this section were determined experimentally for each of the 39 PEACE Polymers and pyrolytic graphite. Ash content was defined as the fraction of the initial dehydrated polymer mass that was nonvolatile and that remained after the polymer had been completely oxidized in an RF plasma asher. This was accomplished by placing pieces of each polymer in thin Al foil cups and ashing them for several hundred hours in an RF plasma asher operated on air until only ash remained (Banks et al., 2009). The Al cups had been previously exposed to atomic oxygen to remove organic coatings that typically reside on Al foil as a result of foil processing. Figure 46, SEM Images of the Ash Remaining after Several Hundred Hours of RF Plasma Asher Air Plasma Exposure, shows the ash remaining from white Tedlar® and PEO. Energy-dispersive spectroscopy revealed the presence of titanium in the white Tedlar® ash, as expected because of the titanium dioxide pigment particles, and the presence of a mix of metal elements in the ash from PEO.

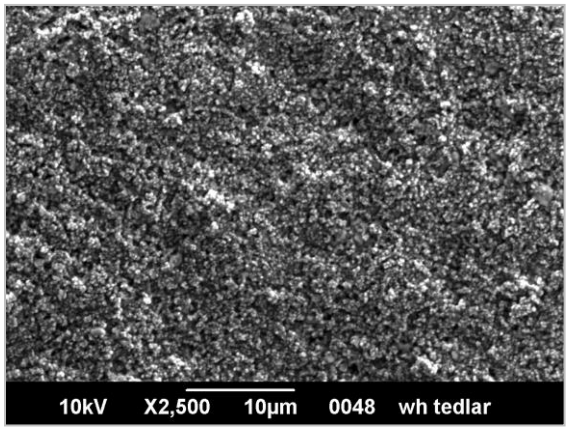

(a) White Tedlar® Titanium Dioxide Ash Particles

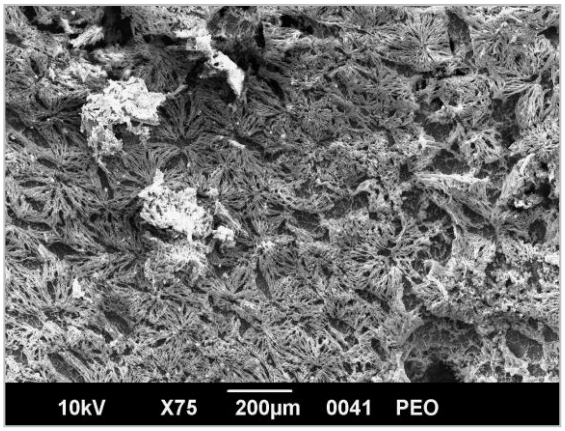

(b) Ash Remaining from PEO

Figure 46—SEM Images of the Ash Remaining after Several Hundred Hours of RF Plasma Asher Air Plasma Exposure

Unfortunately, a gradual buildup of inorganic contamination from the asher itself complicates the process of determining ash content because the added mass from contaminants is observed as additional ash. This buildup is especially prevalent if the ashing is continued long after the organic portion of the polymer is completely oxidized. Additionally, materials with low erosion yields tend to accumulate more contamination in the asher environment than those with high erosion yields. Correcting for this contamination is problematic because it depends on the surface area of the ash, which is difficult to measure.

The effect of ash content on erosion yield in an end Hall hyperthermal atomic oxygen facility (Banks et al., 2006) was determined by measuring the erosion yield of five epoxy resin samples that were purposely filled with various amounts of fumed silica. Epoxy resin with no added fumed silica was found to also contain some ash, as indicated in table 11, Ash Content of the Five Samples used to Measure Erosion Yield Dependence on Mass Fraction Ash, as a result of ashing samples of the cured epoxy. Additional ash, in the form of fumed silica, was weighed and mixed with both parts of the uncured epoxy to achieve the total mass fraction ash (fraction of ash in the polymer determined by the mass) indicated in table 11, which was used to plot figure 47, Erosion Yield Dependence on Mass Fraction Ash in Epoxy for a Kapton® H Effective Fluence of 1.24×10^{20} atoms/cm^2.

Table 11—Ash Content of the Five Samples used to Measure Erosion Yield Dependence on Mass Fraction Ash

Mass Fraction Ash in As-Received Epoxy	Mass Fraction of Fumed Silica Added (as Ash) to Epoxy	Total Mass Fraction Ash of Sample	Ratio of Atomic Oxygen Erosion Yield Relative to Neat (No Ash) Polymer
0.0453	0.0000	0.0453	0.912
0.0453	0.0837	0.1252	0.758
0.0453	0.1662	0.2039	0.758
0.0453	0.3336	0.3638	0.330
0.0453	0.4167	0.4431	0.214
0.0453	0.4998	0.5225	0.120

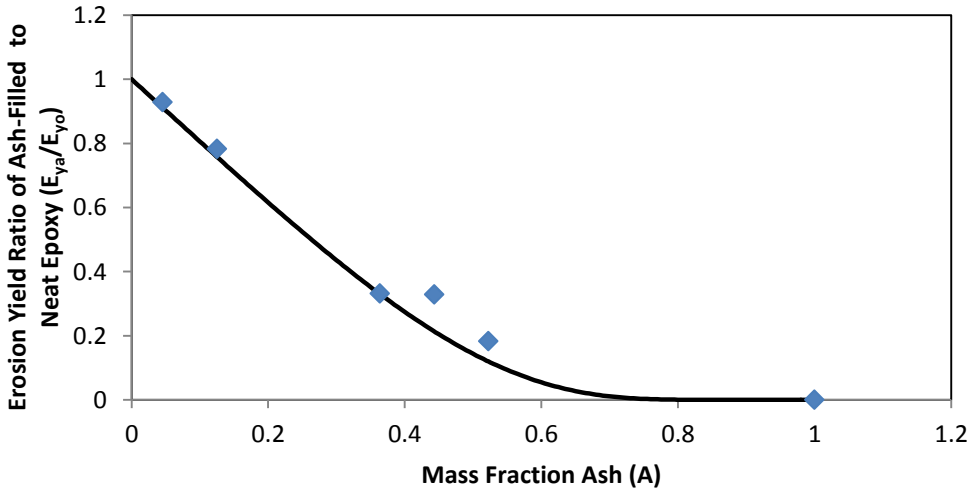

Figure 47—Erosion Yield Dependence on Mass Fraction Ash in Epoxy for a Kapton® H Effective Fluence of 1.24×10^{20} atoms/cm^2

The effect of the total mass fraction ash on erosion yield was measured using an end Hall hyperthermal atomic oxygen source operated on pure oxygen at ~70 eV. It was necessary to use hyperthermal rather than thermal energy atomic oxygen attack because thermal energy atomic oxygen is not greatly attenuated (compared to LEO hyperthermal atomic oxygen) in reaction probability as a result of arrival on ash surfaces. Because particle-filled epoxy resins tend to have a resin-rich surface, all the samples were abraded before atomic oxygen exposure to ensure that the exposed surfaces were representative of the bulk material.

Erosion yield dependence upon mass fraction ash for a Kapton® H effective fluence of 1.24×10^{20} atoms/cm^2 is shown in figure 47. The erosion yield of the neat (containing no ash) epoxy resin was estimated based on the slope of the curve shown in figure 47 and the intercept at zero mass fraction ash.

The line in figure 47 is described by the following equation, which models the observed dependence of erosion yield on mass fraction ash:

$$E_{ya} = E_{yo}\, e^{-K\cdot A/(1-A)} \qquad \text{(Eq. 6)}$$

where:

E_{ya} = erosion yield of epoxy with ash content (cm^3/atom)
E_{yo} = erosion yield of epoxy without any ash content in end Hall test (cm^3/atom)
K = erosion yield attenuation constant
A = mass fraction ash of the polymer.

The solid line represents the best fit curve for both the ash-filled epoxy of figure 47 and the ash-filled Tedlar® in figure 48, Erosion Yield of Tedlar® Relative to Neat Tedlar® as a Function of Ash.

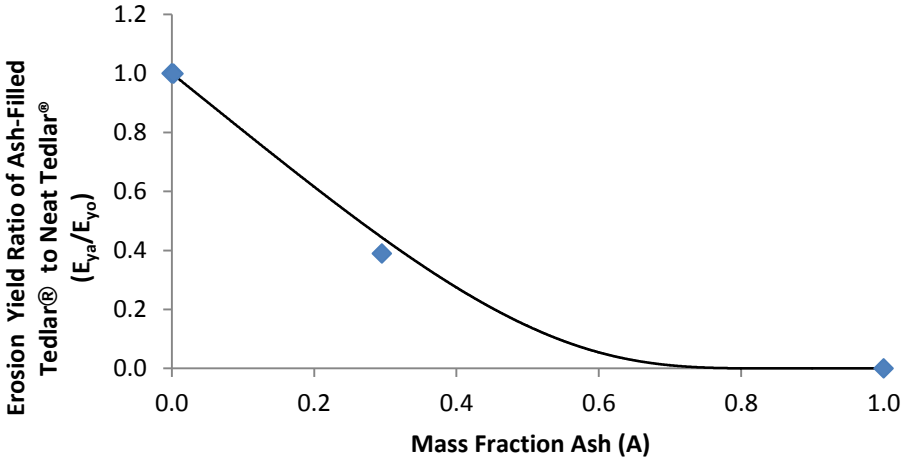

Figure 48—Erosion Yield of Tedlar® Relative to Neat Tedlar® as a Function of Ash

The erosion yield dependence function in Eq. 6 was designed to produce an erosion yield of 0 if the ash mass fractional content is 1, and an erosion yield of E_{yo} if the ash content is 0 (known as a "neat" polymer). This observed erosion yield dependence on ash content was also quantifiably consistent with end Hall atomic oxygen exposure of clear and white Tedlar®, suggesting that the equation is probably reasonably accurate for all ash-containing polymers.

The solid line in figure 48 represents the same Eq. 6 erosion yield attenuation constant as in the figure 47 plot, $K = 1.94$.

Table 12, MISSE 2 PEACE Polymers Density and Fractional Ash Content, lists the density and mass fraction ash (Banks et al., 2008) for each of the MISSE 2 PEACE polymers. Density gradient columns and highly accurate density calibration samples allowed the density of many materials to be measured to five decimal places (de Groh et al., 2008).

Table 12—MISSE 2 PEACE Polymers Density and Fractional Ash Content

Material	Abbreviation	Density[1] (ρ (g/cm^3))	Mass Fraction Ash[2] (A)
Acrylonitrile butadiene styrene	ABS	1.05	0.0458
Cellulose acetate	CA	1.2911	0.00283
Poly-(p-phenylene terephthalamide)	PPDT	1.4422	0.00372
Polyethylene	PE	0.918	0.0203
Polyvinylfluoride	PVF	1.3792	0.00285
Crystalline polyvinylfluoride with white pigment	PVF-W	1.6241	0.295
Polyoxymethylene; acetal; polyformaldehyde	POM	1.3984	0.00902
Polyacrylonitrile	PAN	1.1435	0.00184
Allyl diglycol carbonate	ADC	1.3173	0.00265
Polystyrene	PS	1.0503	0.00042
Polymethyl methacrylate	PMMA	1.1628	0.00028
Polyethylene oxide	PEO	1.1470	0.00112
Poly(p-phenylene-2,6-benzobisoxazole)	PBO	1.3976	0.0109
Epoxide or epoxy	EP	1.1150	0.0304
Polypropylene	PP	0.9065	0.00184
Polybutylene terephthalate	PBT	1.3318	0.0629
Polysulfone	PSU	1.2199	0.00348
Polyurethane	PU	1.2345	0.00664
Polyphenylene isophthalate	PPPA	0.7200	0.0476
Pyrolytic graphite	PG	2.2200	0.00154
Polyetherimide	PEI	1.2873	0.00105
Polyamide 6	PA 6	1.1233	0.00388
Polyamide 66	PA 66	1.2252	0.00459
Polyimide	PI (CP1)	1.4193	0.00171
Polyimide (PMDA)	PI (Kapton® H)	1.4273	0.00284
Polyimide (PMDA)	PI (Kapton® HN)	1.4345	0.00441
Polyimide (BPDA)	PI (Upilex-S® or US)	1.3866	0.00164
High-temperature polyimide resin	PI (PMR-15)	1.3232	0.000531
Polybenzimidazole	PBI	1.2758	0.000927
Polycarbonate	PC	1.1231	0.000992
Polyetheretherketone	PEEK	1.2259	0.00177
Polyethylene terephthalate	PET	1.3925	0.00826
Chlorotrifluoroethylene	CTFE	2.1327	0.00204
Ethylene-chlorotrifluoroethylene	ECTFE	1.6761	0.000655
Ethylene-tetrafluoroethylene	ETFE	1.7397	0.00123
Fluorinated ethylene propylene	FEP	2.1443	0.00534
Polytetrafluoroethylene	PTFE	2.1503	0.0427
Perfluoroalkoxy copolymer resin	PFA	2.1383	0.000298

Amorphous fluoropolymer	AF	2.1463	0.0362
Polyvinylidene fluoride	PVDF	1.7623	0.0358

Notes:
1. de Groh et al., 2008
2. Banks et al., 2008

It is expected that the erosion yield attenuation constant increases with fluence for ash-containing polymers as ash accumulates on the surface of these polymers with increasing atomic oxygen fluence. An approximation of this ash-shielding dependence on fluence was determined by modeling the erosion yield of white Tedlar® in hyperthermal atomic oxygen environments for the low-fluence end Hall test and the high-fluence MISSE 2 LEO exposure, as shown in figure 49, Erosion Yield Ash Attenuation Constant (*K*) as a Function of Fluence (*F*). In this figure, the erosion yield for the end Hall test was corrected to account for the differences between the Kapton® H effective fluence of the end Hall exposure and in-space exposure using the ratio between Kapton® H and white Tedlar® erosion yields for both environments.

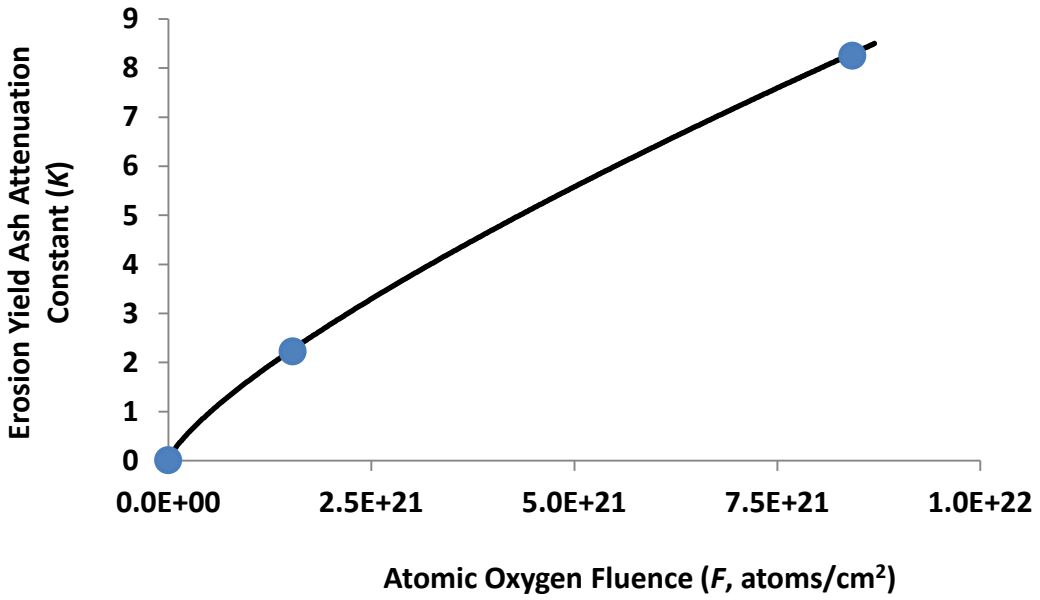

Figure 49—Erosion Yield Ash Attenuation Constant (*K*) as a Function of Fluence (*F*)

A best-fit curve drawn through the data is given by:

$$K = \left(1.80 \times 10^{-16}\right) F^{0.76} \qquad \text{(Eq. 7)}$$

Although a linear fit could also be applied to the three data points in figure 49, the best fit is with a power law dependence, which implies that, if the fluence doubles, the attenuation constant is slightly less than doubled. This is reasonable, because the buildup of ash on the surface of a polymer, which causes the attenuation, occurs faster at low fluences.

Additional erosion yield dependencies were considered for the predictive model, including physical density (ρ (g/cm^3)). Also considered was the packing density of atoms (V_Σ/V_r), which relates to how densely the atoms could theoretically be packed in comparison to the actual

volume of the repeat unit, where larger spaces would occur between atoms because of van der Waals bonding or void spaces. The minimum volume of the atoms that make up a polymer repeat unit (V_Σ) was based on the sum of the atoms making up the polymer repeat unit, assuming each atom's volume to be determined by its covalent radii.

The actual volume of each repeat unit (V_r) was determined based on the chemical structure of the repeat unit as well as the molecular weight and density of the material. Thus, for a ratio of V_Σ/V_r of much less than 1, the polymer's erosion yield would be higher than that of a similarly structured polymer with tightly packed atoms. Values of V_Σ/V_r are given in Banks et al., (2008).

11.3 Single Organic Material Atomic Oxygen Erosion Yield Predictive Model (2009 Version)

Over 100 different equations were tested using the information in the previous section to determine a formula that had a high correlation coefficient (R^2) with the actual LEO erosion yield data. An initial erosion yield model (Banks et al., 2008) produced a correlation coefficient of 0.914. That model used an assumption of linear dependency and made extensive use of information about the bonding of atoms in a repeat unit (Banks et al., 2008). However, the equation for that model produced negative erosion yields for some polymers that were not flown as part of the MISSE 2 PEACE Polymers experiment.

To correct this problem, an alternative approach (the September 2009 version) was pursued; this version used the dependency variables (such as atomic populations per repeat unit) as exponents with appropriate constants to optimize the correlation coefficient. This concept used weighted exponents rather than weighted additive terms. It allowed for dependency on the numbers and types of chemical bonds, polymer density information, and fractional ash content data and atomic oxygen fluence, while preventing negative erosion yield values. It enabled significant simplification of the predictive equation with very little loss in the correlation coefficient from the September 2009 version (Banks et al., 2009; Banks et al., 2011).

This simpler approach still resulted in a reasonably high correlation coefficient with LEO MISSE 2 PEACE Polymers data. The resulting equation used atomic populations in the repeat unit as well as physical density, packing density, ash content, and the number of single and double oxygen bonds in the repeat unit. The predictive LEO erosion yield equation is given by:

$$E_y = C_o \left(V_\Sigma / V_r\right)^{C_{\Sigma/r}} \left(\rho\right)^{C_\rho} e^X \qquad \text{(Eq. 8)}$$

where:

$$\begin{aligned} X = {} & \left(C_{C/t} \cdot N_C + C_{H/t} \cdot N_H + C_{sO/t} \cdot N_{sO} + C_{dO/t} \cdot N_{dO} + C_{N/t} \cdot N_N + C_{Cl/t} \cdot N_{Cl} + C_{F/t} \cdot N_F + C_{S/t} \cdot N_S\right) / N_t \\ & + \left(C_{O/C} \cdot N_O + C_{N/C} \cdot N_N + C_{F/C} \cdot N_F + C_{H/C} \cdot N_H + C_{Cl/C} \cdot N_{Cl} + C_{S/C} \cdot N_S\right) / N_C \\ & - K \cdot A / \left(1 - A\right) \end{aligned} \qquad \text{(Eq. 9)}$$

and

$$K = \left(1.80 \times 10^{-16}\right) F^{0.76} \qquad \text{(Eq. 10)}$$

K and the C coefficients C_o, $C_{\Sigma/r}$, C_ρ, $C_{C/t}$, $C_{H/t}$, $C_{sO/t}$, $C_{dO/t}$, $C_{N/t}$, $C_{Cl/t}$, $C_{F/t}$, $C_{S/t}$, $C_{O/C}$, $C_{N/C}$, $C_{F/C}$, $C_{H/C}$, $C_{Cl/C}$, *and* $C_{S/C}$are constants associated with the various terms relating to the number of atoms, bonds, or physical characteristics of the polymers The first set of terms ($(V_\Sigma / V_r)^{C_{\Sigma/r}}$) relates to how densely the atoms are packed compared to how densely they could theoretically be packed. Thus, the $(V_\Sigma / V_r)^{C_{\Sigma/r}}$ term is the ratio of volume computed based on the covalent radii atoms to the actual volume based on the molecular weight and density. The constant $C_{\Sigma/r}$ is the exponential weighting factor, which prevents negative values of the erosion yield but allows dependency upon the packing ratio. The $(\rho)^{C_\rho}$ term, similarly, addresses the variations in density of materials with an exponential constant (C_ρ). The term e^X addresses the numbers and types of chemical bonds relative to the total number of atoms or carbon atoms in the polymer repeat unit, where X is the exponential weighted sum of all the numbers and types of bonds in the polymer repeat unit. The $-K \cdot A/(1 - A)$ term in Eq. 9 for the exponent X models the ash content effect on the erosion yield. The constant (K) is fluence-dependent as described by Eq. 10.

All of the C coefficients for Eq. 9 were optimized to produce the highest correlation coefficient possible using the available data. The equation yielded a correlation coefficient between predicted erosion yield and LEO measured erosion yield of 0.895. This includes all of the MISSE 2 PEACE Polymers except PEO, which, for some reason, had an anomalously low erosion yield compared to what is predicted based on its chemical and physical properties. The values of the optimized C coefficients are listed in table 13, Definitions and Values of the Optimized Coefficients Associated with Each Variable. The covalent radii of atoms in the PEACE Polymers are given in table 14, Covalent Radii of MISSE PEACE Polymer Atoms.

Table 13—Definitions and Values of the Optimized Coefficients Associated with Each Variable

Symbol	Definition	Value (cm^3/atom)
$C_{C/t}$	Constant for the ratio of carbon atoms to total atoms	-0.10
$C_{Cl/C}$	Constant for the ratio of the chlorine atoms to carbon atoms in the repeat unit	1.48
$C_{Cl/t}$	Constant for chlorine atoms in polymer repeat unit	–8.60
$C_{dO/t}$	Constant for double bonded oxygen atoms in the polymer repeat unit	–3.59
$C_{F/C}$	Constant for the ratio of the fluorine atoms to carbon atoms in the repeat unit	–1.70
$C_{F/t}$	Constant for fluorine atoms in polymer repeat unit	–1.54
$C_{H/C}$	Constant for the ratio of the hydrogen atoms to carbon atoms in the repeat unit	0.053
$C_{H/t}$	Constant for the ratio of hydrogen atoms to total atoms	4.87
$C_{N/C}$	Constant for the ratio of the nitrogen atoms to carbon atoms in the repeat unit	–5.02
$C_{N/t}$	Constant for nitrogen atoms in the polymer repeat unit	4.42
C_o	Proportionality constant that resulted from best-fit linear equation relating the measured atomic erosion yield to predicted erosion yield	3.02×10^{30}
$C_{O/C}$	Constant for the ratio of oxygen atoms to carbon atoms in the repeat unit	0.395
$C_{S/C}$	Constant for the ratio of sulfur atoms to carbon atoms in the repeat unit	3.90
$C_{S/t}$	Constant for sulfur atoms in polymer repeat unit	–22.0
$C_{sO/t}$	Constant for single bonded oxygen atoms in the polymer repeat unit	–0.94
C_ρ	Constant for polymer density	4.87
$C_{\Sigma/r}$	Constant for ratio of sum of volume of atoms in repeat unit (based on their covalent radii) to volume of the repeat unit	–2.86
K	Erosion yield ash attenuation constant	8.30 for a fluence of 8.43×10^{21} atoms/cm^2

Table 14—Covalent Radii of MISSE PEACE Polymer Atoms

Atom	Covalent radius (cm)
Carbon	7.70E–09
Hydrogen	3.70E–09
Oxygen	7.30E–09
Nitrogen	7.50E–09
Fluorine	7.10E–09
Chlorine	9.90E–09
Sulfur	1.02E–08

A plot of the optimized predicted erosion yields versus the LEO measured MISSE 2 PEACE Polymers experiment erosion yields (with the exception of PEO) using Eqs. 8 to 10 and the constants in table 13 is shown in figure 50, Optimized Linear Fit between the LEO MISSE 2 PEACE Polymers Atomic Oxygen Erosion Yields and the Predicted Erosion Yields for an Atomic Oxygen Fluence of 8.43×10^{21} atoms/cm^2.

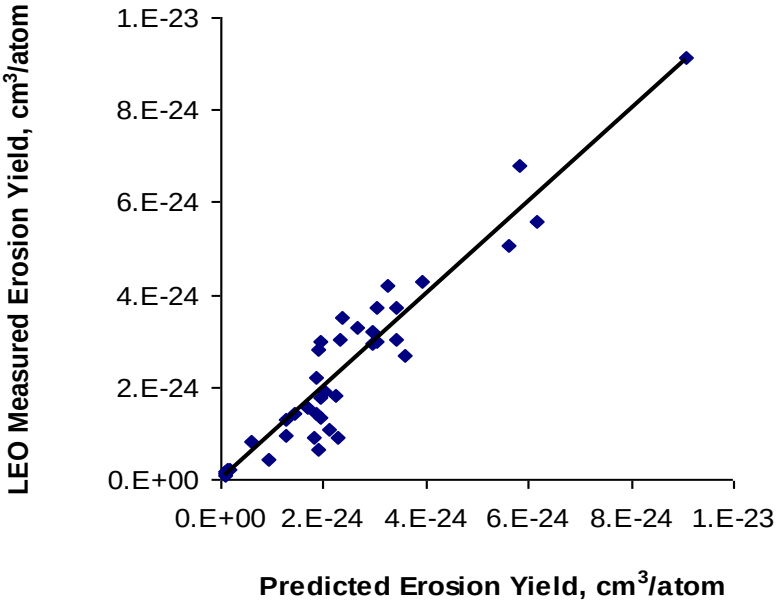

Figure 50—Optimized Linear Fit between the LEO MISSE 2 PEACE Polymers Atomic Oxygen Erosion Yields and the Predicted Erosion Yields for an Atomic Oxygen Fluence of 8.43×10^{21} atoms/cm^2

The resulting predicted erosion yields for the 38 polymers and pyrolytic graphite have a correlation coefficient of 0.895 with the actual measured erosion yields and an uncertainty (standard deviation) of $\pm1.27\times10^{-24}$ cm^3/atom. The predictive tool of Eqs. 8 to 10 allows for erosion yield prediction at any atomic oxygen fluence. This is especially relevant for polymers with high fractional ash contents. Table 15, Comparison of Predicted and Measured Atomic Oxygen Erosion Yields, lists the PEACE polymer materials, their predicted erosion yields for the MISSE 2 fluence, and their MISSE 2 measured erosion yields.

Table 15—Comparison of Predicted and Measured Atomic Oxygen Erosion Yields

Material	Abbreviation	Predicted Erosion Yield (cm^3/atom)	MISSE 2 Erosion Yield (cm^3/atom)
Acrylonitrile butadiene styrene	ABS	2.12E–24	1.09E–24
Cellulose acetate	CA	5.63E–24	5.05E–24
Poly-(p-phenylene terephthalamide)	PPD-T	1.92E–24	6.28E–25
Polyethylene	PE	3.04E–24	>3.74E–24*
Polyvinylfluoride	PVF	2.94E–24	3.19E–24
Crystalline polyvinylfluoride with white pigment	PVF-W	9.39E–26	1.01E–25
Polyoxymethylene; acetal; polyformaldehyde	POM	9.03E–24	9.14E–24
Polyacrylonitrile	PAN	1.42E–24	1.41E–24
Allyl diglycol carbonate	ADC	5.83E–24	>6.80E–24*
Polystyrene	PS	3.43E–24	3.74E–24
Polymethyl methacrylate	PMMA	6.17E–24	>5.60E–24*
Polyethylene oxide	PEO	7.02E–24	1.93E–24
Poly(p-phenylene-2,6-benzobisoxazole)	PBO	1.91E–24	1.36E–24

Epoxide or Epoxy	EP	3.24E–24	4.21E–24
Polypropylene	PP	3.58E–24	2.68E–24
Polybutylene terephthalate	PBT	2.31E–24	9.11E–25
Polysulfone	PSU	2.95E–24	2.94E–24
Polyurethane	PU	1.73E–24	1.56E–24
Polyphenylene isophthalate	PPPA	1.84E–24	1.41E–24
Pyrolytic graphite	PG	9.41E–25	4.15E–25
Polyetherimide	PEI	2.66E–24	>3.31E–24*
Polyamide 6	PA 6	2.40E–24	3.51E–24
Polyamide 66	PA 66	2.28E–24	1.80E–24
Polyimide	PI (CP1)	2.02E–24	1.91E–24
Polyimide (PMDA)	PI (Kapton® HN)	1.91E–24	2.81E–24
Polyimide (BPDA)	PI (Upilex-S®)	1.83E–24	9.22E–25
Polyimide (PMDA)	PI (Kapton® H)	1.93E–24	3.00E–24**
High-temperature polyimide resin	PI (PMR-15)	2.33E–24	>3.02E–24*
Polybenzimidazole	PBI	1.83E–24	>2.21E–24*
Polycarbonate	PC	3.94E–24	4.29E–24
Polyetheretherketone	PEEK	3.03E–24	2.99E–24
Polyethylene terephthalate	PET	3.44E–24	3.01E–24
Chlorotrifluoroethylene	CTFE	6.03E–25	8.31E–25
Ethylene-chlorotrifluoroethylene	ECTFE	1.94E–24	1.79E–24
Ethylene-tetrafluoroethylene	ETFE	1.26E–24	9.61E–25
Fluorinated ethylene propylene	FEP	9.82E–26	2.00E–25
Polytetrafluoroethylene	PTFE	7.09E–26	1.42E–25
Polyvinylidene fluoride	PVDF	1.26E–24	1.29E–24
Perfluoroalkoxy copolymer resin	PFA	7.54E–26	1.73E–25
Amorphous fluoropolymer	AF	1.38E–25	1.98E–25

* E_y is greater than this value because the sample was eroded partially, or fully, through all layers.
** Banks, et al., TSF; Visentine et al., 1985; Koontz et al., 1995; Silverman, 1995, P1.

These results represent a significant improvement over the earliest atomic oxygen erosion yield predictive tool (Integrity Testing Laboratory, Inc., 1998) as a result of incorporating additional physical and chemical properties of the materials, utilizing actual and accurate in-space erosion yield data, and taking into account polymer ash content.

11.4 Summary

Based on the results of the MISSE 2 PEACE Polymers experiment, which accurately measured the erosion yields of a wide variety of polymers as well as pyrolytic graphite, a predictive tool was developed to estimate the LEO atomic oxygen erosion yield of polymers. The flight experiment materials were selected specifically to represent a variety of polymers used in space and a wide variety of chemical structures. The September 2009 predictive tool utilizes the chemical structure, atomic populations of the polymer repeat unit, oxygen bonding information, and physical properties, such as density and ash content, that can be measured in ground laboratory tests. The prediction does not require the use of asher erosion yield information. The tool has a correlation coefficient of 0.895 and an uncertainty of $\pm 1.27 \times 10^{-24}$ cm^3/atom when compared with actual MISSE 2 PEACE Polymers space data (for 38 polymers and pyrolytic graphite). One polymer, PEO, was found to be significantly off the linear fit and so was not used in the predictive tool equation. The predictive tool does appear to predict reasonable atomic oxygen erosion yields, even for those polymers for which the previous predictive process yielded

negative erosion yield values. The tool also allows for the prediction of atomic oxygen erosion yields as a function of fluence, which is relevant for polymers with high fractional ash contents. The purpose of the predictive tool is to enable estimations of LEO atomic oxygen erosion yields for new polymers and composites without expensive and time-consuming in-space testing.

12. ATOMIC OXYGEN EROSION YIELD VALUES FOR SIMPLE AND COMPOSITE MATERIALS

12.1 Single Polymer Materials

Once the atomic oxygen erosion yield for a polymer has been determined by experiment or predictive modeling, the expected thickness loss (X) is given by:

$$X = E_y \cdot F \qquad \text{(Eq. 11)}$$

However, because the erosion yield may be fluence dependent if the polymer contains ash or a non-oxidizable pigment, the thickness of the material that is eroded is not simply proportional to the fluence. The erosion yield must be calculated for the specific fluence being considered. This can be accomplished if the following are known: the fluence, the ash content of the material, and the dependence on erosion yield of the ash content of the polymer as discussed in section 11 of this Handbook. Polymers with high fractional ash content typically show greater erosion yield dependence than polymers with low ash content.

Some polymers, such as Teflon® FEP, have been found to exhibit an erosion yield dependence on ESH (de Groh et al., 2010, NSMMS), as shown in figure 51, Erosion Yield Dependence upon ESH for Teflon® FEP. This may be related to greater volatility of oxidized polymer scission fragments on the surface, the number of which gradually increases with VUV exposure.

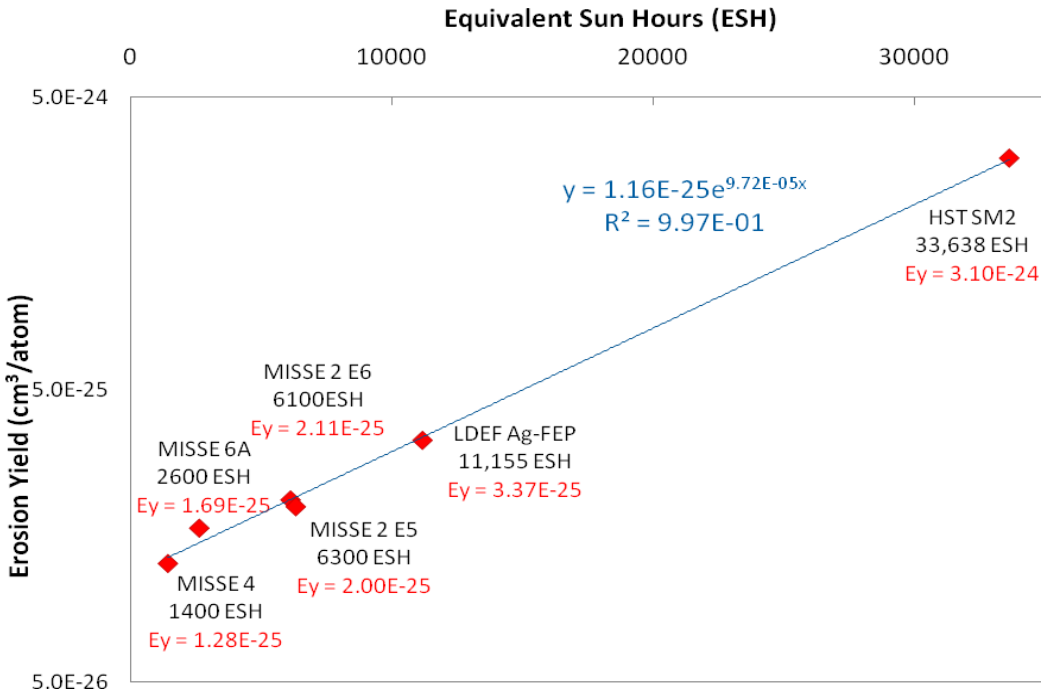

Notes: Ag-FEP = silvered FEP
HST SM2 = Hubble Space Telescope Servicing Mission 2

Figure 51—Erosion Yield Dependence upon ESH for Teflon® FEP

The amount of erosion is also dependent upon the orientation of the surface relative to the ram direction because of cosine losses in flux (table 16, Atomic Oxygen Fluences Based on Orientation of Surface). However, at angles near and beyond 90° from the ram direction, the flux of atomic oxygen is higher than that predicted by cosine losses. That is because the fluence beyond 90° is related to the velocity vector contributions caused by the Maxwell Boltzman distribution of the atomic oxygen velocities, spacecraft orbital inclination, and the co-rotation of the thermosphere. If a spacecraft is spinning with its axis of rotation perpendicular to the orbital plane, then the average flux to any surface that is perpendicular to that plane is simply $1/\pi$ of that of the ram direction. If the spacecraft is rotating in random directions, then the average flux is 1/4 that of the ram flux.

Table 16—Atomic Oxygen Fluences Based on Orientation of Surface

Orientation of Surface	Atomic Oxygen Fluence Relative to the Ram Fluence
Ram facing	1
Solar facing	0.253
Anti-solar facing	0.317
Sweeping	$1/\pi = 0.318$
90° from the ram direction	~0.04
Random orientation	0.25

If the polymer is a foam, then the extent of erosion is greater than what would be predicted for a fully dense polymer, where the actual erosion yield (E_A) is given by

$$E_A = \frac{E_y \rho}{\rho_f} \quad \text{(Eq. 12)}$$

where:

ρ = the density of the fully dense polymer
ρ_f = the density of the foam polymer.

12.2 Polysiloxane Copolymers and Fiberglass Composites

The atomic oxygen erosion yield of a hydro- or halocarbon polymer mixed with a polysiloxane polymer and/or a fiberglass composite is simply treated as a pure hydro- or halocarbon polymer with an ash content that is largely a result of the polysiloxane and/or fiberglass. Therefore, the polysiloxane and/or fiberglass-containing composite is evaluated for ash content just as any other polymer would be. However, the ash content for this material is substantially larger than for a pure (neat) hydro- or halocarbon polymer. As a consequence, the erosion yield is lower than for a neat polymer, matrix, carbon-fiber composite. In addition, the erosion yield of this material decreases with fluence as the surface becomes more and more protected by the oxides that remain on the surface after erosion of the hydrocarbon components of the composite. Ash content, in terms of fractional mass ash, can be most effectively determined by taking weight loss measurements of filings of composite samples and ashing them in an RF plasma asher. This provides a representative sampling of the fiber and matrix components of the composite. The resulting fractional mass ash is then substituted into the predictive erosion yield equation.

12.3 Mixed Organic Materials and Carbon Fiber Polymer Matrix Composites

Carbon-fiber-filled organic matrix composites do not have a constant erosion yield throughout the entire material volume because the carbon-fiber-fill fraction may vary throughout the composite. For example, the surface of a carbon-fiber-filled organic matrix composite may have a greater volume fraction of matrix material than deep within the bulk. Foam (open- or closed-pore) materials also have a higher erosion yield than their denser versions. The erosion yield of the polymer component of the foam material is simply the erosion yield of a fully dense polymer, but the erosion yield of the pores component is infinity, because it does not take any oxygen atoms to erode through a pore. Therefore, using the rule of mixtures based on the erosion yields of each material erroneously predicts an infinite erosion yield of the mixed material.

However, the rule of mixtures based on the erosion resistance and volume fraction of each material predicts a correct erosion yield for the mixture. The erosion resistance is simply the inverse of the erosion yield, a concept similar to the addition of electrical resistors in parallel to obtain the overall resistance. Therefore, the erosion resistance of the mixed materials (E_R) is as follows:

$$E_R = \frac{1}{E_y} = F_f \cdot E_{Rf} + F_p \cdot E_{Rp} \quad \text{(Eq. 13)}$$

where:

E_y = atomic oxygen erosion yield of the mixed material (cm^3/atom)
F_f = fractional volume of fibers in the composite
F_p = fractional volume of polymer in the composite
E_{Rf} = atomic oxygen erosion resistance of fibers (atoms/cm^3)
E_{Rp} = atomic oxygen erosion resistance of polymer matrix (atoms/cm^3).

Therefore, the atomic oxygen erosion yield of the fiber-filled composite, written in terms of erosion yields, is as follows:

$$E_y = \frac{1}{\frac{F_f}{E_{yf}} + \frac{F_P}{E_{yp}}} \quad \text{(Eq. 14)}$$

where:

E_{yf} = erosion yield of the fibers in the composite
E_{yp} = erosion yield of the polymer in the composite.

The ash content of a carbon-fiber-based hydrocarbon matrix composite can be evaluated by ashing samples (typically filings) of the material. This allows the matrix polymer and fiber components of the composite to contribute in proper proportions to the measured ash content. If the polymer matrix material is a co-polymer that contains polysiloxanes, then the erosion yield for that polymer, which takes into account its ash content, should be used in the above formula.

12.4 Materials that are Partially Transmissive to Atomic Oxygen

Some materials, such as fiberglass and beta cloth fabrics, have apertures that allow atomic oxygen to propagate through their thickness, thus allowing for potential interaction with underlying materials. Data comparing the fractional flux being transmitted, i.e., fractional open area, for individual materials are currently not available, but the fractional flux would be dependent on the details of the fabric geometry, thickness, and atomic oxygen arrival impact angle. In addition, atomic oxygen that did pass through the fabric would be trapped and produce an erosion yield beyond what would be based on the fractional open area of the fabric.

13. SUMMARY AND CONCLUSIONS

Low Earth orbital spacecraft frequently use thin-film polymers for blankets to support solar cells, for thermal-control surfaces such as multilayer insulation blanket layers, and for lightweight structural components. The atomic oxygen durability of such components is critical to mission reliability and performance, and knowledge of the durability of typical spacecraft materials and

anticipated materials is crucial to spacecraft design considerations. To address this need, LEO spaceflight experiment data were obtained, along with space environment data, ground-laboratory analyses, and predictive modeling to provide atomic oxygen erosion yield predictions for current and future spacecraft polymers.

A total of 41 different polymer samples, collectively called the PEACE Polymers, were exposed to the LEO space environment on the exterior of the ISS for 3.95 years as part of MISSE 2. The objective of this experiment was to accurately determine the atomic oxygen erosion yields of a wide variety of polymeric materials after long-term exposure to the space environment. The MISSE 2 PEACE Polymers experiment (flown on MISSE 2, Tray 1, sample Tray E5) was exposed to ram atomic oxygen, along with solar and charged-particle radiation. Mass loss was determined to be the best technique for characterizing the atomic oxygen erosion yield values for this experiment because, for some samples, erosion occurred through several layers at once, resulting in a cone–and-valley formation; for others, some sample layers were left as fragile gossamer films.

Atomic oxygen erosion yield values were determined for the MISSE 2 PEACE Polymers experiment based on mass loss measurements obtained from pre-flight and post-flight vacuum-dehydrated samples. Exposure areas were determined based on post-flight measurements of each individual flight sample's tray exposure opening. Density values for 36 of the 41 polymers were obtained using calibrated density gradient columns; the densities of the other 5 samples were obtained from referenced literature or manufacturers' MSDSs. The atomic oxygen fluence for the experiment was calculated based on two Kapton® H witness samples. (No significant difference in atomic oxygen fluence was found between the technique of back-extrapolation of the mass data to time zero to get a theoretically dehydrated mass and the technique of using the average mass values.) The average atomic oxygen fluence for the MISSE 2 PEACE Polymers experiment was determined to be 8.43×10^{21} atoms/cm^2. As some samples may have experienced a synergistic effect of solar exposure with atomic oxygen erosion, it is important to note that the solar exposure for Tray E5 was computed to be approximately 6,300 ESH. There was partial or complete full-thickness erosion of 6 of the 41 flight samples; therefore, because the mass loss would likely have been greater had more material been flown, the erosion yield values for these samples are greater than the values reported. Planning for a 3-year exposure (as opposed to the anticipated 1 year) was found to be crucial to the success of this experiment because of the unexpectedly long mission duration (3.95 years).

It is also important to know how accurate the atomic oxygen erosion yield data are. To address this, the error in each polymer's experimental erosion yield value was calculated using equations for fractional uncertainty derived from the equations used to compute erosion yield. Because three different post-flight sample-weighing procedures were used, three different equations were derived for determining the fractional uncertainty of the erosion yield values. The uncertainty and fractional uncertainty in erosion yield for each of the MISSE 2 PEACE Polymers samples have been determined; the average fractional standard deviation uncertainties in erosion yield were very small: ±3.30 percent.

The MISSE 2 PEACE Polymers experiment is unique because it included the widest variety of well-characterized polymers flown in LEO for a long duration under identical conditions. In addition, this experiment was exposed to an environment with unusually little contamination.

Therefore, the atomic oxygen erosion yield data from this LEO flight experiment provide extremely valuable information for spacecraft design and predictive model development purposes.

In addition to documenting the LEO atomic oxygen erosion yield values of the MISSE 2 PEACE Polymers, this Handbook reviews background information on the LEO atomic oxygen environment, atomic oxygen interaction with materials, ground-laboratory-to-in-space correlation data for the PEACE Polymers in an RF plasma asher, an atomic oxygen erosion yield predictive tool developed at NASA GRC based on the PEACE Polymers flight data, and tools for using atomic oxygen erosion yield data for spacecraft durability predictions. In addition, appendices in this Handbook review the MISSE 2 PEACE Polymers atomic oxygen erosion yield error analyses (Appendix B), review optical and thermal data for the MISSE 2 PEACE Polymers (Appendix C), provide individual summary pages for each of the MISSE 2 PEACE Polymers samples (Appendix D), and provide an overview of lessons learned from experiments investigating atomic oxygen interaction with spacecraft materials in LEO (Appendix E).

14. REFERENCES

14.1 References

14.1.1 Government Documents

NASA

NASA/TM—2006-214482	MISSE PEACE Polymers Atomic Oxygen Erosion Results
NASA-TM-X-74335	U.S. Standard Atmosphere 1976

14.1.2 Non-Government Documents

ASTM International

ASTM E 595	Standard Test Method for Total Mass Loss and Collected Volatile Condensable Materials from Outgassing in a Vacuum Environment
ASTM E 2089-00	Standard Practices for Ground Laboratory Atomic Oxygen Interaction Evaluation of Materials for Space Applications

Additional References

Banks, B.; Miller, S; de Groh, K.; Chan, A.; Sahota, M. (November 26-30, 2001). *The Development of Surface Roughness and Implications for Cellular Attachment in Biomedical Applications*. Paper presented at the Materials Research Society 2001 Fall Meeting. Boston, MA. Also published as NASA/TM—2001-211288.

Banks, B.A.; Auer, B.M.; Rutledge, S.K.; Gebauer, L.; Sechkar, E.A. (April 27-May 1, 1992). "Monte Carlo Modeling of Atomic Oxygen Interaction with Protected Polymers for Projection of Materials Durability in Low Earth Orbit." *Materials Research Society Symposium Proceedings Volume 278, Proceedings of the Materials Research Society 1992 Spring Meeting*. San Francisco, CA.

Banks, B.A.; Backus, J.A.; de Groh, K.K. (December 2008). *Atomic Oxygen Erosion Yield Predictive Tool for Spacecraft Polymers in Low Earth Orbit*. NASA/TM—2008-215490. Cleveland, OH: NASA GRC.

Banks, B.A.; Backus, J.A.; Manno, M.V.; Waters, D.L.; Cameron, K.C.; de Groh, K.K. (September 15-18, 2009). "Atomic Oxygen Erosion Yield Prediction for Spacecraft Polymers in Low Earth Orbit." *Proceedings of the International Symposium on Materials in a Space Environment (ISMSE-11), September 15-18, 2009*. Aix-en-Provence, France. Also published as NASA/TM—2009-215812.

Banks, B.A.; Backus, J.A.; Manno, M.V.; Waters, D.L; Cameron, K.C.; de Groh, K.K. (January-February 2011). "Prediction of Atomic Oxygen Erosion Yield for Spacecraft Polymers." *Journal of Spacecraft and Rockets*. Vol. 48, No. 1, pp. 14-22.

Banks, B.A.; de Groh, K.K.; Miller, S.K. (November 2004). "Low Earth Orbital Atomic Oxygen Interactions with Spacecraft Materials." *MRS Proceedings*, 851, NN8.1. Also published as NASA/TM—2004-213400.

Banks, B.A.; Miller, S.K.; de Groh, K.K. (August 16-19, 2004). *Low Earth Orbital Atomic Oxygen Interactions with Materials*. Paper presented at the 2nd International Energy Conversion Engineering Conference. Providence, RI. Also published as AIAA-2004-5638 and NASA/TM—2004-213223.

Banks, B.A.; Miller, S.K.R.; de Groh, K.K.; Demko, R. (September 2003). "Scattered Atomic Oxygen Effects on Spacecraft Materials." *Proceedings of the 9th International Symposium on Materials in a Space Environment, Noordwijk, The Netherlands, June 16-20, 2003*. 145-152. Published as ESA SP-540.

Banks, B.A.; Mirtich, M.J.; Rutledge, S.K.; Swec, D.M. (April 9-13, 1984). *Sputtered Coatings for Protection of Spacecraft Polymers*. Paper presented at the11th International Conference on Metallurgical Coatings (AVS), San Diego, CA. Also published as NASA TM-83706.

Banks, B.A.; Mirtich, M.J.; Rutledge, S.K.; Swec, D.M. (1985). "Sputtered Coatings for Protection of Spacecraft Polymers." *Thin Solid Films*. Vol. 127, pp. 107-114.

Banks B.A.; Mirtich, M.J.; Rutledge, S.K.; Swec, D.M.; Nahra, H.K. (January 14-17, 1985). *Ion Beam Sputter-Deposited Thin Film Coatings for Protection of Spacecraft Polymers in Low Earth Orbit*. Paper presented at the 23rd Aerospace

Sciences Meeting, American Institute of Aeronautics and Astronautics**.** Reno, NV. Also published as NASA-TM-87051.

Banks, B.A.; Rutledge, S.K.; Auer, B.M.; DiFilippo, F.J. (1990). "Atomic Oxygen Undercutting of Defects on SiO_2 Protected Polyimide Solar Array Blankets." In V. Srinivasan and B. Banks, Eds., *Materials Degradation in Low Earth Orbit (LEO).* 15-33. Warrenburg, PA: The Minerals, Metals & Materials Society (TMS)

Banks, B.A.; Rutledge, S.K.; de Groh, K.K. (May 7-9, 1991). *Low Earth Orbital Atomic Oxygen, Micrometeoroid, and Debris Interactions with Photovoltaic Arrays*. Paper presented at the 11th Space Photovoltaic Research and Technical Conference (SPRAT XI). NASA Lewis Research Center (LeRC), Cleveland, OH.

Banks, B.; Rutledge, S.; Sechkar, E.; Stueber, T.; Snyder, A.; Haytas, C.; Brinker, D. (June 4-9, 2000). "Issues and Effects of Atomic Oxygen Interactions with Silicone Contamination on Spacecraft in Low Earth Orbit." In *Materials in a Space Environment, Proceedings of the 8th International Symposium, and Protection of Materials and Structures from the LEO Space Environment, Proceedings of the 5th International Conference. ICPMSE-5.* Arcachon, France. Also published as NASA/TM—2000-210056.

Banks, B.A.; Snyder, A.; Miller, S.K.; Demko, R. (May 1-3, 2002). *Issues and Consequences of Atomic Oxygen Undercutting of Protected Polymers in Low Earth Orbit*. Paper presented at the 6th International Conference on Protection of Materials and Structures from Space Environment. Toronto, Canada. Also published as NASA/TM—2002-211577.

Banks, B.A.; Snyder, A.; Miller, S.K.; de Groh, K.K.; Demko, R. (May-June 2004). "Atomic-Oxygen Undercutting of Protected Polymers in Low Earth Orbit." *Journal of Spacecraft and Rockets*. Vol. 41, No. 3, pp. 335-339.

Banks, B.A.; Stueber, T.J. (1997). "Monte Carlo Computational Techniques for Prediction of Atomic Oxygen Erosion of Materials." In R.C. Tennyson and A.E. Kiv, Eds., *Proceedings of the NATO Advanced Research Workshop on Computer Modeling of Electronic and Atomic Processes in Solids, Wroclaw, Poland, May 20-23, 1996.* The Netherlands: Kluwer Academic Publishing.

Banks, B.; Stueber, T.; Norris, M. (April 23-24, 1998). *Monte Carlo Computational Modeling of the Energy Dependence of Atomic Oxygen Undercutting of Protected Polymers*. Paper presented at the 4th International Space Conference ICPMSE-4. Toronto, Canada. Also published as NASA/TM—1998-207423.

Banks, B.A.; Stueber, T.J.; Snyder, S.A.; Rutledge, S.K.; Norris, M.J. (September 23-25, 1997). *Atomic Oxygen Erosion Phenomena*. Paper presented at the American Institute of Aeronautics and Astronautics, Defense and Space Programs Conference. Huntsville, AL.

Banks, B.A.; Waters, D.L.; Thorson, S.D.; de Groh, K.K.; Snyder, A.; Miller, S.K. (June 19-23, 2006). "Comparison of Atomic Oxygen Erosion Yields of Materials at Various Energies and Impact Angles." In B. Battrick, Ed., *Proceedings of the 10th ISMSE, 8th ICPMSE: 19-23 June, 2006.* Collioure, France.. Also published as NASA/TM—2006-214363.

Berger, L.; Roberts, L.; de Groh, K.; Banks, B. (August 2007). *Use of Atomic Oxygen for Increased Water Contact Angles of Various Polymers for Biomedical Applications*. NASA/TM—2007-214925. NASA GRC: Cleveland, OH.

Bourassa, R.; Gillis, J. (1991). *Atomic Oxygen Flux and Fluence Calculation for Long Duration Exposure Facility (LDEF).* NASA-CR-187418. NASA LaRC: Hampton, VA.

de Groh, K.K. (2010). "Materials Spaceflight Experiments." In R. Blockley and W. Shyy, Eds., *Encyclopedia of Aerospace Engineering*. 2535-2552. Chichester, UK: John Wiley & Sons Ltd.

de Groh, K.K.; Banks, B.A. (July-August 1994). "Atomic Oxygen Undercutting of Long Duration Exposure Facility Aluminized-Kapton Multilayer Insulation." *Journal of Spacecraft and Rockets*. Vol. 31, No. 4, pp. 656-664.

de Groh, K.K.; Banks, B.A.; Clark, G.W.; Hammerstrom, A.M.; Youngstrom, E.E.; Kaminski, C.; Fine, E.S.; Marx, L.M. (December 2001). *A Sensitive Technique Using Atomic Force Microscopy to Measure the Low Earth Orbit Atomic Oxygen Erosion of Polymers*. NASA/TM—2001-211346. NASA GRC: Cleveland, OH.

de Groh, K.K.; Banks, B.A.; Dever, J.A.; Jaworske, D.J.; Miller, S.K.; Sechkar, E.A.; Panko, S.R. (March 2009). "NASA Glenn Research Center's Materials International Space Station Experiments (MISSE 1-7)." *Proceedings of the International Symposium on "SM/MPAC&SEED Experiment."* JAXA-SP-08-015E. pp. 91–119. Tsukuba, Japan. Also published as NASA/TM—2008-215482.

de Groh, K.K.; Banks, B.A.; Guo, Aobo; Ashmead, C.C.; Mitchell, G.G.; Yi, Grace T. (June 28-July 2, 2010). *MISSE 6 PEACE Polymers Atomic Oxygen Erosion Data*. Paper presented at the 2010 National Space & Missile Materials Symposium. Scottsdale, AZ.

de Groh, K.K.; Banks, B.A.; Hammerstrom, A.M.; Youngstrom, E.E.; Kaminski, C.; Marx, L.M.; Fine, E.S.; Gummow J.D.; Wright, D. (October 15-18, 2001). "MISSE PEACE Polymers: An International Space Station Environmental Exposure Experiment." *Proceedings of the AIAA Conference on International Space Station Utilization.* Paper AIAA #2001-4923. Also published as NASA/TM—2001-211311.

de Groh, K.K.; Banks, B.A.; Ma, D. (March-April 2006). "Ground-to-Space Effective Atomic Oxygen Fluence Correlation for DC 93-500 Silicone." *Journal of Spacecraft and Rockets.* Vol. 43, No. 2, pp. 414-420.

de Groh, K.K.; Banks, B.A.; McCarthy, C.E.; Berger, L.A.; Roberts, L.M. (June 19-23, 2006). "Analysis of the MISSE PEACE Polymers International Space Station Environmental Exposure Experiment." *Proceedings of the 10th ISMSE, 8th ICPMSE: 19-23 June, 2006.* Collioure, France. ESA SP-616.

de Groh, K.K.; Banks, B.A.; McCarthy, C.E.; Rucker, R.N.; Roberts, L.M.; Berger, L.A. (2008). "MISSE 2 PEACE Polymers Atomic Oxygen Erosion Experiment on the International Space Station." *High Performance Polymers.* Vol. 20, pp. 388-409.

de Groh, K.K.; Banks, B.A.; McCarthy, C.E.; Rucker, R.N.; Roberts, L.M.; Berger, L.A. (June 26-30, 2006). "MISSE PEACE Polymers Atomic Oxygen Erosion Results." *Proceedings of the 2006 National Space & Missile Materials Symposium.* Orlando, FL. Also published as NASA/TM—2006-214482.

de Groh, K.K.; Jaworske, D.A.; Kinard, W.H.; Pippin, H.G; Jenkins, P.P. (2011). "Tough Enough for Space: Testing Spacecraft Materials on the ISS." *NASA Technology Innovation*. Vol. 15, No. 4, pp. 50-53.

de Groh, K.K.; McCollum, T.A. (January-February 1995). "Low Earth Orbit Durability of Protected Silicone for Refractive Photovoltaic Concentrator Arrays." *Journal of Spacecraft and Rockets*. Vol. 32, No. 1, pp. 103-109.

de Groh, K.K.; McCue, T.R. (August 1999). "Analyses of Contaminated Solar Array Handrail Samples Retrieved from Mir." *Proceedings of the 34th Intersociety Energy Conversion Engineering Conference, August 2-5, 1999, Vancouver, B.C.* Warrendale, PA: Society of Automotive Engineers. Also published as NASA/TM—1999-209399.

Dever, J.A. (February 1991). *Low Earth Orbital Atomic Oxygen and Ultraviolet Radiation Effects on Polymers*. NASA TM-103711.

Dever, J.; Banks, B.; de Groh, K.; Miller, S. (2005). "Degradation of Spacecraft Materials." In Myer Kutz, Ed., *Handbook of Environmental Degradation of Materials*. 465-501. Norwich, NY: William Andrew Publishing.

Dever, J.A.; Miller S.K.; Sechkar, E.A.; Wittberg, T.N. (June 26-30, 2006). "Preliminary Analysis of Polymer Film Thermal Control and Gossamer Materials Experiments on MISSE 1 and MISSE 2." *Proceedings of the 2006 National Space & Missile Materials Symposium.* Orlando, FL.

Dever, J.A.; Rutledge, S.K.; Hambourger, P.D.; Bruckner, E.; Ferrante, R.; Pal, A.M.; Mayer, K.; Pietromica, A.J. (April 24-26, 1996). *Indium Tin Oxide-Magnesium*

Fluoride Co-Deposited Films for Spacecraft Applications. Paper presented at the International Conference on Metallurgical Coatings (AVS). San Diego, CA. Also published as NASA/TM─1988-208499.

Dickerson, R.E.; Gray, H.B.; Haight, G.P. (1979). *Chemical Principles 3rd Edition*. Menlo Park, CA: Benjamin Cummings Publishing Co. Inc. p. 457.

Goode, D.C.; Williams, A.W.; Wood, N.J.; Binzakaria, A. (November 1994). "Photothermal Imaging of Gold and Vermiculite Coated Kapton Exposed to Atomic Oxygen." *ESA Proceedings of the 6th International Symposium on Materials in a Space Environment*. 201-206. SEE N95-27568 09-23.

Gregory, J.C. (November 10-11, 1986). "Interaction of Hyperthermal Atoms on Surfaces in Orbit: The University of Alabama Experiment." In David E. Brinza, Ed., *Proceedings of the NASA Workshop on Atomic Oxygen Effects, Nov. 10-11, 1986*. JPL 87-14, pp. 29-30.

Gulino, D.A. (1988). "Atomic-Oxygen Durability of Impact-Damaged Solar Reflectors." *Journal of Spacecraft and Rockets*. Vol. 25, No. 1, pp. 39-44.

Hansen, R.H.; Pascale, J.V.; De Benedictis, T.; Rentzepis, P.M. (1965). "Effects of Atomic Oxygen on Polymers." *Journal of Polymer Science*. Part A, Vol. 3, pp. 2205-2214.

Hedin, A.E. (1987). "MSIS-86 Thermospheric Model." *Journal of Geophysical Research*. Vol. 92, pp. 4649-4662.

Hung, C.; Cantrell, G. (November 1994). *Reaction and Protection of Electrical Wire Insulators in Atomic-Oxygen Environments*. NASA TM-106767. NASA LeRC: Cleveland, OH.

Howland, R.; Benatar, L. (1996). *A Practical Guide to Scanning Probe Microscopy*. Sunnyvale, CA: Park Scientific Instruments.

Integrity Testing Laboratory, Inc. (1998). *Prediction of Erosion of Polymer-Based Materials by Atomic Oxygen in LEO*. (Final Report, GRC Contract #C-72917-G.) Markham, Ontario, Canada.

Jenkins, P.P.; Walters, R.J.; Krasowski, M.J.; Chapman, J.J.; Ballard, P.G.; Vasquez, J.A.; Mahony, D.R.; LaCava, S.N.; Braun, W.R.; Prokop, N.F.; Flatico, J.M.; Greer, L.C.; Gibson, K.B.; Kinard, W.H.; Pippin, H.G. (2008). "MISSE-7: Building a Permanent Environmental Testbed for the International Space Station." In J.I. Kleiman, Ed., *Protection of Materials and Structures from Space Environment: Proceedings of the 9th International Conference (ICPMSE-9), Toronto, Canada, 20-23 May 2008*. 273-276. AIP Conference Proceedings 1087.

Juhl, Shane. (2010). Personal communication. S. Juhl, Air Force Research Laboratory.

Koontz, S.L.; Leger, L.J.; Visentine, J.T.; Hunton, D.E.; Cross, J.B.; Hakes, C.L. (May-June 1995). "EOIM-III Mass Spectrometry and Polymer Chemistry: STS 46, July-August 1992." *Journal of Spacecraft and Rockets*. Vol. 32, No. 3, pp. 483-495.

Leger, L.J. (1982). *Oxygen Atom Reaction with Shuttle Materials at Orbital Altitudes*. NASA TM-58246. NASA Johnson Space Center (JSC): Houston, TX.

Leger, L.J. (1983). "Oxygen Atom Reaction with Shuttle Materials at Orbital Altitudes – Data and Experiment Status." *Proceedings of AIAA 21st Aerospace Sciences Meeting, 1983*. AIAA-83-0073.

Mata, A.; Su, X.; Fleischman, A.; Banks, B.; Miller, S.; Midura, R. (December 2003). "Osteoblast Attachment to a Textured Surface in the Absence of Exogenous Adhesion Proteins." *IEEE Transactions on Nanobioscience*. Vol. 2, No. 4, pp. 287-294.

McCarthy, C.E.; Banks, B.A.; de Groh, K.K. (November 2010). *MISSE 2 PEACE Polymers Experiment Atomic Oxygen Erosion Yield Error Analysis.* NASA/TM—2010-216903. NASA GRC: Cleveland, OH.

Mende, S.B.; Swenson, G.R.; Clifton, K.S. (1984). "Space Plasma Physics Atmospheric Emissions Photometric Imaging Experiment," *Science*. Vol. 225, pp. 191.

Miller, S.K.R.; Banks, B.A.; Waters, D.L. (2008). "Investigation into the Differences in Atomic Oxygen Erosion Yields of Materials in Ground Based Facilities Compared to Those in LEO." *High Performance Polymers*. Vol. 20, pp. 523-534.

Minton, T.K. (1995). *Protocol for Atomic Oxygen Testing of Materials in Ground-Based Facilities*. JPL Publication 95-17, Version 2. Jet Propulsion Laboratory: Pasadena, CA.

low earth orbit. 2011 in *Merriam-Webster, An Encyclopedia Britannica Company*. Accessed August 9, 2012.

O'Neal, R.L.; Levine, A.S.; Kiser, C.C. (1996). *Photographic Survey of the LDEF Mission*. NASA SP-531. NASA LaRC: Hampton, VA.

Palusinski, Iwona A. (2010). Personal communication. I.A. Palusinski, The Aerospace Corporation.

Pippin, G., (2006). *Summary Status of MISSE-1 and MISSE-2 Experiments and Details of Estimated Environmental Exposures for MISSE-1 and MISSE-2*. Final Report for 24 June 2002–31 July 2006. AFRL-ML-WP-TR-2006-4237, TECHNICAL

OPERATIONS SUPPORT (TOPS) II (Delivery Order 0011). Wright-Patterson Air Force Base, Air Force Research Laboratory, OH.

Picone, J.M.; Hedin, A.E.; Drob, D.P.; Aikin, A.C. (2002). "NRLMSISE-00 Empirical Model of the Atmosphere: Statistical Comparisons and Scientific Issues." *Journal of Geophysical Research: Space Physics (1978-2012).* Vol. 107, Issue A12, pp. SIA 15-1 – SIA 15-16.

Rutledge, S.K.; Banks, B.A.; Cales, M. (1994). *A Comparison of Atomic Oxygen Erosion Yields of Carbon and Selected Polymers Exposed in Ground Based Facilities and in Low Earth Orbit*. NASA-TM-106622. NASA GRC: Cleveland, OH.

Rutledge, S.K.; Banks, B.A.; DiFilippo, F.; Brady, J.A.; Dever, T.M.; Hotes, D. (1986). *An Evaluation of Candidate Oxidation Resistant Materials for Space Applications in LEO*. NASA-TM-100122. NASA GRC: Cleveland, OH.

Rutledge, S.K.; Mihelcic, J.A. (1990). "The Effect of Atomic Oxygen on Altered and Coated Kapton Surfaces for Spacecraft Applications in Low Earth Orbit." In V. Srinivasan and B. Banks., Eds., *Materials Degradation in Low Earth Orbit*. 35-48. Warrenburg, PA: TMS.

Rutledge, S.K.; Olle, R.M. (May 10-13,1993). "Space Station Freedom Solar Array Blanket Coverlay Atomic Oxygen Durability Testing Results." In V. Bailey, G.C. Janicki, and T. Haulik, Eds., *Proceedings of the 38th International SAMPE Symposium and Exhibition*. 679-693.

Shpilman, Z.; Gouzman, I.; Grossman, E.; Shen, L.; Minton, T.K.; Paci, J.T.; Schatz, G.C.; Akhvlediani, R.; Hoffman, A. (2010). "Oxidation and Etching of CVD Diamond by Thermal and Hyperthermal Atomic Oxygen." *Journal of Physical Chemistry* C. Vol. 114, pp. 18,996–19,003.

Silverman, E.M. (August 1995). *Space Environmental Effects on Spacecraft: LEO Materials Selection Guide*. NASA CR-4661, Part 1 and Part 2. NASA MSFC: Huntsville, AL.

Stambler, A.H.; Inoshita, K.E.; Roberts, L.M.; Barbagallo, C.E.; de Groh K.K.; Banks, B.A. (2009). "Ground-Laboratory to In-Space Atomic Oxygen Correlation for the PEACE Polymers." In J.I. Kleiman, Ed., *Proceedings of the 9th International Conference Protection of Materials and Structures from Space Environmen*t. 51-66. AIP Conference Proceedings 1087. Also published as NASA/TM—2011-216904, January 2011.

Visentine, J.T.; Leger, L.J.; Kuminecz, J.F.; Spiker, I.K. (1985). *STS-8 Atomic Oxygen Effects Experiment*. Paper AIAA-85-0415 presented at the AIAA 23rd Aerospace Sciences Meeting. Reno, NV.

Walters, R.J.; Garner, J.C.; Lam, S.N.; Vasquez, J.A.; Braun, W.R.; Ruth, R.E.; Messenger, S.R.; Lorentzen, J.R.; Bruninga, R.; Jenkins, P.P.; Flatico, J.M.; Wilt, D.M.; Piszczor, M.F.; Greer, L.C.; M.J. Krasowski. (2005). "Materials on the International Space Station—Forward Technology Solar Cell Experiment." *Materials Science and Engineering*. Vol. 116, Issue 3, pp. 257-263.

Wert, J. (June 28–July 1, 2010). "Passive Radiation Dose Measurements on MISSE-1 through MISSE-4 and MISSE-6." *Proceedings of the 2010 National Space & Missile Materials Symposium.* Scottsdale, AZ.

Yang, J.C.; de Groh, K.K. (January 2010). "Materials Issues in the Space Environment." *MRS Bulletin*. Vol. 35, pp. 12-19.

14.2 Additional Reading

MIL-STD-1809 Military Standard, Space Environment for USAF Space Vehicles

APPENDIX A

AUTHORS AND ACKNOWLEDGEMENTS

A.1 Purpose and/or Scope

The purpose of this appendix is to acknowledge the authors and significant contributors and contributions to this publication.

A.2 Authors

Kim K. de Groh	NASA Glenn Research Center 21000 Brookpark Rd. M.S. 309-2 Cleveland, OH 44135	Phone: (216) 433-2297 Fax: (216) 433-2221 E-mail: kim.k.degroh@nasa.gov
Bruce A. Banks	Science Applications International Corporation at NASA Glenn Research Center 21000 Brookpark Rd. M.S. 309-2 Cleveland, OH 44135	Phone: (216) 433-2308 Fax: (216) 433-2221 E-mail: bruce.a.banks@nasa.gov
Catherine E. McCarthy	Hathaway Brown School 19600 North Park Boulevard Shaker Heights, OH 44122	Phone: (216) 408-1546 E-mail: catherine.e.mccarthy@gmail.com

A.3. Acknowledgements

The authors would like to thank Don Jaworske of NASA GRC for coordinating all the GRC MISSE experiments and for his help and dedication to the MISSE program. We would like to acknowledge and thank former students Jon Gummow of Ohio Aerospace Institute and Doug Wright of Cleveland State University for pre-flight fabrication and characterization of the MISSE 2 PEACE samples. There are many companies who kindly provided samples of polymers, which we sincerely appreciate. We would like to thank all of the PEACE Team students for their dedication to this program and for their crucial help with pre-flight research, sample fabrication, and pre- and post-flight characterization of samples. We gratefully acknowledge Patty Hunt of Hathaway Brown School for making it possible for the Hathaway Brown School students to be a part of the MISSE program. We thank Laura Becker and Lisa Greeney of Wyle Information Systems, LLC, at NASA GRC for their dedicated help in preparing this Handbook, which included creating Appendix D, working on equations, and creating symbol lists. We thank Don Thomas (retired) and Julie Robinson of NASA JSC for their appreciation of the MISSE program and of the PEACE experiments. We greatly appreciate the support provided by Carl Walz (retired) and Fran Chiaramonte of NASA Headquarters and of Fred Kohl and Tom St. Onge of NASA GRC. Finally, we would like to show our sincere

appreciation to Bill Kinard (retired) of NASA LaRC and Gary Pippin (retired) of Boeing for providing the unique opportunity to be a part of the MISSE program. This Handbook was supported by the ISS Research and MISSE-X Projects and the NASA Technical Standards Program.

APPENDIX B

MISSE 2 PEACE POLYMERS EXPERIMENT ATOMIC OXYGEN EROSION YIELD ERROR ANALYSIS

B.1 Purpose and/or Scope

The purpose of this appendix is to provide details on the MISSE 2 PEACE Polymers experiment atomic oxygen erosion yield error analyses as documented in McCarthy et al. (2010).

B.2 Introduction

In any experiment, it is critical to determine the accuracy of the data obtained. To address this for the MISSE 2 PEACE Polymers experiment, the error in each polymer's experimental LEO erosion yield value was calculated using equations for fractional uncertainty derived from the equation used to find erosion yield (McCarthy et al., 2010). The specific equations developed and resulting erosion yield uncertainties are provided in this appendix, which is based on the error analysis conducted by McCarthy et al. (2010).

B.3 Erosion Yield

The equation to find the erosion yield (E) of a polymer calculates the volume lost per incident atomic oxygen atom:

$$E = \frac{4 \cdot \Delta M}{\pi \cdot \rho \cdot D^2 \cdot F} \qquad \text{(Eq. B-1)}$$

where:

ΔM = mass loss (g)
ρ = the polymer density (g/cm^3)
D = the exposed diameter of the polymer (cm)
F = the atomic oxygen fluence (atoms/cm^2): how many atoms of atomic oxygen came into contact with the polymer during the period of exposure.

Two Kapton® H witness samples were used to calculate the fluence, because Kapton® H has a well-established erosion yield in LEO: 3.0×10^{-24} cm^3/atom (ASTM E 2089-00). The atomic oxygen fluence for these samples can be calculated by solving Eq. B-1 for F and using the Kapton® H mass loss and density values. The fluence was based on the frontal exposed area of each sample. It is believed that the 45°-slanted edges of the Al sample holders contributed to a slight increase in fluence around the perimeters of the samples, causing some samples to erode through around the edge only; however, since this was the case for all of the samples, no further calculations needed to be done to correct for this anomalous effect.

B.4 Fractional Uncertainty

Fractional uncertainty, also called relative uncertainty or percent error, is a way of quantifying error. In this investigation, the fractional uncertainty represents the fractional standard deviation of the values and is calculated by dividing the standard deviation of the value by the value itself. The general equation for fractional uncertainty in atomic oxygen erosion yield is as follows:

$$\frac{\delta E}{E} = \sqrt{\sum_i \left[\left(\frac{1}{E} \cdot \frac{\partial E}{\partial x_i} \cdot \delta x \right)^2 \right]} \qquad \text{(Eq. B-2)}$$

where:

E = the atomic oxygen erosion yield
x_i = the ith variable in the equation for erosion yield.

The complete equation derivations are explained in section B.7 of this Handbook.

B.5 Mass Loss Situations

As previously mentioned, each flight sample included two sets of sample layers: Part A was enough material to theoretically last for 1.5 years in space, and the additional layers of Part B extended the time to 3 years, as shown in figure 52, Illustration of the Flight Sample Setup. Each flight sample also had a corresponding identical backup sample, including both Parts A and B, that was kept on the ground as a control. Though flight sample Parts A and B were not separated during flight, they were separated for pre- and post-flight weighing. Because of mission time constraints, Part B of each sample was not weighed pre-flight, and so a theoretical value for the pre-flight mass of Part B was calculated: the pre-flight mass of flight sample Part A (M_F) and the pre-flight mass of control sample Part A (M_C) were used to calculate the average mass per layer (M_A), which was multiplied by the number of layers (n) in flight sample Part B to get Part B's theoretical pre-flight mass ($n \cdot M_A$).

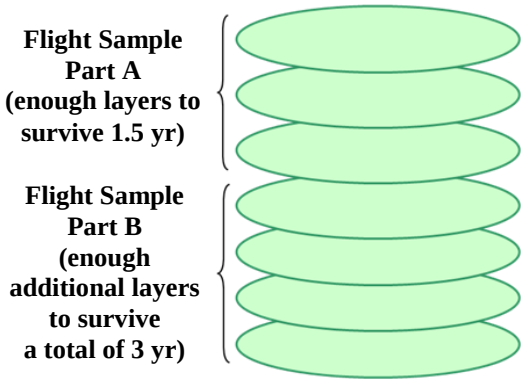

Figure 52—Illustration of the Flight Sample Setup

There were three different situations for post-flight sample weighing, so three different equations to determine mass loss were required. Mass loss (ΔM) is a factor in calculating the erosion yield of a polymer (see Eq. B-1), and so it was also necessary to develop three different equations for fractional uncertainty in erosion yield. The different mass loss equations were simply substituted into the equation for erosion yield, and then, from each of the three resulting equations, an equation for fractional uncertainty was derived to calculate the percent error for that situation.

In Situation 1, either only one sample layer was flown or the atomic oxygen eroded through only some of the layers in flight sample Part A and all of flight sample Part B was still pristine (figure 53, Illustration of Situation 1 Sample Erosion).

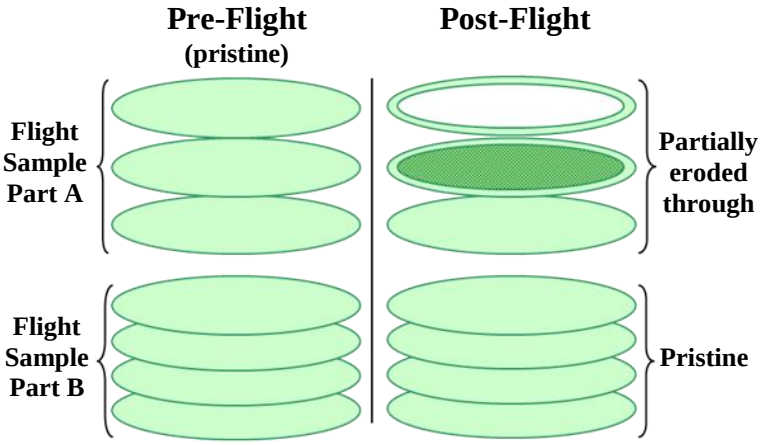

Figure 53—Illustration of Situation 1 Sample Erosion

Because flight sample Part A and flight sample Part B were weighed separately pre-flight, in this situation only Part A needed to be weighed post-flight and compared with its pre-flight mass; so to minimize error, the terms for pre- and post-flight mass for flight sample Part B were omitted from the Situation 1 mass loss equation:

$$\Delta M_1 = M_F - M'_F \qquad \text{(Eq. B-3)}$$

where:

M_F = the pre-flight mass of flight sample Part A
M'_F = the post-flight mass of Part A.

The Situation 1 erosion yield equation is:

$$E_1 = \frac{4 \cdot \left(M_F - M'_F\right)}{\pi \cdot \rho \cdot D^2 \cdot F} \qquad \text{(Eq. B-4)}$$

In Situation 2, atomic oxygen erosion occurred through all of the layers of flight sample Part A and through some of the layers of flight sample Part B (figure 54, Illustration of Situation 2 Sample Erosion).

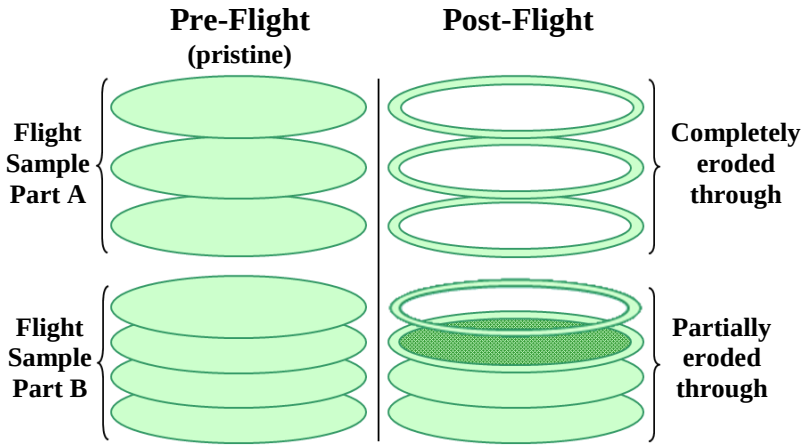

Figure 54—Illustration of Situation 2 Sample Erosion

In this situation, flight sample Parts A and B were able to be separated for post-flight weighing. However, because flight sample Part B had not been weighed pre-flight, its theoretical pre-flight mass was used. Therefore, the Situation 2 equation for mass loss is:

$$\Delta M_2 = M_F - M'_F + n \cdot M_A - M'_E \qquad \text{(Eq. B-5)}$$

where:,

M_F and M'_F	=	the pre- and post-flight mass values, respectively, of flight sample Part A
$n \cdot M_A$	=	the theoretical pre-flight mass of flight sample Part B
M'_E	=	the post-flight mass of Part B.

The erosion yield equation for Situation 2 is:

$$E_2 = \frac{4 \cdot \left(M_F - M'_F + n \cdot M_A - M'_E\right)}{\pi \cdot \rho \cdot D^2 \cdot F} \qquad \text{(Eq. B-6)}$$

In Situation 3, the sample layers were stuck together and fragmented and were too fragile to separate without losing particles of the material, thereby compromising the erosion yield data (figure 55, Illustration of Situation 3 Sample Erosion).

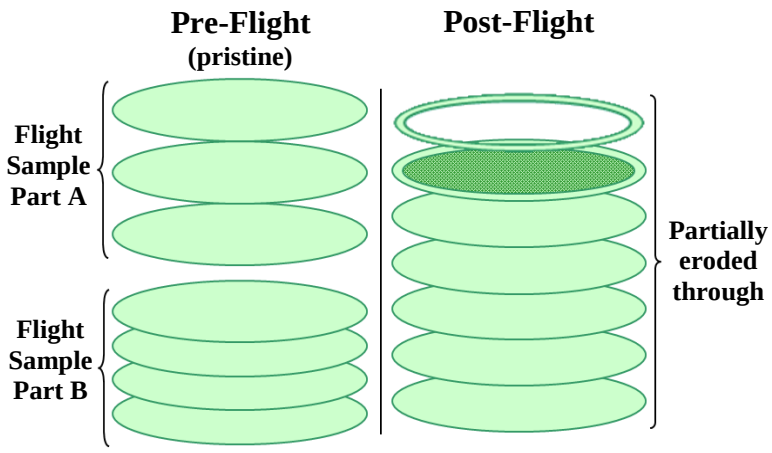

Figure 55—Illustration of Situation 3 Sample Erosion

Because of this, flight sample Parts A and B were weighed together post-flight. Therefore, the Situation 3 mass loss equation is:

$$\Delta M_3 = M_F + n \cdot M_A - M'_S \qquad \text{(Eq. B-7)}$$

where:

M_F = the pre-flight mass of flight sample Part A
$n \cdot M_A$ = the theoretical pre-flight mass of flight sample Part B
M'_S = the post-flight mass of the entire flight sample.

The Situation 3 erosion yield equation is:

$$E_3 = \frac{4 \cdot \left(M_F + n \cdot M_A - M'_S\right)}{\pi \cdot \rho \cdot D^2 \cdot F} \qquad \text{(Eq. B-8)}$$

One of the variables in the erosion yield equations is atomic oxygen fluence (F), which is itself found from rearranging the erosion yield equation (Eq. B-1). The equation for F needed to be substituted into the erosion yield equations so that the error calculations could take into account all sources of error.

The equation for the fluence of the Kapton® witness samples is:

$$F_K = \frac{4 \cdot \Delta M_K}{\pi \cdot \rho_K \cdot D_K^2 \cdot E_K} \qquad \text{(Eq. B-9)}$$

However, the atomic oxygen fluence value used in the experiment was actually the average of the F values of the two Kapton® H witness samples that were flown. This needed to be taken into account as well. The equation for the average of the two fluence values is found through the following:

$$F_{AVG\ K} = \frac{1}{2}\left(\frac{4 \cdot \Delta M_{K1}}{\pi \cdot \rho_K \cdot D_{K1}^2 \cdot E_K} + \frac{4 \cdot \Delta M_{K2}}{\pi \cdot \rho_K \cdot D_{K2}^2 \cdot E_K} \right) = \frac{4}{2\pi \cdot \rho_K \cdot E_K} \cdot \left(\frac{\Delta M_{K1}}{D_{K1}^2} + \frac{\Delta M_{K2}}{D_{K2}^2} \right) \quad \text{(Eq. B-10)}$$

This expression for $F_{AVG\,K}$ is then substituted into the equation for sample erosion yield:

$$E_S = \frac{4 \cdot \Delta M_S}{\pi \cdot \rho_S \cdot D_S^2 \cdot F_{AVG\ K}} = \frac{4 \cdot \Delta M_S}{\pi \cdot \rho_S \cdot D_S^2} \cdot \frac{2\pi \cdot \rho_K \cdot E_K}{4 \cdot \left(\frac{\Delta M_{K1}}{D_{K1}^2} + \frac{\Delta M_{K2}}{D_{K2}^2} \right)} = \frac{2 \cdot \Delta M_S \cdot \rho_K \cdot E_K}{\rho_S \cdot D_S^2 \cdot \left(\frac{\Delta M_{K1}}{D_{K1}^2} + \frac{\Delta M_{K2}}{D_{K2}^2} \right)} \quad \text{(Eq. B-11)}$$

Therefore, the erosion yield equations for the three situations are now:

$$E_1 = \frac{2 \cdot \left(M_F - M'_F \right) \cdot \rho_K \cdot E_K}{\rho_S \cdot D_S^2 \cdot \left(\frac{\Delta M_{K1}}{D_{K1}^2} + \frac{\Delta M_{K2}}{D_{K2}^2} \right)} \quad \text{(Eq. B-12)}$$

$$E_2 = \frac{2 \cdot \left(M_F - M'_F + n \cdot M_A - M'_E \right) \cdot \rho_K \cdot E_K}{\rho_S \cdot D_S^2 \cdot \left(\frac{\Delta M_{K1}}{D_{K1}^2} + \frac{\Delta M_{K2}}{D_{K2}^2} \right)} \quad \text{(Eq. B-13)}$$

$$E_3 = \frac{2 \cdot \left(M_F + n \cdot M_A - M'_S \right) \cdot \rho_K \cdot E_K}{\rho_S \cdot D_S^2 \cdot \left(\frac{\Delta M_{K1}}{D_{K1}^2} + \frac{\Delta M_{K2}}{D_{K2}^2} \right)} \quad \text{(Eq. B-14)}$$

In the final equations for fractional uncertainty, $\frac{\Delta M_{K1}}{D_{K1}^2} + \frac{\Delta M_{K2}}{D_{K2}^2}$ is replaced by the variable *R*.

B.6 Atomic Oxygen Fluence Uncertainty

Table 17, Kapton® H Witness Sample Measurement and Uncertainty Values**,** shows the mass loss, density, erosion yield, and exposed diameter values, along with the corresponding uncertainty values, for the two Kapton® fluence witness samples. The erosion yield for Kapton® H polyimide was assumed to be 3.0×10^{-24} cm^3/atom (ASTM E 2089-00) with a probable error of $\pm0.05\times10^{-24}$ cm^3/atom, which is a standard deviation error of $\pm7.41\times10^{-26}$ cm^3/atom (or 0.024700, a ±2.5 percent fractional uncertainty).

Table 17—Kapton® H Witness Sample Measurement and Uncertainty Values

Kapton H Sample #	ΔM_K (g)	$\delta\Delta M_K$ (g)	ρ_K (g/cm^3)	$\delta\rho_K$ (g/cm^3)	D_K (cm)	δD_K (cm)	E_K (cm^3/atom)	δE_K (cm^3/atom)	$\delta E_K/E_K$
1	0.124785	0.0000513	1.42725	0.0077	2.0986	0.00582	3.00E-24	7.41E-26	0.024700
2	0.129219	0.0000808			2.1342	0.00410			

B.7 Fractional Uncertainty Equation Derivations and Results

The equations for fractional standard deviation uncertainty in erosion yield were derived from the previous three erosion yield equations, using partial derivatives. In all of the following derivations, ∂x is the partial derivative of x, δx is the uncertainty of x, and $\frac{\delta x}{x}$ is the fractional uncertainty of x. The following variable definitions apply to all of the derived equations:

E = erosion yield (cm^3/atom)
ΔM = mass loss (g)
ρ = density (g/cm^3)
D = diameter of the exposed area of the sample (cm)
F = atomic oxygen fluence ($atoms/cm^2$)
M_F = pre-flight mass of flight sample Part A (g)
M'_F = post-flight mass of flight sample Part A (g)
$n \cdot M_A$ = theoretical pre-flight mass for flight sample Part B (g)
M'_E = post-flight mass of flight sample Part B (g)
M'_S = post-flight mass of flight sample Parts A and B weighed together (g).

A subscript of K refers to the value corresponding to the Kapton® fluence witness samples, and a subscript of S refers to the value corresponding to the flight sample in question.

B.7.1 Fractional Uncertainty Equation Derivations for Situation 1

Using Eq. B-12, the equation for Situation 1 erosion yield, the equation for fractional uncertainty in erosion yield for Situation 1 $\left(\frac{\delta E_1}{E_1}\right)$ is derived through the following process:

Term one: $x_1 = M_F$

$$\left(\frac{1}{E_1}\cdot\frac{\partial E_1}{\partial M_F}\cdot\delta M_F\right)^2$$

$$= \left[\frac{\rho_S \cdot D_S^2 \cdot \left(\frac{\Delta M_{K1}}{D_{K1}^2}+\frac{\Delta M_{K2}}{D_{K2}^2}\right)}{2\cdot\left(M_F - M'_F\right)\cdot\rho_K\cdot E_K}\cdot\frac{2\cdot\rho_K\cdot E_K}{\rho_S\cdot D_S^2\cdot\left(\frac{\Delta M_{K1}}{D_{K1}^2}+\frac{\Delta M_{K2}}{D_{K2}^2}\right)}\cdot\delta M_F\right]^2 \quad \text{(Eq. B-15)}$$

$$= \left(\frac{\delta M_F}{\Delta M_1}\right)^2$$

Term two: $x_2 = M'_F$

$$\left(\frac{1}{E_1}\cdot\frac{\partial E_1}{\partial M'_F}\cdot\delta M'_F\right)^2$$

$$=\left[\frac{\rho_S\cdot D_S^2\cdot\left(\frac{\Delta M_{K1}}{D_{K1}^2}+\frac{\Delta M_{K2}}{D_{K2}^2}\right)}{2\cdot\left(M_F-M'_F\right)\cdot\rho_K\cdot E_K}\cdot\frac{-2\cdot\rho_K\cdot E_K}{\rho_S\cdot D_S^2\cdot\left(\frac{\Delta M_{K1}}{D_{K1}^2}+\frac{\Delta M_{K2}}{D_{K2}^2}\right)}\cdot\delta M'_F\right]^2 \quad \text{(Eq. B-16)}$$

$$=\left(\frac{-\delta M'_F}{\Delta M_1}\right)^2$$

Term three: $x_3 = \rho_S$

$$\left(\frac{1}{E_1}\cdot\frac{\partial E_1}{\partial \rho_S}\cdot\delta\rho_S\right)^2$$

$$=\left[\frac{\rho_S\cdot D_S^2\cdot\left(\frac{\Delta M_{K1}}{D_{K1}^2}+\frac{\Delta M_{K2}}{D_{K2}^2}\right)}{2\cdot\left(M_F-M'_F\right)\cdot\rho_K\cdot E_K}\cdot\frac{-2\cdot\left(M_F-M'_F\right)\cdot\rho_K\cdot E_K}{\rho_S\cdot D_S^2\cdot\left(\frac{\Delta M_{K1}}{D_{K1}^2}+\frac{\Delta M_{K2}}{D_{K2}^2}\right)}\cdot\delta_{\rho_S}\right]^2 \quad \text{(Eq. B-17)}$$

$$=\left(\frac{-\delta\rho_S}{\rho_S}\right)^2$$

Term four: $x_4 = D_S$

$$\left(\frac{1}{E_1}\cdot\frac{\partial E_1}{\partial D_S}\cdot\delta D_S\right)^2$$

$$=\left[\frac{\rho_S\cdot D_S^2\cdot\left(\frac{\Delta M_{K1}}{D_{K1}^2}+\frac{\Delta M_{K2}}{D_{K2}^2}\right)}{2\cdot\left(M_F-M'_F\right)\cdot\rho_K\cdot E_K}\cdot\frac{-4\cdot\left(M_F-M'_F\right)\cdot\rho_K\cdot E_K}{\rho_S\cdot D_S^3\cdot\left(\frac{\Delta M_{K1}}{D_{K1}^2}+\frac{\Delta M_{K2}}{D_{K2}^2}\right)}\cdot\delta D_S\right]^2 \quad \text{(Eq. B-18)}$$

$$=\left(\frac{-2\cdot\delta D_S}{D_S}\right)^2$$

Term five: $x_5 = \rho_K$

$$\left(\frac{1}{E_1}\cdot\frac{\partial E_1}{\partial \rho_K}\cdot\delta\rho_K\right)^2$$

$$=\left[\frac{\rho_s\cdot D_S^2\cdot\left(\frac{\Delta M_{K1}}{D_{K1}^2}+\frac{\Delta M_{K2}}{D_{K2}^2}\right)}{2\cdot\left(M_F-M'_F\right)\cdot\rho_K\cdot E_K}\cdot\frac{2\cdot\left(M_F-M'_F\right)\cdot E_K}{\rho_S\cdot D_S^2\cdot\left(\frac{\Delta M_{K1}}{D_{K1}^2}+\frac{\Delta M_{K2}}{D_{K2}^2}\right)}\cdot\delta\rho_K\right]^2 \quad \text{(Eq. B-19)}$$

$$=\left(\frac{\delta\rho_K}{\rho_K}\right)^2$$

Term six: $x_6 = E_K$

$$\left(\frac{1}{E_1}\cdot\frac{\partial E_1}{\partial E_K}\cdot\delta E_K\right)^2$$

$$=\left[\frac{\rho_S\cdot D_S^2\cdot\left(\frac{\Delta M_{K1}}{D_{K1}^2}+\frac{\Delta M_{K2}}{D_{K2}^2}\right)}{2\cdot\left(M_F-M'_F\right)\cdot\rho_K\cdot E_K}\cdot\frac{2\cdot\left(M_F-M'_F\right)\cdot\rho_K}{\rho_S\cdot D_S^2\cdot\left(\frac{\Delta M_{K1}}{D_{K1}^2}+\frac{\Delta M_{K2}}{D_{K2}^2}\right)}\cdot\delta E_K\right]^2 \quad \text{(Eq. B-20)}$$

$$=\left(\frac{\delta E_K}{E_K}\right)^2$$

Term seven: $x_7 = \Delta M_{K1}$

$$\left(\frac{1}{E_1}\cdot\frac{\partial E_1}{\partial \Delta M_{K1}}\cdot\delta\Delta M_{K1}\right)^2$$

$$=\left[\frac{\rho_S\cdot D_S^2\cdot\left(\frac{\Delta M_{K1}}{D_{K1}^2}+\frac{\Delta M_{K2}}{D_{K2}^2}\right)}{2\cdot\left(M_F-M'_F\right)\cdot\rho_K\cdot E_K}\cdot\frac{-2\cdot\left(M_F-M'_F\right)\cdot\rho_K\cdot E_K}{\rho_S\cdot D_S^2\cdot\left(\frac{\Delta M_{K1}}{D_{K1}^2}+\frac{\Delta M_{K2}}{D_{K2}^2}\right)^2\cdot D_{K1}^2}\cdot\delta\Delta M_{K1}\right]^2 \quad \text{(Eq. B-21)}$$

$$=\left(\frac{-\delta\Delta M_{K1}}{D_{K1}^2\cdot R}\right)^2$$

Term eight: $x_8 = \Delta M_{K2}$

$$\left(\frac{1}{E_1}\cdot\frac{\partial E_1}{\partial \Delta M_{K2}}\cdot\delta\Delta M_{K2}\right)^2$$

$$=\left[\frac{\rho_S\cdot D_S^2\cdot\left(\frac{\Delta M_{K1}}{D_{K1}^2}\right)+\frac{\Delta M_{K2}}{D_{K2}^2}}{2\cdot\left(M_F-M'_F\right)\cdot\rho_K\cdot E_K}\cdot\frac{-2\cdot\left(M_F-M'_F\right)\cdot\rho_K\cdot E_K}{\rho_S\cdot D_S^2\cdot\left(\frac{\Delta M_{K1}}{D_{K1}^2}+\frac{\Delta M_{K2}}{D_{K2}^2}\right)^2\cdot D_{K2}^2}\cdot\delta\Delta M_{K2}\right]^2 \quad \text{(Eq. B-22)}$$

$$=\left(\frac{-\delta\Delta M_{K2}}{D_{K2}^2\cdot R}\right)^2$$

Term nine: $x_9 = D_{K1}$

$$\left(\frac{1}{E_1}\cdot\frac{\partial E_1}{\partial D_{K1}}\cdot\delta D_{K1}\right)^2$$

$$=\left[\frac{\rho_S\cdot D_S^2\cdot\left(\frac{\Delta M_{K1}}{D_{K1}^2}+\frac{\Delta M_{K2}}{D_{K2}^2}\right)}{2\cdot\left(M_F-M'_F\right)\cdot\rho_K\cdot E_K}\cdot\frac{-4\cdot\left(M_F-M'_F\right)\cdot\Delta M_{K1}\cdot\rho_K\cdot E_K}{\rho_S\cdot D_S^2\cdot\left(\frac{\Delta M_{K1}}{D_{K1}^2}+\frac{\Delta M_{K2}}{D_{K2}^2}\right)^2\cdot D_{K1}^3}\cdot\delta D_{K1}\right]^2 \quad \text{(Eq. B-23)}$$

$$=\left(\frac{-2\cdot\Delta M_{K1}\cdot\delta D_{K1}}{D_{K1}^3\cdot R}\right)^2$$

Term ten: $x_{10} = D_{K2}$

$$\left(\frac{1}{E_1}\cdot\frac{\partial E_1}{\partial D_{K2}}\cdot\delta D_{K2}\right)^2$$

$$=\left[\frac{\rho_S\cdot D_S^2\cdot\left(\frac{\Delta M_{K1}}{D_{K1}^2}+\frac{\Delta M_{K2}}{D_{K2}^2}\right)}{2\cdot\left(M_F-M'_F\right)\cdot\rho_K\cdot E_K}\cdot\frac{-4\cdot\left(M_F-M'_F\right)\cdot\Delta M_{K2}\cdot\rho_K\cdot E_K}{\rho_S\cdot D_S^2\cdot\left(\frac{\Delta M_{K1}}{D_{K1}^2}+\frac{\Delta M_{K2}}{D_{K2}^2}\right)^2\cdot D_{K2}^3}\cdot\delta D_{K2}\right]^2 \quad \text{(Eq. B-24)}$$

$$=\left(\frac{-2\cdot\Delta M_{K2}\cdot\delta D_{K2}}{D_{K2}^3\cdot R}\right)^2$$

Therefore, the equation for fractional uncertainty in erosion yield for Situation 1 is:

$$\frac{\delta E_1}{E_1} = \left[\left(\frac{\delta M_F}{\Delta M_1} \right)^2 + \left(\frac{\delta M'_F}{\Delta M_1} \right)^2 + \left(\frac{\delta \rho_S}{\rho_S} \right)^2 + \left(\frac{2 \cdot \delta D_S}{D_S} \right)^2 + \left(\frac{\delta \rho_K}{\rho_K} \right)^2 + \left(\frac{\delta E_K}{E_K} \right)^2 + \left(\frac{\delta \Delta M_{K1}}{D_{K1}^2 \cdot R} \right)^2 + \left(\frac{\delta \Delta M_{K2}}{D_{K2}^2 \cdot R} \right)^2 + \left(\frac{2 \cdot \Delta M_{K1} \cdot \delta D_{K1}}{D_{K1}^3 \cdot R} \right)^2 + \left(\frac{2 \cdot \Delta M_{K2} \cdot \delta D_{K2}}{D_{K2}^3 \cdot R} \right)^2 \right]^{1/2} \quad \text{(Eq. B-25)}$$

Table 18, Situation 1 Fractional Uncertainty in Erosion Yield, shows the mass loss, density, and exposed diameter values; the corresponding uncertainty values; and the calculated fractional uncertainty values for each polymer in Situation 1.

Table 18—Situation 1 Fractional Uncertainty in Erosion Yield

Material Abbreviation	δM_F (g)	$\delta M'_F$ (g)	ΔM (g)	ρ (g/cm^3)	$\delta\rho$ (g/cm^3)	D (cm)	δD (cm)	$\delta E/E$
ABS	0.000042	0.000020	0.033861	1.0500	0.0074	2.1093	0.0058	0.027017
ADC	0.000036	0.000036	0.267295	1.3173	0.0040	2.1228	0.0033	0.025824
AF	0.000004	0.000003	0.012352	2.1463	0.0086	2.0972	0.0034	0.025975
CTFE	0.000005	0.000012	0.052949	2.1327	0.0086	2.1246	0.0030	0.025927
EP	0.000140	0.000220	0.140720	1.1150	0.0079	2.1283	0.0057	0.027020
FEP	0.000002	0.000084	0.012479	2.1443	0.0089	2.0949	0.0039	0.026890
PAN	0.000066	0.000025	0.047281	1.1435	0.0228	2.1040	0.0054	0.032801
PEO	0.000089	0.000022	0.066395	1.1470	0.0028	2.1288	0.0045	0.025948
PFA	0.000079	0.000005	0.010785	2.1383	0.0086	2.0980	0.0052	0.027248
PG	0.002890	0.000100	0.027730	2.2200	0.0074	2.1321	0.0050	0.107496
PI (Upilex-S®)	0.000009	0.000003	0.038127	1.3866	0.0212	2.1225	0.0049	0.030056
PI (PMR-15)	0.000065	0.000034	0.118887	1.3232	0.0040	2.1187	0.0018	0.025696
POM	0.000041	0.000018	0.378378	1.3984	0.0233	2.1146	0.0030	0.030556
PP	0.000020	0.000003	0.072357	0.9070	0.0007	2.1211	0.0062	0.026127
PPD-T	0.000041	0.000023	0.026790	1.4422	0.0017	2.1140	0.0061	0.026193
PS	0.000058	0.000001	0.115947	1.0503	0.0079	2.1123	0.0045	0.026884
PTFE	0.000002	0.000001	0.008938	2.1503	0.0086	2.1062	0.0043	0.026089
PVF-W	0.000022	0.000012	0.004714	1.6241	0.0518	2.0860	0.0043	0.041361

B.7.2 Fractional Uncertainty Equation Derivations for Situation 2

Using Eq. B-13, the equation for Situation 2 erosion yield, the equation for fractional uncertainty in erosion yield in Situation 2 $\left(\frac{\delta E_2}{E_2} \right)$ is derived as described below. One of the variables seen above in the Situation 2 equation for erosion yield, $n \cdot M_A$, was found from two different measurements: M_A was found by averaging the mass of each layer of that flight sample's Part A and control group over the total number of layers (N). Therefore, as with the fluence equation, the equation for M_A must be substituted into the erosion yield equation to account for all sources of error. The equation for M_A is:

$$M_A = \frac{M_F + M_C}{N} \qquad \text{(Eq. B-26a)}$$

Therefore,

$$\delta M_A = \frac{1}{N} \cdot \sqrt{\sum_{i=1}^{n} \left[\left(\frac{\partial M_A}{\partial x_i} \cdot \delta x_i \right)^2 \right]} = \frac{1}{N} \cdot \sqrt{\left(\delta M_F\right)^2 + \left(\delta M_C\right)^2} \qquad \text{(Eq. B-26b)}$$

This expression for δM_A will be substituted into term 3 of the error equation for this situation.

Term one: $x_1 = M_F$

$$\left(\frac{1}{E_2} \cdot \frac{\partial E_2}{\partial M_F} \cdot \delta M_F \right)^2$$

$$= \left[\frac{\rho_S \cdot D_S^2 \cdot \left(\frac{\Delta M_{K1}}{D_{K1}^2} + \frac{\Delta M_{K2}}{D_{K2}^2} \right)}{2 \cdot \left(M_F - M'_F + n \cdot M_A - M'_E\right) \cdot \rho_K \cdot E_K} \cdot \frac{2 \cdot \rho_K \cdot E_K}{\rho_S \cdot D_S^2 \cdot \left(\frac{\Delta M_{K1}}{D_{K1}^2} + \frac{\Delta M_{K2}}{D_{K2}^2} \right)} \cdot \delta M_F \right]^2 \qquad \text{(Eq. B-27)}$$

$$= \left(\frac{\delta M_F}{\Delta M_2} \right)^2$$

Term two: $x_2 = M'_F$

$$\left(\frac{1}{E_2} \cdot \frac{\partial E_2}{\partial M'_F} \cdot \delta M'_F \right)^2$$

$$= \left[\frac{\rho_S \cdot D_S^2 \cdot \left(\frac{\Delta M_{K1}}{D_{K1}^2} + \frac{\Delta M_{K2}}{D_{K2}^2} \right)}{2 \cdot \left(M_F - M'_F + n \cdot M_A - M'_E\right) \cdot \rho_K \cdot E_K} \cdot \frac{-2 \cdot \rho_K \cdot E_K}{\rho_S \cdot D_S^2 \cdot \left(\frac{\Delta M_{K1}}{D_{K1}^2} + \frac{\Delta M_{K2}}{D_{K2}^2} \right)} \cdot \delta M'_F \right]^2 \qquad \text{(Eq. B-28)}$$

$$= \left(\frac{-\delta M'_F}{\Delta M_2} \right)^2$$

Term three: $x_3 = M_A$

$$\left(\frac{1}{E_2}\cdot\frac{\partial E_2}{\partial M_A}\cdot\delta M_A\right)^2$$

$$=\left[\frac{\rho_S\cdot D_S^2\cdot\left(\frac{\Delta M_{K1}}{D_{K1}^2}+\frac{\Delta M_{K2}}{D_{K2}^2}\right)}{2\cdot\left(M_F-M'_F+n\cdot M_A-M'_E\right)\cdot\rho_K\cdot E_K}\cdot\frac{2n\cdot\rho_K\cdot E_K}{\rho_S\cdot D_S^2\cdot\left(\frac{\Delta M_{K1}}{D_{K1}^2}+\frac{\Delta M_{K2}}{D_{K2}^2}\right)}\cdot\delta M_A\right]^2 \quad \text{(Eq. B-29)}$$

$$=\left(\frac{n\cdot\delta M_A}{\Delta M_2}\right)^2$$

Term four: $x_4 = M'_E$

$$\left(\frac{1}{E_2}\cdot\frac{\partial E_2}{\partial M'_E}\cdot\delta M'_E\right)^2$$

$$=\left[\frac{\rho_S\cdot D_S^2\cdot\left(\frac{\Delta M_{K1}}{D_{K1}^2}+\frac{\Delta M_{K2}}{D_{K2}^2}\right)}{2\cdot\left(M_F-M'_F+n\cdot M_A-M'_E\right)\cdot\rho_K\cdot E_K}\cdot\frac{-2\cdot\rho_K\cdot E_K}{\rho_S\cdot D_S^2\cdot\left(\frac{\Delta M_{K1}}{D_{K1}^2}+\frac{\Delta M_{K2}}{D_{K2}^2}\right)}\cdot\delta M'_E\right]^2 \quad \text{(Eq. B-30)}$$

$$=\left(\frac{-\delta M'_E}{\Delta M_2}\right)^2$$

Term five: $x_5 = \rho_S$

$$\left(\frac{1}{E_2}\cdot\frac{\partial E_2}{\partial \rho_S}\cdot\delta\rho_S\right)^2=\left[\frac{\rho_S\cdot D_S^2\cdot\left(\frac{\Delta M_{K1}}{D_{K1}^2}+\frac{\Delta M_{K2}}{D_{K2}^2}\right)}{2\cdot\left(M_F-M'_F+n\cdot M_A-M'_E\right)\cdot\rho_K\cdot E_K}\right.$$

$$\left.\cdot\frac{-2\cdot\left(M_F-M'_F+n\cdot M_A-M'_E\right)\cdot\rho_K\cdot E_K}{\rho_S^2\cdot D_S^2\cdot\left(\frac{\Delta M_{K1}}{D_{K1}^2}+\frac{\Delta M_{K2}}{D_{K2}^2}\right)}\cdot\delta\rho_S\right]^2 \quad \text{(Eq. B-31)}$$

$$=\left(\frac{-\delta\rho_S}{\rho_S}\right)^2$$

Term six: $x_6 = D_S$

$$\left(\frac{1}{E_2}\cdot\frac{\partial E_2}{\partial D_S}\cdot\delta D_S\right)^2 = \left[\frac{\rho_S\cdot D_S^2\cdot\left(\frac{\Delta M_{K1}}{D_{K1}^2}+\frac{\Delta M_{K2}}{D_{K2}^2}\right)}{2\cdot\left(M_F - M_F' + n\cdot M_A - M_E'\right)\cdot\rho_K\cdot E_K}\right.$$

$$\left.\cdot\frac{-4\cdot\left(M_F - M_F' + n\cdot M_A - M_E'\right)\cdot\rho_K\cdot E_K}{\rho_S\cdot D_S^3\cdot\left(\frac{\Delta M_{K1}}{D_{K1}^2}+\frac{\Delta M_{K2}}{D_{K2}^2}\right)}\cdot\delta D_S\right]^2 \quad \text{(Eq. B-32)}$$

$$= \left(\frac{-2\cdot\delta D_S}{D_S}\right)^2$$

Term seven: $x_7 = \rho_K$

$$\left(\frac{1}{E_2}\cdot\frac{\partial E_2}{\partial \rho_K}\cdot\delta\rho_K\right)^2$$

$$= \left[\frac{\rho_S\cdot D_S^2\cdot\left(\frac{\Delta M_{K1}}{D_{K1}^2}+\frac{\Delta M_{K2}}{D_{K2}^2}\right)}{2\cdot\left(M_F - M_F' + n\cdot M_A - M_E'\right)\cdot\rho_K\cdot E_K}\cdot\frac{2\cdot\left(M_F - M_F' + n\cdot M_A - M_E'\right)\cdot E_K}{\rho_S\cdot D_S^2\cdot\left(\frac{\Delta M_{K1}}{D_{K1}^2}+\frac{\Delta M_{K2}}{D_{K2}^2}\right)}\cdot\delta\rho_K\right]^2 \quad \text{(Eq. B-33)}$$

$$= \left(\frac{\delta\rho_K}{\rho_K}\right)^2$$

Term eight: $x_8 = E_K$

$$\left(\frac{1}{E_2}\cdot\frac{\partial E_2}{\partial E_K}\cdot\delta E_K\right)^2$$

$$= \left[\frac{\rho_S\cdot D_S^2\cdot\left(\frac{\Delta M_{K1}}{D_{K1}^2}+\frac{\Delta M_{K2}}{D_{K2}^2}\right)}{2\cdot\left(M_F - M_F' + n\cdot M_A - M_E'\right)\cdot\rho_K\cdot E_K}\cdot\frac{2\cdot\left(M_F - M_F' + n\cdot M_A - M_E'\right)\cdot\rho_K}{\rho_S\cdot D_S^2\cdot\left(\frac{\Delta M_{K1}}{D_{K1}^2}+\frac{\Delta M_{K2}}{D_{K2}^2}\right)}\cdot\delta E_K\right]^2 \quad \text{(Eq. B-34)}$$

$$= \left(\frac{\delta E_K}{E_K}\right)^2$$

Term nine: $x_9 = \Delta M_{K1}$

$$\left(\frac{1}{E_2}\cdot\frac{\partial E_2}{\partial \Delta M_{K1}}\cdot\delta\Delta M_{K1}\right)^2 = \left[\frac{\rho_S\cdot D_S^2\cdot\left(\frac{\Delta M_{K1}}{D_{K1}^2}+\frac{\Delta M_{K2}}{D_{K2}^2}\right)}{2\cdot\left(M_F - M_F' + n\cdot M_A - M_E'\right)\cdot\rho_K\cdot E_K}\right.$$

$$\left.\cdot\frac{-2\cdot\left(M_F - M_F' + n\cdot M_A - M_E'\right)\cdot\rho_K\cdot E_K}{\rho_S\cdot D_S^2\cdot\left(\frac{\Delta M_{K1}}{D_{K1}^2}+\frac{\Delta M_{K2}}{D_{K2}^2}\right)\cdot D_{K1}^2}\cdot\delta\Delta M_{K1}\right]^2 \quad \text{(Eq. B-35)}$$

$$= \left(\frac{-\delta\Delta M_{K1}}{D_{K1}^2\cdot R}\right)^2$$

Term ten: $x_{10} = \Delta M_{K2}$

$$\left(\frac{1}{E_2}\cdot\frac{\partial E_2}{\partial \Delta M_{K2}}\cdot\delta\Delta M_{K2}\right)^2 = \left[\frac{\rho_S\cdot D_S^2\cdot\left(\frac{\Delta M_{K1}}{D_{K1}^2}+\frac{\Delta M_{K2}}{D_{K2}^2}\right)}{2\cdot\left(M_F - M_F' + n\cdot M_A - M_E'\right)\cdot\rho_K\cdot E_K}\right.$$

$$\left.\cdot\frac{-2\cdot\left(M_F - M_F' + n\cdot M_A - M_E'\right)\cdot\rho_K\cdot E_K}{\rho_S\cdot D_S^2\cdot\left(\frac{\Delta M_{K1}}{D_{K1}^2}+\frac{\Delta M_{K2}}{D_{K2}^2}\right)\cdot D_{K2}^2}\cdot\delta\Delta M_{K2}\right]^2 \quad \text{(Eq. B-36)}$$

$$= \left(\frac{-\delta\Delta M_{K2}}{D_{K2}^2\cdot R}\right)^2$$

Term eleven: $x_{11} = D_{K1}$

$$\left(\frac{1}{E_2}\cdot\frac{\partial E_2}{\partial D_{K1}}\cdot\delta D_{K1}\right)^2 = \left[\frac{\rho_S\cdot D_S^2\cdot\left(\frac{\Delta M_{K1}}{D_{K1}^2}+\frac{\Delta M_{K2}}{D_{K2}^2}\right)}{2\cdot\left(M_F - M'_F + n\cdot M_A - M'_E\right)\cdot\rho_K\cdot E_K}\right.$$

$$\left.\cdot\frac{-4\cdot\left(M_F - M'_F + n\cdot M_A - M'_E\right)\cdot\Delta M_{K1}\cdot\rho_K\cdot E_K}{\rho_S\cdot D_S^2\cdot\left(\frac{\Delta M_{K1}}{D_{K1}^2}+\frac{\Delta M_{K2}}{D_{K2}^2}\right)^2\cdot D_{K1}^3}\cdot\delta D_{K1}\right]^2 \quad \text{(Eq. B-37)}$$

$$= \left(\frac{-2\cdot\Delta M_{K1}\cdot\delta D_{K1}}{D_{K1}^3\cdot R}\right)^2$$

Term twelve: $x_{12} = D_{K2}$

$$\left(\frac{1}{E_2}\cdot\frac{\partial E_2}{\partial D_{K2}}\cdot\delta D_{K2}\right)^2 = \left[\frac{\rho_S\cdot D_S^2\cdot\left(\frac{\Delta M_{K1}}{D_{K1}^2}+\frac{\Delta M_{K2}}{D_{K2}^2}\right)}{2\cdot\left(M_F - M'_F + n\cdot M_A - M'_E\right)\cdot\rho_K\cdot E_K}\right.$$

$$\left.\cdot\frac{-4\cdot\left(M_F - M'_F + n\cdot M_A - M'_E\right)\cdot\Delta M_{K2}\cdot\rho_K\cdot E_K}{\rho_S\cdot D_S^2\cdot\left(\frac{\Delta M_{K1}}{D_{K1}^2}+\frac{\Delta M_{K2}}{D_{K2}^2}\right)^2\cdot D_{K2}^3}\cdot\delta D_{K2}\right]^2 \quad \text{(Eq. B-38)}$$

$$= \left(\frac{-2\cdot\Delta M_{K2}\cdot\delta D_{K2}}{D_{K2}^3\cdot R}\right)^2$$

Therefore, the equation for fractional uncertainty in erosion yield for Situation 2 is:

$$\frac{\delta E_2}{E_2} = \left[\left(\frac{\delta M_F}{\Delta M_2} \right)^2 + \left(\frac{\delta M'_F}{\Delta M_2} \right)^2 + \left(\frac{\frac{n}{N} \cdot \sqrt{(\delta M_F)^2 + (\delta M_C)^2}}{\Delta M_2} \right)^2 + \left(\frac{\delta M'_E}{\Delta M_2} \right)^2 + \left(\frac{\delta \rho_S}{\rho_S} \right)^2 + \left(\frac{2 \cdot \delta D_S}{D_S} \right)^2 + \left(\frac{\delta \rho_K}{\rho_K} \right)^2 + \left(\frac{\delta E_K}{E_K} \right)^2 + \left(\frac{\delta \Delta M_{K1}}{D_{K1}^2 \cdot R} \right)^2 + \left(\frac{\delta \Delta M_{K2}}{D_{K2}^2 \cdot R} \right)^2 + \left(\frac{2 \cdot \Delta M_{K1} \cdot \delta D_{K1}}{D_{K1}^3 \cdot R} \right)^2 + \left(\frac{2 \cdot \Delta M_{K2} \cdot \delta D_{K2}}{D_{K2}^3 \cdot R} \right)^2 \right]^{1/2} \quad \text{(Eq. B-39)}$$

Table 19, Situation 2 Fractional Uncertainty in Erosion Yield, shows the mass loss, density, and exposed diameter values; the corresponding uncertainty values; and the calculated fractional uncertainty values for each polymer in Situation 2.

Table 19—Situation 2 Fractional Uncertainty in Erosion Yield

Material Abbreviation	δM_F (g)	δM_C (g)	n	N	$\delta M'_F$ (g)	$\delta M'_E$ (g)	ΔM (g)	ρ (g/cm^3)	$\delta\rho$ (g/cm^3)	D (cm)	δD (cm)	$\delta E/E$
CA	0.000790	0.000433	6	14	0.000098	0.000069	0.191482	1.2911	0.0025	2.1059	0.0060	0.026573
ETFE	0.000003	0.000002	1	2	0.000003	0.000005	0.049108	1.7397	0.0029	2.1066	0.0022	0.025598
PA 66	0.000088	0.000034	3	8	0.000007	0.000019	0.065562	1.2252	0.1509	2.1185	0.0051	0.125851
PBI	0.000156	0.000141	2	4	0.000040	0.000029	0.082708	1.2758	0.0036	2.1038	0.0056	0.026275
PBO	0.000062	0.000000	5	13	0.000001	0.000004	0.056778	1.3976	0.0752	2.1268	0.0031	0.059587
PC	0.000020	0.000110	1	2	0.000002	0.000012	0.142287	1.1231	0.0079	2.1113	0.0028	0.026545
PE	0.000018	0.000004	2	8	0.000010	0.000013	0.102760	0.9180	0.0007	2.1257	0.0029	0.025620
PEEK	0.000117	0.000026	3	6	0.000001	0.000013	0.107764	1.2259	0.0457	2.1056	0.0054	0.045436
PEI	0.000018	0.000018	1	2	0.000003	0.000009	0.126853	1.2873	0.0036	2.1216	0.0053	0.026088
PI (Kapton® HN)	0.000052	0.000035	1	4	0.000010	0.000012	0.121315	1.4345	0.0020	2.1313	0.0038	0.025748
PPPA	0.000162	0.000188	3	6	0.000060	0.000102	0.030549	0.7200	0.0074	2.1298	0.0055	0.028987
PSU	0.000035	0.000032	3	6	0.000012	0.000015	0.105948	1.2199	0.0221	2.1113	0.0054	0.031645
PVDF	0.000005	0.000007	1	2	0.000006	0.000001	0.066860	1.7623	0.0086	2.1108	0.0061	0.026549
PVF	0.000011	0.000011	6	13	0.000013	0.000010	0.132537	1.3792	0.0013	2.1331	0.0028	0.025612

B.7.3 Fractional Uncertainty Equation Derivations for Situation 3

Using Eq. B-14, the equation for Situation 3 erosion yield, the equation for fractional uncertainty in erosion yield for Situation 3 $\left(\frac{\delta E_3}{E_3} \right)$ is derived as described below. Eq. B-26b will be used to substitute for δM_A in term 2 of the final equation.

Term one: $x_1 = M_F$

$$\left(\frac{1}{E_3}\cdot\frac{\partial E_3}{\partial M_F}\cdot\delta M_F\right)^2 = \left[\frac{\rho_S\cdot D_S^2\cdot\left(\frac{\Delta M_{K1}}{D_{K1}^2}+\frac{\Delta M_{K2}}{D_{K2}^2}\right)}{2\cdot\left(M_F+n\cdot M_A-M_S'\right)\cdot\rho_K\cdot E_K}\cdot\frac{2\cdot\rho_K\cdot E_K}{\rho_S\cdot D_S^2\cdot\left(\frac{\Delta M_{K1}}{D_{K1}^2}+\frac{\Delta M_{K2}}{D_{K2}^2}\right)}\cdot\delta M_F\right]^2 \quad \text{(Eq. B-40)}$$

$$= \left(\frac{\delta M_F}{\Delta M_3}\right)^2$$

Term two: $x_2 = M_A$

$$\left(\frac{1}{E_3}\cdot\frac{\partial E_3}{\partial M_A}\cdot\delta M_A\right)^2$$

$$= \left[\frac{\rho_S\cdot D_S^2\cdot\left(\frac{\Delta M_{K1}}{D_{K1}^2}+\frac{\Delta M_{K2}}{D_{K2}^2}\right)}{2\cdot\left(M_F+n\cdot M_A-M_S'\right)\cdot\rho_K\cdot E_K}\cdot\frac{2n\cdot\rho_K\cdot E_K}{\rho_S\cdot D_S^2\cdot\left(\frac{\Delta M_{K1}}{D_{K1}^2}+\frac{\Delta M_{K2}}{D_{K2}^2}\right)}\cdot\delta M_A\right]^2 \quad \text{(Eq. B-41)}$$

$$= \left(\frac{n\cdot\delta M_A}{\Delta M_3}\right)^2$$

Term three: $x_3 = M_S'$

$$\left(\frac{1}{E_3}\cdot\frac{\partial E_3}{\partial M_S}\cdot\delta M_S'\right)^2$$

$$= \left[\frac{\rho_S\cdot D_S^2\cdot\left(\frac{\Delta M_{K1}}{D_{K1}^2}+\frac{\Delta M_{K2}}{D_{K2}^2}\right)}{2\cdot\left(M_F+n\cdot M_A-M_S'\right)\cdot\rho_K\cdot E_K}\cdot\frac{-2\cdot\rho_K\cdot E_K}{\rho_S^2\cdot D_S^2\cdot\left(\frac{\Delta M_{K1}}{D_{K1}^2}+\frac{\Delta M_{K2}}{D_{K2}^2}\right)}\cdot\delta M_S'\right]^2 \quad \text{(Eq. B-42)}$$

$$= \left(\frac{-\delta M_S'}{\Delta M_3}\right)^2$$

Term four: $x_4 = \rho_S$

$$\left(\frac{1}{E_3}\cdot\frac{\partial E_3}{\partial \rho_S}\cdot\delta\rho_S\right)^2$$

$$=\left[\frac{\rho_S\cdot D_S^2\cdot\left(\frac{\Delta M_{K1}}{D_{K1}^2}+\frac{\Delta M_{K2}}{D_{K2}^2}\right)}{2\cdot\left(M_F+n\cdot M_A-M_S'\right)\cdot\rho_K\cdot E_K}\cdot\frac{-2\cdot\left(M_F+n\cdot M_A-M_S'\right)\cdot\rho_K\cdot E_K}{\rho_S^2\cdot D_S^2\cdot\left(\frac{\Delta M_{K1}}{D_{K1}^2}+\frac{\Delta M_{K2}}{D_{K2}^2}\right)}\cdot\delta\rho_S\right]^2 \quad \text{(Eq. B-43)}$$

$$=\left(\frac{-\delta\rho_S}{\rho_S}\right)^2$$

Term five: $x_5 = D_S$

$$\left(\frac{1}{E_3}\cdot\frac{\partial E_3}{\partial D_S}\cdot\delta D_S\right)^2$$

$$=\left[\frac{\rho_s\cdot D_S^2\cdot\left(\frac{\Delta M_{K1}}{D_{K1}^2}+\frac{\Delta M_{K2}}{D_{K2}^2}\right)}{2\cdot\left(M_F+n\cdot M_A-M_S'\right)\cdot\rho_K\cdot E_K}\cdot\frac{-4\cdot\left(M_F+n\cdot M_A-M_S'\right)\cdot\rho_K\cdot E_K}{\rho_S\cdot D_S^3\cdot\left(\frac{\Delta M_{K1}}{D_{K1}^2}+\frac{\Delta M_{K2}}{D_{K2}^2}\right)}\cdot\delta D_S\right]^2 \quad \text{(Eq. B-44)}$$

$$=\left(\frac{-2\cdot\delta D_S}{D_S}\right)^2$$

Term six: $x_6 = \rho_K$

$$\left(\frac{1}{E_3}\cdot\frac{\partial E_3}{\partial \rho_K}\cdot\delta\rho_K\right)^2$$

$$=\left[\frac{\rho_S\cdot D_S^2\cdot\left(\frac{\Delta M_{K1}}{D_{K1}^2}+\frac{\Delta M_{K2}}{D_{K2}^2}\right)}{2\cdot\left(M_F+n\cdot M_A-M_S'\right)\cdot\rho_K\cdot E_K}\cdot\frac{2\cdot\left(M_F+n\cdot M_A-M_S'\right)\cdot E_K}{\rho_S\cdot D_S^2\cdot\left(\frac{\Delta M_{K1}}{D_{K1}^2}+\frac{\Delta M_{K2}}{D_{K2}^2}\right)}\cdot\delta\rho_K\right]^2 \quad \text{(Eq. B-45)}$$

$$=\left(\frac{\delta\rho_K}{\rho_K}\right)^2$$

Term seven: $x_7 = E_K$

$$\left(\frac{1}{E_3}\cdot\frac{\partial E_3}{\partial E_K}\cdot\delta E_K\right)^2$$

$$=\left[\frac{\rho_S\cdot D_S^2\cdot\left(\frac{\Delta M_{K1}}{D_{K1}^2}+\frac{\Delta M_{K2}}{D_{K2}^2}\right)}{2\cdot\left(M_F+n\cdot M_A-M_S'\right)\cdot\rho_K\cdot E_K}\cdot\frac{2\cdot\left(M_F+n\cdot M_A-M_S'\right)\cdot\rho_K}{\rho_S\cdot D_S^2\cdot\left(\frac{\Delta M_{K1}}{D_{K1}^2}+\frac{\Delta M_{K2}}{D_{K2}^2}\right)}\cdot\delta E_K\right]^2 \quad \text{(Eq. B-46)}$$

$$=\left(\frac{\delta E_K}{E_K}\right)^2$$

Term eight: $x_8 = \Delta M_{K1}$

$$\left(\frac{1}{E_3}\cdot\frac{\partial E_1}{\partial \Delta M_{K1}}\cdot\delta\Delta M_{K1}\right)^2$$

$$=\left[\frac{\rho_s\cdot D_S^2\cdot\left(\frac{\Delta M_{K1}}{D_{K1}^2}+\frac{\Delta M_{K2}}{D_{K2}^2}\right)}{2\cdot\left(M_F+n\cdot M_A-M_S'\right)\cdot\rho_K\cdot E_K}\cdot\frac{-2\cdot\left(M_F+n\cdot M_A-M_S'\right)\cdot\rho_K\cdot E_K}{\rho_S\cdot D_S^2\cdot\left(\frac{\Delta M_{K1}}{D_{K1}^2}+\frac{\Delta M_{K2}}{D_{K2}^2}\right)\cdot D_{K1}^2}\cdot\delta\Delta M_{K1}\right]^2 \quad \text{(Eq. B-47)}$$

$$=\left(\frac{-\delta\Delta M_{K1}}{D_{K1}^2\cdot R}\right)^2$$

Term nine: $x_9 = \Delta M_{K2}$

$$\left(\frac{1}{E_3}\cdot\frac{\partial E_3}{\partial \Delta M_{K2}}\cdot\delta\Delta M_{K2}\right)^2$$

$$=\left[\frac{\rho_s\cdot D_S^2\cdot\left(\frac{\Delta M_{K1}}{D_{K1}^2}+\frac{\Delta M_{K2}}{D_{K2}^2}\right)}{2\cdot\left(M_F+n\cdot M_A-M_S'\right)\cdot\rho_K\cdot E_K}\cdot\frac{-2\cdot\left(M_F+n\cdot M_A-M_S'\right)\cdot\rho_K\cdot E_K}{\rho_S\cdot D_S^2\cdot\left(\frac{\Delta M_{K1}}{D_{K1}^2}+\frac{\Delta M_{K2}}{D_{K2}^2}\right)^2\cdot D_{K2}^2}\cdot\delta\Delta M_{K2}\right]^2 \quad \text{(Eq. B-48)}$$

$$=\left(\frac{-\delta\Delta M_{K2}}{D_{K2}^2\cdot R}\right)^2$$

Term ten: $x_{10} = D_{K1}$

$$\left(\frac{1}{E_3}\cdot\frac{\partial E_3}{\partial D_{K1}}\cdot\delta D_{K1}\right)^2 = \left[\frac{\rho_S\cdot D_S^2\cdot\left(\frac{\Delta M_{K1}}{D_{K1}^2}+\frac{\Delta M_{K2}}{D_{K2}^2}\right)}{2\cdot\left(M_F+n\cdot M_A-M_S'\right)\cdot\rho_K\cdot E_K}\right.$$

$$\left.\cdot\frac{-4\cdot\left(M_F+n\cdot M_A-M_S'\right)\cdot\Delta M_{K1}\cdot\rho_K\cdot E_K}{\rho_S\cdot D_S^2\cdot\left(\frac{\Delta M_{K1}}{D_{K1}^2}+\frac{\Delta M_{K2}}{D_{K2}^2}\right)^2\cdot D_{K1}^3}\cdot\delta D_{K1}\right]^2 \qquad \text{(Eq. B-49)}$$

$$=\left(\frac{-2\cdot\Delta M_{K1}\cdot\delta D_{K1}}{D_{K1}^3\cdot R}\right)^2$$

Term eleven: $x_{11} = D_{K2}$

$$\left(\frac{1}{E_3}\cdot\frac{\partial E_3}{\partial D_{K2}}\cdot\delta D_{K2}\right)^2 = \left[\frac{\rho_S\cdot D_S^2\cdot\left(\frac{\Delta M_{K1}}{D_{K1}^2}+\frac{\Delta M_{K2}}{D_{K2}^2}\right)}{2\cdot\left(M_F+n\cdot M_A-M_S'\right)\cdot\rho_K\cdot E_K}\right.$$

$$\left.\cdot\frac{-4\cdot\left(M_F+n\cdot M_A-M_S'\right)\cdot\Delta M_{K2}\cdot\rho_K\cdot E_K}{\rho_S\cdot D_S^2\cdot\left(\frac{\Delta M_{K1}}{D_{K1}^2}+\frac{\Delta M_{K2}}{D_{K2}^2}\right)^2\cdot D_{K2}^3}\cdot\delta D_{K2}\right]^2 \qquad \text{(Eq. B-50)}$$

$$=\left(\frac{-2\cdot\Delta M_{K2}\cdot\delta D_{K2}}{D_{K2}^3\cdot R}\right)^2$$

Therefore, the equation for fractional uncertainty in erosion yield for Situation 3 is:

$$\frac{\delta E_3}{E_3} = \left[\left(\frac{\delta M_F}{\Delta M_3} \right)^2 + \left(\frac{\frac{n}{N} \cdot \sqrt{(\delta M_F)^2 + (\delta M_C)^2}}{\Delta M_3} \right)^2 + \left(\frac{-\delta M'_S}{\Delta M_3} \right)^2 + \left(\frac{\delta \rho_S}{\rho_S} \right)^2 + \left(\frac{2 \cdot \delta D_S}{D_S} \right)^2 + \left(\frac{\delta \rho_K}{\rho_K} \right)^2 + \left(\frac{\delta E_K}{E_K} \right)^2 + \left(\frac{\delta \Delta M_{K1}}{D_{K1}^2 \cdot R} \right)^2 + \left(\frac{\delta \Delta M_{K2}}{D_{K2}^2 \cdot R} \right)^2 + \left(\frac{2 \cdot \Delta M_{K1} \cdot \delta D_{K1}}{D_{K1}^3 \cdot R} \right)^2 + \left(\frac{2 \cdot \Delta M_{K2} \cdot \delta D_{K2}}{D_{K2}^3 \cdot R} \right)^2 \right]^{1/2} \quad \text{(Eq. B-51)}$$

Table 20, Situation 3 Fractional Uncertainty in Erosion Yield, shows the mass loss, density, and exposed diameter values; the corresponding uncertainty values; and the calculated fractional uncertainty values for each polymer in Situation 3.

Table 20—Situation 3 Fractional Uncertainty in Erosion Yield

Material Abbreviation	δM_F (g)	δM_C (g)	n	N	$\delta M'_S$ (g)	ΔM (g)	ρ (g/cm^3)	$\delta\rho$ (g/cm^3)	D (cm)	δD (cm)	$\delta E/E$
ECTFE	0.000008	0.000004	1	4	0.000012	0.088869	1.6761	0.0059	2.1141	0.0027	0.025821
PA 6	0.000088	0.000112	4	8	0.000055	0.118376	1.1233	0.0079	2.1304	0.0033	0.026617
PBT	0.000027	0.000017	2	6	0.000049	0.036429	1.3318	0.0040	2.1296	0.0026	0.025798
PET	0.000160	0.000010	4	8	0.000033	0.125187	1.3925	0.0029	2.1240	0.0058	0.026157
PI (CP1)	0.000038	0.000038	2	4	0.000025	0.080648	1.4193	0.0167	2.1205	0.0030	0.028199
PMMA	0.000495	0.000126	5	10	0.000017	0.194588	1.1628	0.0028	2.1247	0.0034	0.025932
PU	0.000051	0.000040	4	10	0.000042	0.057227	1.2345	0.0174	2.1165	0.0039	0.029353

B.8 Results and Discussion

The MISSE 2 PEACE Polymers LEO atomic oxygen erosion yield data (de Groh et al., 2006, ESA; de Groh et al., 2006, NSMMS; de Groh et al., 2008, HPP) are given in table 21, MISSE 2 PEACE Polymers Experiment Fractional Uncertainty Data Summary. These results represent the widest variety of extremely accurately measured high atomic oxygen fluence data to date.

Table 21—MISSE 2 PEACE Polymers Experiment Fractional Uncertainty Data Summary

Material	Abbreviation	Trade Name(s)	Fractional Uncertainty in Erosion Yield	Uncertainty in Erosion Yield (cm^3/atom)	Erosion Yield (cm^3/atom)*
Acrylonitrile butadiene styrene	ABS	Cycolac®, Absylux®, Lustran®	0.027017	2.96 E–26	1.09 (±0.03) E–24
Allyl diglycol carbonate	ADC	CR-39, Homalite™ H-911	0.025824	1.76 E–25	>6.80 E–24
Amorphous fluoropolymer	AF	Teflon® AF 1601	0.025975	5.13 E–27	1.98 (±0.05) E–25
Cellulose acetate	CA	Cellidor®, Tenite™ Acetate, Dexel	0.026573	1.34 E–25	5.05 (±0.13) E–24
Chlorotrifluoroethylene	CTFE	Kel-F®, Neoflon® M-300,	0.025927	2.15 E–26	8.31 (±0.22) E–25
Crystalline polyvinylfluoride with white pigment	PVF	White Tedlar® TWH10BS3	0.041361	4.17 E–27	1.01 (±0.04) E–25
Epoxide or epoxy	EP	Hysol® EA 956	0.027020	1.14 E–25	4.21 (±0.11) E–24
Ethylene-chlorotrifluoroethylene	ECTFE	Halar® 300	0.025821	4.63 E–26	1.79 (±0.05) E–24
Ethylene-tetrafluoroethylene	ETFE	Tefzel® ZM	0.025598	2.46 E–26	9.61 (±0.25) E–25
Fluorinated ethylene propylene	FEP	Teflon® FEP 200A	0.026890	5.39 E–27	2.00 (±0.05) E–25
High-temperature polyimide resin	PI	PMR-15	0.025696	7.77 E–26	>3.02 E–24
Perfluoroalkoxy copolymer resin	PFA	Teflon® PFA 200 CLP	0.027248	4.72 E–27	1.73 (±0.05) E–25
Poly-(p-phenylene terephthalamide)	PPD-T	Kevlar® 29, fabric	0.026193	1.64 E–26	6.28 (±0.16) E–25
Poly(p-phenylene-2,6-benzobisoxazole)	PBO	Zylon® (balanced biaxial film)	0.059587	8.08 E–26	1.36 (±0.08) E–24
Polyacrylonitrile	PAN	Barex® 210	0.032801	4.63 E–26	1.41 (±0.05) E–24
Polyamide 6	PA 6	Nylon 6,Akulon® K, Ultramid® B	0.026617	9.33 E–26	3.51 (±0.09) E–24
Polyamide 66	PA 66	Nylon 6 6, Maranyl™ A, Zytel®	0.125851	2.27 E–25	1.80(±0.23) E–24
Polybenzimidazole	PBI	Celazole™ PBI 22	0.026275	5.81 E–26	>2.21 E–24
Polybutylene terephthalate	PBT	VALOX® 357	0.025798	2.35 E–26	9.11 (±0.24) E–25
Polycarbonate	PC	PEEREX® 61	0.026545	1.14 E–25	4.29 (±0.11) E–24
Polyetheretherketone	PEEK	Vitrex® PEEK™ 450	0.045436	1.36 E–25	2.99 (±0.14) E–24

Material	Abbreviation	Trade Name(s)	Fractional Uncertainty in Erosion Yield	Uncertainty in Erosion Yield (cm^3/atom)	Erosion Yield (cm^3/atom)*
Polyetherimide	PEI	Ultem® 1000	0.026088	8.63 E–26	>3.31 E–24
Polyethylene	PE	-	0.025620	9.59 E–26	>3.74 E–24
Polyethylene oxide	PEO	Alkox® E-30 (powder)	0.025948	5.01 E–26	1.93 (±0.05) E–24
Polyethylene terephthalate	PET	Mylar® A-200	0.026157	7.87 E–26	3.01 (±0.08) E–24
Polyimide	PI	LaRC CP1 (CP1-300)	0.028199	5.38 E–26	1.91 (±0.05) E–24
Polyimide (BPDA)	PI	Upilex-S®	0.030056	2.77 E–26	9.22 (±0.28) E–25
Polyimide (PMDA)	PI	Kapton® H	0.024700	7.41 E–26	3.00 (±0.07) E–24
Polyimide (PMDA)	PI	Kapton® H	0.024700	7.41 E–26	3.00 (±0.07) E–24
Polyimide (PMDA)	PI	Kapton® HN	0.025748	7.24 E–26	2.81 (±0.07) E–24
Polymethyl methacrylate	PMMA	Plexiglas®, Acrylite® (Impact Modified)	0.025932	1.45 E–25	>5.60 E–24
Polyoxymethylene; acetal; polyformaldehyde	POM	Delrin® Acetal (natural)	0.030556	2.79 E–25	9.14 (±0.28) E–24
Polyphenylene isophthalate	PPPA	Nomex® Crepe Paper T-410	0.028987	4.10 E–26	1.41 (±0.04) E–24
Polypropylene	PP	Contour 28, GOEX	0.026127	7.00 E–26	2.68 (±0.07) E–24
Polystyrene	PS	Trycite® 1000	0.026884	1.00 E–25	3.74 (±0.10) E–24
Polysulfone	PSU	Thermalux® P1700-NT11, Udel® P-1700	0.031645	9.31 E–26	2.94 (±0.09) E–24
Polytetrafluoroethylene	PTFE	Chemfilm® DF 100	0.026089	3.69 E–27	1.42 (±0.04) E–25
Polyurethane	PU	Dureflex® PS 8010	0.029353	4.59 E–26	1.56 (±0.05) E–24
Polyvinylfluoride	PVF	Tedlar® TTR10SG3 (clear)	0.025612	8.17 E–26	3.19 (±0.08) E–24
Polyvinylidene fluoride	PVDF	Kynar® 740	0.026549	3.41 E–26	1.29 (±0.03) E–24
Pyrolytic graphite	PG	Pyrolytic graphite	0.107496	4.46 E–26	4.15 (±0.45) E–25

*Darker blue cells indicate calculated erosion yields are less than the actual erosion yields. See following paragraph for details.

Including enough material for each flight sample to theoretically last for 3 years was crucial to the experiment's success: although the experiment received nearly 4 years of atomic oxygen exposure, only one polymer (PBI) was completely eroded away. However, for five other samples (PE, ADC, PMMA, polyetherimide (PEI), and PMR-15), atomic oxygen did, in some places, erode through all layers. For these six samples, therefore, the calculated erosion yields are less than the actual erosion yields, because the mass loss would have been greater had there had been more material. These six erosion yield values are highlighted in table 21. Since the samples in these cases appeared to have eroded partially or completely through at a fluence level close to the full mission fluence, the measured erosion yields of these samples were still included in the data set as estimates to develop a predictive erosion yield equation (Banks et al., 2009). These samples have been reflown in LEO for actual erosion yield determination as part of the Stressed PEACE Polymers experiment on MISSE 6 (de Groh et al., 2008, JAXA).

Table 21 also includes the uncertainty and fractional uncertainty in erosion yield values for each of the MISSE 2 PEACE Polymers samples (McCarthy et al., 2010). The highest fractional uncertainty was for PA 66 (±12.59 percent), and the lowest fractional uncertainty was for ethylene-tetrafluoroethylene (ETFE) (±2.56 percent). The average fractional uncertainty in erosion yield was very small: ±3.30 percent.

B.9 References

B.9.1 Non-Government Documents

ASTM International

ASTM E 2089-00 Standard Practices for Ground Laboratory Atomic Oxygen Interaction Evaluation of Materials for Space Applications

B.9.2 Additional References

Banks, B.A., Backus, J.A., Manno, M.V., Waters, D.L., Cameron, K.C., de Groh, K.K. (September 15-18, 2009). "Atomic Oxygen Erosion Yield Prediction for Spacecraft Polymers in Low Earth Orbit." *Proceedings of the International Symposium on Materials in a Space Environment (ISMSE-11), September 15-18, 2009*. Aix-en-Provence, France. Also published as NASA TM-2009-215812.

de Groh, K.K.; Banks, B.A.; Dever, J.A.; Jaworske, D.J.; Miller, S.K.; Sechkar, E.A.; Panko, S.R. (March 10-11, 2008). "NASA Glenn Research Center's Materials International Space Station Experiments (MISSE 1-7)." *Proceedings of the International Symposium on "SM/MPAC&SEED Experiment."* JAXA-SP-08-015E. pp. 91–119. Tsukuba, Japan. Also published as NASA/TM—2008-215482.

de Groh, K.K.; Banks, B.A.; McCarthy, C.E.; Berger, L.A.; Roberts, L.M. (June 19-23, 2006). "Analysis of the MISSE PEACE Polymers International Space Station Environmental Exposure Experiment." *Proceedings of the 10th ISMSE, 8th ICPMSE: June 19-23, 2006*. Collioure, France. ESA SP-616.

de Groh, K.K.; Banks, B.A.; McCarthy, C.E.; Rucker, R.N.; Roberts, L.M.; Berger, L.A. (June 26 - 30, 2006). "MISSE PEACE Polymers Atomic Oxygen Erosion Results." *Proceedings of the 2006 National Space & Missile Materials Symposium*. Orlando, FL. Also published as NASA/TM—2006-214482.

de Groh, K.K.; Banks, B.A.; McCarthy, C.E.; Rucker, R.N.; Roberts, L.M.; Berger, L.A. (2008). "MISSE 2 PEACE Polymers Atomic Oxygen Erosion Experiment on the International Space Station." *High Performance Polymers.* Vol. 20, no. 4/5, pp. 388-409.

McCarthy, C.E.; Banks, B.A.; de Groh, K.K. (November 2010). *MISSE 2 PEACE*

Polymers Experiment Atomic Oxygen Erosion Yield Error Analysis. NASA/TM—2010-216903. NASA GRC: Cleveland, OH.

APPENDIX C

MISSE 2 PEACE POLYMERS OPTICAL AND THERMAL DATA

C.1 Purpose and/or Scope

The purpose of this appendix is to provide details on the optical and thermal properties of the MISSE 2 PEACE Polymers experiment after 4 years of space exposure, as documented in Waters et al., (2009).

C.2 Introduction

Because atomic oxygen and other hazards in the space environment can result in serious optical and thermal property degradation of spacecraft materials, changes in the optical and thermal properties of the MISSE 2 PEACE Polymers samples as a result of LEO exposure have been analyzed and compared with control samples to determine the extent of change on orbit.

Total and diffuse reflectance and total and diffuse transmittance were measured as a function of wavelength and were compared with the corresponding values of non-exposed control samples. Specular reflectance and specular transmittance were then computed. Thermal emittance data were also generated. The wavelength-dependent data also allow for computation of the change in solar absorptance and in thermal emittance, both of which are critical for predicting thermal-control characteristics of a spacecraft.

C.3 Procedures

Many of the MISSE PEACE Polymer samples were comprised of several layers so as to survive a 3-year LEO exposure. Because the mission was 3.95 years in duration, many of the polymers were eroded through several layers; several were eroded through all layers in some places; and one sample was completely eroded away. Therefore, it was determined that the best way to measure the optical and thermal properties of the flight samples was to determine which layers of each sample should be measured, based on the erosion pattern, and then to compare the same number of layers of the control flight sample. If a sample was partially eroded, the layer or layers that experienced partial erosion (rather than full erosion, as was the case with the layers above partially eroded layers) along with the intact layer immediately underneath were analyzed, and the control sample included the same number of layers, as shown in figure 56, Schematic Diagram of MISSE 2 Flight Sample Layer Erosion and the Corresponding Control Layers used for Optical and Thermal Property Measurements. If the top layers would be damaged by separation, the sample was left as a whole, and an equal number of control sample layers were used for analysis.

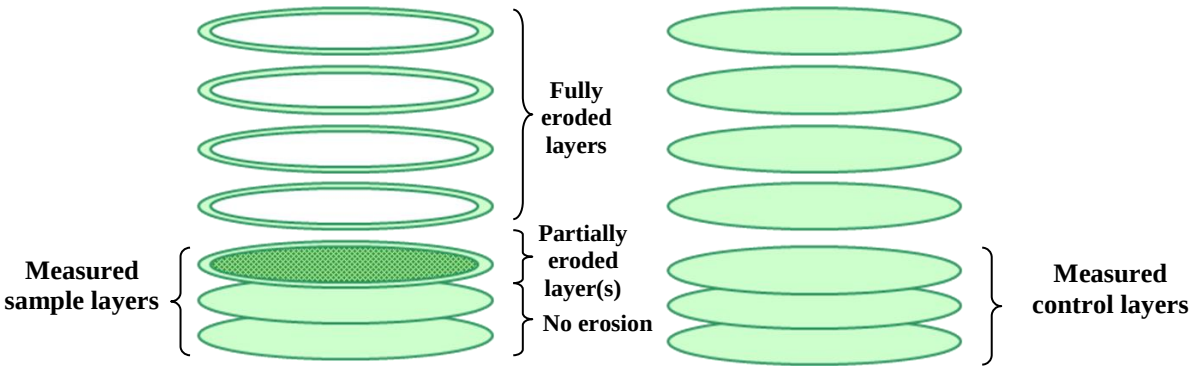

Figure 56—Schematic Diagram of MISSE 2 Flight Sample Layer Erosion and the Corresponding Control Layers used for Optical and Thermal Property Measurements

The samples were loaded into a holder that mimicked the flight hardware mounting plate, which protected them from damage during handling and placement in the optical and thermal equipment. (See figure 57, Sample Holder for Optical and Thermal Measurements.) The front of the sample holder recessed the sample by 0.013 cm, and the back of the holder allowed for a cavity of up to 0.305 cm, depending on sample thickness.

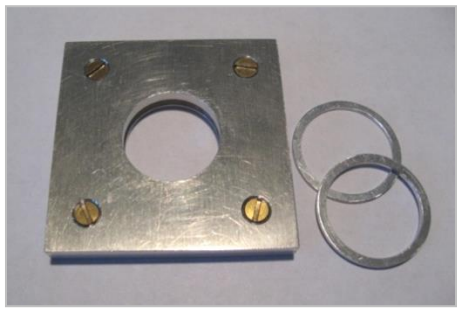

Figure 57—Sample Holder for Optical and Thermal Measurements

C.3.1 Spectrophotometer used for Optical Characterization

A Perkin Elmer Lambda 19 spectrophotometer was used to measure TR, DR, TT, and DT from 250 to 2500 nm. The instrument is equipped with a 15-cm Spectralon integrating sphere, shown in figure 58, Perkin Elmer Lambda 19 Spectrophotometer with Closeup of Integrating Sphere. The SR and ST were calculated using the difference between total and diffuse values. Absorptance data (1 – (reflectance + transmittance)) were integrated with respect to the air mass zero solar spectrum to obtain α_s. A Labsphere-certified Spectralon standard was used for calibration. The beam size was checked for each of the samples to verify that optical alignment was correct.

Figure 58—Perkin Elmer Lambda 19 Spectrophotometer with Closeup of Integrating Sphere

C.3.2 Reflectometer used for Thermal Characterization

The Surface Optics Corporation Model SOC 400T (figure 59, SOC 400T Reflectometer) can accurately measure the TR of surfaces over a large spectral range (2 to 25 μm) to obtain the ε over a large temperature range (–150 to 1,150 °C). The equipment has a sample aperture diameter of 1.27 cm. Automatic integration of infrared reflectivity with respect to blackbody curves is used to calculate total ε for a user-selectable temperature range. Data were obtained at 200 K, 300 K, 400 K, 500 K, and 573 K. The samples were placed in the sample holder shown in figure 57 and were backed by a Gier Dunkle gold standard. The samples had to be placed upside down on the instrument over an aperture opening and so needed to be mechanically stable enough to remain stationary and not fall into the instrument during the 3.5-minute scan. Several samples could not be analyzed because of mechanical instability.

Figure 59—SOC 400T Reflectometer

Before thermal measurement of all of the samples, a test was conducted to evaluate the effect of using the sample holder on the resulting ε value. Pristine Kapton® H (127 μm thick) was first measured directly on the instrument backed with a gold standard and then measured in the sample holder with the gold standard backing the holder. Table 22, Kapton® Thermal Emittance Values with and without a Holder, shows the results of these measurements. There is a slight

increase in ε that is attributable to the sample holder, but the sample holder was needed to minimize sample handling and to best preserve the delicate surface texture of the flight samples. This difference will be more noticeable for transparent thin-film, transparent samples than for thicker or opaque samples. Because of the interference of the sample holder, the thermal ε values were not interpreted as absolute ε values and were used instead as more of a comparison tool.

Table 22—Kapton® Thermal Emittance Values with and without a Holder

Sample	Temperature and Corresponding Thermal Emittance Value (ε)				
	200 K	300 K	400 K	500 K	573 K
Kapton® – No Holder	0.88	0.88	0.88	0.87	0.85
Kapton® – Holder	0.91	0.91	0.91	0.90	0.89

C.4 MISSE 2 PEACE Polymers Optical and Thermal Properties

Because of the unexpectedly long duration of the flight mission (3.95 years rather than the originally planned 1 year), several of the samples were too degraded for optical and thermal properties to be obtained. These included PE (2-E5-9), PMMA (2-E5-16), PA 66 (2-E5-28), PI (CP1, 2-E5-29), PBI (2-E5-35), and PET (2-E5-38). The samples too damaged to be mounted upside down over the aperture opening on SOC 400T included PS (2-E5-15), PBO (2-E5-18), and PPPA (2-E5-24).

Post-retrieval and control optical measurements, including TR, DR, TT, and DT, were taken of the remaining samples and are listed in table 23, Post-Retrieval and Control Optical Properties Integrated from 250 to 2,500 nm. The calculated of the SR, ST, and α_s values are also listed in table 23. The number of layers measured is also shown for each sample. Figure 60, Absorptance, Total Reflectance, Total Transmittance, and Emittance Spectral Data for Flight and Control Samples, provides the spectral data of α_s, TR, and TT for each material and its corresponding control sample.

Table 23—Post-Retrieval and Control Optical Properties Integrated from 250 to 2,500 nm

MISSE 2 Samples (2-E5-XX)	Film Thickness (μm)	# Layers Measured	TR	DR	SR	TT	DT	ST	α_s
-06 ABS Flight	127	2	0.279	0.279	0.000	0.401	0.399	0.001	0.321
-06 ABS Control	127	2	0.258	0.212	0.046	0.538	0.391	0.146	0.204
-07 CA Flight	51	2	0.203	0.148	0.055	0.642	0.236	0.406	0.155
-07 CA Control	51	2	0.140	0.018	0.123	0.789	0.069	0.721	0.070
-08 PPD-T Kevlar® Flight	56	3	0.622	0.621	0.001	N/A	N/A	N/A	0.378
-08 PPD-T Kevlar® Control	56	3	0.609	0.607	0.003	N/A	N/A	N/A	0.391
-10 PVF Tedlar® Flight	51	3	0.197	0.188	0.009	0.701	0.508	0.193	0.102
-10 PVF Tedlar® Control	51	3	0.242	0.155	0.087	0.753	0.295	0.457	0.006
-11 PVF white Tedlar® Flight	25	2	0.732	0.729	0.003	0.045	0.045	0.000	0.223
-11 PVF white Tedlar® Control	25	2	0.813	0.626	0.186	0.047	0.047	0.000	0.140
-12 POM Delrin® Flight	254	1	0.350	0.349	0.001	0.459	0.456	0.002	0.191
-12 POM Delrin® Control	254	1	0.270	0.265	0.005	0.581	0.579	0.003	0.149
-13 PAN Flight	51	4	0.254	0.236	0.018	0.447	0.374	0.073	0.299

-13 PAN Control	51	4	0.251	0.186	0.065	0.696	0.149	0.546	0.053
-14 ADC CR-29 Flight	787	1	0.194	0.186	0.008	0.465	0.460	0.005	0.341
-14 ADC CR-39® Control	787	1	0.119	0.043	0.076	0.829	0.035	0.795	0.052
-15 PS Flight	51	3	0.306	0.256	0.050	0.610	0.359	0.251	0.085
-15 PS Control	51	3	0.254	0.019	0.235	0.720	0.020	0.700	0.026
-17 PEO Flight	~740	1	0.302	0.302	0.001	0.449	0.447	0.003	0.249
-17 PEO Control	~740	1	0.210	0.189	0.021	0.609	0.596	0.013	0.181
-18 PBO Flight	25	3	0.438	0.419	0.019	0.123	0.122	0.001	0.439
-18 PBO Control	25	3	0.530	0.449	0.081	0.104	0.103	0.001	0.366
-19 EP Flight	~2,300	1	0.087	0.084	0.002	0.382	0.381	0.001	0.531
-19 EP Control	~2,300	1	0.094	0.049	0.045	0.641	0.629	0.012	0.265
-20 PP Flight	508	1	0.194	0.193	0.001	0.616	0.613	0.003	0.190
-20 PP Control	508	1	0.089	0.037	0.052	0.866	0.403	0.462	0.045
-21 PBT Flight	76	4	0.649	0.620	0.029	0.150	0.150	0.000	0.201
-21 PBT Control	76	4	0.706	0.669	0.037	0.159	0.160	-0.000	0.135
-22 PSU Flight	51	1	0.107	0.103	0.004	0.746	0.684	0.063	0.147
-22 PSU Control	51	1	0.125	0.063	0.062	0.853	0.454	0.399	0.022
-23 PU Flight	51	7	0.411	0.402	0.009	0.389	0.314	0.075	0.199
-23 PU Control	51	7	0.356	0.278	0.078	0.546	0.467	0.079	0.098
-24 PPPA Nomex® Flight	51	2	0.506	0.497	0.009	0.301	0.290	0.011	0.193
-24 PPPA Nomex® Control	51	2	0.647	0.635	0.012	0.200	0.198	0.002	0.153
-25 PG Flight	2,030	1	0.017	0.014	0.003	N/A	N/A	N/A	0.983
-25 PG Control	2,030	1	0.268	0.253	0.015	N/A	N/A	N/A	0.732
-26 PEI Flight	254	1	0.151	0.152	-0.000	0.625	0.570	0.055	0.224
-26 PEI Control	254	1	0.110	0.080	0.030	0.757	0.267	0.490	0.133
-27 PA 6 Flight	51	2	0.155	0.136	0.020	0.743	0.478	0.265	0.102
-27 PA 6 Control	51	2	0.162	0.115	0.047	0.790	0.365	0.425	0.047
-30 PI Kapton® H Flight	127	2	0.212	0.211	0.001	0.404	0.391	0.013	0.384
-30 PI Kapton® H Control	127	2	0.173	0.043	0.130	0.445	0.030	0.415	0.382
-31 PI Kapton® HN Flight	127	2	0.223	0.223	0.000	0.312	0.302	0.010	0.465
-31 PI Kapton® HN Control	127	2	0.171	0.044	0.127	0.403	0.117	0.286	0.426
-32 PI Upilex-S® Flight	25	2	0.293	0.293	-0.000	0.362	0.338	0.025	0.345
-32 PI Upilex-S® Control	25	2	0.218	0.034	0.184	0.444	0.020	0.424	0.338
-33 PI Kapton® H Flight	127	1	0.078	0.075	0.003	0.515	0.495	0.019	0.407
-33 PI Kapton® H Control	127	1	0.117	0.013	0.104	0.554	0.019	0.534	0.330
-34 PI PMR-15 Flight	305	1	0.160	0.133	0.027	0.347	0.344	0.003	0.493
-34 PI PMR-15 Control	305	1	0.099	0.078	0.021	0.332	0.257	0.075	0.568
-36 PC Flight	254	1	0.178	0.178	0.000	0.591	0.590	0.001	0.231
-36 PC Control	254	1	0.099	0.094	0.005	0.835	0.754	0.081	0.066
-37 PEEK Flight	76	3	0.278	0.276	0.002	0.369	0.365	0.005	0.353
-37 PEEK Control	76	3	0.249	0.173	0.075	0.563	0.522	0.040	0.189
-39 CTFE Kel-F® Flight	127	4	0.124	0.121	0.003	0.770	0.770	-0.000	0.106
-39 CTFE Kel-F® Control	127	4	0.069	0.011	0.058	0.931	0.014	0.917	0.001
-40 ECTFE Halar® Flight	76	1	0.058	0.041	0.016	0.795	0.166	0.629	0.148
-40 ECTFE Halar® Control	76	1	0.082	0.033	0.049	0.885	0.064	0.822	0.032
-41 ETFE Tefzel® Flight	76	1	0.066	0.066	0.000	0.840	0.835	0.005	0.094
-41 ETFE Tefzel® Control	76	1	0.062	0.015	0.047	0.939	0.021	0.919	-0.001
-42 FEP Teflon® Flight	51	1	0.051	0.025	0.025	0.944	0.017	0.928	0.005
-42 FEP Teflon® Control	51	1	0.051	0.011	0.040	0.948	0.015	0.933	0.001
-43 PTFE Flight	51	1	0.085	0.071	0.014	0.886	0.234	0.652	0.029
-43 PTFE Control	51	1	0.095	0.074	0.020	0.865	0.218	0.647	0.040

-44 PFA Flight	51	2	0.088	0.060	0.029	0.904	0.046	0.858	0.008
-44 PFA Control	51	2	0.088	0.018	0.070	0.911	0.026	0.885	0.001
-45 AF Flight	51	1	0.052	0.044	0.008	0.932	0.073	0.859	0.016
-45 AF Control	51	1	0.054	0.021	0.033	0.944	0.030	0.914	0.002
-46 PVDF Kynar® Flight	76	1	0.088	0.085	0.003	0.759	0.733	0.025	0.154
-46 PVDF Kynar® Control	76	1	0.078	0.064	0.014	0.921	0.629	0.292	0.001

2-E5-6 Acrylonitrile butadiene styrene (ABS)

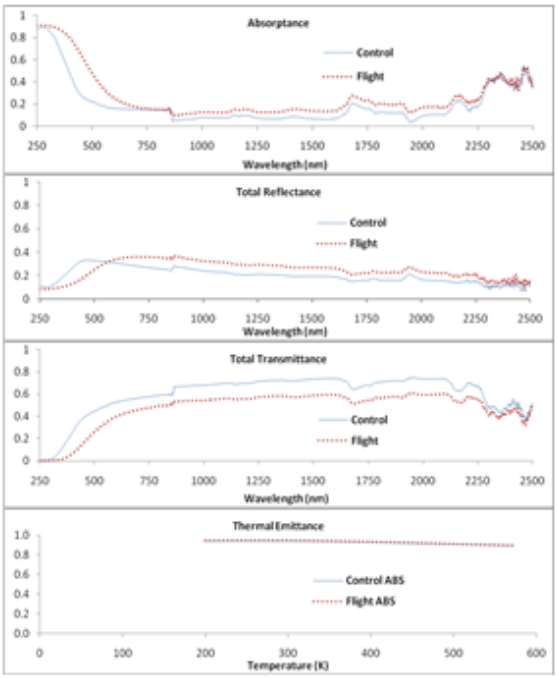

2-E5-8 Poly-(*p*-phenylene terephthalamide) (PPD-T, Kevlar)

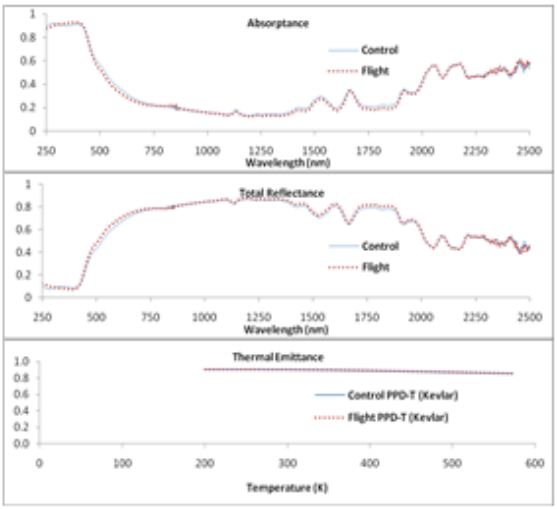

2-E5-7 Cellulose acetate (CA)

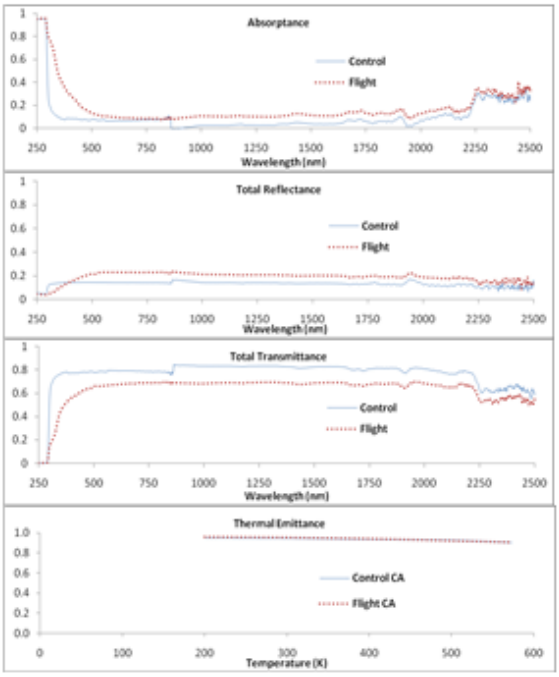

2-E5-10 Polyvinyl fluoride (PVF, Tedlar)

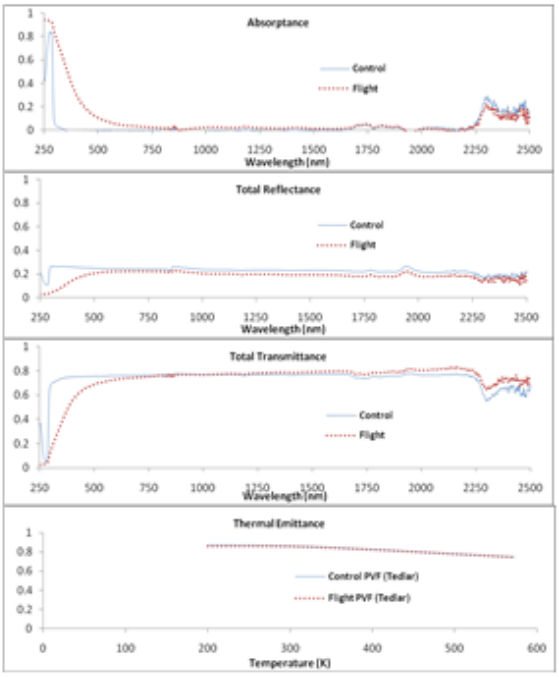

Figure 60—Absorptance, Total Reflectance, Total Transmittance, and Emittance Spectral Data for Flight and Control Samples (1 of 9)

2-E5-11 Polyvinyl fluoride with white pigment (PVF, White Tedlar)

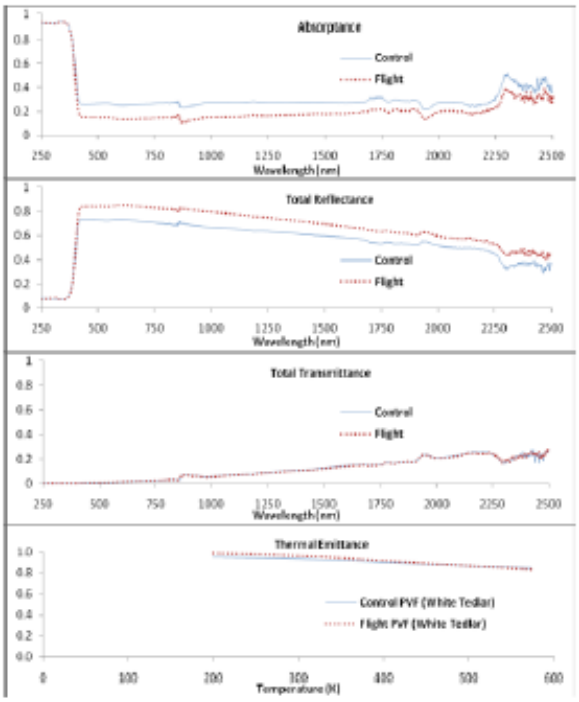

2-E5-13 Polyacrylonitrile (PAN)

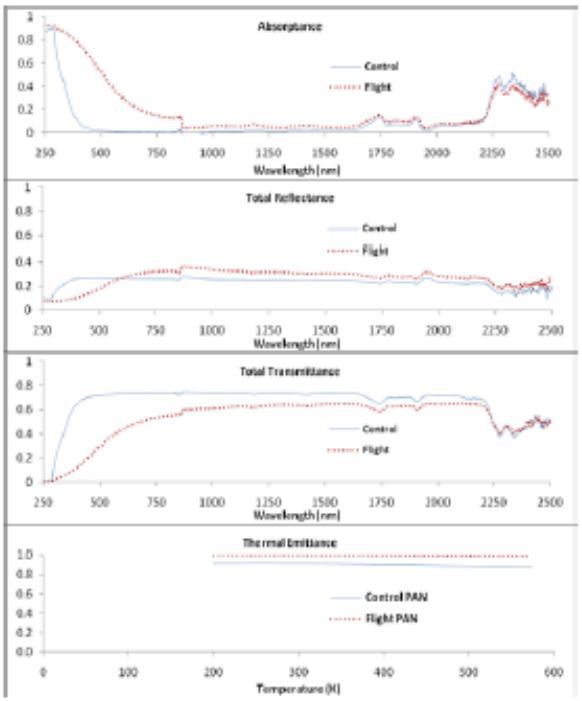

2 -E5-12 Polyoxymethylene, acetal (POM, Delrin)

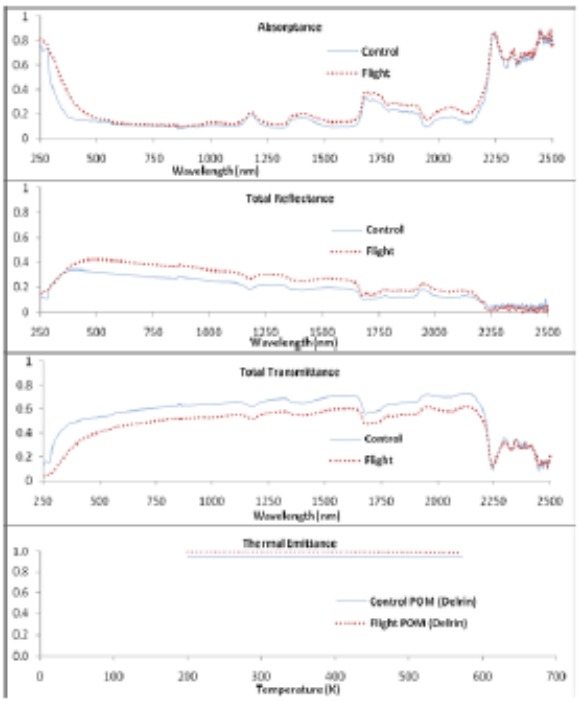

2-E5-14 Allyl diglycol carbonate (ADC, CR-39)

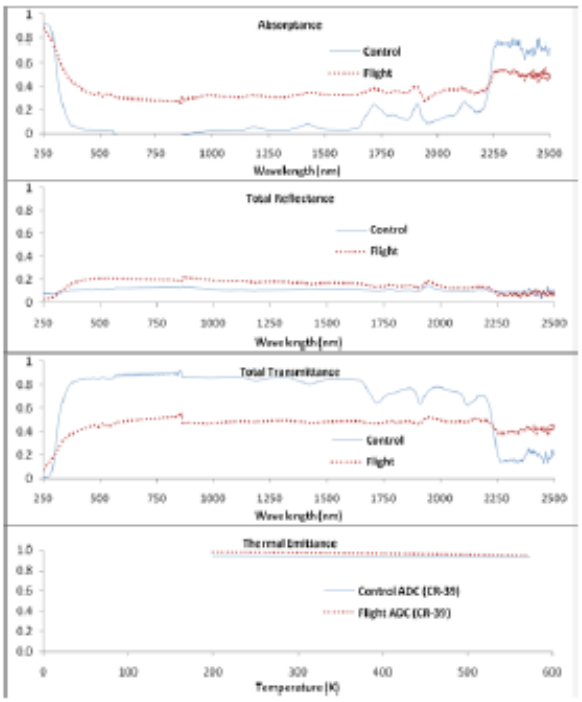

Figure 60—Absorptance, Total Reflectance, Total Transmittance, and Emittance Spectral Data for Flight and Control Samples (2 of 9)

2-E5-15 Polystyrene (PS)

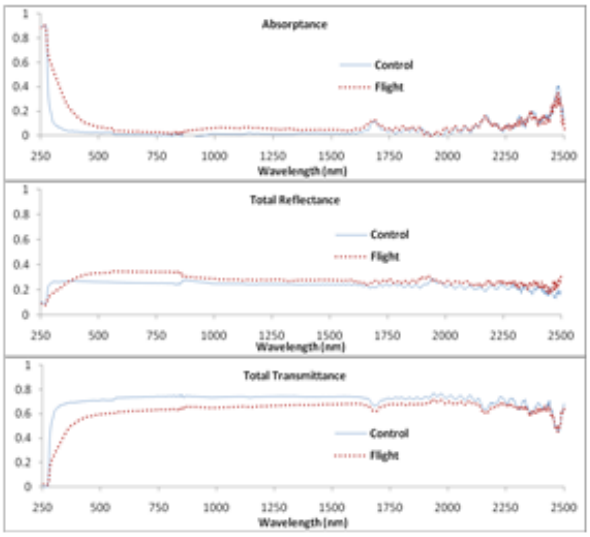

2-E5-18 Poly(p-phenylene-2 6-benzobisoxazole) (PBO, Zylon)

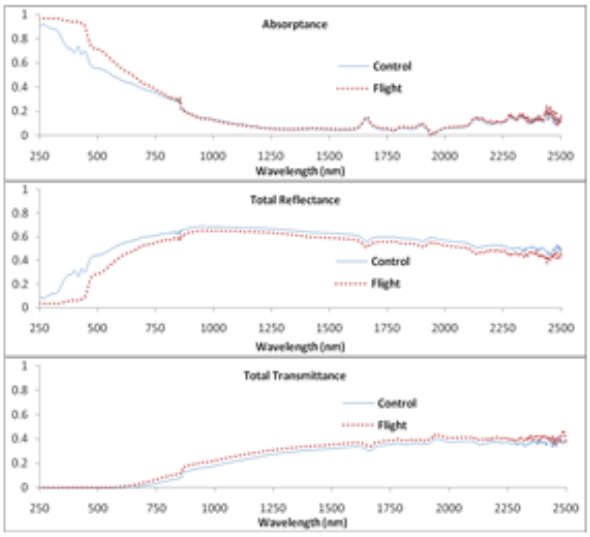

2-E5-17 Polyethylene oxide (PEO)

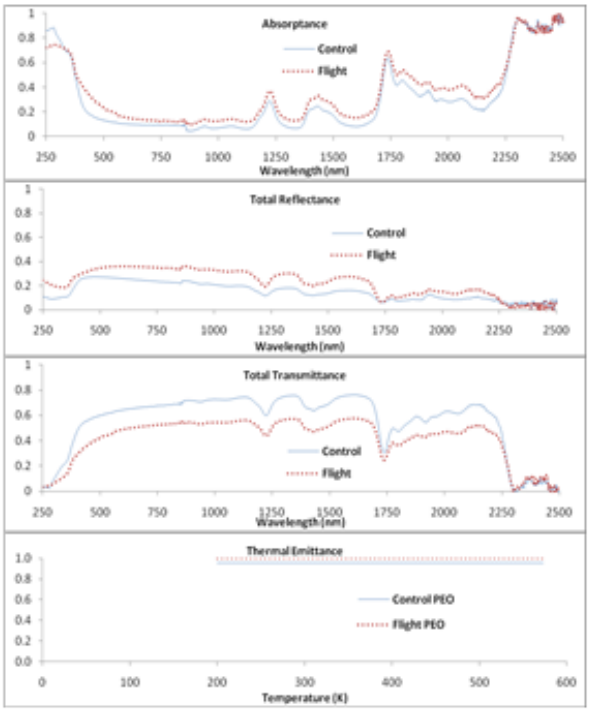

2-E5-19 Epoxy (EP)

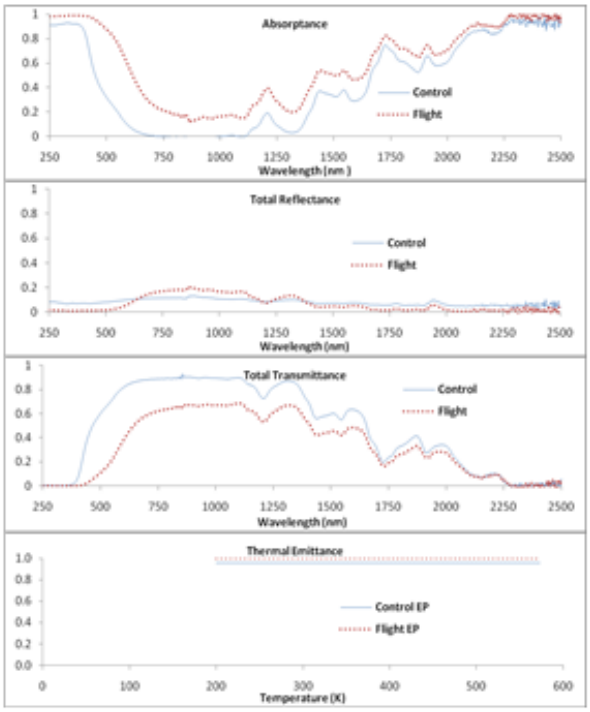

Figure 60—Absorptance, Total Reflectance, Total Transmittance, and Emittance Spectral Data for Flight and Control Samples (3 of 9)

2-E5-20 Polypropylene (PP)

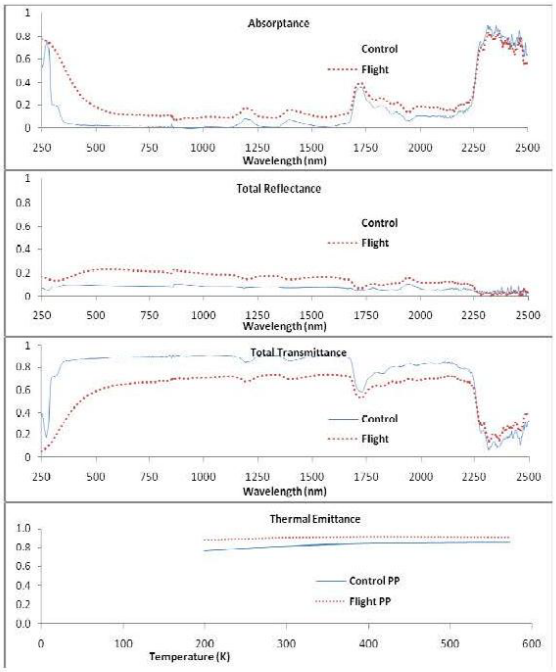

2-E5-22 Polysulfone **(PSU)**

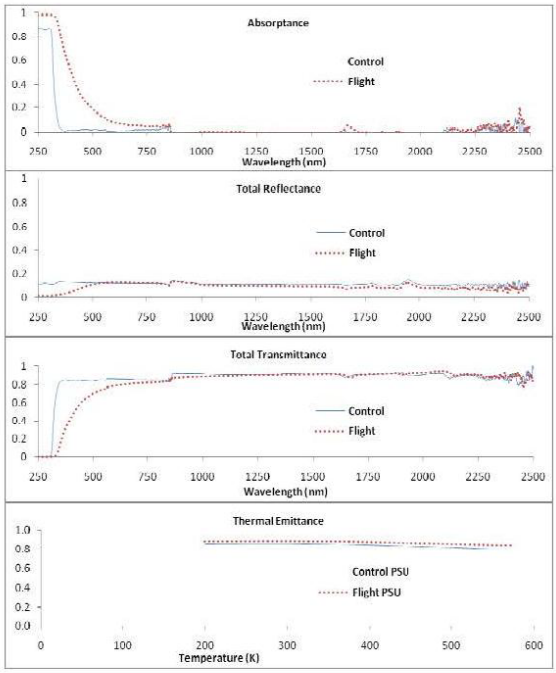

2-E5-21 Polybutylene terephthalate (PBT)

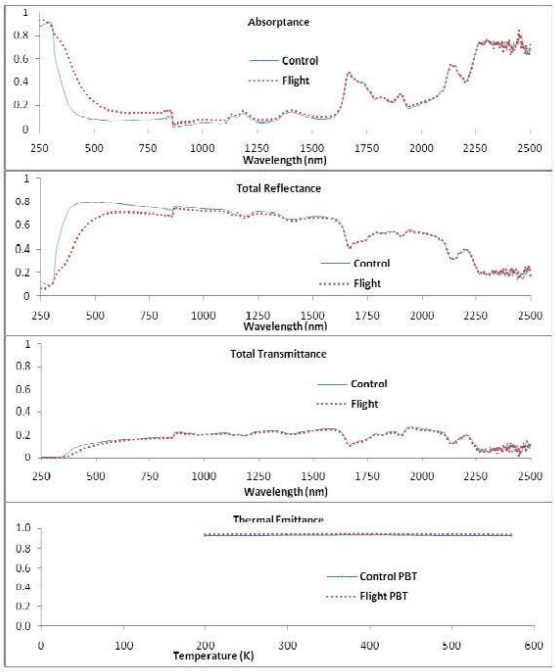

2-E5-23 Polyurethane (PU)

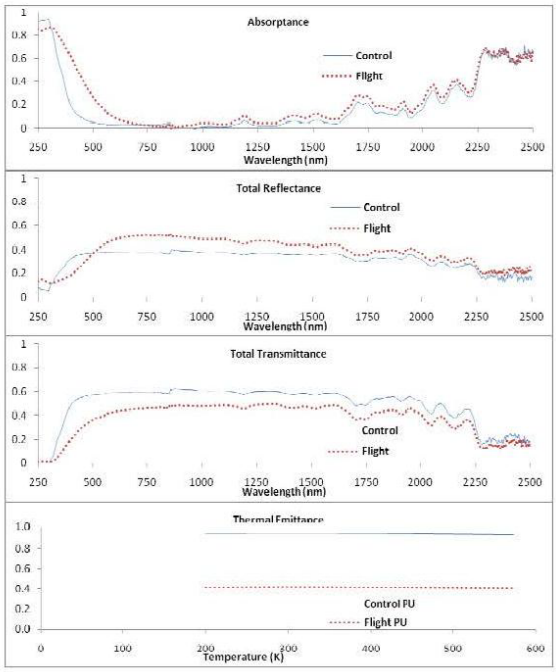

Figure 60—Absorptance, Total Reflectance, Total Transmittance, and Emittance Spectral Data for Flight and Control Samples (4 of 9)

2-E5-24 Polyphenylene isophthalate (PPPA, Nomex)

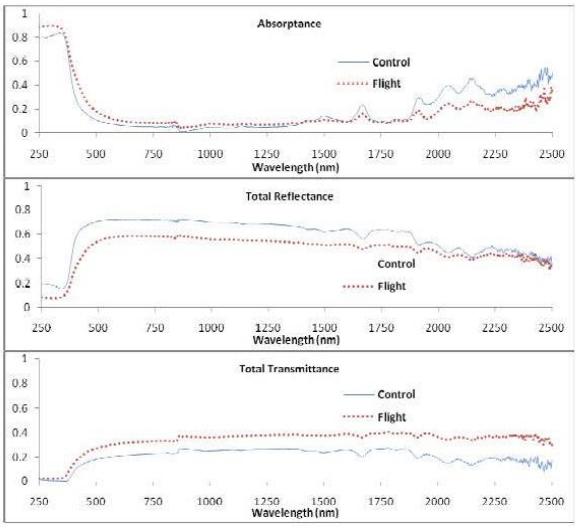

2-E5-26 Polyetherimide (PEI)

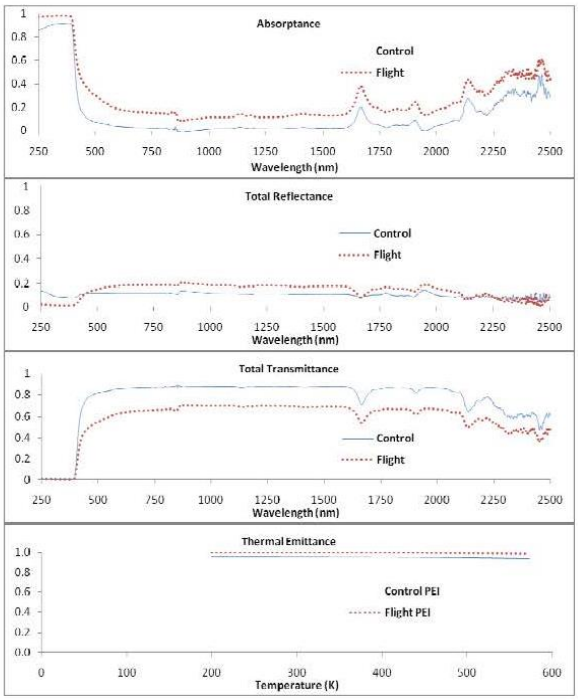

2-E5-25 Pyrolytic graphite (PG)

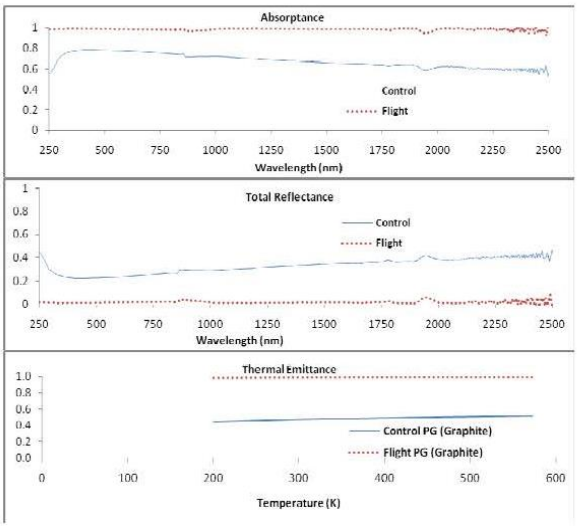

2-E5-27 Polyamide 6 (PA 6, Nylon 6)

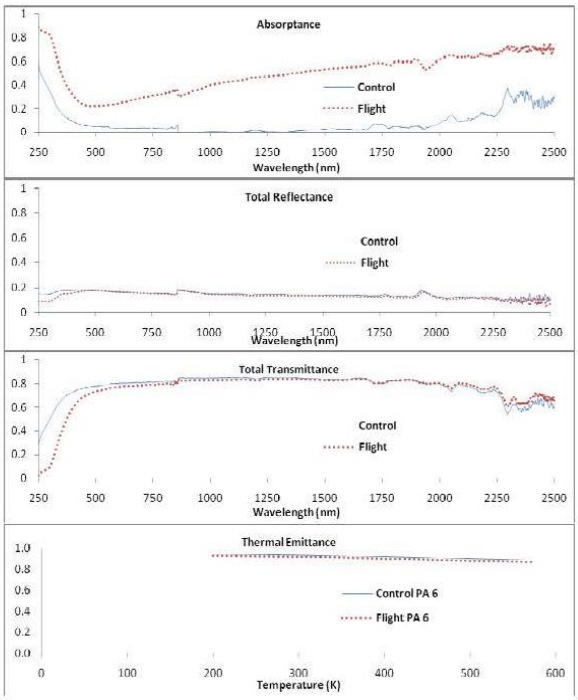

Figure 60—Absorptance, Total Reflectance, Total Transmittance, and Emittance Spectral Data for Flight and Control Samples (5 of 9)

2-E5-30 Polyimide (PMDA,PI, Kapton H)

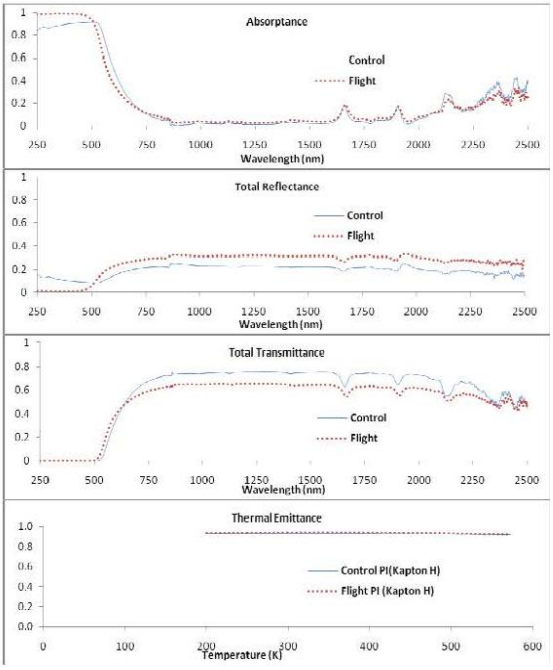

2-E5-32 Polyimide (BPDA, PI, Upilex-S)

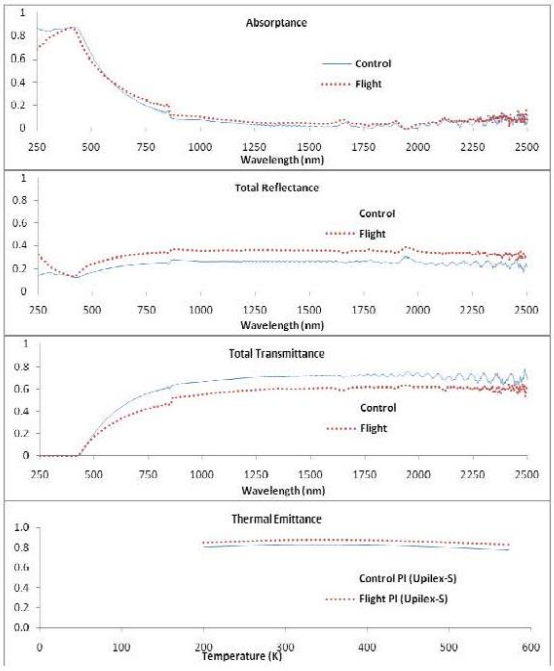

2-E5-31 Polyimide (PMDA, PI, Kapton HN)

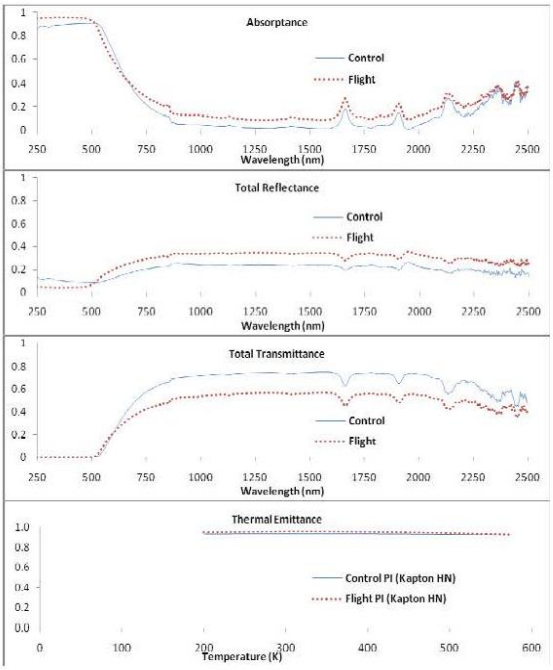

2-E5-33 Polyimide (PMDA, PI, Kapton H)

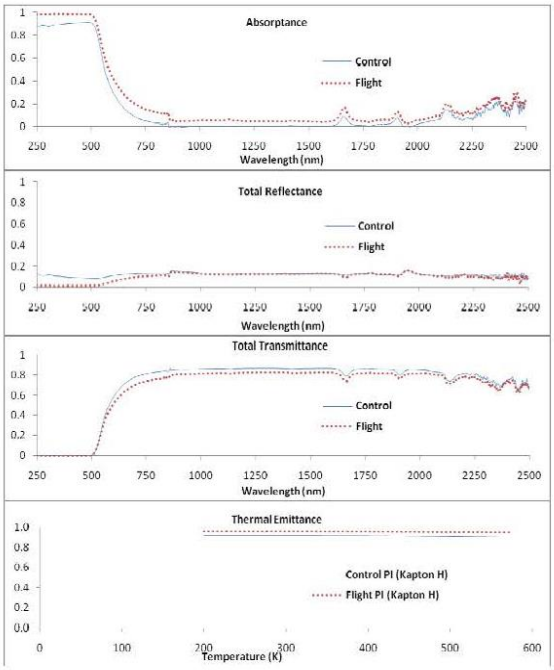

Figure 60—Absorptance, Total Reflectance, Total Transmittance, and Emittance Spectral Data for Flight and Control Samples (6 of 9)

2-E5-34 High temperature polyimide resin (PI, PMR-15)

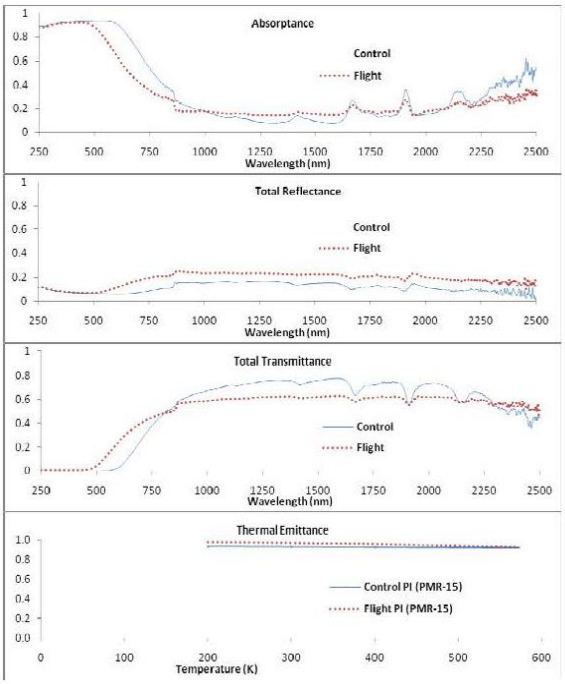

2-E5-37 Polyetheretherketone (PEEK)

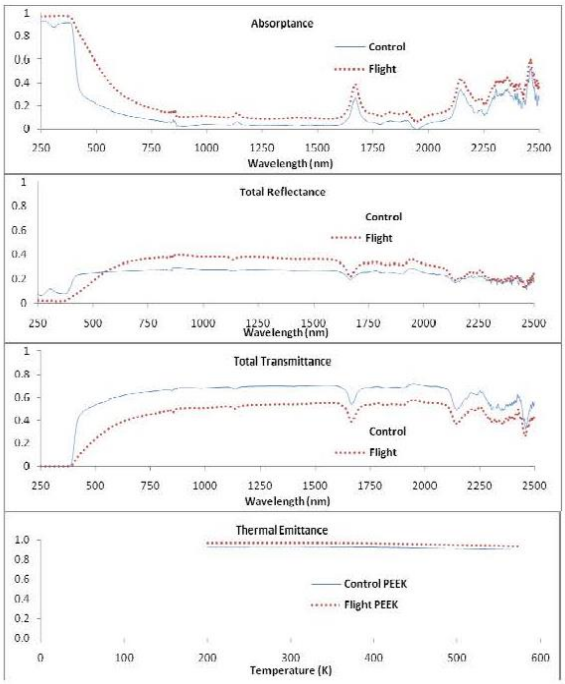

2-E5-36 Polycarbonate (PC)

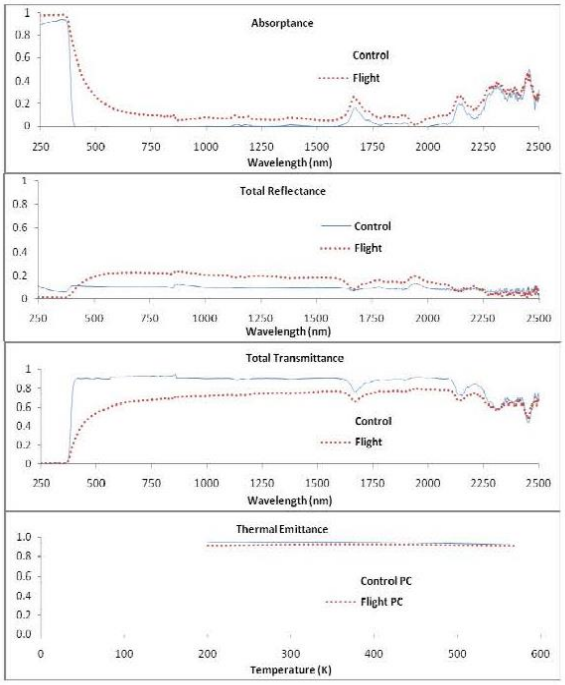

2-E5-39 Chlorotrifluoroethylene (CTFE, Kel-F)

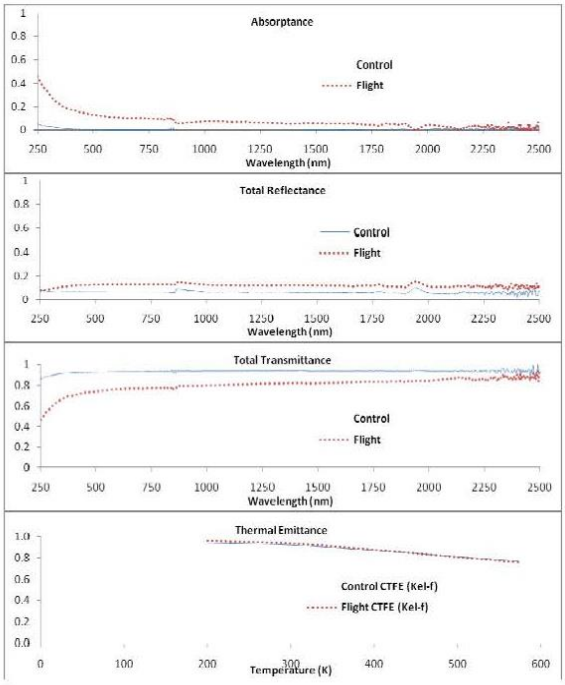

Figure 60—Absorptance, Total Reflectance, Total Transmittance, and Emittance Spectral Data for Flight and Control Samples (7 of 9)

2-E5-40 Ethylene-chlorotrifluoroethylene (ECTFE, Halar)

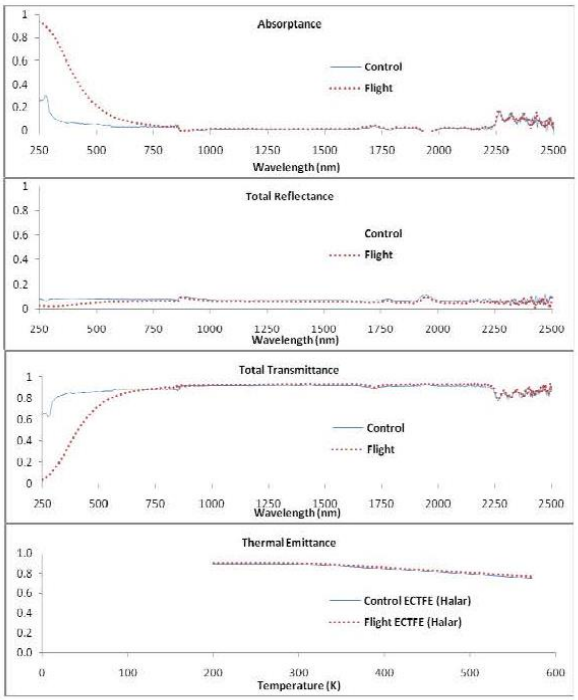

2-E5-42 Fluorinated ethylene propylene (FEP, Teflon FEP)

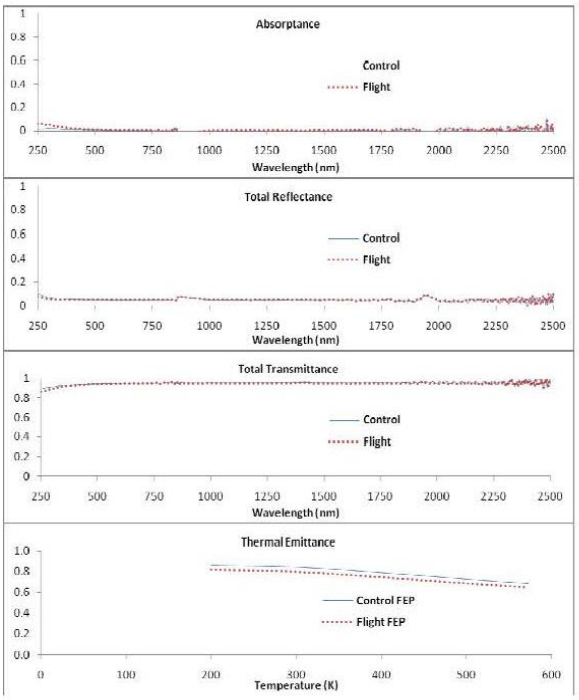

2-E5-41 Tetrafluorethylene-ethylene copolymer (ETFE, Tefzel)

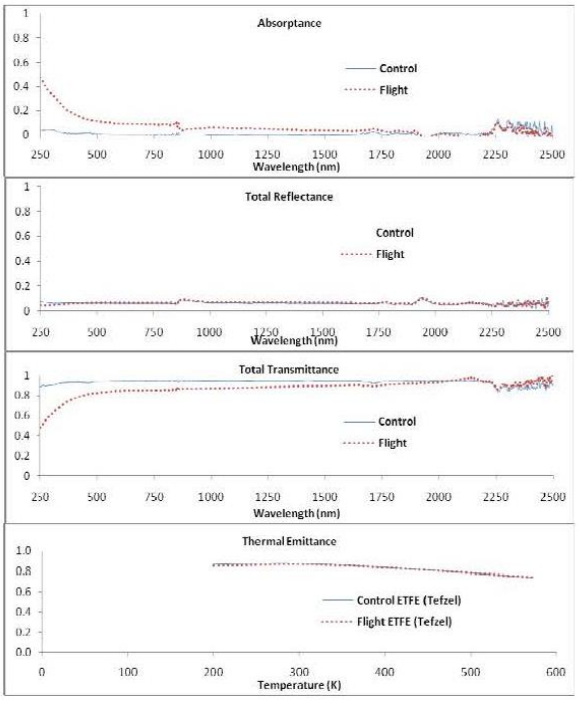

2-E5-43 Polytetrafluoroethylene (PTFE)

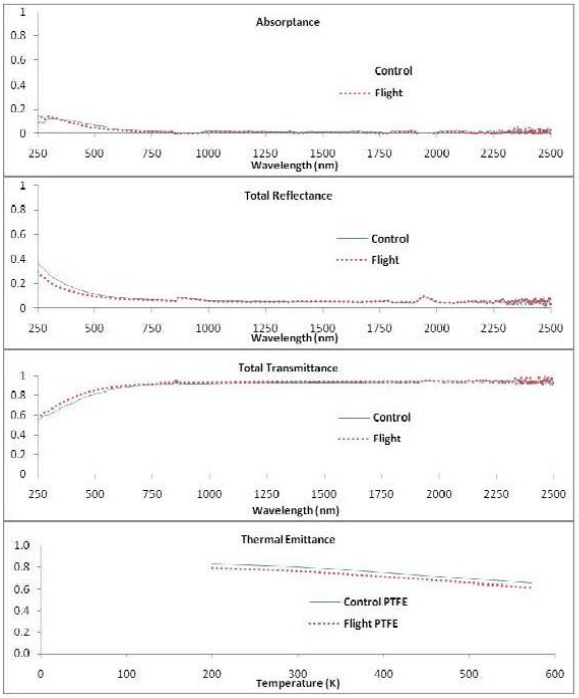

Figure 60—Absorptance, Total Reflectance, Total Transmittance, and Emittance Spectral Data for Flight and Control Samples (8 of 9)

2-E5-44 Perfluoroalkoxy copolymer resin (PFA, Teflon PFA)

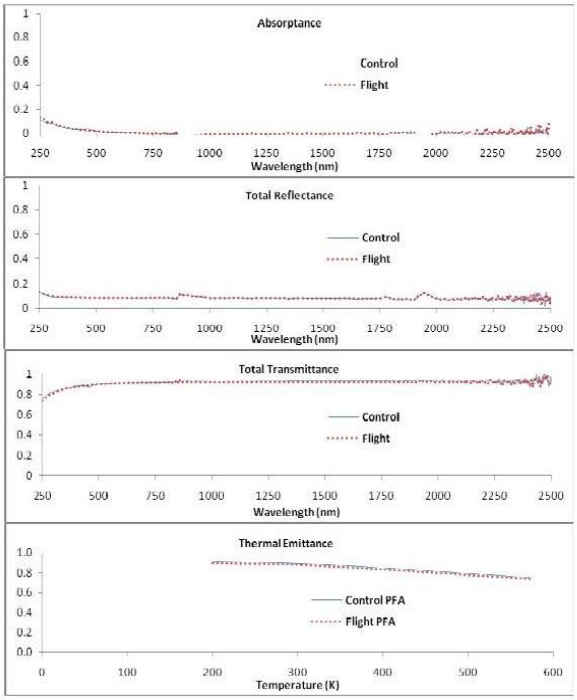

2-E5-46 Polyvinylidene fluoride (PVDF, Kynar)

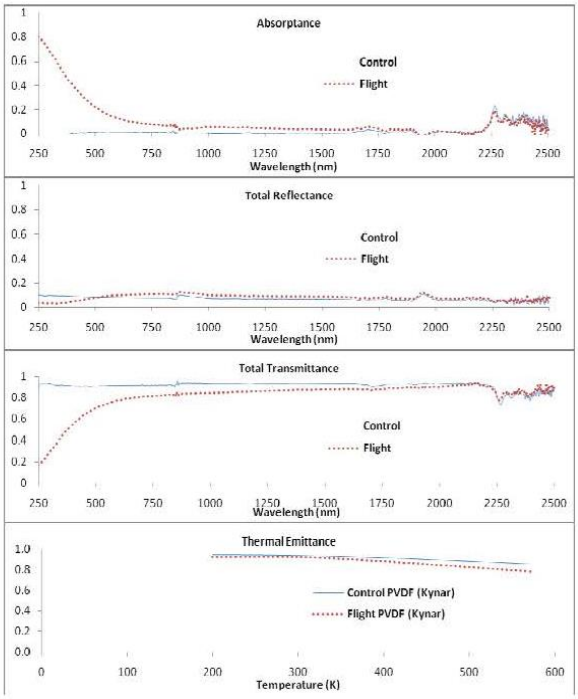

2-E5-45 Amorphous Fluoropolymer (AF, Teflon AF)

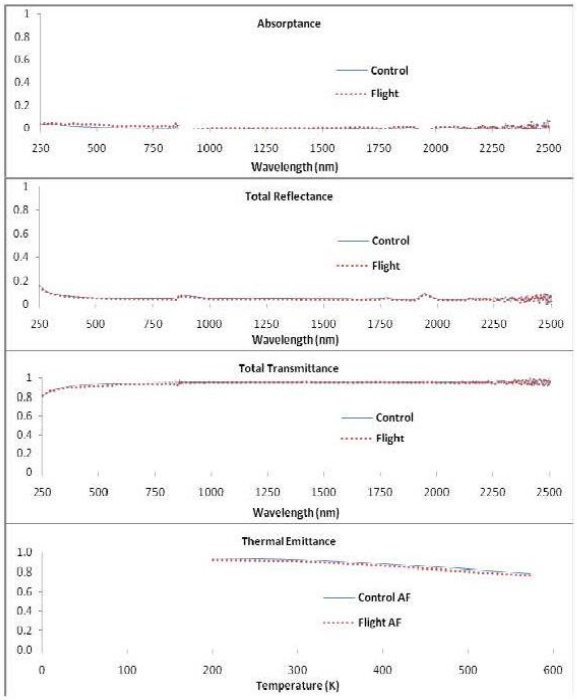

Figure 60—Absorptance, Total Reflectance, Total Transmittance, and Emittance Spectral Data for Flight and Control Samples (9 of 9)

Several trends were noted in the optical and thermal data. TR generally increased at least slightly with exposure; exceptions were mainly the fluorinated polymers and pyrolytic graphite. The DR showed a significant increase with exposure for most materials because of surface texturing; notable exceptions were PBO, polybutylene terephthalate (PBT), PPPA, pyrolytic graphite, and PTFE. SR decreased with exposure for every sample measured, also because of surface texturing, with the exception of PMR-15. PMR-15 had an eroded hole, which may have affected its SR value. TT decreased with exposure for most samples measured, with the exceptions of PBO, PPPA, and PTFE. DT increased significantly with exposure for most materials, but this trend had many exceptions (PVF-W, POM, PEO, EP, PBT, polyurethane (PU), polycarbonate (PC), and polyetheretherketone (PEEK). ST decreased with exposure for every sample with the exceptions of PPPA and PTFE. With the exceptions of PPD-T, PMR-15, and PTFE, α_s increased with exposure.

Table 24, Post-Retrieval and Control Thermal Properties (ε), lists the calculated thermal emittance data over the wavelength range of 2 to 25 μm at various temperatures, as well as the number of layers measured. Many of the ε values remained similar before and after space exposure. Several materials, e.g., PU, FEP, and PTFE, experienced a decrease in ε, possibly caused by differences in thickness between the flight sample and the control sample. Many materials showed an increase in ε, most likely because of the development of cone structures on the surface of the materials. PG showed the largest increase in ε, along with the development of a black velvet appearance after space exposure. Other samples that showed increased ε values included POM, polyacrylonitrite (PAN), PEO, EP, PP, polysulfone (PSU), PEI, PI (Upilex-S®), PI (Kapton® H), and PEEK. It should be noted that the samples were all measured in the sample holder, which was not flush with the SOC 400T face (there was a 0.013-cm gap) in an effort to not damage the surface morphology. The gold standard used as a backing material for the measurements was also separated from the sample by a 0.013-cm gap. Therefore, the values obtained should not be interpreted as absolute values and should be used instead as a comparison tool. Figure 60 provides graphs of the ε data for each material and its control sample.

Table 24—Post-Retrieval and Control Thermal Properties (ε)

MISSE 2 Samples (2-E5-XX)	Layers Measured	ε (200 K)	ε (300 K)	ε (400 K)	ε (500 K)	ε (573 K)
-06 ABS Flight	2	0.95	0.95	0.94	0.91	0.90
-06 ABS Control	2	0.94	0.94	0.93	0.91	0.89
-07 CA Flight	2	0.96	0.95	0.94	0.92	0.91
-07 CA Control	2	0.95	0.94	0.93	0.93	0.90
-08 PPD-T Kevlar® Flight	3	0.91	0.91	0.90	0.88	0.86
-08 PPD-T Kevlar® Control	3	0.91	0.91	0.89	0.87	0.85
-10 PVF Tedlar® Flight	3	0.86	0.86	0.83	0.78	0.75
-10 PVF Tedlar® Control	3	0.87	0.87	0.83	0.78	0.75
-11 PVF white Tedlar® Flight	2	0.99	0.96	0.92	0.87	0.84
-11 PVF white Tedlar® Control	2	0.95	0.94	0.90	0.87	0.84
-12 POM Delrin® Flight	1	1.00	1.00	1.00	0.99	0.99
-12 POM Delrin® Control	1	0.94	0.94	0.94	0.95	0.95
-13 PAN Flight	4	1.00	1.00	1.00	0.99	0.99
-13 PAN Control	4	0.92	0.92	0.91	0.89	0.87
-14 ADC CR-29 Flight	1	0.98	0.98	0.97	0.95	0.95
-14 ADC CR-39® Control	1	0.94	0.94	0.94	0.94	0.94
-17 PEO Flight	1	1.00	1.00	1.00	1.00	1.00
-17 PEO Control	1	0.96	0.96	0.96	0.96	0.96
-19 EP Flight	1	1.00	1.00	1.00	1.00	1.00
-19 EP Control	1	0.96	0.96	0.96	0.96	0.96
-20 PP Flight	1	0.88	0.91	0.92	0.92	0.91
-20 PP Control	1	0.76	0.82	0.85	0.85	0.86
-21 PBT Flight	4	0.94	0.95	0.95	0.94	0.94
-21 PBT Control	4	0.92	0.93	0.93	0.93	0.92
-22 PSU Flight	1	0.89	0.89	0.88	0.86	0.84
-22 PSU Control	1	0.86	0.86	0.84	0.82	0.79
-23 PU Flight	7	0.42	0.42	0.42	0.41	0.40
-23 PU Control	7	0.94	0.94	0.94	0.93	0.93
-25 PG Flight	1	0.99	0.99	0.99	0.99	1.00
-25 PG Control	1	0.45	0.47	0.49	0.50	0.51
-26 PEI Flight	1	1.00	1.00	1.00	0.99	0.99
-26 PEI Control	1	0.95	0.95	0.95	0.94	0.93
-27 PA 6 Flight	2	0.92	0.92	0.90	0.88	0.87
-27 PA 6 Control	2	0.94	0.93	0.92	0.90	0.89
-30 PI Kapton® H Flight	2	0.94	0.94	0.94	0.93	0.92
-30 PI Kapton® H Control	2	0.93	0.93	0.93	0.92	0.92
-31 PI Kapton® HN Flight	2	0.95	0.96	0.95	0.94	0.93
-31 PI Kapton® HN Control	2	0.93	0.93	0.93	0.93	0.92
-32 PI Upilex-S® Flight	2	0.85	0.87	0.87	0.85	0.83
-32 PI Upilex-S® Control	2	0.81	0.83	0.83	0.80	0.78
-33 PI Kapton® H Flight	1	0.96	0.96	0.96	0.95	0.95
-33 PI Kapton® H Control	1	0.92	0.92	0.92	0.91	0.90
-34 PI PMR-15 Flight	1	0.98	0.97	0.96	0.94	0.93
-34 PI PMR-15 Control	1	0.93	0.93	0.93	0.93	0.92
-36 PC Flight	1	0.91	0.92	0.93	0.92	0.91

-36 PC Control	1	0.94	0.95	0.94	0.93	0.92
-37 PEEK Flight	3	0.97	0.97	0.97	0.95	0.94
-37 PEEK Control	3	0.93	0.93	0.92	0.91	0.90
-39 CTFE Kel-F® Flight	4	0.96	0.94	0.88	0.81	0.76
-39 CTFE Kel-F® Control	4	0.94	0.92	0.87	0.81	0.77
-40 ECTFE Halar® Flight	1	0.91	0.90	0.86	0.80	0.76
-40 ECTFE Halar® Control	1	0.90	0.89	0.85	0.79	0.75
-41 ETFE Tefzel® Flight	1	0.85	0.87	0.84	0.78	0.75
-41 ETFE Tefzel® Control	1	0.87	0.88	0.84	0.78	0.74
-42 FEP Teflon® Flight	1	0.82	0.80	0.74	0.69	0.65
-42 FEP Teflon® Control	1	0.86	0.85	0.79	0.73	0.69
-43 PTFE Flight	1	0.79	0.76	0.71	0.65	0.61
-43 PTFE Control	1	0.83	0.80	0.75	0.69	0.65
-44 PFA Flight	2	0.89	0.88	0.83	0.77	0.73
-44 PFA Control	2	0.91	0.90	0.85	0.79	0.75
-45 AF Flight	1	0.92	0.90	0.86	0.81	0.77
-45 AF Control	1	0.93	0.92	0.88	0.83	0.79
-46 PVDF Kynar® Flight	1	0.92	0.92	0.88	0.83	0.78
-46 PVDF Kynar® Control	1	0.94	0.94	0.91	0.88	0.86

C.5 Summary

Optical and thermal properties were measured for the MISSE 2 PEACE Polymers experiment samples after long-term space exposure on the ISS. The majority of the PEACE Polymer samples were comprised of numerous thin-film layers stacked together. Because the MISSE 2 mission was much longer (3.95 years) than planned (1 year), one sample was completely eroded away (PBI), and several other samples were severely degraded. Therefore, optical and thermal measurements could not be obtained for all samples. Optical properties of 43 flight samples and thermal properties of 40 flight samples were obtained and compared to those of the corresponding control samples. Several trends were observed in the data. For most samples, SR and DR characteristics changed greatly upon directed LEO atomic oxygen exposure; typically, there was a decrease in SR and an increase in DR. These optical property changes affect glare issues, Fresnel lens photovoltaic concentrator power loss issues, and issues with spatial variations in the thermal load on a spacecraft. The wavelength-dependent data allowed for computation of the changes in α_s and thermal ε, which are critical data for predicting the thermal control characteristics of a spacecraft. Because many of the PEACE Polymers are commonly used for spacecraft applications, it is very important to understand potential changes in their optical and thermal properties after long-term space exposure.

C.6 Reference

Waters, D.L.; de Groh, K.K.; Banks, B.A.; Cameron, K.C. (September 15-18, 2009). “Changes in Optical and Thermal Properties of the MISSE 2 PEACE Polymers and Spacecraft Silicones.” *Proceedings of the International Symposium on Materials in a Space Environment (ISMSE-11.)* Aix-en-Provence, France.

APPENDIX D

SUMMARY PAGES FOR INDIVIDUAL MISSE 2 PEACE POLYMERS FLIGHT SAMPLES

D.1 Purpose and/or Scope

The purpose of Appendix D is to provide individual summary pages for each of the MISSE 2 PEACE Polymers experiment flight samples, with details such as thickness of the polymer film, number of sample layers flown, pre- and post-flight dehydrated mass, density, exposed area, and the MISSE 2 LEO erosion yield (E_y) value. Also included are photos of each flight sample and its corresponding control sample.

D.2 Measurement System Identification

In this appendix, sample thickness data are reported in metric (SI)/English units, to reflect the English measurement (mil) used to record thickness of each layer.

MISSE
2-E5-6
ABS

Atomic oxygen (AO) fluence = 8.43×10^{21} atoms/cm^2

Post-flight photograph of flight sample in E5 tray

Polymer:	Acrylonitrile butadiene styrene
Abbreviation:	ABS
Trade name(s):	Cycolac®, Absylux®, Lustran®
Thickness of each layer:	127 μm (5 mil)
Number layers flown:	3 (2 Part A + 1 Part B)
Total thickness:	381 μm (15 mil)
Vacuum heat treatment:	24 hr at 90 °

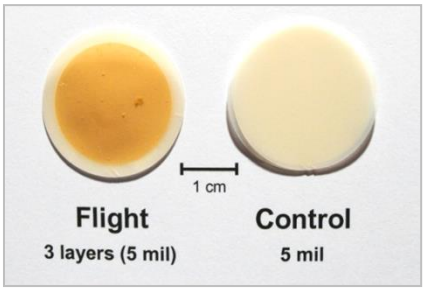

Post-flight photograph of stacked sample layers

Pre-Flight Data

Part A:	
Layers in Part A:	2
Average mass of flight sample Part A:	130.362 mg
Part B:	N/A
Total pre-flight sample mass:	**130.362 mg**

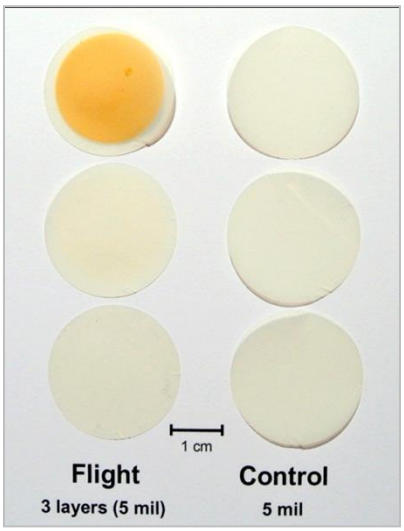

Post-flight photograph of individual sample layers. Layers were separated for weighing.
(Mass loss Situation 1)

Post-Flight Data

Mass loss situation:	Situation 1
Layers needed to be weighed for E_y:	2 (Part A)
Layers weighed in Part A:	2
Average mass of Part A:	96.501 mg
Total post-flight sample mass:	**96.501 mg**

Erosion Yield Data

Flight sample mass loss:	0.033861 g
Average density:	1.05 g/cm^3
Exposed area:	3.4944 cm^2

MISSE 2 E_y: $1.09\ (\pm0.03)\times10^{-24}$ cm^3/atom

MISSE 2
2-E5-7
CA

AO fluence = 8.43×10^{21} atoms/cm^2

Post-flight photograph of flight sample in E5 tray

Polymer:	Cellulose acetate
Abbreviation:	CA
Trade Name(s):	Cellidor®, Tenite™, Acetate, Dexel
Thickness of each layer:	50.8 μm (2 mil)
Number layers flown:	13 (7 Part A + 6 Part B) *Back-up sample flown*
Total thickness:	660 μm (26 mil)
Vacuum heat treatment:	68.75 hr at 128 °C

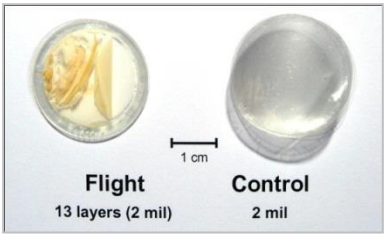

Post-flight photograph of stacked sample layers

Pre-Flight Data

Part A:

Layers in Part A:	7
Average mass of flight sample Part A:	236.777 mg
Average mass of control sample Part A:	238.659 mg

Part B:

Layers in Part B:	6
Computed mass for flight sample Part B:	203.758 mg*
Total pre-flight sample mass:	**440.535 mg**

Post-flight photograph of individual sample layers. Layers were separated for weighing. (Mass loss Situation 2)

Post-Flight Data

Mass loss situation:	Situation 2
Layers needed to be weighed for E_y:	13 (7 Part A + 6 Part B)
Layers weighed in Part A:	7
Average mass of Part A:	92.444 mg
Layers weighed in Part B:	6
Average mass of Part B:	156.609 mg
Average mass of Part A + Part B:	249.053 mg

Erosion Yield Data

Flight sample mass loss:	0.191482 g
Average density:	1.2911 g/cm^3
Exposed area:	3.4831 cm^2

MISSE 2 E_y: 5.05 (±0.13) ×10^{-24} cm^3/atom

* Computed mass for Part B is based on the average mass for Part A flight and control samples.

MISSE 2
2-E5-8
PPD-T (Fabric)

AO fluence = 8.43×10^{21} atoms/cm^2

Polymer:	Poly-(p-phenylene terephthalamide)
Abbreviation:	PPD-T
Trade name(s):	Kevlar® 29, fabric
Thickness of each layer:	55.88 μm (2.2 mil) of fabric
Number layers flown:	3 (wrapped in Al foil)
Total thickness:	167.64 μm (6.6 mil)
Vacuum heat treatment:	24 hr at 128 °C

Post-flight photograph of flight sample in E5 tray

Pre-Flight Data

Part A:	
Layers in Part A:	3 (in Al foil)
Average mass of flight sample Part A:	345.313 mg
Part B:	N/A
Total pre-flight sample mass:	**345.313 mg**

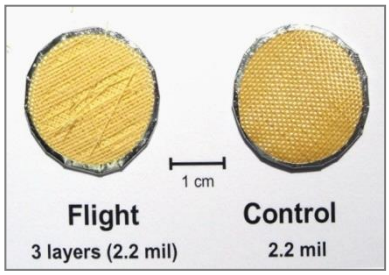

Post-flight photograph of stacked sample layers in Al foil holders. Sample layers were weighed together in Al foil. (Mass loss Situation 1)

Post-Flight Data

Mass loss situation:	Situation 1
Layers needed to be weighed for E_y:	3 (Part A)
Layers weighed in Part A:	3
Average mass of Part A:	318.523 mg
Total post-flight sample mass:	**318.523 mg**

Erosion Yield Data

Flight sample mass loss:	0.026790 g
Average density	1.4422 g/cm^3
Exposed area:	3.5099 cm^2
MISSE 2 E_y:	**6.28 (± 0.16) ×10^{-25} cm^3/atom**

MISSE 2
2-E5-9
PE

AO fluence = 8.43×10^{21} atoms/cm^2

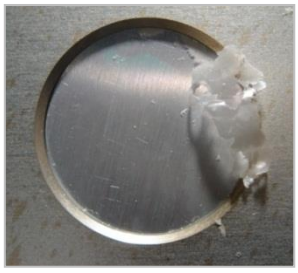

Post-flight photograph of flight sample in E5 tray

Polymer:	Polyethylene
Abbreviation:	PE (Low oxygen content)
Trade name(s):	N/A
Thickness of each layer:	50.8 μm (2 mil)
Numbers layers flown:	6 (4 Part A + 2 Part B)
Total thickness:	304.8 μm (12 mil)

Post-flight photograph of stacked sample layers

Pre-Flight Data

Part A:

Layers in Part A:	4
Average mass of flight sample Part A:	96.411 mg
Average mass of control sample Part A:	95.555 mg

Part B:

Layers in Part B:	2
Computed mass of flight sample Part B:	47.992 mg*
Total pre-flight sample mass:	**144.403 mg**

Post-Flight Data

Mass loss situation:	Situation 2
Layers needed to be weighed for E_y:	6 (4 Part A + 2 Part B)
Layers weighed in Part A:	4
Average mass of Part A:	26.669
Layers weighed in Part B:	2
Average mass of Part B:	14.974 mg
Average mass of Part A + Part B:	41.643 mg
Total post-flight sample mass:	**41.643 mg**

Erosion Yield Data

Flight sample mass loss:	0.102760
Average density	0.9180 g/cm^3
Exposed area:	3.5489 cm^2

Post-flight photograph of individual sample layers. Layers were separated for weighing. (Mass loss Situation 2)

MISSE 2 E_y: >3.74×10^{-24} cm^3/atom**

* Computed mass for Part B is based on the average mass for Part A flight and control samples.

** The PE sample eroded completely through all layers in the center of the sample; therefore, the obtained erosion yield value is a minimum value.

MISSE 2
2-E5-10
PVF

AO fluence = 8.43×10^{21} atoms/cm^2

Post-flight photograph of flight sample in E5 tray

Polymer:	Polyvinylfluoride
Abbreviation:	PVF
Trade name(s):	Tedlar® TTR10SG3 (clear)
Thickness of each layer:	25.4 μm (1 mil)
Numbers layers flown:	13 (7 Part A + 6 Part B)
Total thickness:	330.2 μm (13 mil)
Vacuum heat treatment:	36 hr at 100 °C

Post-flight photograph of stacked sample layers

Pre-Flight Data

Part A:

Layers in Part A:	7
Average mass of flight sample Part A:	125.771 mg

Part B:

Layers in Part B:	6
Mass of flight sample Part B:	108.625 mg*
Total pre-flight sample mass:	**234.396 mg**

Post-Flight Data

Mass loss situation:	Situation 2
Layers needed to be weighed for E_y:	13 (7 Part A + 6 Part B)
Layers weighed in Part A:	7
Average mass of Part A:	35.851 mg
Layers weighed in Part B:	6
Average mass of Part B:	66.008 mg
Average mass of Part A + Part B:	101.859 mg
Total post-flight sample mass:	**101.859 mg**

Erosion Yield Data

Flight sample mass loss:	0.132537 g
Average density:	1.3792 g/cm^3
Exposed area:	3.5737 cm^2

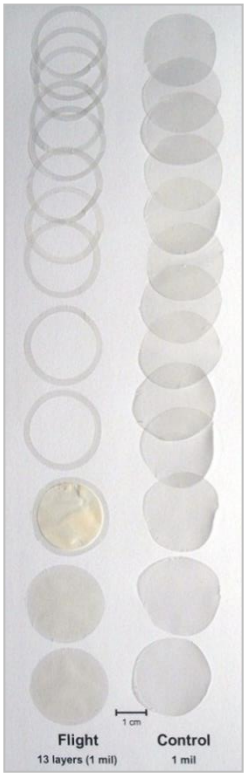

Post-flight photograph of individual sample layers. Layers were separated for weighing. (Mass loss Situation 2)

MISSE 2 E_y: 3.19 (±0.08) ×10^{-24} cm^3/atom

* Mass of a 6-layer control sample

MISSE 2
2-E5-11
PVF-W (white Tedlar®)

AO fluence = 8.43×10^21 atoms/cm^2

Polymer:	Crystalline polyvinylfluoride with white pigment
Abbreviation:	PVF
Trade name(s):	white Tedlar® TWH10B53
Thickness of each layer:	25.4 μm (1 mil)
Numbers layers flown:	13 (7 Part A + 6 Part B)
Total thickness:	645.16 μm (13 mil)

Post-flight photograph of flight sample in E5 tray

Pre-Flight Data

Part A:	
Layers in Part A:	7
Average mass of flight sample Part A:	149.524 mg
Part B:	N/A
Total pre-flight sample mass:	**149.524 mg**

Post-Flight Data

Mass loss situation:	Situation 1
Layers needed to be weighed for E_y:	7 (Part A)
Layers weighed in Part A:	7
Average mass of Part A:	**144.810 mg**
Total post-flight sample mass:	**144.810 mg**

Erosion Yield Data

Flight sample mass loss:	0.004714 g
Average density:	1.6241 g/cm^3
Exposed area:	3.4176 cm^2

Post-flight photograph of individual sample layers. Layers were separated for weighing. (Mass loss Situation 1)

MISSE 2 E_y: 1.01 (±0.04) ×10^{-25} cm^3/atom

MISSE 2
2-E5-12
POM

AO fluence = 8.43×10^{21} atoms/cm^2

Post-flight photograph of flight sample in E5 tray

Polymer:	Polyoxymethylene; acetal; polyformaldehyde
Abbreviation:	POM
Trade name(s):	Delrin® Acetal (Natural)
Thickness of each layer:	254 μm (10 mil)
Numbers layers flown:	5 (3 Part A + 2 Part B)
Total thickness:	1270 μm (50 mil)

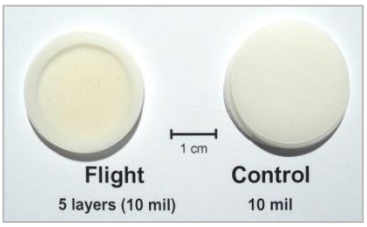

Post-flight photograph of stacked sample layers

Pre-Flight Data

Part A:	
Layers in Part A:	3
Average mass of flight sample Part A:	717.341 mg
Part B:	N/A
Total pre-flight sample mass:	**717.341 mg**

Post-Flight Data

Mass loss situation:	Situation 1
Layers needed to be weighed for E_y:	3 (Part A)
Layers weighed in Part A:	3
Average mass of Part A:	338.963 mg
Total post-flight sample mass:	**338.963 mg**

Erosion Yield Data

Flight sample mass loss:	0.378378 g
Average density:	1.3984 g/cm^3
Exposed area:	3.5119 cm^2

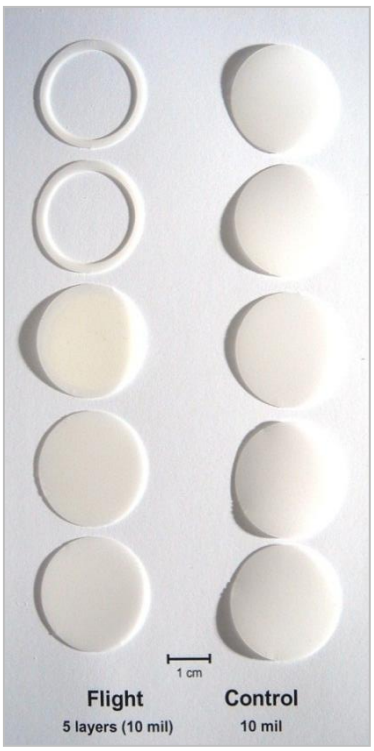

Post-flight photograph of individual sample layers. Layers were separated for weighing. (Mass loss Situation 1)

MISSE 2 E_y: 9.14 (±0.28) ×10 $^{-24}$ cm^3/atom

MISSE 2
2-E5-13
PAN

AO fluence = 8.43×10^{21} atoms/cm^2

Post-flight photograph of flight sample in E5 tray

Polymer:	Polyacrylonitrile
Abbreviation:	PAN
Trade name(s):	Barex® 210
Thickness of each layer:	50.8 μm (2 mil)
Numbers layers flown:	9 (5 Part A + 4 Part B)
Total thickness:	457.2 μm (18 mil)
Vacuum heat treatment:	24.25 hr at 126 °C

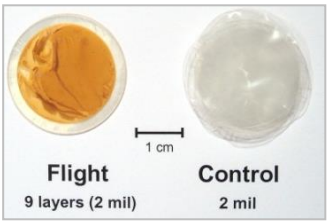

Post-flight photograph of stacked sample layers

Pre-Flight Data

Part A:	
Layers in Part A:	5
Average mass of flight sample Part A:	152. 484 mg
Part B:	N/A
Total pre-flight sample mass:	**152.484 mg**

Post-Flight Data

Mass loss situation:	Situation 1
Layers needed to be weighed for E_y:	5 (Part A)
Layers weighed in Part A:	5
Average mass of Part A:	105. 203 mg
Total post-flight sample mass:	**105.203 mg**

Erosion Yield Data

Flight sample mass loss:	0.047281 g
Average density:	1.1435 g/cm^3
Exposed area:	3.4768 cm^2

Post-flight photograph of individual sample layers. Layers were separated for weighing post flight. (Mass loss Situation 1)

MISSE 2 E_y: 1.41 (±0.05) $\times 10^{-24}$ cm^3/atom

MISSE 2
2-E5-14
ADC

AO fluence = 8.43×10^{21} atoms/cm^2

Polymer:	Allyl diglycol carbonate
Abbreviation:	ADC
Trade name(s):	CR-39®, Homalite™ H-911
Thickness of each layer:	787.4 μm (31 mil)
Numbers layers flown:	1 (1 Part A)
Total thickness:	787.4 μm (31 mil)

Post-flight photograph of flight sample in E5 tray

Pre-Flight Data

Part A:	
Layers in Part A:	1
Average mass of flight sample Part A:	397.782 mg
Part B:	N/A
Total pre-flight sample mass:	**397.782 mg**

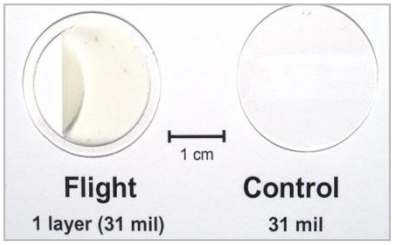

Post-flight photograph of flight and control samples
(Mass loss Situation 1)

Post-Flight Data

Mass loss situation:	Situation 1
Layers needed to be weighed for E_y:	1 (Part A)
Layers weighed in Part A:	1
Average mass of Part A:	130.487 mg
Total post-flight sample mass:	**130.487 mg**

Erosion Yield Data

Flight sample mass loss:	0.267295 g
Average density:	1.3173 g/cm^3
Exposed area:	3.5392 cm^2

MISSE 2 E_y: $>6.80 \times 10^{-24}$ cm^3/atom*

* The ADC sample eroded completely through the single layer at one edge; therefore, the obtained erosion yield value is a minimum value.

MISSE 2
2-E5-15
PS

AO fluence = 8.43×10^{21} atoms/cm^2

Post-flight photograph of flight sample in E5 tray

Polymer:	Polystyrene
Abbreviation:	PS
Trade name(s):	Trycite® 1000 PS
Thickness of each layer:	50.8 μm (2 mil)
Numbers layers flown:	22 (12 Part A + 10 Part B)
Total thickness:	558.8 μm (22 mil)

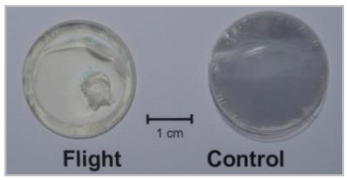

Post-flight photograph of stacked sample layers

Pre-Flight Data

Part A:	
Layers in part A:	12
Average mass of flight sample part A:	209.757 mg
Part B:	N/A
Total pre-flight sample mass:	**209.757 mg**

Post-flight photograph of individual sample layers. Layers were separated for weighing. (Mass loss Situation 1)

Post-Flight Data

Mass loss situation:	Situation 1
Layers needed to be weighed for E_y:	12 (Part A)
Layers weighed in Part A:	12
Average mass of Part A + Part B:	93.810 mg
Total post-flight sample mass:	**93.810 mg**

Erosion Yield Data

Flight sample mass loss:	0.115947 g
Average density:	1.0503 g/cm^3
Exposed area:	3.5043 cm^2

MISSE 2 E_y: 3.74 (±0.10) ×10^{-24} cm^3/atom

MISSE 2
2-E5-16
PMMA

AO fluence = 8.43×10^{21} atoms/cm^2

Polymer:	Polymethyl methacrylate
Abbreviation:	PMMA
Trade name(s):	Plexiglas®; Acrylite® (Impact Mod.)
Layer thickness:	50.8 μm (2 mil)
Number layers flown:	10 (5 Part A + 5 Part B)
Total thickness:	254 μm (20 mil)

Post-flight photograph of flight sample in E5 tray

Pre-Flight Data

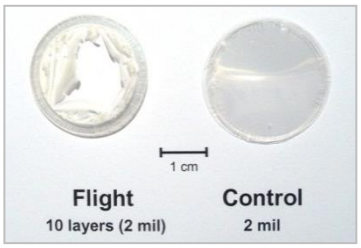

Post-flight photograph of stacked sample layers. Layers could not be separated for weighing post flight. (Mass loss Situation 3)

Part A:

Layers in Part A:	5
Average mass of flight sample Part A:	150.438 mg
Average mass of control sample Part A:	146.653 mg

Part B:

Layers in Part B:	5
Computed mass for flight sample Part B:	148.546 mg*
Total pre-flight sample mass:	**298.984 mg**

Post-Flight Data

Mass loss situation:	Situation 3
Layers needed to be weighed for E_y:	10 (5 Part A + 5 Part B)
Layers weighed in Part A + Part B:	10
Average mass of Part A + Part B:	104.396 mg
Total post-flight sample mass:	**104.396 mg**

Erosion Yield Data

Flight sample mass loss:	0.194588 g
Average density:	1.1628 g/cm^3
Exposed area:	3.5456 cm^2

MISSE 2 E_y: $>5.60\times10^{-24}$ cm^3/atom**

* Computed mass for Part B is based on the average mass for Part A flight and control samples.

** The PMMA sample eroded completely through all layers in the center of the sample; therefore, the obtained erosion yield value is a minimum value.

MISSE 2
2-E5-17
PEO

AO fluence = 8.43×10^{21} atoms/cm^2

Polymer:	Polyethylene oxide
Abbreviation:	PEO
Trade name(s):	Alkox® E-30 (powder)*
Thickness of each layer:	736.6 μm (29 mil)
Numbers layers flown:	1 (Part A)
Total thickness:	736.6 μm (29 mil)
Vacuum heat treatment:	24 hr at 60 °C

Post-flight photograph of flight sample in E5 tray

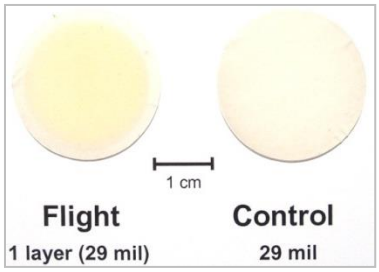

Post-flight photograph of flight and control samples
(Mass loss Situation 1)

Pre-Flight Data

Part A:	
Layers in Part A:	1 (Part A)
Average mass of flight sample Part A:	471.393 mg
Part B:	N/A
Total pre-flight sample mass:	**471.393 mg**

Post-Flight Data

Mass loss situation:	Situation 1
Layers needed to be weighed for E_y:	1 (Part A)
Layers weighed in Part A:	1
Average mass of Part A + Part B:	404.998 mg
Total post-flight sample mass:	**404.998 mg**

Erosion Yield Data

Flight sample mass loss:	0.066395 g
Average density:	1.1470 g/cm^3
Exposed area:	3.5591 cm^2
MISSE 2 E_y:	**1.93 (± 0.05) ×10^{-24} cm^3/atom**

* This sample was pressured into a solid from powder.

MISSE 2
2-E5-18
PBO

AO fluence = 8.43×10^{21} atoms/cm^2

Post-flight photograph of flight sample in E5 tray

Polymer:	Poly (p-phenylene-2,6-benzobisoxazole)
Abbreviation:	PBO
Trade name(s):	Zylon®, (Balanced biaxial film)
Thickness of each layer:	25.4 μm (1 mil)
Numbers layers flown:	11 (6 Part A + 5 Part B)
Total thickness:	279.4 μm (11 mil)

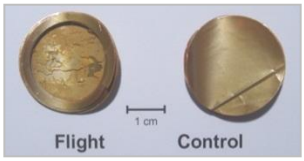

Post-flight photograph of stacked sample layers (11 flight; 4 control)

Pre-Flight Data

Part A:	
Layers in Part A:	6
Average mass of flight sample Part A:	89.146 mg
Average mass of control sample Part A:	N/A
Part B:	
Layers in Part B:	5
Computed mass for flight sample Part B:	74.288 mg*
Total pre-flight sample mass:	**163.434 mg**

Post-Flight Data

Mass loss situation:	Situation 2
Layers needed to be weighed for E_y:	11 (6 Part A + 5 Part B)
Layers weighed in Part A:	6
Average mass of Part A:	33.235 mg
Layers weighed in Part B:	5
Average mass of Part B:	73.421 mg
Average mass of Part A + Part B:	106.656 mg
Total post-flight sample mass:	**106.656 mg**

Erosion Yield Data

Flight sample mass loss:	0.056778 g
Average density:	1.3976 g/cm^3
Exposed area:	3.5526 cm^2

Post-flight photograph of individual sample layers (11 flight; 4 control). Layers were separated for weighing postflight. (Mass loss Situation 2)

MISSE 2 E_y: 1.36 (±0.08) ×10^{-24} cm^3/atom

* Computed mass for part B is based on the average mass for Part A flight sample layers.

MISSE 2
2-E5-19
EP

AO fluence = 8.43×10^{21} atoms/cm^2

Polymer:	Epoxide or epoxy
Abbreviation:	EP
Trade name(s):	Hysol® EA 956
Thickness of each layer:	2,286 μm (90 mil) Thickness of flight sample from 2,286 to 2,336.8 μm (90 to 92 mil)
Numbers layers flown:	1 (Part A)
Total thickness:	2,286 μm (90 mil)

Post-flight photograph of flight sample in E5 tray

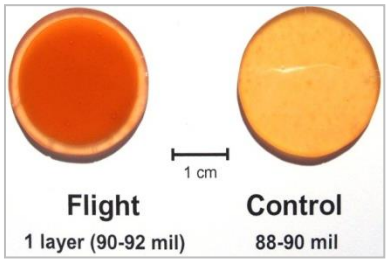

Post-flight photograph of flight and control samples
(Mass loss Situation 1)

Pre-Flight Data

Part A:	
Layers in Part A:	1
Average mass of flight sample Part A:	1,325.610 mg
Part B:	N/A
Total pre-flight sample mass:	**1,325.610 mg**

Post-Flight Data

Mass loss situation:	Situation 1
Layers needed to be weighed for E_y:	1 (Part A)
Layers weighed in Part A:	1
Average mass of Part A:	1,184.890 mg
Total post-flight sample mass:	**1,184.890 mg**

Erosion Yield Data

Flight sample mass loss:	0.140720 g
Average density:	1.1150 g/cm^3
Exposed area:	3.5576 cm^2
MISSE 2 E_y:	**4.21 (±0.11) ×10^{-24} cm^3/atom**

MISSE 2
2-E5-20
PP

AO fluence = 8.43×10^{21} atoms/cm^2

Polymer:	Polypropylene
Abbreviation:	PP
Trade name(s):	Contour 28, Goex
Thickness of each layer:	508 μm (20 mil)
Numbers layers flown:	1 (part A)
Total thickness:	508 μm (20 mil)

Post-flight photograph of flight sample in E5 tray

Pre-Flight Data

Part A:	
Layers in Part A:	1
Average mass of flight sample Part A:	235.923 mg
Part B:	N/A
Total pre-flight sample mass:	**235.923 mg**

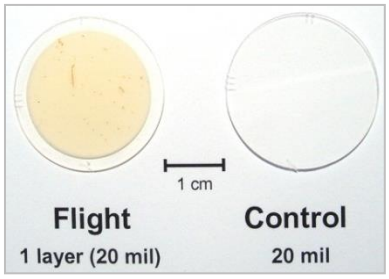

Post-flight photograph of flight and control samples
(Mass loss Situation 1)

Post-Flight Data

Mass loss situation:	Situation 1
Layers needed to be weighed for E_y:	1 (Part A)
Layers weighed in Part A:	1
Average mass of Part A:	163.566 mg
Total post-flight sample mass:	**163.566 mg**

Erosion Yield Data

Flight sample mass loss:	0.072357 g
Average density:	0.9065 g/cm^3
Exposed area:	3.5336 cm^2

MISSE 2 E_y: 2.68 (±0.07) ×10^{-24} cm^3/atom

MISSE 2
2-E5-21
PBT

AO fluence = 8.43×10^{21} atoms/cm^2

Polymer:	Polybutylene terephthalate
Abbreviation:	PBT
Trade name(s):	VALOX® 357
Thickness of each layer:	76.2 μm (3 mil)
Numbers layers flown:	5 (3 Part A + 2 Part B)
Total thickness:	381 μm (15 mil)

Post-flight photograph of flight sample in E5 tray

Pre-Flight Data

Part A:

Layers in Part A:	3
Average mass of flight sample Part A:	153.324 mg
Average mass of control sample Part A:	144.845 mg

Part B:

Layers in Part B:	2
Computed mass of flight sample Part B:	99.390 mg*
Total pre-flight sample mass:	**252.714 mg**

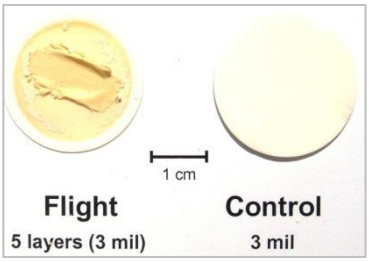

Post-flight photograph of stacked sample layers. Sample layers could not be separated for weighing.
(Mass loss Situation 3)

Post-Flight Data

Mass loss situation:	Situation 3
Layers needed to be weighed for E_y:	5 (3 Part A + 2 Part B)
Layers weighed in Part A + Part B:	5
Average mass of Part A + Part B:	216.285 mg
Total post-flight sample mass:	**216.285 mg**

Erosion Yield Data

Flight sample mass loss:	0.036429 g
Average density:	1.3318 g/cm^3
Exposed area:	3.5619 cm^2

MISSE 2 E_y: 9.11 (±0.24) ×10^{-25} cm^3/atom*

* Computed mass for Part B is based on the average mass for Part A flight and control samples.

MISSE 2
2-E5-22
PSU

AO fluence = 8.43×10^{21} atoms/cm^2

Post-flight photograph of flight sample in E5 tray

Polymer:	Polysulfone
Abbreviation:	PSU
Trade name(s):	Thermalux® P1700-NT11, Udel® P-1700

Thickness of each layer:	50.8 μm (2 mil)
Numbers layers flown:	6 (3 Part A + 3 Part B)
Total thickness:	304.8 μm (12 mil)

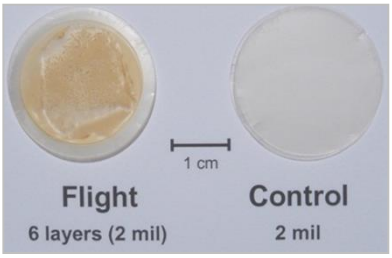

Post-flight photograph of stacked sample layers

Pre-Flight Data

Part A:

Layers in Part A:	3
Average mass of flight sample Part A:	91.437 mg
Average mass of control sample Part A:	92.409 mg

Part B:

Layers in Part B:	3
Computed mass of flight sample Part B:	91.923 mg*
Total pre-flight sample mass:	**183.360 mg**

Post-Flight Data

Mass loss situation:	Situation 2
Layers needed to be weighed for E_y:	6 (3 Part A + 3 Part B)
Layers weighed in Part A:	3
Average mass of Part A:	28.850 mg
Layers weighed in Part B:	3
Average mass of Part B:	48.562
Average mass of Part A + Part B:	77.412 mg
Total post-flight sample mass:	**77.412 mg**

Erosion Yield Data

Flight sample mass loss:	0.0105948 g
Average density:	1.2199 g/cm^3
Exposed area:	3.5010 cm^2

Post-flight photograph of individual sample layers. Layers were separated for weighing. (Mass loss Situation 2)

MISSE 2 E_y: 2.94 (±0.09) ×10^{-24} cm^3/atom

* Computed mass for Part B is based on the average mass for Part A flight and control samples.

MISSE 2
2-E5-23
PU

AO fluence = 8.43×10^{21} atoms/cm^2

Polymer:	Polyurethane
Abbreviation:	PU
Trade name(s):	Dureflex® PS8010
Thickness of each layer:	50.8 μm (2 mil)
Numbers layers flown:	9 (5 Part A + 4 Part B)
Total thickness:	50.8 μm (18 mil)

Post-flight photograph of flight sample in E5 tray

Pre-Flight Data

Part A:

Layers in Part A:	5
Average mass of flight sample Part A:	169.325 mg
Average mass of control sample Part A:	171.875 mg

Part B:

Layers in Part B:	4
Computed mass of flight sample Part B:	136.480 mg*
Total pre-flight sample mass:	**305.805 mg**

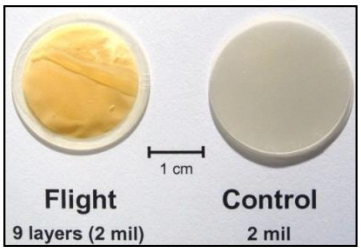

Post-flight photograph of flight and control stacked sample layers. Sample layers could not be separated for weighing. (Mass loss Situation 3)

Post-Flight Data

Mass loss situation:	Situation 3
Layers needed to be weighed for E_y:	9 (5 Part A + 4 Part B)
Layers weighed in Part A + Part B:	9
Average mass of Part A + Part B:	248.578 mg
Total post-flight sample mass:	**248.578 mg**

Erosion Yield Data

Flight sample mass loss:	0.057227 g
Average density:	1.2345 g/cm^3
Exposed area:	3.5182 cm^2
MISSE 2 E_y:	**1.56 (±0.05) ×10^{-24} cm^3/atom**

* Computed mass for Part B is based on the average mass for Part A flight and control samples.

MISSE 2
2-E5-24
PPPA

AO fluence = 8.43×10^{21} atoms/cm^2

Post-flight photograph of flight sample in E5 tray

Polymer:	Polyphenylene isophthalate
Abbreviation:	PPPA
Trade name(s):	Nomex® Crepe Paper T-410
Thickness of each layer:	50.8 μm (2 mil)
Numbers layers flown:	6 (3 Part A + 3 Part B)
Total thickness:	304.8 μm (12 mil)
Vacuum heat treatment:	24 hr at 125 °C

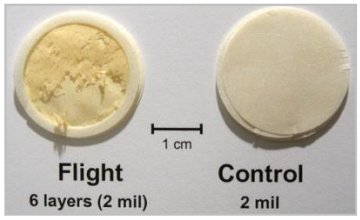

Post-flight photograph of stacked sample layers

Pre-Flight Data

Part A:

Layers in Part A:	3
Average mass of flight sample Part A:	60.895 mg
Average mass of control sample Part A:	59.950 mg

Part B:

Layers in Part B:	3
Computed mass of flight sample Part B:	60.423 mg*
Total pre-flight sample mass:	**121.318 mg**

Post-Flight Data

Mass loss situation:	Situation 2
Layers needed to be weighed for E_y:	6 (3 Part A + 3 Part B)
Layers weighed in Part A:	3
Average mass of Part A:	32.112 mg
Layers weighed in Part B:	3
Average mass of Part B:	58.657 mg
Average mass of Part A + Part B:	90.769 mg
Total post-flight sample mass:	**90.769 mg**

Erosion Yield Data

Flight sample mass loss:	0.030549 g
Average density:	0.72 g/cm^3
Exposed area:	3.5626 cm^2

Post-flight photograph of individual sample layers. Layers were separated for weighing. (Mass loss Situation 2)

MISSE 2 E_y: 1.41 (±0.04) ×10^{-24} cm^3/atom

* Computed mass for Part B is based on the average mass for Part A flight and control samples.

MISSE 2
2-E5-25
PG

AO fluence = 8.43×10^{21} atoms/cm^2

Polymer:	Graphite
Abbreviation:	PG
Trade name(s):	Pyrolytic graphite
Thickness of each layer:	2,032 μm (80 mil)
Numbers layers flown:	1 (Part A)
Total thickness:	2,032 μm (80 mil)

Post-flight photograph of flight sample in E5 tray

Pre-Flight Data

Part A:	
Layers in Part A:	1
Average mass of flight sample Part A:	2,098.73 mg
Part B:	N/A
Total pre-flight sample mass:	**2,098.73 mg**

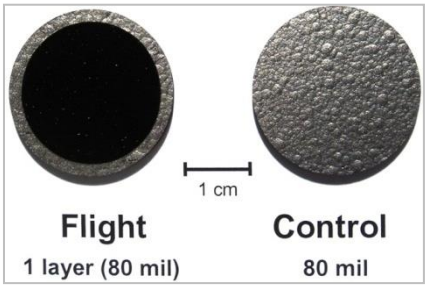

Post-flight photograph of flight and control samples
(Mass loss Situation 1)

Post-Flight Data

Mass loss situation:	Situation 1
Layers needed to be weighed for E_y:	1 (Part A)
Layers weighed in Part A:	1
Average mass of Part A:	2,071 mg
Total post-flight sample mass:	**2,071 mg**

Erosion Yield Data

Flight sample mass loss:	0.02773 g
Average density:	2.22 g/cm^3
Exposed area:	3.5703 cm^2

MISSE 2 E_y: 4.15 (±0.45) ×10^{-25} cm^3/atom

MISSE 2
2-E5-26
PEI

AO fluence = 8.43×10^{21} atoms/cm^2

Polymer:	Polyetherimide
Abbreviation:	PEI
Trade name(s):	Ultem® 1000
Thickness of each layer:	254 μm (10 mil)
Numbers layers flown:	2 (1 Part A + 1 Part B)
Total thickness:	508 μm (20 mil)

Post-flight photograph of flight sample in E5 tray

Pre-Flight Data

Part A:

Layers in Part A:	1
Average mass of flight sample Part A:	165.411 mg
Average mass of control sample Part A:	162.855 mg

Part B:

Layers in Part B:	1
Computed mass of flight sample Part B:	164.133 mg*
Total pre-flight sample mass:	**329.544 mg**

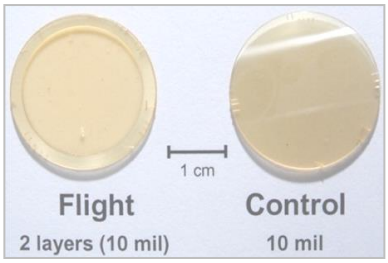

Post-flight photograph of stacked sample layers

Post-Flight Data

Mass loss situation:	Situation 2
Layers needed to be weighed for E_y:	2 (1 Part A + 1 Part B)
Layers weighed in Part A:	1
Average mass of Part A:	50.379 mg
Layers weighed in Part B:	1
Average mass of Part B:	152.312 mg
Average mass of Part A + Part B:	202.691 mg
Total post-flight sample mass:	**202.691 mg**

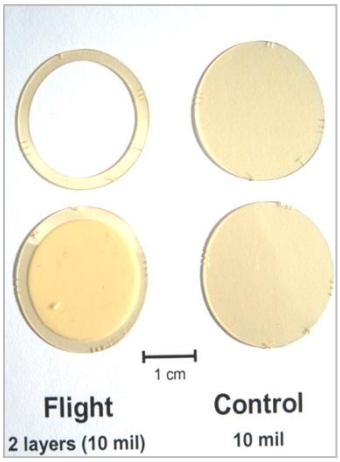

Post-flight photograph of individual sample layers. Layers were separated for weighing. (Mass loss Situation 2)

Erosion Yield Data

Flight sample mass loss:	0.126853 g
Average density:	1.2873 g/cm^3
Exposed area:	3.5352 cm^2

MISSE 2 E_y: >3.31×10^{-24} cm^3/atom**

* Computed mass for Part B is based on the average mass for Part A flight and control samples.

** The PEI sample eroded through both layers leaving pinhole windows in the second layer; therefore, the obtained erosion yield value is a minimum value.

MISSE 2
2-E5-27
PA 6

AO fluence = 8.43×10^{21} atoms/cm^2

Post-flight photograph of flight sample in E5 tray

Post-flight photograph of stacked sample layers

Polymer:	Polyamide 6
Abbreviation:	PA 6
Trade name(s):	Nylon 6
Thickness of each layer:	50.8 μm (2 mil)
Numbers layers flown:	8 (4 Part A + 4 Part B)
Total thickness:	406.4 μm (16 mil)
Vacuum heat treatment:	24 hr at 90 °C

Pre-Flight Data

Part A:	
Layers in Part A:	4
Average mass of flight sample Part A:	103.716 mg
Average mass of control sample Part A:	105.508 mg
Part B:	
Layers in Part B:	4
Computed mass of flight sample Part B:	104.612 mg*
Total pre-flight sample mass:	**208.328 mg**

Post-Flight Data

Mass loss situation:	Situation 3
Layers needed to be weighed for E_y:	8 (4 Part A + 4 Part B)
Layers weighed in Part A + Part B:	8
Average mass of Part A + Part B:	89.952 mg
Total post-flight sample mass:	**89.952 mg**

Post-flight photograph of individual sample layers (layers 6, 7, and 8 are together. Layers could be separated but were weighed together because of fragile pieces. (Mass loss Situation 3)

Erosion Yield Data

Flight sample mass loss:	0.118376 g
Average density:	1.1233 g/cm^3
Exposed area:	3.5646 cm^2

MISSE 2 E_y: 3.51 (±0.09)×10^{-24} cm^3/atom

* Computed mass for Part B is based on the average mass for Part A flight and control samples.

MISSE 2
2-E5-28
PA 66

AO fluence = 8.43×10^{21} atoms/cm^2

Post-flight photograph of flight sample in E5 tray

Polymer:	Polyamide 66
Abbreviation:	PA 66
Trade name(s):	Nylon 66
Thickness of each layer:	50.8 μm (2 mil)
Numbers layers flown:	7 (4 Part A + 3 Part B)
Total thickness:	355.6 μm (14 mil)
Vacuum heat treatment:	24 hr at 90 °C

Post-flight photograph of stacked sample layers

Pre-Flight Data

Part A:	
Layers in Part A:	4
Average mass of flight sample Part A:	123.209 mg
Average mass of control sample Part A:	119.719 mg
Part B:	
Layers in Part B:	3
Computed mass of flight sample Part B:	91.098 mg*
Total pre-flight sample mass:	**214.307 mg**

Post-Flight Data

Mass loss situation:	Situation 2
Layers needed to be weighed for E_y:	7 (4 Part A + 3 Part B)
Layers weighed in Part A:	4
Average mass of Part A:	58.331 mg
Layers weighed in Part B:	3
Average mass of Part B:	90.414 mg
Average mass of Part A + Part B:	148.745
Total post-flight sample mass:	**148.745 mg**

Erosion Yield Data

Flight sample mass loss:	0.065562 g
Average density:	1.2252 g/cm^3
Exposed area:	3.5249 cm^2

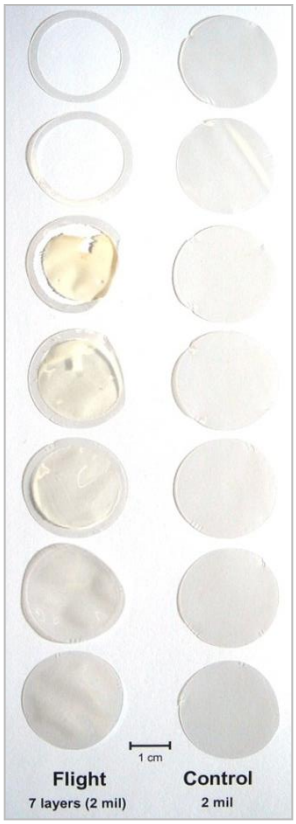

Post-flight photograph of flight and control sample individual sample layers. Layers were separated for weighing post-flight. (Mass loss Situation 2)

MISSE 2 E_y: $1.80\ (\pm0.23)\times10^{-24}$ cm^3/atom

* Computed mass for Part B is based on the average mass for Part A flight and control samples.

MISSE 2
2-E5-29
PI (CP1)

AO fluence = 8.43×10^{21} atoms/cm^2

Polymer:	Polyimide
Abbreviation:	PI
Trade name(s):	CP1
Thickness of each layer:	76.2 μm (3 mil)
Numbers layers flown:	4 (2 Part A + 2 Part B)
Total thickness:	304.8 μm (12 mil)

Post-flight photograph of flight sample in E5 tray

Pre-Flight Data

Part A:

Layers in Part A:	2
Average mass of flight sample Part A:	118.260 mg
Average mass of control sample Part A:	118.067 mg

Part B:

Layers in Part B:	2
Computed mass of flight sample Part B:	118.164 mg*
Total pre-flight sample mass:	**236.424 mg**

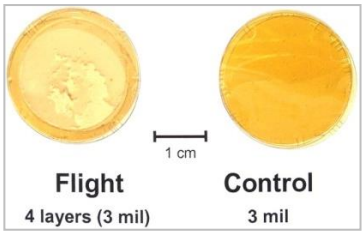

Post-flight photograph of stacked sample layers. Sample layers could not be separated for weighing.
(Mass loss Situation 3)

Post-Flight Data

Mass loss situation:	Situation 3
Layers needed to be weighed for E_y:	4 (2 Part A + 2 Part B)
Layers weighed in Part A + Part B:	4
Average mass of Part A + Part B:	155.776 mg
Total post-flight sample mass:	**155.776 mg**

Erosion Yield Data

Flight sample mass loss:	0.080648 g
Average density:	1.4193 g/cm^3
Exposed area:	3.5316 cm^2
MISSE 2 E_y:	**$1.91\ (\pm0.05)\times10^{-24}$ cm^3/atom**

* Computed mass for Part B is based on the average mass for Part A flight and control samples.

MISSE 2
2-E5-30
PI (Kapton® H) (AO fluence witness sample)

MISSE 2 E_y: 3.00 (±0.07)×10^{-24} cm^3/atom (based on prior LEO flight data)

Polymer: Polyimide (PMDA)
Abbreviation: PI
Trade name(s): Kapton® H

Thickness of each layer: 127 μm (5 mil)
Numbers layers flown: 3 (2 Part A + 1 Part B)
Total thickness: 381 μm (15 mil)

Post-flight photograph of flight sample in E5 tray

Pre-Flight Data

Part A:

Layers in Part A: 2
Average mass of flight sample Part A: 187.793 mg
Average mass of control sample Part A: 187.053 mg

Part B:

Layers in Part B: 1
Computed mass of flight sample Part B: 93.712 mg*

Total pre-flight sample mass: **281.505 mg**

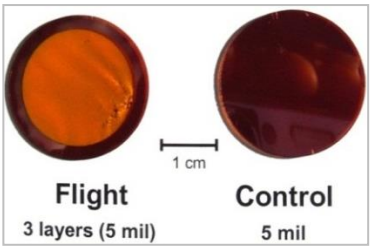

Post-flight photograph of stacked sample layers

Post-Flight Data

Mass loss situation: Situation 2
Layers needed to be weighed for E_y: 3 (2 Part A + 1 Part B)
Layers weighed in Part A: 2
Average mass of Part A: 65.411 mg
Layers weighed in Part B: 1
Average mass of Part B: 91.309 mg
Average mass of Part A + Part B: 156.720 mg

Total post-flight sample mass: **156.720 mg**

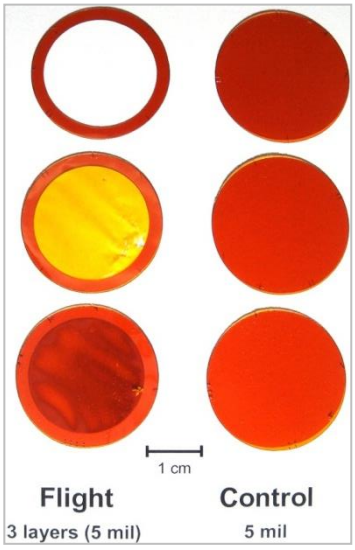

Post-flight photograph of individual sample layers. Layers were separated for weighing. (Mass loss Situation 2)

Atomic Oxygen Fluence Data

Flight sample mass loss: 0.124785 g
Average density: 1.4273 g/cm^3
Exposed area: 3.4590 cm^2

Atomic Oxygen Fluence: 8.425×10^{21} atoms/cm^2

* Computed mass for Part B is based on the average mass for Part A flight and control samples.

MISSE 2
2-E5-31
PI (Kapton® HN)

AO fluence = 8.43×10^{21} atoms/cm^2

Polymer:	Polyimide (PMDA)
Abbreviation:	PI
Trade name(s):	Kapton® HN
Thickness of each layer:	127 μm (5 mil)
Numbers layers flown:	3 (2 Part A + 1 Part B)
Total thickness:	381 μm (15 mil)

Post-flight photograph of flight sample in E5 tray

Pre-Flight Data

Part A:	
Layers in Part A:	2
Average mass of flight sample Part A:	183.483 mg
Average mass of control sample Part A:	182.544 mg
Part B:	
Layers in Part B:	1
Computed mass of flight sample Part B:	91.507 mg*
Total pre-flight sample mass:	**274.990 mg**

Post-flight photograph of stacked sample layers

Post-Flight Data

Mass loss situation:	Situation 2
Layers needed to be weighed for E_y:	3 (2 Part A + 1 Part B)
Layers weighed in Part A:	2
Average mass of Part A:	62.924 mg
Layers weighed in Part B:	1
Average mass of Part B:	90.751 mg
Average mass of Part A + Part B:	153.675

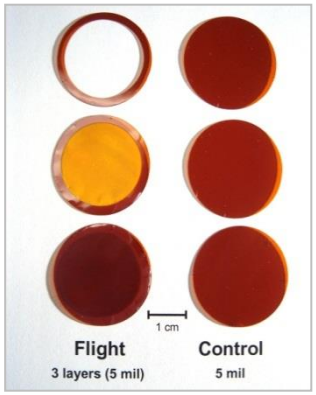

Post-flight photograph of individual sample layers. Layers were separated for weighing. (Mass loss Situation 2)

Erosion Yield Data

Flight sample mass loss:	0.121315 g
Average density:	1.4346 g/cm^3
Exposed area:	3.5676 cm^2

MISSE 2 E_y: 2.81 (±0.07)×10^{-24} cm^3/atom

* Computed mass for Part B is based on the average mass for Part A flight and control samples.

MISSE 2
2-E5-32
PI (Upilex-S®)

AO fluence = 8.43×10^{21} atoms/cm^2

Post-flight photograph of flight sample in E5 tray

Polymer:	Polyimide (BPDA)
Abbreviation:	PI
Trade name(s):	Upilex-S®
Thickness of each layer:	25.4 μm (1 mil)
Numbers layers flown:	11 (6 Part A + 5 Part B)
Total thickness:	279.4 μm (11 mil)

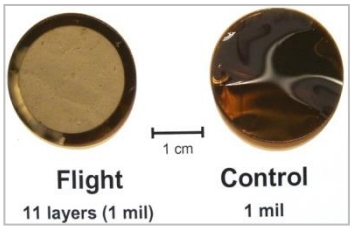

Post-flight photograph of stacked sample layers

Pre-Flight Data

Part A:	
Layers in Part A:	6
Average mass of flight sample Part A:	116.016
Part B:	N/A
Total pre-flight sample mass:	**116.016 mg**

Post-flight photograph of individual sample layers (11 flight; 10 control). Layers were separated for weighing. (Mass loss Situation 1)

Post-Flight Data

Mass loss situation:	Situation 1
Layers needed to be weighed for E_y:	6 (Part A)
Layers weighed in Part A:	6
Average mass of Part A:	77.889 mg
Total post-flight sample mass:	**77.889 mg**

Erosion Yield Data

Flight sample mass loss:	0.038127 g
Average density:	1.3866 g/cm^3
Exposed area:	3.5382 cm^2

MISSE 2 E_y: 9.22 (±0.28)×10^{-25} cm^3/atom

MISSE 2
2-E5-33
PI (Kapton® H) (AO fluence witness sample)

MISSE 2 E_y: 3.00 (±0.07)×10^{-24} cm^3/atom (based on prior LEO flight data)

Polymer:	Polyimide (PMDA)
Abbreviation:	PI
Trade name(s):	Kapton® H
Thickness of each layer:	127 μm (5 mil)
Numbers layers flown:	3 (2 Part A + 1 Part B)
Total thickness:	381 μm (15 mil)

Post-flight photograph of flight sample in E5 tray

Pre-Flight Data

Part A:

Layers in Part A:	2
Average mass of flight sample Part A:	185.329 mg
Average mass of control sample Part A:	186.192 mg

Part B:

Layers in Part B:	1
Computed mass of flight sample Part B:	92.880 mg*
Total pre-flight sample mass:	**278.209 mg**

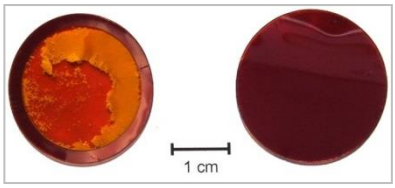

Post-flight photograph of stacked sample layers. Sample layers could not be separated for weighing. (Mass loss Situation 3)

Post-Flight Data

Mass loss situation:	Situation 3
Layers needed to be weighed for E_y:	3 (2 Part A + 1 Part B)
Layers weighed in Part A + Part B:	3
Average mass of Part A + Part B:	148.990 mg
Total post-flight sample mass:	**148.990 mg**

Atomic Oxygen Fluence Data

Flight sample mass loss:	0.129219 mg
Average density:	1.4273 g/cm^3
Exposed area:	3.5773 cm^2

Atomic Oxygen Fluence: **8.436×10^{21} atoms/cm^2**

* Computed mass for Part B is based on the average mass for Part A flight and control samples.

MISSE 2
2-E5-34
PI (PMR-15)

AO fluence = 8.43×10^{21} atoms/cm^2

Polymer:	High temperature polyimide resin
Abbreviation:	PI
Trade name(s):	PMR-15
Thickness of each layer:	304.8 μm (12 mil)
Numbers layers flown:	1 (1 Part A)
Total thickness:	304.8 μm (12 mil)

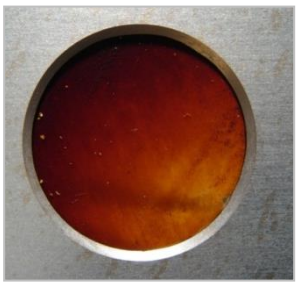

Post-flight photograph of flight sample in E5 tray

Pre-Flight Data

Part A:	
Layers in Part A:	1
Average mass of flight sample Part A:	198.186 mg
Part B:	N/A
Total pre-flight sample mass:	**198.186 mg**

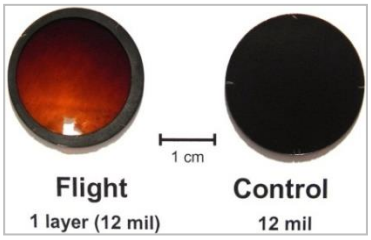

Post-flight photograph of flight and control samples
(Mass loss Situation 1)

Post-Flight Data

Mass loss situation:	Situation 1
Layers needed to be weighed for E_y:	1 (Part A)
Layers weighed in Part A:	1
Average mass of Part A:	79.299 mg
Total post-flight sample mass:	**79.299 mg**

Erosion Yield Data

Flight sample mass loss:	0.118887 mg
Average density:	1.3232 g/cm^3
Exposed area:	3.5256 cm^2
MISSE 2 E_y:	**>3.02×10^{-24} cm^3/atom***

* The PI sample eroded completely through the single layer at one edge; therefore, the obtained erosion yield value is a minimum value.

MISSE 2
2-E5-35
PBI

AO fluence = 8.43×10^{21} atoms/cm^2

Polymer:	Polybenzimidazole
Abbreviation:	PBI
Trade name(s):	Celazole™, PBI 22
Thickness of each layer:	50.8 μm (2 mil)
Numbers layers flown:	4 (2 Part A + 2 Part B) in Al foil
Total thickness:	203.2 μm (8 mil)
Vacuum heat treatment:	24 hr at 125 °C

Post-flight photograph of flight sample in E5 tray

Pre-Flight Data

Part A:

Layers in Part A:	2
Average mass of flight sample Part A:	53.749 mg
Average mass of control sample Part A: (samples weighed without Al foil)	53.531 mg

Part B:

Layers in Part B:	2
Computed mass of flight sample Part B:	53.640 mg*
Total pre-flight sample mass:	**107.389 mg**

Post-flight photograph of stacked sample layers. Sample layers could not be separated for weighing. (Mass loss Situation 2)

Post-Flight Data

Mass loss situation:	Situation 2
Layers needed to be weighed for E_y:	4 (2 Part A + 2 Part B)
Layers weighed in Part A:	2
Average mass of Part A:	12.022 mg
Layers weighed in Part B:	2
Average mass of Part B:	12.659 mg
Average mass of Part A + Part B:	24.681 mg
Total post-flight sample mass:	**24.681 mg**

Erosion Yield Data

Flight sample mass loss:	0.082708 g
Average density:	1.2758 g/cm^3
Exposed area:	3.4762 cm^2
MISSE 2 E_y:	**$>2.21\times10^{-24}$ cm^3/atom****

* Computed mass for Part B is based on the average mass for Part A flight and control samples.

** The PBI sample eroded completely through all layers (only protected edge "rings" left); therefore, the obtained erosion yield value is a minimum value.

MISSE 2
2-E5-36
PC

AO fluence = 8.43×10^{21} atoms/cm^2

Polymer:	Polycarbonate
Abbreviation:	PC
Trade name(s):	PEEREX® 61
Thickness of each layer:	254 μm (10 mil)
Numbers layers flown:	2 (1 Part A + 1 Part B)
Total thickness:	508 μm (20 mil)

Post-flight photograph of flight sample in E5 tray

Pre-Flight Data

Part A:

Layers in Part A:	1
Average mass of flight sample Part A:	142.017 mg
Average mass of control sample Part A:	142.936 mg

Part B:

Layers in Part B:	1
Computed mass of flight sample Part B:	142.477 mg*
Total pre-flight sample mass:	**284.494 mg**

Post-flight photograph of stacked sample layers

Post-Flight Data

Mass loss situation:	Situation 2
Layers needed to be weighed for E_y:	2 (1 Part A + 1 Part B)
Layers weighed in Part A:	1
Average mass of Part A:	44.276 mg
Layers weighed in Part B:	1
Average mass of Part B:	97.931 mg
Average mass of Part A + Part B:	142.207 mg
Total post-flight sample mass:	**142.207 mg**

Post-flight photograph of individual sample layers. Layers were separated for weighing. (Mass loss Situation 2)

Erosion Yield Data

Flight sample mass loss:	0.142287 g
Average density:	1.1231 g/cm^3
Exposed area:	3.5010 cm^2
MISSE 2 E_y:	**4.29 (±0.11)×10^{-24} cm^3/atom**

* Computed mass for Part B is based on the average mass for Part A flight and control samples.

MISSE 2
2-E5-37
PEEK

AO fluence = 8.43×10^{21} atoms/cm^2

Post-flight photograph of flight sample in E5 tray

Polymer:	Polyetheretherkeytone
Abbreviation:	PEEK
Trade name(s):	Victrex® PEEK™ 450
Thickness of each layer:	76.2 μm (3 mil)
Numbers layers flown:	6 (3 Part A + 3 Part B)
Total thickness:	457.2 μm (18 mil)

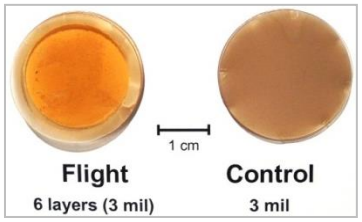

Post-flight photograph of stacked sample layers

Pre-Flight Data

Part A:	
Layers in Part A:	3
Average mass of flight sample Part A:	136.462 mg
Average mass of control sample Part A:	136.815 mg
Part B:	
Layers in Part B:	3
Computed mass of flight sample Part B:	136.639 mg*
Total pre-flight sample mass:	**273.101 mg**

Post-Flight Data

Mass loss situation:	Situation 2
Layers needed to be weighed for E_y:	6 (3 Part A + 3 Part B)
Layers weighed in Part A:	3
Average mass of Part A:	43.728 mg
Layers weighed in Part B:	3
Average mass of Part B:	121.609
Average mass of Part A + Part B:	165.337
Total post-flight sample mass:	**165.337 mg**

Erosion Yield Data

Flight sample mass loss:	0.107764 g
Average density:	1.2259 g/cm^3
Exposed area:	3.4821 cm^2

Post-flight photograph of individual sample layers. Layers were separated for weighing. (Mass loss Situation 2)

MISSE 2 E_y: $2.99\ (\pm0.14)\times10^{-24}$ cm^3/atom

* Computed mass for Part B is based on the average mass for Part A flight and control samples.

MISSE 2
2-E5-38
PET

AO fluence = 8.43×10^{21} atoms/cm^2

Polymer:	Polyethylene terephthalate
Abbreviation:	PET
Trade name(s):	Mylar® A-200
Thickness of each layer:	50.8 μm (2 mil)
Numbers layers flown:	8 (4 Part A + 4 Part B)
Total thickness:	406.4 μm (16 mil)

Post-flight photograph of flight sample in E5 tray

Pre-Flight Data

Part A:

Layers in Part A:	4
Average mass of flight sample Part A:	145.133 mg
Average mass of control sample Part A:	143.953 mg

Part B:

Layers in Part B:	4
Computed mass of flight sample Part B:	144.543 mg*
Total pre-flight sample mass:	**289.676 mg**

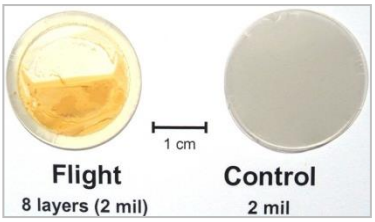

Post-flight photograph of stacked sample layers. Sample layers could not be separated for weighing.
(Mass loss Situation 3)

Post-Flight Data

Mass loss situation:	Situation 3
Layers needed to be weighed for E_y:	8 (4 Part A + 4 Part B)
Layers weighed in Part A + Part B:	8
Average mass of Part A + Part B:	164.489 mg
Total post-flight sample mass:	**164.489 mg**

Erosion Yield Data

Flight sample mass loss:	0.125187 g
Average density:	1.3925 g/cm^3
Exposed area:	3.5432 cm^2

MISSE 2 E_y: $3.01\ (\pm0.08)\times10^{-24}$ cm^3/atom

* Computed mass for Part B is based on the average mass for Part A flight and control samples.

MISSE 2
2-E5-39
CTFE

AO fluence = 8.43×10^{21} atoms/cm^2

Polymer:	Chlorotrifluoroethylene
Abbreviation:	CTFE
Trade name(s):	Kel-F®, Neoflon® M-300
Thickness of each layer:	127 μm (5 mil)
Numbers layers flown:	1 (Part A)
Total thickness:	127 μm (5 mil)

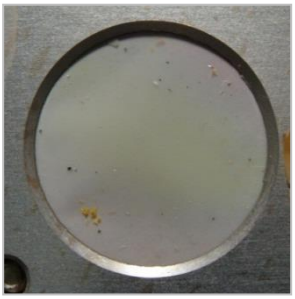

Post-flight photograph of flight sample in E5 tray

Pre-Flight Data

Part A:	
Layers in Part A:	1
Average mass of flight sample Part A:	136.230 mg
Part B:	N/A
Total pre-flight sample mass:	**136.230 mg**

Post-flight photograph of stacked sample layers. Sample layers could not be separated for weighing.
(Mass loss Situation 1)

Post-Flight Data

Mass loss situation:	Situation 1
Layers needed to be weighed for E_y:	1 (Part A)
Layers weighed in Part A:	1
Average mass of Part A:	83.281 mg
Total post-flight sample mass:	**83.281 mg**

Erosion Yield Data

Flight sample mass loss:	0.052949 g
Average density:	2.1327 g/cm^3
Exposed area:	3.5452 cm^2
MISSE 2 E_y:	**8.31 (±0.22)×10^{-25} cm^3/atom**

MISSE 2
2-E5-40
ECTFE

AO fluence = 8.43×10^{21} atoms/cm^2

Polymer:	Ethylene-chlorotrifluoroethylene
Abbreviation:	ECTFE
Trade name(s):	Halar® 300
Thickness of each layer:	76.2 μm (3 mil)
Numbers layers flown:	3 (2 Part A + 1 Part B)
Total thickness:	228.6 μm (9 mil)

Post-flight photograph of flight sample in E5 tray

Pre-Flight Data

Part A:	
Layers in Part A:	2
Average mass of flight sample Part A:	126.118 mg
Average mass of control sample Part A:	125.456 mg
Part B:	
Layers in Part B:	1
Computed mass of flight sample Part B:	62.894 mg*
Total pre-flight sample mass:	**189.012 mg**

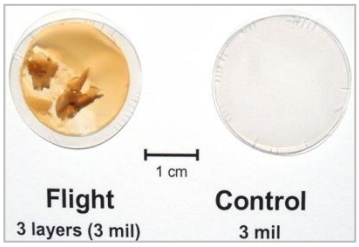

Post-flight photograph of stacked sample layers. Sample layers could not be separated for weighing.
(Mass loss Situation 3)

Post-Flight Data

Mass loss situation:	Situation 3
Layers needed to be weighed for E_y:	3 (2 Part A + 1 Part B)
Layers weighed in Part A + Part B:	3
Average mass of Part A + Part B:	100.143 mg
Total post-flight sample mass:	**100.143 mg**

Erosion Yield Data

Flight sample mass loss:	0.088869 g
Average density:	1.6761 g/cm^3
Exposed area:	3.5103 cm^2

MISSE 2 E_y: 1.79 (±0.05)×10^{-24} cm^3/atom

* Computed mass for Part B is based on the average mass for Part A flight and control samples.

MISSE 2
2-E5-41
ETFE

AO fluence = 8.43×10^{21} atoms/cm^2

Polymer:	Ethylene-tetrafluoroethylene
Abbreviation:	ETFE
Trade name(s):	Tefzel® ZM
Thickness of each layer:	76.2 μm (3 mil)
Numbers layers flown:	2 (1 Part A + 1 Part B)
Total thickness:	152.4 μm (6 mil)

Post-flight photograph of flight sample in E5 tray

Pre-Flight Data

Part A:

Layers in Part A:	1
Average mass of flight sample Part A:	55.710 mg
Average mass of control sample Part A:	54.568 mg

Part B:

Layers in Part B:	1
Computed mass of flight sample Part B:	55.139 mg*
Total pre-flight sample mass:	**110.849 mg**

Post-flight photograph of stacked sample layers

Post-Flight Data

Mass loss situation:	Situation 2
Layers needed to be weighed for E_y:	2 (1 Part A + 1 Part B)
Layers weighed in Part A:	1
Average mass of Part A:	17.845 mg
Layers weighed in Part B:	1
Average mass of Part B:	43.896
Average mass of Part A + Part B:	61.741 mg
Total post-flight sample mass:	**61.741 mg**

Post-flight photograph of individual sample layers. Layers were separated for weighing. (Mass loss Situation 2)

Erosion Yield Data

Flight sample mass loss:	0.049108 g
Average density:	1.7397 g/cm^3
Exposed area:	3.4854 cm^2

MISSE 2 E_y: 9.61 (±0.25)×10^{-25} cm^3/atom

* Computed mass for Part B is based on the average mass for Part A flight and control samples.

MISSE 2
2-E5-42
FEP

AO fluence = 8.43×10^{21} atoms/cm^2

Polymer:	Fluorinated ethylene propylene
Abbreviation:	FEP
Trade name(s):	Teflon® FEP
Thickness of each layer:	50.8 μm (2 mil)
Numbers layers flown:	1 (Part A)
Total thickness:	50.8 μm (2 mil)

Post-flight photograph of flight sample in E5 tray

Pre-Flight Data

Part A:	
Layers in Part A:	1
Average mass of flight sample Part A:	55.402 mg
Part B:	N/A
Total pre-flight sample mass:	**55.402 mg**

Post-flight photograph of sample single layer
(Mass loss Situation 1)

Post-Flight Data

Mass loss situation:	Situation 1
Layers needed to be weighed for E_y:	1 (Part A)
Layers weighed in Part A:	1
Average mass of Part A:	49.923 mg
Total post-flight sample mass:	**42.923 mg**

Erosion Yield Data

Flight sample mass loss:	0.012479 g
Average density:	2.1443 g/cm^3
Exposed area:	3.4468 cm^2
MISSE 2 E_y:	**2.00 (±0.05)×10^{-25} cm^3/atom**

MISSE 2
2-E5-43
PTFE

AO fluence = 8.43×10^{21} atoms/cm^2

Polymer:	Polytetrafluoroethylene
Abbreviation:	PTFE
Trade name(s):	Chemfilm® DF 100
Thickness of each layer:	50.8 μm (2 mil)
Numbers layers flown:	1 (Part A)
Total thickness:	50.8 μm (2 mil)

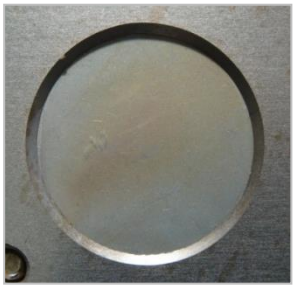

Post-flight photograph of flight sample in E5 tray

Pre-Flight Data

Part A:	
Layers in Part A:	1
Average mass of flight sample Part A:	53.063 mg
Part B:	N/A
Total pre-flight sample mass:	**53.063 mg**

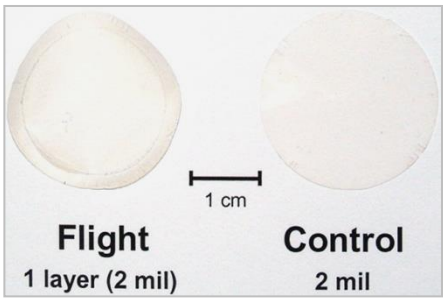

Post-flight photograph of sample single layer
(Mass loss Situation 1)

Post-Flight Data

Mass loss situation:	Situation 1
Layers needed to be weighed for E_y:	1 (Part A)
Layers weighed in Part A:	1
Average mass of Part A:	44.125 mg
Total post-flight sample mass:	**44.125 mg**

Erosion Yield Data

Flight sample mass loss:	0.008938 g
Average density:	2.1503 g/cm^3
Exposed area:	3.4841 cm^2
MISSE 2 E_y:	**1.42 (±0.04)×10^{-25} cm^3/atom**

MISSE 2
2-E5-44
PFA

AO fluence = 8.43×10^{21} atoms/cm^2

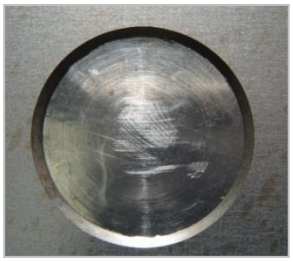

Post-flight photograph of flight sample in E5 tray

Polymer:	Perfluoroalkoxy copolymer resin
Abbreviation:	PFA
Trade name(s):	Teflon® PFA 200 CLP
Thickness of each layer:	50.8 μm (2 mil)
Numbers layers flown:	4 (2 Part A + 2 Part B)
Total thickness:	203.2 μm (8 mil)

Post-flight photograph of stacked sample layers

Pre-Flight Data

Part A:	
Layers in Part A:	2
Average mass of flight sample Part A:	109.264 mg
Part B:	N/A
Total pre-flight sample mass:	**109.264 mg**

Post-flight photograph of individual sample layers. Layers were separated for weighing. (Mass loss Situation 1)

Post-Flight Data

Mass loss situation:	Situation 1
Layers needed to be weighed for E_y:	2 (Part A)
Layers weighed in Part A:	2
Average mass of Part A:	98.479 mg
Total post-flight sample mass:	**98.479 mg**

Erosion Yield Data

Flight sample mass loss:	0.010785 g
Average density:	2.1383 g/cm^3
Exposed area:	3.4570 cm^2

MISSE 2 E_y: 1.73 (±0.05)×10^{-25} cm^3/atom

MISSE 2
2-E5-45
AF

AO fluence = 8.43×10^{21} atoms/cm^2

Polymer:	Amorphous fluoropolymer
Abbreviation:	AF
Trade name(s):	Teflon® AF 1601
Thickness of each layer:	50.8 μm (2 mil)
Numbers layers flown:	1 (Part A)
Total thickness:	50.8 μm (2 mil)

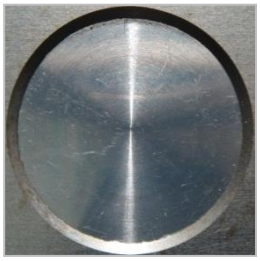

Post-flight photograph of flight sample in E5 tray

Pre-Flight Data

Part A:	
Layers in Part A:	1
Average mass of flight sample Part A:	131.851 mg
Part B:	N/A
Total pre-flight sample mass:	**131.851 mg**

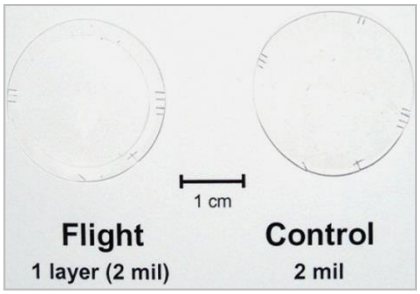

Post-flight photograph of flight and control samples
(Mass loss Situation 1)

Post-Flight Data

Mass loss situation:	Situation 1
Layers needed to be weighed for E_y:	1 (Part A)
Layers weighed in Part A:	1
Average mass of Part A:	119.499 mg
Total post-flight sample mass:	**119.499 mg**

Erosion Yield Data

Flight sample mass loss:	0.012352 g
Average density:	2.1463 g/cm^3
Exposed area:	3.4544 cm^2
MISSE 2 E_y:	**$1.98\ (\pm0.05)\times10^{-25}$ cm^3/atom**

MISSE 2
2-E5-46
PVDF

AO fluence = 8.43×10^{21} atoms/cm^2

Polymer:	Polyvinylidene fluoride
Abbreviation:	PVDF
Trade name(s):	Kynar® 740
Thickness of each layer:	76.2 μm (3 mil)
Numbers layers flown:	2 (1 Part A + 1 Part B)
Total thickness:	152.4 μm (6 mil)

Post-flight photograph of flight sample in E5 tray

Pre-Flight Data

Part A:

Layers in Part A:	1
Average mass of flight sample Part A:	69.266 mg
Average mass of control sample Part A:	71.647 mg

Part B:

Layers in Part B:	1
Computed mass of flight sample Part B:	70.457 mg*
Total pre-flight sample mass:	**139.723 mg**

Post-flight photograph of stacked sample layers

Post-Flight Data

Mass loss situation:	Situation 2
Layers needed to be weighed for E_y:	2 (1 Part A + 1 Part B)
Layers weighed in Part A:	1
Average mass of Part A:	21.347 mg
Layers weighed in Part B:	1
Average mass of Part B:	51.516 mg
Average mass of Part A + Part B:	72.863 mg

Post-flight photograph of individual sample layers. Layers were separated for weighing. (Mass loss Situation 2)

Erosion Yield Data

Flight sample mass loss:	0.066860 g
Average density:	1.7623 g/cm^3
Exposed area:	3.4993 cm^2

MISSE 2 E_y: $1.29\ (\pm0.03)\times10^{-24}$ cm^3/atom

* Computed mass for Part B is based on the average mass for Part A flight and control samples.

APPENDIX E

LESSONS LEARNED FROM ATOMIC OXYGEN INTERACTION WITH SPACECRAFT MATERIALS IN LOW EARTH ORBIT

E.1 Purpose and/or Scope

The purpose of this appendix is to provide lessons learned from MISSE and other flight experiments.

E.2 Introduction

As a result of post-retrieval analyses of early MISSE experiments and space experiments such as LDEF, valuable lessons have been learned and needs identified that are worthy of documentation for use in the planning, design, and analysis of future space environment experiments. Some of these lessons involve techniques, concepts, and issues associated with measuring atomic oxygen erosion yields.

This appendix represents a collection of lessons with respect to atomic oxygen interactions resulting from a variety of space experiments, as well as retrieved spacecraft materials and components, such as from NASA's LDEF, NASA's EOIM III experiment, the Russian Space Station Mir, NASA's MISSE 2, the Japanese Aerospace Exploration Agency's (JAXA's) Service Module/Micro-Particles Capturer & Space Environment Exposure Device (SM/MPAC & SEED), and the Hubble Space Telescope (Banks et al., 2008). These are presented, along with several issues to be considered when designing experiments, such as uncertainty in mission duration, scattering and contamination effects on results, and the accuracy of measuring atomic oxygen erosion. The collective experiences from these LEO flights provide useful considerations for future experiments that involve atomic oxygen interaction with materials. The objective of this appendix is to explain and capture these experiences to benefit the quality of future spacecraft experiments and missions.

E.3 Lessons Learned

E.3.1 Written Instructions and Procedures

Written instructions and procedures should be used for preparing, assembly, mounting, testing and examination, or testing of coupon substrate and coated samples for flight experiments. Good research practices, which provide repeatable results at the level of credibility requisite for space flight hardware, should be used. Materials, processes, equipment, and systems are required to be designed, procured, fabricated, assembled, tested, and inspected in accordance with Agency-, program-, and project-specific quality assurance requirements.

Occasionally, written instructions and procedures for mounting and assembly of space flight hardware are not followed closely by those who are tasked with final installation. An example of this is the experience of one of the authors regarding an experiment on EOIM-III involving a

pinhole camera. The cover on the experiment contained a small hole that was to act as a lens for the camera, and a written note was provided in the installation instructions with a warning to "not remove the cover of the Pinhole Camera which contains the pinhole;" however, post-flight inspection of the Shuttle cargo bay containing the experiment revealed that the cover had in fact been removed before flight and then had been reattached after removal of the hardware from the cargo bay. Because the cover was reattached after removal from the Shuttle cargo bay, it appeared to have been on during flight. The experiment was a total failure as a result of the cover's removal before flight. High-resolution images of experiments taken just after launch can help validate proper installation. Pictures taken at various time intervals throughout the duration of the experiment can also provide valuable information about experiment function and material degradation.

The lesson learned is that it is important to make sure there is a process to verify and/or witness that instructions and procedures are properly followed.

E.3.2 Estimates of Mission Durations

The durations of space experiments that involve retrieval of hardware are frequently much longer than initially planned because of a variety of factors that cannot be accurately predicted at the time the experiments are being developed. Table 25, Comparison of Planned and Actual Mission Durations, lists the planned and actual mission durations for four missions in which experiment retrievals were accomplished (O'Neal and Lightner, 1991; Silverman, 1995; Banks et al., 1993; Pippin, 2006). The average mission lasted 2.63 times longer than initially planned.

Table 25—Comparison of Planned and Actual Mission Durations

Mission	**Planned Duration** (yr)	**Actual Duration** (yr)	**Ratio of Actual/Planned**
LDEF	1	5.75	5.75
EURECA*	0.83	0.89	1.07
MISSE 1-2	1-1.5	3.95	2.64
MISSE 3-4	1	1.04	1.04

*European Retrievable Carrier.

For NASA GRC's MISSE 2 PEACE Polymers experiment, the principal investigators designed the experiment so that the thicknesses of the samples used for atomic oxygen erosion yield testing were three times thicker than what was needed to survive the original planned mission duration (1 year), based on estimated erosion yields. This procedure resulted in 85 percent of the material samples surviving the mission, which lasted four times longer than initially planned (de Groh et al., 2008).

The lesson learned is to design experiments to survive a considerably longer duration — at least three times longer than the planned mission duration — to ensure that meaningful results will be obtained, even if the mission duration is significantly longer than planned. For example, multiple layers of thin-film polymers can be stacked together rather than one single layer being flown.

E.3.3 Silicone Contamination Sources and Consequences

Silicones that have not been vacuum-stripped frequently contain short-chain molecules that are volatile and readily transported onto neighboring surfaces. Vacuum stripping consists of vacuum removal of the short-chain, highly volatile components of the polymer before polymerization. When these contaminated spacecraft surfaces are exposed to atomic oxygen in LEO, the silicones oxidize to form silica (or silicates). Hydrocarbons can also be trapped on the surface during this process. The resulting deposit can form an atomic-oxygen-protective coating that can darken as a result of solar radiation exposure. Evidence of the consequence of silicone contamination could be seen on selected samples flown on LDEF, as shown in figure 61, Post-Flight Photograph of Solar Array Materials Passive LDEF Experiment AO171, where several samples outgassed volatile silicones (Banks et al, 1991). The photograph shows silicone RTV-511 samples, the lighter color samples within the blue-bordered area. These samples were exposed to an atomic oxygen fluence of 7.17×10^{21} atoms/cm^2, with the atoms arriving from the upper left at an angle of 38° from normal incidence. Some of the volatile silicone deposits on the sample holder plate became oxidized by atomic oxygen. These became fixed on the surface and darkened with UV radiation exposure. Where the volatile silicones were deposited and not exposed to atomic oxygen, they gradually re-evaporated, and no darkening resulted, hence, the light boundary to the right of the samples, shown in the enlarged picture.

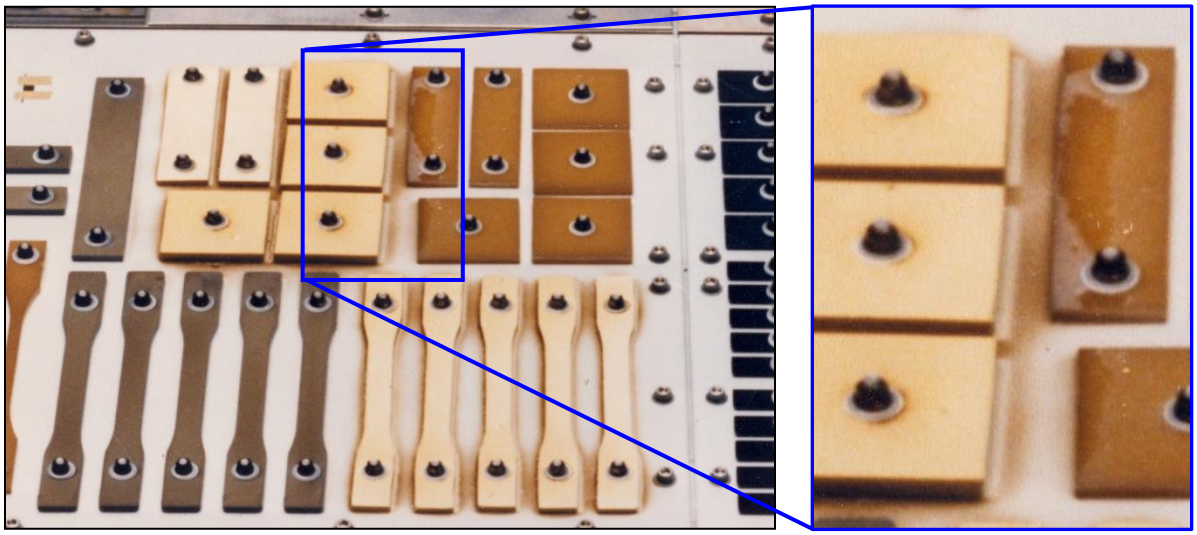

Figure 61—Post-Flight Photograph of Solar Array Materials Passive LDEF Experiment AO171

In November 1997, Russian cosmonauts retrieved a non-articulating, foldable panel solar array from the Mir core module after 10.4 years in LEO and returned it for an international cooperative analysis (Visentine et al., 1999; Banks et al., 1999). The solar array panels included a clad structure of solar cells, fiberglass scrim, cover glasses, optical solar reflectors, and an open-weave organic fabric coated with BF-4 adhesive. Silicone adhesives and thread sutures were used to clad the solar array structure together. Over time, volatile silicones (evolved from the suture holes surrounding the solar cells on both sides of the solar array) became deposited on the surface of the array. Figure 62, Oxidized Silicone Contamination on Solar Cell Components from a Mir Solar Array Retrieved after 10.4 years in LEO, shows photographs of the silica

deposits on the front and back of Mir solar cells resulting from atomic oxygen oxidization of the silicone adhesives that had been transported in the gaseous phase onto neighboring surfaces. The thick contamination appears as a white diffuse deposit. On the front surface of the array, the oxidized silicone contamination was up to 4.6 µm thick near suture sites (figure 62(a)). On the back surface of a solar reflector, a tape peel test was conducted (see the two black stripes at the upper right corner of figure 62(b)), which revealed that the contaminant layer was between 1.06 and 1.24 µm thick.

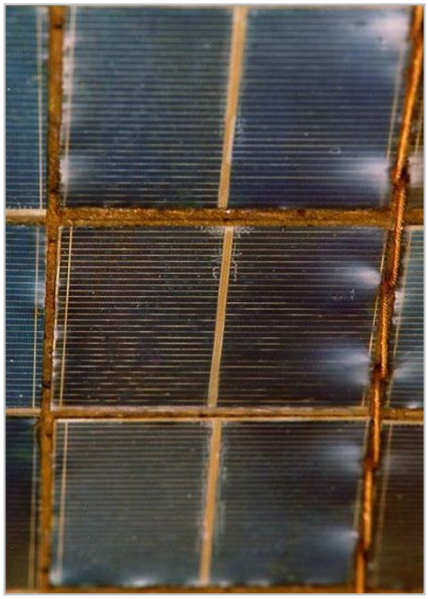

(a) Front surface of solar array with contamination up to 4.6 µm thick near suture sites

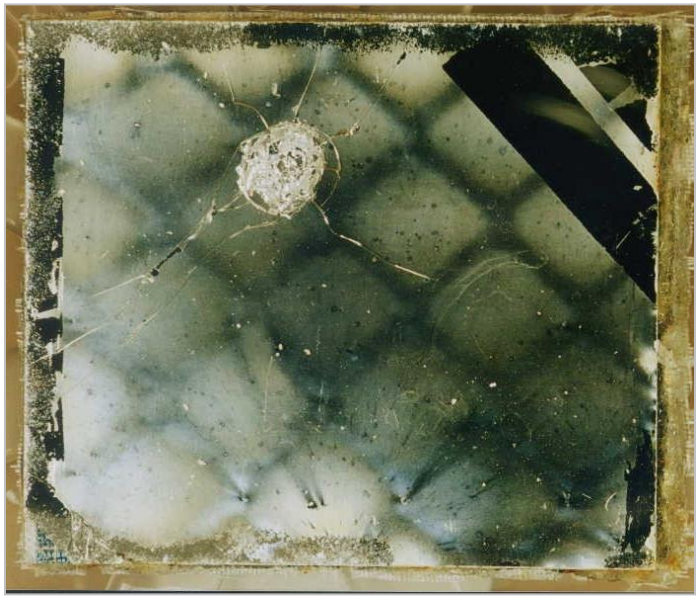

(b) Back surface of a solar reflector with contaminants between 1.06 and 1.24 µm thick at tape peel site

Figure 62—Oxidized Silicone Contamination on Solar Cell Components from a Mir Solar Array Retrieved after 10.4 years in LEO

Although the solar array did not significantly degrade in performance from the silica contamination, there was significant darkening of the optical solar reflector surfaces and neighboring thermal-control white paint surfaces. This solar array technology was also used for the Russian-supplied solar array for the ISS. Silicone deposition onto surfaces on the ISS from hardware such as this may result in contamination that could affect atomic oxygen erosion and solar absorptance.

Table 26, Silica-Based Contamination on ISS Experiment Surfaces, shows the large variation in silica-based contamination on surfaces from experiments placed at different locations on the ISS (Dever et al, 2006; Steagall et al., 2008). The MISSE PEC 2 had two orders of magnitude less contaminant thickness than the three JAXA experiment units (Dever 2006, Steagall 2008.) This is probably related to differences in the total arrival of silicones based on each experiment's respective view of, and distance from, contaminant sources on the ISS.

Table 26—Silica-Based Contamination on ISS Experiment Surfaces

Location	Contaminant Thickness(nm)	Duration of Exposure (yr)	Contaminant Thickness/Year (nm)
MISSE 2; Tray 1; ram facing	1.3 – 1.4	3.95	0.326 – 0.351
JAXA: Unit 1, ram facing Unit 2, ram facing Unit 3, ram facing	 30.0 75.0 93.5	 0.863 2.37 3.84	 34.8 31.7 24.3

The lesson learned concerning silicone contamination is that care must be taken to avoid experiment self-contamination. Experiments should also be out of the view of other sources of silicone to be sure that atomic oxygen does not produce silica deposits that can affect erosion yields or cause changes in solar absorptance.

E.3.4 Scattering of Atomic Oxygen

It has long been suspected that some of the atomic oxygen arriving at a surface will scatter with partial accommodation from surfaces with which the atomic oxygen reacts, as well as from non-reactive surfaces, such as most metal oxides (Banks et al., 2002; Banks et al., 2003; Banks et al., 2006). The scattered, un-reacted oxygen atoms can travel in a line-of-sight manner until they encounter another surface, where they may react, recombine, or scatter again. This can occur over thousands of meters. However, only recently have quantifiable scattering data been available, from a small scattering chamber flown on MISSE 2. The experiment consisted of a 2.54-cm-diameter scattering chamber containing a SiO_2-coated (on the ram-facing surface only) polyimide Kapton® H disk with a 3.05-mm-diameter aperture that allowed atomic oxygen to enter the chamber. The atomic oxygen would then scatter off an Al disk and react with the Kapton® on the bottom of the aperture disk. The bottom of the aperture disk was also coated in many microscopic salt particles, which served as protective areas from scattered atomic oxygen attack. Figure 63, MISSE 2 Atomic Oxygen Scattering Chamber Experiment, shows the experiment setup, and figure 64, Kapton® H Butte Remaining at Site of Protective Salt Particle, shows a salt particle site. After the salt particles were washed off, the amount of atomic oxygen erosion was measured as a function of ejection angle using profilometry. Although cosine (or Lambertian) scattering had been expected, the results indicated that normal incident atomic oxygen scattered in a rather narrow angular distribution, at approximately 45° from normal, as shown in figure 65, Atomic Oxygen Erosion as a Function of Ejection Angle. The scattered atomic oxygen produced a surprisingly high effective erosion yield: 21.8 percent of that of ram atomic oxygen for Kapton® H polyimide (Banks et al., 2006).

The lesson learned is that atomic oxygen does not scatter in a cosine distribution or in a specular direction but instead at 45° from normal for Al. This means that scattered atomic oxygen erosion of materials must be considered, depending upon the particular geometry of a spacecraft.

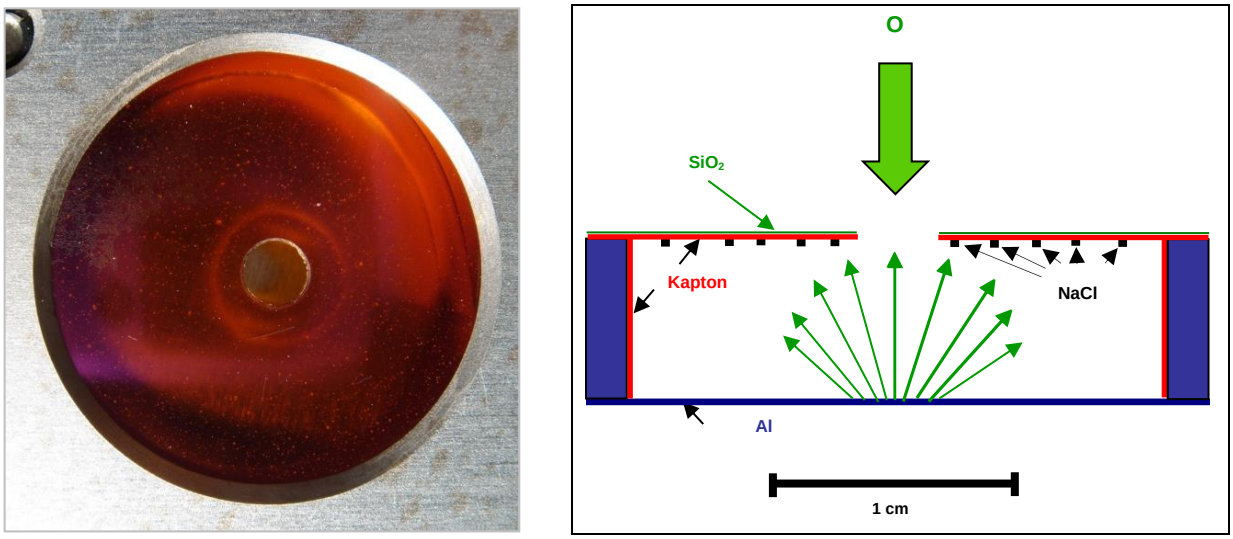

(a) Post-Flight Photograph (b) Section View Drawing

Figure 63—MISSE 2 Atomic Oxygen Scattering Chamber Experiment

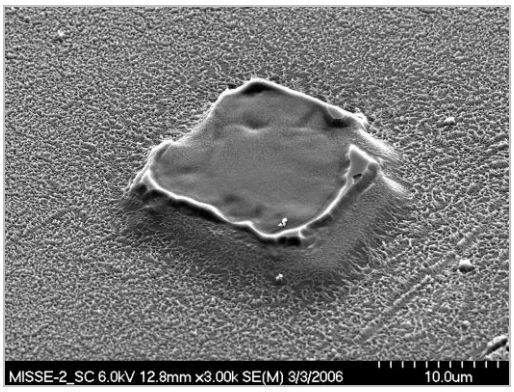

Figure 64—Kapton® H Butte Remaining at Site of Protective Salt Particle

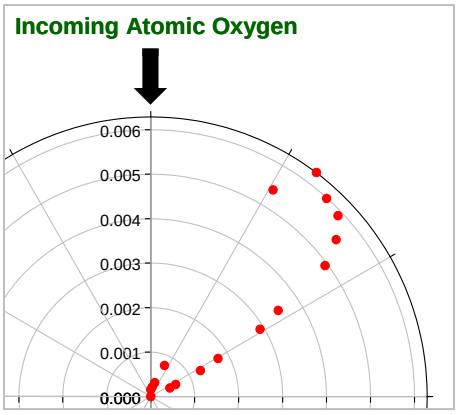

Figure 65—Atomic Oxygen Erosion as a Function of Ejection Angle

E.3.5 Sample Holder Geometry

The geometry of sample holders can influence the flux of atomic oxygen. The typical MISSE sample trays with chamfered circular apertures can allow atomic oxygen to scatter from the chamfered surfaces onto the samples, thus locally increasing the flux, as shown in figure 66, Flux Concentration from Chamfered MISSE Sample Holders. A consequence of the perimeter-scattered atomic oxygen is that the erosion around the sample perimeter is greater than in the central area. An example of this for measurements of the MISSE 2 PEACE PEO sample is shown in figure 67, Comparison of Pre- and Post-Flight Surface Profiles for the PEO Sample (2-E5-17). If the atomic oxygen is arriving off normal, then there will be a variation in flux around the perimeter of each sample depending on the scattering geometry. As can be seen in figure 68, MISSE 2 Tray 1 E5 Showing Samples Peeling up on Their Lower-Left Sides, two of the MISSE 2 samples peeled up from their lower left edge, and atomic oxygen was found to be arriving at 8° from normal and coming from the upper right direction. Therefore, there appears to be a flux concentration near the perimeter of the samples from the atomic oxygen that impinged upon the chamfered surface.

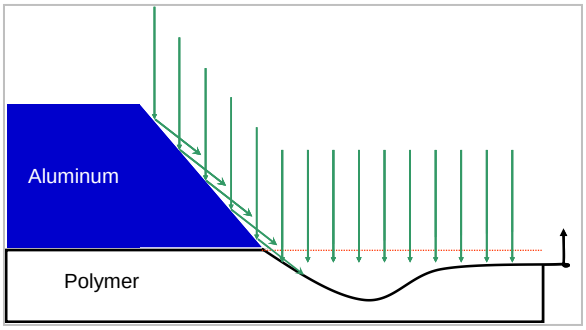

Figure 66—Flux Concentration from Chamfered MISSE Sample Holders

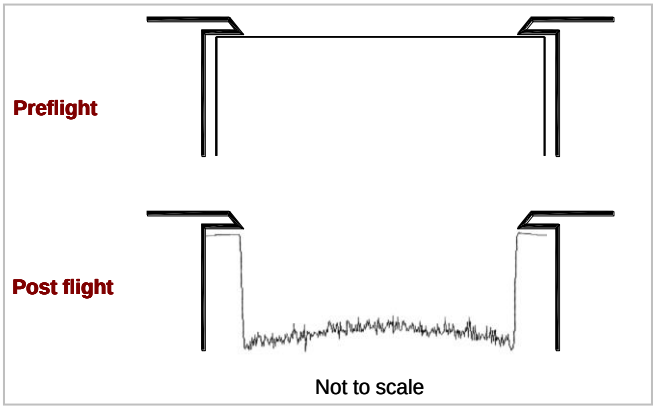

Figure 67—Comparison of Pre- and Post-Flight Surface Profiles for the PEO Sample (2-E5-17)

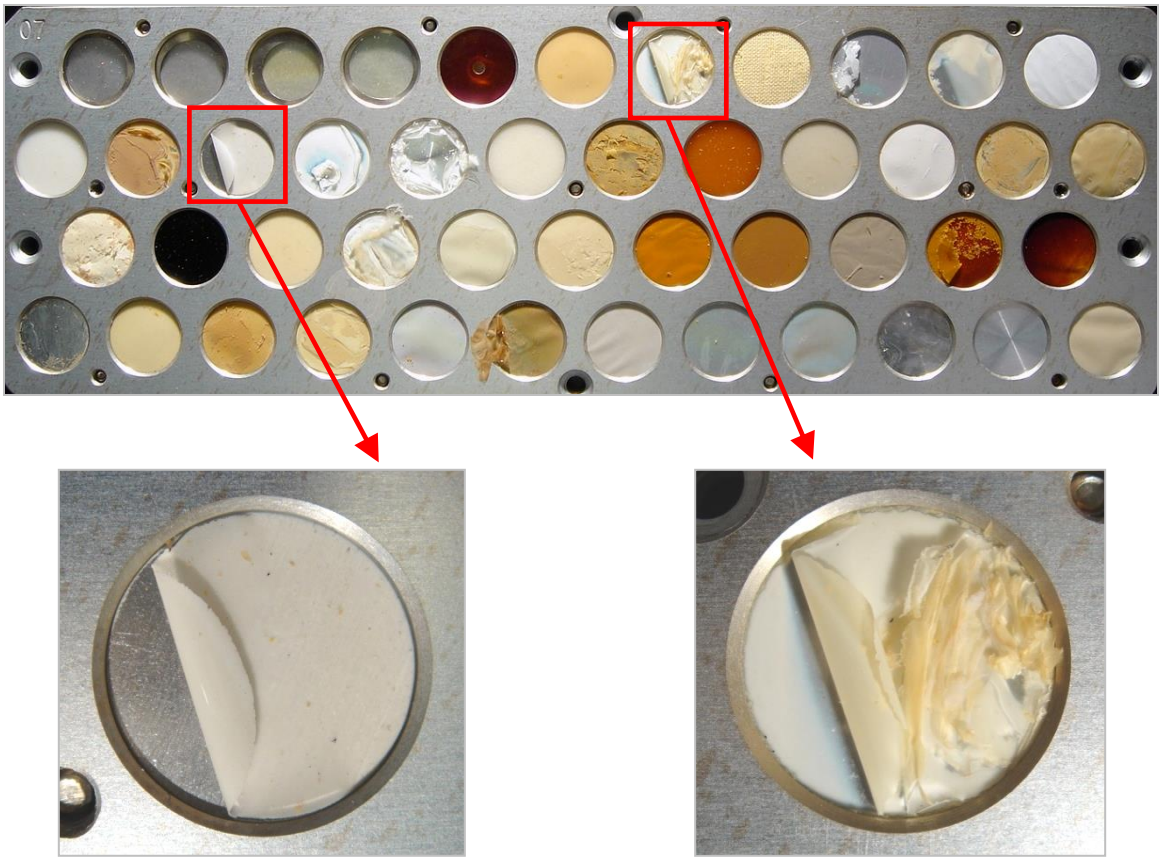

(a) Allyl Diglycol Carbonate (2-E5-14) (b) Cellulose Acetate (2-E5-7)

Figure 68—MISSE 2 Tray 1 E5 Showing Two Samples Peeling up on Their Lower-Left Sides

For the MISSE 2 trays with circular 2.54-cm-diameter samples, the chamfer was at 45°, and the lip was 0.763 mm thick. The maximum possible additional fluence for 2.54-cm-diameter samples caused by atomic oxygen scattering would be ~15 percent but, based on the previously discussed scattering chamber experiments, is more likely ~3.3 percent. Therefore, the concern is not a higher average fluence but rather sample peeling and potential release before full sample erosion, which could lead to incorrect erosion yield calculations.

The problem of flux concentration and premature peeling could be eliminated if a reverse chamfer were used on the sample holders, which would prevent scattering of atomic oxygen onto the sample surfaces. A potential disadvantage of this would be the loss of intimate contact at the edge of the sample, which is used for profiling purposes, but this would not be a concern for mass loss measurements.

The lesson learned is that sample holder chamfers can be a source of flux concentrations, which can disproportionately erode the perimeters of samples and, in some cases, cause the samples to roll up or potentially be released before full sample erosion. This problem could be eliminated by using a reverse chamfer on the sample holder.

E.3.6 Documentation of Sample Orientation s with Respect to Atomic Oxygen Ram Direction

Understanding the exact orientation of atomic oxygen arrival and arrival of contaminants can be very helpful in interpretation of environmental degradation results. Often, this information can be determined if the orientation of samples is documented before their removal from experiment trays. The exact orientation of the MISSE 2 atomic-oxygen-scattering chamber lid was documented, which allowed for the determination that holes had been drilled as a result of atomic oxygen arriving at 8° off-normal incidence and coming from the upper left of the photograph in figure 68 (Banks et al., 2006). This explained the preferential cutting out and peeling of thin samples around the lower left perimeter, as shown in figure 68.

The lesson learned is that critical information can be gained by either marking samples for orientation or photo-documenting the experiment before sample removal to determine sample orientation.

E.3.7 Duration between Retrieval and Tensile Testing

The time between retrieval of samples from space and ground-laboratory tensile testing can have a significant impact on the elongation-to-failure results for FEP and possibly other polymers that have been exposed to the LEO environment. For example, samples of 0.127-mm-thick silvered FEP (Ag-FEP) retrieved from the wake side (rows 1 and 4) of the LDEF in January 1990 and aluminized-FEP (Al-FEP) retrieved from the HST retrieved in December 1993 indicated a significant reduction in elongation-to-failure as time progressed after the retrieval dates (Banks et al.,1998; de Groh and Gummow, 2001), as shown in figure 69, Reduction in Elongation-to-Failure as a Result of Time after Retrieval for Ag-FEP and Al-FEP. Samples were taken from near-neighbor locations in both cases. Interestingly, the reduction in elongation-to-failure appears to continue long after radiation exposure occurs; this is thought to be caused by the formation and presence of long-lived free radicals (Judeikis et al., 1968; Li et al., 2005).

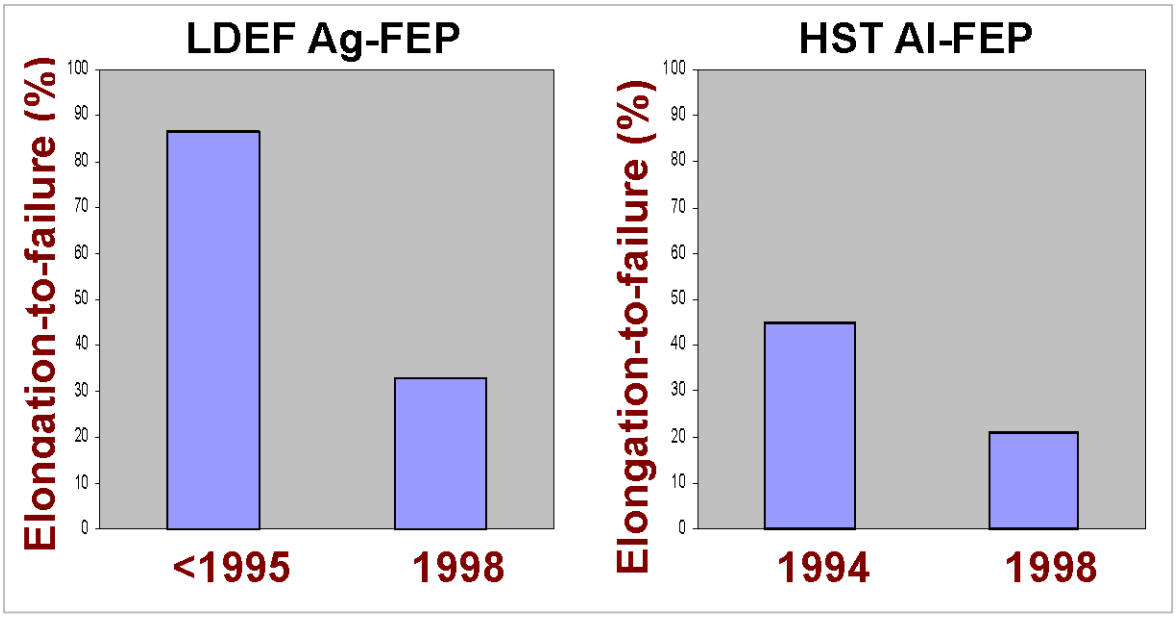

Figure 69—Reduction in Elongation-to-Failure as a Result of Time after Retrieval for Ag-FEP and Al-FEP

Ground testing also indicated that storage of FEP samples in a vacuum slows the rate of tensile property degradation (de Groh and Morgana, 2004). Polymer chain scission is believed to be responsible for the degradation of FEP and is initiated by the impact of energetic electrons and protons combined with thermal exposure (Townsend et al., 1999). Storing samples in air or elevated temperatures increases degradation rates as compared to storage in vacuum or low temperatures (Dever et al., 1999).

The lesson learned is that to properly evaluate radiation-induced tensile property damage in thin-film polymers, it is important to store samples in vacuum and at low (room) temperatures and to test them as soon as possible after retrieval. Use of multiple samples stored and tested over time after retrieval may allow back-extrapolation to the in-space properties if the degradation profile follows an exponential decay curve.

E.3.8 Erosion Depth versus Mass Loss for Erosion Yield Measurement

Measurement of the atomic oxygen erosion yields of thin-film polymers is complicated by the fact that cone-and-valley formation can result in erosion occurring through more than one stacked polymer sheet, as seen in figure 70, MISSE 2 PEEK Sample Stack Showing Partial Erosion of the Fourth and Fifth Layers. Figure 71, Atomic Oxygen Texturing Occurring across Two Layers of a Flight Stack of Polymer Samples, illustrates how the valleys between the cones can extend into a lower sample layer by providing a pathway for atomic oxygen to erode the layer below. This renders erosion yield measurement based on profilometry very inaccurate because the erosion is through (at least) two separate layers.

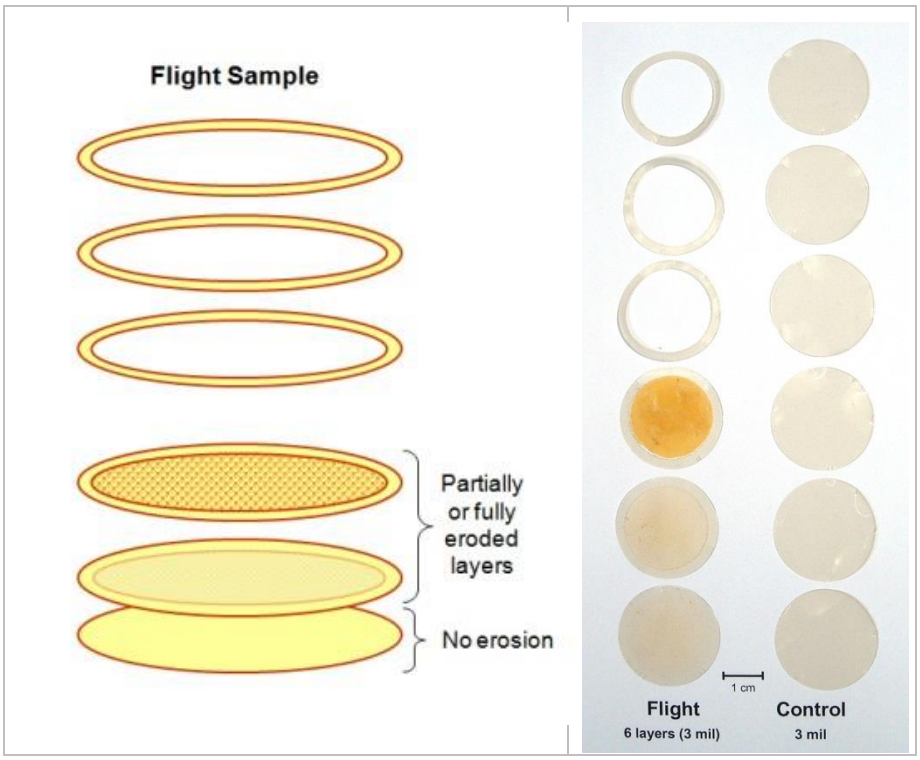

Figure 70—MISSE 2 PEEK Sample Stack Showing Partial Erosion of the Fourth and Fifth Layers

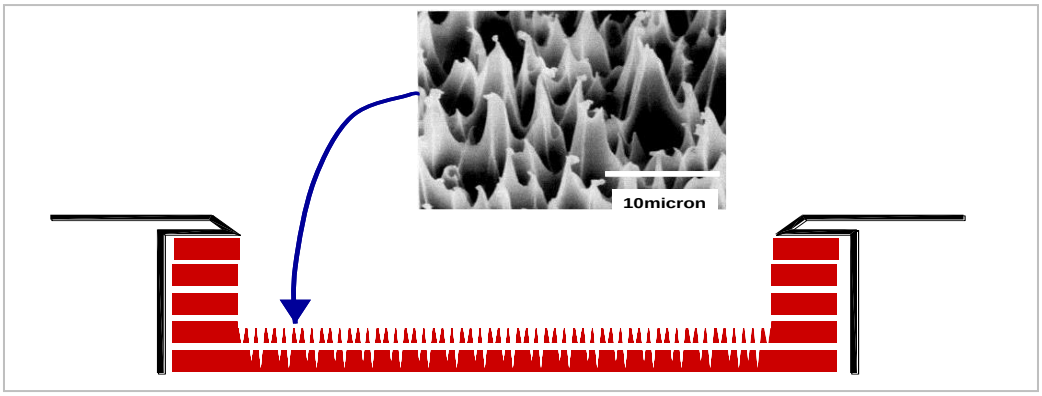

Figure 71—Atomic Oxygen Texturing Occurring across Two Layers of a Flight Stack of Polymer Samples

Dehydrated weight loss measurements can easily take this complication into account. Complete dehydration of samples is very important to avoid weight inaccuracies related to variations in the degree of absorbed water in the samples. However, for erosion yield determination based on mass loss, the densities of the samples need to be accurately known, and this information is not always readily available.

The lesson learned is to use dehydrated weight measurements to measure erosion yields of stacked thin-film polymers to avoid complications related to atomic oxygen texturing of samples.

E.3.9 Polymer Ash Content Effects on Atomic Oxygen Erosion Yield

Most polymers contain some fraction of inorganic material. As atomic oxygen erodes a polymer that contains inorganic material, the resulting nonvolatile ash begins to accumulate on the eroded surface of the polymer. For high-fluence missions, such as the MISSE 2 PEACE Polymers experiment (for which the fluence was 8.43×10^{21} atoms/cm^2) (de Groh et al., 2008), the underlying polymer can gradually become somewhat shielded from reacting with atomic oxygen. Therefore, it is theorized that a polymer's ash content has an effect on its erosion yield. Table 27, Comparison of the Erosion Yields of Two Pairs of Chemically Similar Polymers with Different Ash Contents, lists the erosion yields for two pairs of MISSE 2 PEACE Polymers that shared similar chemical structures. The data (de Groh et al., 2008) show that, in spite of the similar structures, the polymers' erosion yields differed, based largely on their ash content, which was measured by weighing and then exposing samples of the polymers (held in small Al foil cups) to atomic oxygen in an RF plasma asher until further weight loss occurred, which indicated that all the polymer was oxidized and only ash remained.

Table 27—Comparison of the Erosion Yields of Two Pairs of Chemically Similar Polymers with Different Ash Contents

Polymer	Ash Content (% by weight)	MISSE 2 Atomic Oxygen Erosion Yield (cm^3/atom)
PI (Kapton® H)	0.028	3.0×10^{-24}
PI (Kapton® HN)	0.289	2.81×10^{-24}
PA 6 (Nylon 6)	0.112	3.51×10^{-24}
PA 66 (Nylon 66)	0.361	1.80×10^{-24}

The lesson learned is that the ash content of polymers can significantly impact erosion yield, especially for high-fluence missions.

E.4 Summary

As a result of the data and experiences obtained from numerous spaceflight experiments, several lessons stand out as worthy of consideration by investigators designing experiments addressing the space environmental durability of materials. These lessons include the following:

a. It is important to witness and verify that instructions and procedures are properly followed and that variations or deviations are reported and dispositioned.

b. Experiments should be designed to provide useful results, even if the mission is significantly longer than planned.

c. Care should be taken to avoid experiment self-contamination and to place experiments out of the view of sources of silicone to reduce the possibility that volatile silicone deposits and atomic oxygen will react to produce silica deposits, which can affect erosion yields and cause changes in solar absorptance.

d. Atomic oxygen does not scatter in a cosine distribution or in a specular direction but instead at 45° from normal for Al. This means that the geometry of the spacecraft, which may lead to scattered atomic oxygen erosion of materials, should be taken into consideration.

e. Sample holder chamfers can be a source of flux concentrations that can cut out the perimeter of thin samples and, in some cases, cause the samples to roll up or be released before full sample erosion.

f. Samples to be evaluated for atomic oxygen interaction or durability evaluation should be marked so that their orientation is known. This allows for potential determination of causes of anomalous behavior with respect to the ram direction or possible contamination.

g. To properly evaluate radiation-induced tensile property damage in thin-film polymers, it is important to store samples in vacuum and at low (room) temperatures and to test them as soon as possible after retrieval.

h. Dehydrated weight measurements should be used in erosion yield measurement of stacked thin-film polymers to avoid complications related to atomic oxygen texturing of samples.

i. High ash content can result in a reduction in a polymer's erosion yield, especially for high-fluence missions. This should be taken into account when projecting the durability of a polymer being exposed to atomic oxygen.

E.6 References

Banks, B.; Lenczewski, M.; Demko, R. (October 10-19, 2002). *Durability Issues for the Protection of Materials from Atomic Oxygen Attack in Low Earth Orbit*. Paper IAC-02-1.5.02 presented at The 53rd International Astronautical Congress, The World Space Congress – 2002. Houston, TX. Also published as NASA/TM─2002-211830.

Banks, B.A.; de Groh, K.K.; Miller, S.K. (June 26-30, 2006). *MISSE Scattered Atomic Oxygen Characterization Experimen*t. Paper presented at the 2006 MISSE Post-Retrieval Conference, Orlando, FL. Also published as NASA/TM─2006-214355.

Banks, B.A.; de Groh, K.K.; Miller, S.K.; Waters, D.K. (May 19-23, 2008). "Lessons Learned from Atomic Oxygen Interaction with Spacecraft Materials in Low Earth Orbit." In J.I. Kleiman, Ed., *Proceedings of the 9th International Conference: Protection of Materials and Structures from Space Environment.* AIP Conference Proceedings 1087, pp. 312-328. Toronto, Canada. Also published as NASA/TM─2008-215264.

Banks, B.A.; de Groh, K.K.; Rutledge, S.K.; Haytas, C.A. (July 21, 1999). *Consequences of Atomic Oxygen Interaction with Silicone and Silicone Contamination on Surfaces in Low Earth Orbit*. Paper presented at the 44th Annual Meeting

sponsored by the International Society for Optical Engineering. Denver, CO. Also published as NASA/TM─1999-209179.

Banks, B.A.; Dever, J.A.; Gebauer, L.; Hill, C.M. (1991). "Atomic Oxygen Interactions with FEP Teflon® and Silicones on LDEF." In A.S. Levine, Ed., NASA CP-3134, *LDEF: 69 Months in Space. First Post-Retrieval Symposium, Part 2*. 801-815.

Banks, B.A.; Miller, S.K.R.; de Groh, K.K.; Demko. R., (June 16-20, 2003). "Scattered Atomic Oxygen Effects on Spacecraft Materials." In K. Fletcher, Ed., *Proceedings of the 9th International Symposium on Materials in a Space Environment*. Noordwijk, The Netherlands. ESA SP-540, 145-152.

Banks, B.A.; Rutledge, S.K.; Cales, M. (November 8-12, 1993). *Performance Characterization of EURECA Retroreflectors with Fluoropolymer-Filled SiO_x Protective Coatings*. Paper presented at the Third LDEF Post-Retrieval Symposium. NASA LaRC: Williamsburg, VA.

Banks, B.A.; Stueber, T.J.; Rutledge, S.K.; Jaworske, D.J.; Peters, W. (January 12-15, 1998). *Thermal Cycling Caused Degradation of Hubble Space Telescope Aluminized FEP Thermal Insulation*. AIAA paper No. 98-0896 presented at the 36th Aerospace Sciences Meeting & Exhibit. Reno, NV.

de Groh, K.K.; Banks, B.A.; McCarthy, C.E.; Rucker, R.N.; Roberts, L.M.; Berger, L.A. (August 2008). "MISSE 2 PEACE Polymers Atomic Oxygen Erosion Experiment on the International Space Station." *High Performance Polymers*. Vol. 20, pp. 388-409.

de Groh, K.; Morgana, M. (May-June 2004). "Thermal Contributions to the Degradation of Ground Laboratory and Space-Irradiated Teflon." *Journal of Spacecraft and Rockets*. Vol. 41, No. 3, pp. 366-372.

de Groh, Kim K.; Gummow, J.D. (September 2001). "Effect of Air and Vacuum Storage on the Tensile Properties of X-Ray Exposed Aluminized-FEP." *High Performance Polymers*. Vol, 13, 3, pp. S421-S431.

Dever, J.A.; de Groh, K.K.; Banks, B.A.; Townsend, J.A. (March 1999). "Effects of Radiation and Thermal Cycling on Teflon FEP." *High Performance Polymers*. Vol 11, 1. pp.123-140.

Dever, J.A.; Miller, S.K.; Sechkar, E.A.; Wittberg, T.N. (June 26-30, 2006). "Preliminary Analysis of Polymer Film Thermal Control and Gossamer Materials Experiments on MISSE 1 and MISSE 2." *Proceedings of the 2006 National Space & Missile Materials Symposium*. Orlando, FL.

Judeikis, H.; Hedgpeth, H.; Siegel, S. (August 1968). "Fee Radical Yields in Polytetrafluoroethylene as the Basis of a Radiation Dosimeter." *Radiation Research*. Vol. 35, No. 2, , pp. 247-262.

Li, C.; Yang, D.; He, S. (June 2005). "Effects of Proton Exposure on Aluminized Teflon FEP Film Degradation." *Nuclear Instruments and Methods in Physics Research Section B: Beam Interactions with Materials and Atoms*. Vol. 234, Issue 3, pp. 249-255.

O'Neal, R.L.; Lightner, E.B.; (June 2-8 1991). "Long Duration Exposure Facility--A General Overview." In A.S. Levine, Ed., NASA CP-3134, *LDEF-69 Months in Space, First Post-Retrieval Symposium, Part 1*. pp. 3–48.

Pippin, G. (2006). *Summary Status of MISSE-1 and MISSE-2 Experiments and Details of Estimated Environmental Exposures for MISSE-1 and MISSE-2."* Final Report for 24 June 2002 – 31 July 2006. AFRL-ML-WP-TR-2006-4237, TECHNICAL OPERATIONS SUPPORT (TOPS) II (Delivery Order 0011). Wright-Patterson Air Force Base, Air Force Research Laboratory, OH.

Silverman, E.M. (August 1995). *Space Environmental Effects on Spacecraft: LEO Materials Selection Guide.* NASA CR 4661, Part 1. NASA MSFC: Huntsville, AL.

Steagall, C.; Smith, K.; Huang, A.; Soares, C.; Mikatarian, R. (2008). "Induced Contamination Predictions for JAXA's Micro-Particles Capturer and Space Environment Exposure Devices." *Proceedings of the International Symposium on SM/MPAC&SEED Experiment*. JAXA-SP-08-015E, pp. 19-25. Tsukuba, Japan.

Townsend, J.; Hansen, P.; McClendon, M.; deGroh, K.; Banks, B.; Triolo, J. (March 1999). "Ground-Based Testing of Replacement Thermal Control Materials for the Hubble Space Telescope." *High Performance Polymers*. Vol. 11, pp. 63-79.

Visentine, J.; Kinard, W.; Pinkerton, R.; Brinker, D.; Scheiman, D.; Banks, B.; Zweiner, J.; Albyn, K.; Farrell, T.; Hornung, S.; See, T. (January 11-14, 1999). *Mir Solar Array Return Experiment*. AIAA paper 99-0100 presented at the 37th AIAA Aerospace Sciences Meeting. Reno, NV.

APPENDIX F

ADDITIONAL REFERENCE DOCUMENTS

F.1 Purpose and/or Scope

The purpose of this appendix is to recommend relevant documents for further reading.

F.2 Additional References

Henninger, J. H. (April 1984.) *Solar Absorptance and Thermal Emittance of Some Common Spacecraft Thermal-Control Coatings.* NASA RP 1121. NASA Goddard Space Flight Center: Greenbelt, MD. Retrieved June 12, 2013, http://www.dtic.mil/cgi-bin/GetTRDoc?Location=U2&doc=GetTRDoc.pdf&AD=ADA305864.

Silverman, E.M. (August 1995). *Space Environmental Effects on Spacecraft: LEO Materials Selection Guide.* NASA CR-4661, Part 1 and Part 2. NASA MSFC: Huntsville, AL.

Dooling, D.; Finchenor, M.M. (June 1999.) *Material Selection Guidelines to Limit Atomic Oxygen Effects on Spacecraft Surfaces.* NASA/TP-1999-209260. NASA MSFC: Huntsville, AL. Retrieved June 25, 2013. http://sisko.colorado.edu/CRIA/FILES/REFS/Materials/NASA%20mtl%20selection%20guide%20to%20limit%20atomic%20oxy%20effects.pdf